Search for Astrophysical Tau-Neutrinos in Six Years of High-Energy Starting Events in the IceCube Detector

D I S S E R T A T I O N

zur Erlangung des akademischen Grades
doctor rerum naturalium
(Dr. rer. nat.)

im Fach Physik

eingereicht an der
Mathematisch-Naturwissenschaftlichen Fakultät
der Humboldt-Universität zu Berlin

von

Marcel Usner, M.Sc.

Präsidentin der Humboldt-Universität zu Berlin:
Prof. Dr.-Ing. Dr. Sabine Kunst

Dekan der Mathematisch-Naturwissenschaftlichen Fakultät:
Prof. Dr. Elmar Kulke

Gutachter:
1. Prof. Dr. Marek Kowalski
2. Prof. Dr. Sebastian Böser
3. Prof. Dr. Achim Stahl

Tag der mündlichen Prüfung: 21. September 2018

Abstract

The sources that accelerate the highest-energy cosmic rays have yet to be identified. Astrophysical neutrinos are messenger particles because they point back to the sources which produce them in interactions of cosmic rays with ambient matter or photons. The observable flavor composition on Earth may constrain possible production scenarios at these sources. The appearance of tau-neutrinos due to neutrino oscillations over cosmic baselines is a clear astrophysical signature.

The IceCube Neutrino Observatory is a Cherenkov detector, located at the geographic South Pole, whose purpose is to measure high-energy neutrinos of astrophysical origin. About $1\,\mathrm{km}^3$ of the ultra-transparent glacial ice located deep below the surface is instrumented with 5160 optical photo-sensors. Neutrinos are detected via Cherenkov light emitted by secondary particles from deep-inelastic neutrino-nucleon interactions. A diffuse flux of astrophysical neutrinos between $\sim 60\,\mathrm{TeV}$ to $\sim 10\,\mathrm{PeV}$ energy was discovered with IceCube. Previously published measurements of the flavor composition are compatible with $\nu_e : \nu_\mu : \nu_\tau \simeq 1 : 1 : 1$ expected from pion production and decay at the sources. However, the electron- and tau-neutrino fractions remain largely unconstrained, because they cannot be distinguished by the readily identifiable cascade- and track-like events.

The work presented in this thesis aims to identify a tau-neutrino interaction in IceCube for the first time while measuring the astrophysical neutrino flavor composition and constraining the tau-neutrino fraction with unprecedented accuracy. The search is based on the "double bang" event topology, which is unique to the tau-flavor and characterized by two consecutive cascades from the charged-current interaction of a tau-neutrino with a nucleus in the ice and the subsequent decay of the produced tau lepton. A tau-neutrino identification method is developed by explicitly reconstructing this event topology, for which the distance between both cascades is an estimator of the tau decay length. The well-established binary topology ID (cascade, track) is extended to a ternary topology ID (single cascade, double cascade, track), thereby allowing a neutrino flavor discrimination that is sensitive to all flavors. Additional observables are the deposited energy, the zenith angle, and the tau decay length. A previously unexamined systematic error caused by an anisotropy of the light scattering in the Antarctic ice is incorporated and tested with experimental data from the in-situ flasher LED calibration system. The astrophysical neutrino flavor composition is measured via a binned maximum likelihood fit using the high-energy starting event sample collected between 2010 and 2016.

Above $\sim 200\,\mathrm{TeV}$ deposited energy, the identification efficiency of tau-neutrinos is between $\sim 30 - 50\%$ and the background contamination $\sim 5 - 25\%$. The tau decay length is resolved to $\sim 2\,\mathrm{m}$ above the experimental resolution limit of $\sim 10\,\mathrm{m}$. The double cascade event sample is expected to contain $\sim 1-3$ identifiable tau-neutrino interactions and ~ 1 background event, depending on the assumed neutrino energy spectrum. No such event is observed in experimental data. The astrophysical tau-neutrino flux is constrained by $\phi^{\mathrm{u.l.}}_{\nu_\tau} \leq 2.68 \cdot 10^{-18}\,(E_{\nu_\tau}/100\,\mathrm{TeV})^{-2.97}\,\mathrm{GeV}^{-1}\,\mathrm{cm}^{-2}\,\mathrm{sr}^{-1}\,\mathrm{s}^{-1}$ at 90% confidence level. The measured flavor composition of $\nu_e : \nu_\mu : \nu_\tau \simeq 0.51 : 0.49 : 0$ is compatible with the production and decay of charged pions at the sources ($p = 37.5\%$).

The results entail the most sensitive search for highly energetic tau-neutrino interactions in IceCube. For the first time, a measurement of the neutrino flavor composition is able to simultaneously constrain all flavors.

Zusammenfassung

Die Quellen der höchstenergetischen kosmischen Strahlung sind bislang unbekannt. Astrophysikalische Neutrinos sind Botenteilchen, da die auf der Erde beobachtete Ankunftsrichtung auf ihren Ursprungsort deutet. Sie entstehen in der Wechselwirkung kosmischer Strahlungsteilchen mit Materie oder Photonen nahe der Quellen. Die auf der Erde erwartete Flavor-Zusammensetzung kann mögliche Neutrino Produktionsmechanismen einschränken. Die Detektion von Tau-Neutrinos wäre aufgrund von Flavor-Oszillationen über kosmische Distanzen ein Nachweis für einen astrophysikalischen Ursprung.

Das IceCube Neutrino Observatorium befindet sich am geografischen Südpol und ist ein Cherenkov-Detektor zur Messung hochenergetischer astrophysikalischer Neutrinos. Ein Volumen von $\sim 1\,\mathrm{km}^3$ des tiefen, transparenten Gletschereises ist mit 5160 optischen Fotosensoren instrumentiert. Neutrinos werden über Cherenkovstrahlung detektiert, die von Sekundärteilchen aus der tiefinelastischen Streuung von Neutrinos mit Atomkernen im Eis emittiert wird. Ein astrophysikalischer Neutrinofluss wurde von IceCube bei Energien zwischen $\sim 60\,\mathrm{TeV}$ und $\sim 10\,\mathrm{PeV}$ entdeckt. Messungen der Flavor-Zusammensetzung sind kompatibel mit einem Verhältnis von $\nu_e : \nu_\mu : \nu_\tau \simeq 1 : 1 : 1$, wie von Produktion und Zerfall geladener Pionen an den Quellen erwartet wird. Die Elektron- und Tau-Neutrino Anteile sind jedoch weitestgehend unbestimmt, weil sie durch die bislang einzig identifizierbaren Ereignistopologien von Kaskaden und Spuren ununterscheidbar sind.

Die in dieser Dissertation präsentierte Forschungsarbeit hat das Ziel, die erste Tau-Neutrino Wechselwirkung in IceCube nachzuweisen und die astrophysikalische Neutrino Flavor-Zusammensetzung mit bislang unerreichter Genauigkeit des Tau-Neutrino Anteils zu messen. Die Suche basiert auf der „Double Bang“ Ereignistopologie, die einzigartig für den Tau-Flavor ist. Sie ist durch zwei aufeinanderfolgende Kaskaden beschrieben, welche durch die Wechselwirkung eines Tau-Neutrinos mit einem Atomkern im Eis beziehungsweise durch den Zerfall des erzeugten Tau Leptons erzeugt werden. Eine Methode zur Identifizierung von Tau-Neutrinos wird entwickelt, indem diese Ereignistopologie explizit rekonstruiert wird. Der Abstand zwischen beiden Kaskaden schätzt die Tau-Zerfallslänge ab. Die bislang genutzte binäre Topologie ID (Kaskade, Spur) wird zu einer tertiären Topologie ID (Einzel-Kaskade, Doppel-Kaskade, Spur) erweitert. Dadurch wird eine Unterscheidung von Neutrinos aller Flavor ermöglicht. Die Anisotropie der Lichtstreuung im Antarktischen Eis ist eine zuvor unberücksichtigte systematische Fehlerquelle, die integriert und mit dem in situ LED Kalibrationssystem getestet wird. Die astrophysikalische Neutrino Flavor-Zusammensetzung wird mithilfe eines gebinnten Maximum-Likelihood Fits gemessen. Dafür wird der zwischen 2010 und 2016 aufgenommene Datensatz hochenergetischer startender Ereignisse verwendet.

Tau-Neutrinos können oberhalb einer deponierten Energie von $\sim 200\,\mathrm{TeV}$ mit einer Effizienz zwischen $\sim 30 - 50\%$ bei einer Untergrundkontamination von $\sim 5 - 25\%$ identifiziert werden. Oberhalb der experimentellen Auflösungsgrenze von $\sim 10\,\mathrm{m}$ wird die Tau-Zerfallslänge auf $\sim 2\,\mathrm{m}$ genau bestimmt. In Abhängigkeit des angenommenen Neutrino-Energiespektrums werden $\sim 1 - 3$ identifizierbare Tau-Neutrinos und ~ 1 Untergrundereignis erwartet. Kein solches Ereignis wird in den experimentellen Daten beobachtet. Der astrophysikalische Tau-Neutrino Fluss wird mit einem Konfidenzniveau von 90% durch $\phi^{\mathrm{u.l.}}_{\nu_\tau} \leq 2.68 \cdot 10^{-18} \left(E_{\nu_\tau}/100\,\mathrm{TeV}\right)^{-2.97}\,\mathrm{GeV}^{-1}\,\mathrm{cm}^{-2}\,\mathrm{sr}^{-1}\,\mathrm{s}^{-1}$ beschränkt. Die gemessene Flavor-Zusammensetzung von $\nu_e : \nu_\mu : \nu_\tau \simeq 0.51 : 0.49 : 0$ ist mit der Produktion und dem Zerfall geladenener Pionen an den Quellen kompatibel ($p = 37.5\%$).

Die Ergebnisse beinhalten die aktuellste und sensitivste Suche nach hochenergetischen Tau-Neutrinos in IceCube. Zum ersten Mal ist eine Messung der Neutrino Flavor-Zusammensetzung mit simultaner Einschränkung aller Flavor möglich.

Für Lena und Jakob.

Contents

1 Introduction **1**

2 The High-Energy Neutrino Landscape **7**
2.1 Cosmic Rays . . . 8
2.2 Extensive Air Showers . . . 11
2.2.1 Atmospheric Muons . . . 12
2.2.2 Atmospheric Neutrinos . . . 14
2.3 Astrophysical Neutrinos . . . 16
2.3.1 Production Mechanisms and Source Candidates . . . 16
2.3.2 Observation of a Diffuse Astrophysical Neutrino Flux . . . 18
2.3.3 Neutrino Oscillations and Flavor Composition . . . 20
2.3.4 Sterile Neutrinos, Neutrino Decay, and Other More Exotic Phenomena 25

3 The IceCube Neutrino Observatory **27**
3.1 Neutrino Detection . . . 28
3.1.1 Neutrino Interaction Channels . . . 28
3.1.2 Lepton Propagation in Ice . . . 29
3.1.3 Particle Showers . . . 31
3.1.4 Cherenkov Radiation . . . 33
3.2 Detector Components . . . 34
3.2.1 IceCube, DeepCore, and IceTop . . . 34
3.2.2 Digital Optical Modules and Flasher LEDs . . . 36
3.2.3 Triggering, Data Acquisition, and Event Filtering . . . 37
3.2.4 Optical Properties of the South Pole Ice . . . 38
3.3 (Re)construction of an IceCube Event . . . 39
3.3.1 Event Topologies . . . 40
3.3.2 Monte Carlo Event Simulation . . . 41
3.3.3 Maximum Likelihood Event Reconstruction . . . 44

4 Development of Tau-Neutrino Identification **47**
4.1 Tau-Neutrino Interactions in IceCube . . . 48
4.2 High-Energy Starting Event Selection . . . 49
4.3 Double Cascade Event Reconstruction . . . 52
4.3.1 Implementation and Tau-Neutrino-Related Observables . . . 52
4.3.2 Neutrino Flavor Discrimination . . . 60
4.3.3 Distributions and Resolution of Event Properties . . . 67
4.4 Tau-Neutrino Identification Efficiency . . . 73

5 Systematic Treatment of the Ice Anisotropy **79**
5.1 Effect of the Ice Anisotropy on Tau-Neutrino Identification . . . 80
5.2 Incorporation of the Ice Anisotropy into Reconstruction . . . 81
5.2.1 Photo Spline Tables and Technical Limitations . . . 81
5.2.2 Effective Distance Parametrization . . . 84
5.2.3 Implementation and Simulation Test Results . . . 90
5.2.4 Double Cascade Reconstruction and Identification . . . 98

5.3 Experimental Test with Flasher LED Data . . . 102
5.3.1 Single Flasher LED Anisotropy Data Sample . . . 102
5.3.2 Construction of an Experimental Double Flasher . . . 104
5.3.3 Double Flasher Reconstruction and Identification . . . 110
5.4 Summary and Conclusions to Tau-Neutrino Identification . . . 116

6 Likelihood-Based Measurement of the Astrophysical Neutrino Flavor Composition 117
6.1 Analysis Method . . . 118
6.2 Components of the Likelihood Fit . . . 120
6.2.1 Model Parameters . . . 121
6.2.2 Observables . . . 122
6.2.3 Systematic Uncertainties . . . 125
6.3 Sensitivity . . . 133
6.3.1 Signal and Background Expectations . . . 133
6.3.2 Astrophysical Tau-Neutrino Flux Sensitivity . . . 136
6.3.3 Astrophysical Neutrino Flavor Composition Sensitivity . . . 140
6.3.4 Dependence on the Spectral Shape of the Astrophysical Neutrino Flux 141

7 Results 151
7.1 Fit Results and Data-Monte-Carlo Agreement . . . 152
7.2 Upper Limit on the Astrophysical Tau-Neutrino Flux . . . 155
7.3 Measurement of the Astrophysical Neutrino Flavor Composition . . . 156
7.4 Discussion . . . 158

8 Summary and Outlook 163

A Parametrization of the Ice Anisotropy as a Nuisance Parameter 167

B Selected Single LED Flasher DOMs 177

C Construction of Confidence Regions via Monte Carlo Pseudo Experiments 179
C.1 Sensitivity Estimation . . . 179
C.2 Measurement Results . . . 181

Bibliography 202

List of Figures 203

List of Tables 207

List of Frequently Used Acronyms 209

Acknowledgements 211

Selbstständigkeitserklärung 213

1 Introduction

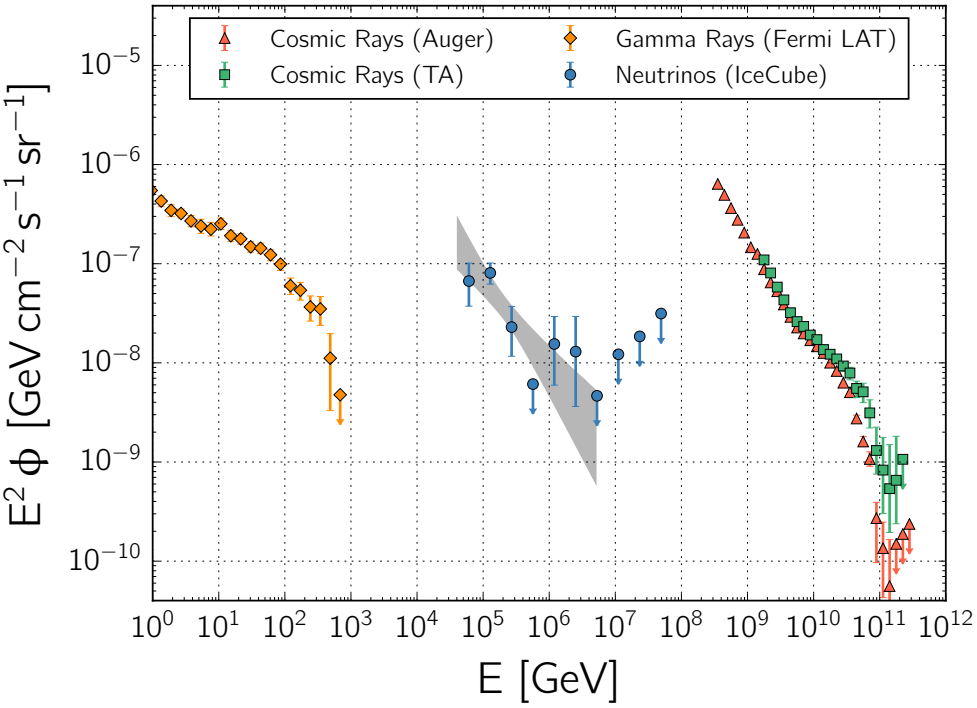

Figure 1.1: Comparison of the diffuse fluxes of cosmic rays, gamma rays, and neutrinos. The flux ϕ is depicted as a function of the energy E and scaled by E^2 to enhance the visibility of spectral features. The measurement of the diffuse extra-galactic gamma-ray flux has been performed by Fermi LAT [1]. The ultra-high-energy cosmic-ray flux has been measured by the Pierre Auger Observatory [2] and by Telescope Array [3]. The diffuse neutrino flux is a recently updated measurement by the IceCube Neutrino Observatory [4]. Figure adapted from [5].

The universe is a mysterious place, and many questions remain unanswered. For centuries, astronomers have used optical telescopes to observe the visible part of the night sky and study its objects. Great technological advances over the last decades have enabled the investigation of the universe using a much wider range of electromagnetic frequencies. It has been extended to radio waves at the lower and to gamma rays at the upper part of the spectrum, thus spanning many orders of magnitude in energy. The discovery of cosmic rays at the beginning of the 20th century and the incremental development of the standard model of particle physics during the latter half of the 20th century set the foundations for a new and supplementary discipline: Astroparticle physics emerged to observe the universe "with different eyes" through the use of matter instead of electromagnetic radiation. An important aim is to identify the sources of cosmic rays at the highest energies and connect the observed flux to gamma rays and possibly neutrinos. Neutrino astronomy has a key role for this purpose. Until the discovery of the first resolved neutrino source, the characterization of the astrophysical neutrino spectrum and flavor composition can constrain potential sources.

In 1912, Victor Hess discovered cosmic rays during multiple balloon ascents by measuring an increasing ionization rate in the atmosphere with higher altitudes [6]. He also performed a measurement during a near-total eclipse of the Sun and observed no change. The conclusion was that the observed radiation can only originate in outer space and that the Sun cannot be its source. More than a hundred years later, the cosmic-ray flux is characterized much better. It consists of ionized nuclei (most of which are protons) and spans a wide energy range from about 10^9 eV to 10^{20} eV. High-energy cosmic rays interact with nuclei in the atmosphere and induce extensive air showers. They are measured with experiments such as the *High Resolution Fly's Eye Cosmic-Ray Detector* (HiRes), which used fluorescence light for detection [7], and the *Pierre Auger Observatory* (Auger) [8] and *Telescope Array* (TA) [9]. The latter two combine fluorescence techniques with large surface detectors. The cosmic-ray spectrum is described by multiple power-laws, which can be attributed to different source populations and propagation effects. The high-energy part of the spectrum between 10^{17} eV and 10^{20} eV measured by Auger and TA is depicted in Figure 1.1. Sources that are capable of accelerating particles up to the highest energies remain unknown because magnetic fields between the source and Earth deflect the particles and thus obfuscate their origin. These sources may well only be identifiable by a combination of gamma-ray and neutrino observatories.

In 1958, Philip Morrison and others hypothesized that sources in the universe should emit gamma radiation [10]. The first significant detection of gamma rays from within the Milky Way was achieved with the *High-Energy Gamma-Ray* experiment aboard the *Third Orbiting Solar Observatory* (OSO-3) satellite [11]. Today, the cosmic gamma-ray flux is known much more precisely. It spans energies ranging from about 10^5 eV to 10^{14} eV. Several important space-based experiments have been continuously measuring the low-energy part of the spectrum up to $\sim 10^{12}$ eV. The *International Gamma-Ray Astrophysics Laboratory* (INTEGRAL) has been operational since 2002 [12], the *Neil Gehrels Swift Observatory* since 2004 [13], and the *Fermi Large Area Telescope* and *Gamma-Ray Burst Monitor* (Fermi LAT/GBM) since 2008 [14]. The extra-galactic gamma-ray flux measured by Fermi LAT is also shown in Figure 1.1. Ground-based *imaging atmospheric Cherenkov telescopes* (IACT) continue measurements of the gamma-ray flux at energies well above 10^{12} eV by using the atmosphere as detection medium. In this energy range, the flux is too low to be detectable with satellite experiments. Major IACTs are the *High Energy Stereoscopic System* (H.E.S.S.), which has been operating since 2002 [15], the *Major Atmospheric Gamma Imaging Cherenkov Telescopes* (MAGIC) since 2004 [16], and the *Very Energetic Radiation Imaging Telescope Array System* (VERITAS) since 2005 [17]. Unlike the sources of cosmic rays, many galactic and extra-galactic gamma-ray sources have been identified, because electromagnetic radiation is not deflected between its source and Earth.[1]

In 1930, Wolfgang Pauli postulated the existence of the neutrino in order to explain the continuous energy spectrum of the electron from the β-decay while obeying the laws of energy and momentum conservation [18]. It had to be a very elusive particle, as it was initially not detected. It took more than 20 years before Frederick Reines and Clyde Cowan announced the discovery of the neutrino in 1953 [19]. They observed electron-antineutrinos from a nuclear reactor via the inverse β-decay $\bar{\nu}_e + p \rightarrow e^+ + n$ by detecting the produced positron and neutron in coincidence. The existence of other neutrino flavors was already inferred from the standard model of particle physics but not proven until much later. The muon-neutrino was first observed by Leon Lederman, Mel Schwartz, and Jack Steinberger in a particle accelerator experiment at CERN in 1962 [20]. The discovery of the tau-neutrino took much longer, as it is less abundant and more difficult to detect. It was first seen by the *Direct Observation Of The NuTau* (DONUT) experiment in 2000 [21]. It took ten more years before a second experiment, the *Oscillation Project With Emulsion-Tracking Apparatus* (OPERA), detected its first tau-neutrino [22].

[1] An exception is the deflection of electromagnetic radiation due to very massive structures such as black holes that are close to its propagation path (known as gravitational lensing).

The first extra-terrestrial neutrinos were discovered by Raymond Davis and John Bahcall at the *Homestake experiment* in 1968 [23, 24]. They detected electron-neutrinos produced in nuclear fusion reactions in the Sun and measured a flux that was significantly lower than predicted. This became known as the solar neutrino problem. In the same year, Bruno Pontecorvo proposed a solution that neutrinos may transition between flavors if they have mass [25]. This idea was the foundation of neutrino oscillations. The *Sudbury Neutrino Observatory* (SNO) [26] and the *Super-Kamioka Neutrino Detection Experiment* (Super-K) [27] significantly contributed to the understanding of neutrino oscillations, for which Arthur McDonald and Takaaki Kajita, respectively, were awarded the Nobel Prize in Physics in 2015.

Another extra-terrestrial neutrino source was discovered on February 23, 1987, when the *core-collapse supernova* SN1987A exploded in the Large Magellanic Cloud [28]. Protons and electrons were crushed together during the collapse of the stellar core due to the gravitational force of the massive progenitor star and produced electron-neutrinos in the process. More than 20 neutrinos were recorded over a duration of $\sim 12\,\mathrm{s}$ in the neutrino experiments *Kamiokande-II* [29], *Irvine-Michigan-Brookhaven* (IBM) [30], and the *Baksan Neutrino Observatory* [31]. This observation was a breakthrough for the understanding of core-collapse supernovae.

Neutrinos from the Sun and from core-collapse supernovae both have an energy range of approximately $10^5\,\mathrm{eV}$ to $10^8\,\mathrm{eV}$, as they are produced in nuclear reactions. These low-energy neutrinos are not associated with cosmic-ray acceleration. The high-energy neutrino landscape looks completely different. Terrestrial neutrinos above $10^9\,\mathrm{eV}$ are predominantly produced in cosmic-ray-induced air showers. The first experimental detection of atmospheric neutrinos above this energy was achieved by Frederick Reines with the *Case Western Irvine/South Africa Neutrino Detector* (CWI/SAND) in 1965 [32]. However, the competing *Kolar Gold Field* experiment in India published their results shortly before Reines [33]. Extra-terrestrial (or astrophysical) neutrinos at much higher energies were already postulated in 1960 by Kenneth Greisen [34] and Frederick Reines [35]. They assumed that neutrinos should be produced along with cosmic rays at highly energetic acceleration sites in the universe, but also deduced that the expected flux of astrophysical neutrinos would be substantially lower than the atmospheric neutrino flux.

In the same year, Moisey Markov suggested that a kilometer-scale detector would be necessary to detect such a low astrophysical neutrino flux [36]. His idea was to transform a large volume of water in an underground lake or deep in the ocean into a Cherenkov detector. In 1976, this idea was pursued with the first advancements of constructing the *Deep Underwater Muon And Neutrino Detector Project* (DUMAND) off the shore of Hawaii [37]. Although the project was canceled in 1995, there was still progress with the first deployment of a smaller instrument in Lake Baikal in the same year [38]. Based on the pioneering work of both efforts, the *Astronomy With A Neutrino Telescope And Abyss Environmental Research* experiment (ANTARES) was constructed in the Mediterranean Sea from 2006 to 2008 [39]. It is the largest water Cherenkov detector and is still operating today. In 1988, Francis Halzen and John Learned put forward another approach and suggested using ultra-transparent, deep polar ice instead of water [40]. The *Antarctic Muon And Neutrino Detector Array* (AMANDA) was constructed at the *Amundsen-Scott South Pole Station* from 1996 to 2000 [41]. It was the first large-volume Cherenkov detector to use naturally occurring ice as the detection medium and was the precursor experiment to the *IceCube Neutrino Observatory* [42].

IceCube is a much larger Cherenkov detector built at the South Pole to measure high-energy neutrinos from cosmic sources. It was constructed between 2004 and 2010 by drilling 86 holes into the ice with a depth of $\sim 2500\,\mathrm{m}$. A string with 60 *digital optical modules* (DOMs) is deployed in each hole. The resulting $\sim 1\,\mathrm{km}^3$ volume of Antarctic ice is instrumented with a total of 5160 DOMs. Neutrinos are detected via Cherenkov light emitted by secondary particles produced in deep-inelastic neutrino-nucleon interactions.

The IceCube collaboration discovered the first high-energy astrophysical neutrinos in 2013 [43]. This observation was later confirmed in several follow-up searches [4, 44–51]. In Figure 1.1, a recent measurement of the diffuse astrophysical neutrino flux is shown. It is obtained from an update to the initial search that led to the discovery [4]. A resulting key question is whether the diffuse fluxes of gamma rays, neutrinos, and cosmic rays are connected. Cosmic rays can only be produced in hadronic accelerators, while gamma rays can also be produced by highly energetic leptonic accelerators. A connection between the two is therefore ambiguous. Neutrinos are a smoking gun for identifying the sources of cosmic rays. Unlike gamma rays, they can only be produced in hadronic accelerators. While gamma-ray sources have been mapped for years, both the origin of cosmic neutrinos and cosmic rays remain unknown. Neutrinos have the unique property of only interacting weakly. Therefore, their propagation through the universe is nearly unhindered, and their arrival direction at Earth points back to the sources. Consequently, the detection of a neutrino point source would allow for the identification of a hadronic accelerator and thereby reveal the sources of cosmic rays. However, the diffuse flux is currently a sum of neutrinos emitted by many cosmic sources, none of which is strong enough to be individually detectable [4, 52–57]. Until the first neutrino point source is identified, it is still possible to constrain the properties of these sources by examining the energy spectrum and flavor composition of the currently available measurements of the diffuse flux [58, 59].

The energy spectrum can reveal information about the acceleration process and the environment at the sources of cosmic neutrinos. In accordance with the cosmic-ray flux, the astrophysical neutrino flux is expected to follow a power-law spectrum $E_\nu^{-\gamma}$ as well. A variation of the slope in different energy regions can be caused by different source populations. A potentially softer galactic contribution to the diffuse flux as observed for cosmic rays has not been identified for neutrinos so far [56, 60]. It can be seen in Figure 1.1 that the measured energy spectrum has large uncertainties. However, this result is based on a fairly small number of observed neutrino events ($\lesssim 100$). In a global IceCube analysis, multiple data samples have been combined to characterize the energy spectrum more precisely [46, 48]. A power-law hypothesis of the energy spectrum is still compatible with all observed IceCube data. However, a large variation from a hard $E_\nu^{-2.1}$ to a soft $E_\nu^{-2.9}$ spectrum, depending on the observed energy range, hints towards a more complex spectral shape [4, 43, 45, 46, 48, 49, 51, 61].

The flavor composition measured at Earth may constrain possible production mechanisms of cosmic neutrinos. A commonly considered scenario is the production of neutrinos in the decay of charged pions $\pi \to \mu + \nu_\mu$ and the subsequent muon $\mu \to e + \nu_e + \nu_\mu$ (charge omitted), which leads to a flavor composition of $\nu_e : \nu_\mu : \nu_\tau = 1 : 2 : 0$ at the source [62]. Due to neutrino oscillations over cosmic distances, the composition expected at Earth is $\sim 1 : 1 : 1$. However, other scenarios such as the neutron-beam case with a flavor composition of $1 : 0 : 0$ or the muon-damped case with $0 : 1 : 0$ at the source may cause a significantly different flavor composition at Earth [63, 64]. Previous attempts of measuring the flavor composition with IceCube resulted in $\sim 0 : 0.2 : 0.8$ [65] and $\sim 0.5 : 0.5 : 0$ [46]. These seemingly contradicting results are in fact in good agreement with each other and with the pion-production scenario. This is due to the limited capability of neutrino flavor discrimination available at the time of the analyses. Two event topologies in IceCube have been observed numerously. *Track-like* events are predominantly generated in charged-current muon-neutrino interactions. *Cascade-like* events may be produced in both electron- and tau-neutrino as well as neutral-current interactions of all flavors. In previous measurements, track-like and cascade-like events have been readily distinguished and, as a result, the muon-neutrino fraction has been constrained rather well. However, without separate identification of electron- and tau-neutrino interactions, the corresponding fractions of the flavor composition are largely degenerate. Consequently, a large fraction of the possible flavor phase space is not constrained by the aforementioned IceCube analyses, thus rendering both measured flavor compositions compatible.

Tau-neutrinos are particularly interesting. They can only be produced in charmed meson decays. Due to the much smaller production efficiency compared to light mesons, a negligible tau-neutrino production at the source is reasonable. However, the tau-neutrino fraction expected at Earth must be larger than zero for any production scenario at the source, if standard neutrino oscillations and no beyond-standard-model theories are assumed. Because the production of atmospheric tau-neutrinos in cosmic-ray-induced air showers is strongly suppressed, the detection of a high-energy tau-neutrino would be an unambiguous astrophysical signature. Furthermore, only few tau-neutrinos have ever been detected in dedicated accelerator experiments at much lower energies than is accessible to IceCube. In total, the OPERA experiment observed four and the DONUT experiment nine tau-neutrino events [66, 67]. Consequently, an observation of a high-energy tau-neutrino interaction in IceCube would certainly be extraordinary.

Tau-neutrinos induce many signatures in IceCube, of which the "double bang" is the least ambiguous one: A charged-current tau-neutrino interaction creates a hadronic cascade and a tau lepton. The tau is unstable and decays after a short period of time. Depending on its energy, however, the tau may propagate a detectable distance before it decays. Due to relativistic effects, the decay length scales with energy and is on average $\sim 50\,\mathrm{m}$ per PeV tau energy. All but the muonic decay channel of the tau produce a second (decay) cascade, which is causally connected to the first (interaction) cascade. "Double bang" events account for $\sim 59\%$ of all tau-neutrino interactions. It was thought that a minimum neutrino energy of $\sim 10\,\mathrm{PeV}$ would be required for resolving the corresponding decay length of a few hundred meters in IceCube. Although such a well-resolved "double bang" event has not been observed yet, it is typically counted as the third event topology along with the cascade and track event topologies. However, due to the steeply falling energy spectrum and exponential decay law, a large majority of events occur at low energies and short decay lengths, respectively. In fact, most of these events look cascade-like, thus creating an experimental challenge in detecting them. The most recent search for "double bang" events in IceCube has been based on the *double pulse* method [68]. This approach searches for two separate peaks in the waveform of any DOM in the event which may be attributed to the first and second cascade, respectively. However, the phase space of "double bang" events causing this feature in the waveform is small, and the identification efficiency of this method is therefore low. No tau-neutrino candidate event has been observed using the double pulse method in three years of detector data. An upper limit on the tau-neutrino flux has been set to $E^2_{\nu_\tau}\phi_{\nu_\tau} < 5.1 \cdot 10^{-18}\,\mathrm{GeV}^{-1}\,\mathrm{cm}^{-2}\,\mathrm{sr}^{-1}\,\mathrm{s}^{-1}$. A combination of the double pulse method with the aforementioned identification of cascade- and track-like events has yielded the most stringent measurement of the flavor composition with IceCube so far [48].

The aim of the analysis presented in this thesis is to identify tau-neutrino interactions in IceCube and to measure the astrophysical neutrino flavor composition with unprecedented constraints on the tau-neutrino fraction. A new identification method of tau-neutrino interactions is introduced. It is obtained by the explicit reconstruction of a *double cascade* event topology which assumes two subsequently linked cascades of the "double bang" signature. No specific event selection is developed for this purpose. Instead, the *high-energy starting event sample* collected between 2010 and 2016 is used [4]. Efforts are focused on developing an identification method, enhancing the resolution of observables that are sensitive to tau-neutrino interactions, and incorporating important systematic uncertainties of the ice model. A method for neutrino flavor discrimination is developed which is based on three event topologies (single cascades, double cascades, tracks) and thus sensitive to all neutrino flavors. An anisotropy of the light scattering in the Antarctic ice is properly incorporated into reconstruction algorithms and tested with calibration data. The astrophysical neutrino flavor composition is measured using a binned *maximum likelihood estimation*, which varies a sum of *Monte Carlo* templates until it best describes the observed data. Constraints on the tau-neutrino fraction are improved due to the new identification method using the double cascade event topology.

The thesis is structured as follows. In Chapter 2, the high-energy neutrino landscape is described. Properties of atmospheric and astrophysical neutrinos are discussed with a focus on the energy spectrum and flavor composition. In Chapter 3, the IceCube Neutrino Observatory is introduced. Relevant principles of neutrino detection, detector components and the procedures of simulating and reconstructing an IceCube event are described. In Chapter 4, the development of a tau-neutrino identification method is explained. The implementation of the double cascade event reconstruction is presented and observables sensitive to tau-neutrino interactions are derived. A method for neutrino flavor discrimination and the associated tau-neutrino identification efficiency are examined. In Chapter 5, the systematic treatment of the ice anisotropy as a major error source to tau-neutrino identification is described. The non-trivial incorporation into existing reconstruction methods is solved by the development of a new method. It is based on the combined use of an effective distance parametrization with photo spline tables. The double cascade event reconstruction, including the ice anisotropy, is then tested using experimental flasher LED data. A summary of the systematic treatment and conclusions to tau-neutrino identification are given at the end of the chapter. The results presented in Chapter 4 include the correct treatment of the ice anisotropy. In Chapter 6, the analysis method for measuring the flavor composition is described. The model parameters of the likelihood fit, observables, and systematic uncertainties are described. The sensitivity is presented separately for the astrophysical tau-neutrino flux and astrophysical neutrino flavor composition. The last part of the chapter examines the dependence of the tau-neutrino sensitivity on the imprecisely known spectral shape of the astrophysical neutrino flux. In Chapter 7, the experimental results using the six-year high-energy starting event sample are presented. Implications and possible explanations of the results are discussed. Finally, a summary and a brief outlook are given in Chapter 8.

2 The High-Energy Neutrino Landscape

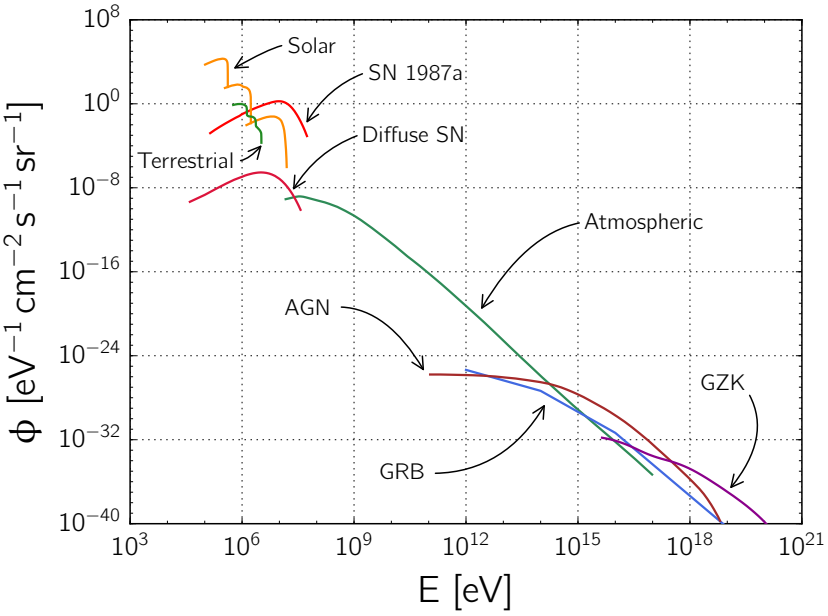

Figure 2.1: Measured and predicted neutrino fluxes from natural sources shown for solar neutrinos [69], terrestrial neutrinos [70], diffuse supernova neutrinos and from SN 1987a [71], atmospheric neutrinos [72], neutrinos from active galactic nuclei (AGN) [73–75], from gamma-ray bursts (GRB) [76], and cosmogenic neutrinos (GZK) [77]. Figure adapted from [5].

Neutrinos are elementary particles that carry no electrical charge, exist in three flavors, and have a very small mass. They are also elusive particles, as they only interact weakly. For neutrino astronomers, this is both favorable and hindering at the same time. On the one hand, the highest-energy cosmic-ray sources in the universe may be discovered via associated neutrinos, as they are likely neither deflected nor absorbed on their long path to Earth. On the other hand, it is experimentally challenging to detect neutrinos precisely because they rarely interact. Aside from particle accelerators and nuclear reactors, neutrinos are produced in many natural sources (see Figure 2.1). The flux is largest at the MeV-scale and is due to nuclear fusion and decay in the Sun and naturally occurring β-decay on Earth. A flux at a similar level was observed for the supernova SN1987a in the Large Magellanic Cloud. However, this transient flux only lasted a few seconds, while a steady diffuse neutrino flux from many supernova explosions throughout the universe is estimated to be much lower. Neutrinos at energies above 1 TeV are either of atmospheric or astrophysical origin and the most interesting in the context of this thesis.

In Section 2.1, cosmic rays are introduced, because neutrinos are assumed to be produced in conjunction at the same acceleration sites. In Section 2.2, atmospheric muons and atmospheric neutrinos originating in cosmic-ray-induced air showers are described. In Section 2.3, the production mechanisms and source candidates of a diffuse astrophysical neutrino flux are discussed and the expected energy spectrum and flavor composition are examined.

2.1 Cosmic Rays

An extra-terrestrial flux of high-energy atomic nuclei, known as *cosmic rays*, is steadily colliding with Earth. It consists mainly of protons ($\sim 79\%$) and helium nuclei ($\sim 15\%$) but may also contain small fractions of all heavier elements up to iron as well as electrons and positrons [78]. In Figure 2.2, the all-particle **cosmic-ray energy spectrum** is depicted from the geomagnetic cutoff around 1 GeV to the highest-energy cosmic rays that have ever been observed at just above 100 EeV. Up to approximately 100 TeV, the flux is large enough to be measured directly with satellite and balloon experiments. At larger energies, cosmic rays are only measured indirectly with air shower experiments. The differential flux can be approximately described by an energy-dependent sequence of three power-laws with varying spectral index

$$\frac{\mathrm{d}N}{\mathrm{d}E} \sim \begin{cases} E^{-2.7} & \text{for} \quad 10\,\mathrm{GeV} \lesssim E \lesssim 4\,\mathrm{PeV}, \\ E^{-3.1} & \text{for} \quad 4\,\mathrm{PeV} \lesssim E \lesssim 400\,\mathrm{PeV}, \\ E^{-3.3} & \text{for} \quad 400\,\mathrm{PeV} \lesssim E \lesssim 6\,\mathrm{EeV}, \\ E^{-2.8} & \text{for} \quad E \gtrsim 6\,\mathrm{EeV}, \end{cases} \tag{2.1}$$

where E is the energy per nucleus and $\mathrm{d}N/\mathrm{d}E \simeq 1.8 \cdot 10^4\,\mathrm{GeV}^{-1}\,\mathrm{s}^{-1}\,\mathrm{m}^{-2}\,\mathrm{sr}^{-1}$ at 1 GeV [78]. The first spectral break point is known as the "knee" near ~ 4 PeV, above which the spectrum softens from $\sim E^{-2.7}$ to $\sim E^{-3.1}$. A more subtle spectral feature is a "second knee" near ~ 400 PeV, above which the spectrum softens even further to $\sim E^{-3.3}$ [79]. It hardens again to $\sim E^{-2.8}$ above the "ankle" around ~ 6 EeV.[1] At even higher energies, there are indications for a spectral cutoff of the cosmic-ray flux. The **GZK-cutoff**, named after Kenneth Greisen, Georgiy Zatsepin, and Vadim Kuzmin, is hypothesized to be caused by the resonant interaction of propagating cosmic rays with the *cosmic microwave background* (CMB), predominantly via

$$\mathrm{p} + \gamma_{\mathrm{CMB}} \;\rightarrow\; \Delta^+ \;\rightarrow\; \begin{cases} \mathrm{p} + \pi^0, \\ \mathrm{n} + \pi^+, \end{cases} \tag{2.2}$$

for protons near ~ 50 EeV [80, 81]. The proton energy is shifted towards lower energies by this process, because a large amount of energy is transferred into the decays of the π^0 and π^+.

Even during extreme flares, the Sun is only capable of accelerating particles up to an energy of ~ 1 GeV [91]. Consequently, it is natural to wonder what mechanisms can accelerate cosmic rays to much higher energies from 10 GeV to 100 EeV and which sources may be involved where this is possible. Enrico Fermi suggested that particles can be accelerated by stochastic scattering across a propagating *shock front* through matter [92]. In first order **Fermi acceleration**,[2] the relative energy gain ΔE of a particle with energy E per scattering process is proportional to the shock front velocity u

$$\frac{\Delta E}{E} \sim \frac{u}{\mathrm{c}}, \tag{2.3}$$

where c is the speed of light [93]. For example, shock fronts of a type II supernova have $u/\mathrm{c} \gtrsim 10^{-2}$ which allows for a rather efficient acceleration. The following summary of the process is based on [93]. The shock front propagates through an unshocked medium (e.g. ionized gas) with a velocity u and drags the shocked medium with a velocity v. A charged particle with an initial energy E_0 crosses the shock front from the unshocked to the shocked medium and elastically scatters off magnetic inhomogeneities until it is back in the unshocked region. During each crossing, the particle gains a net energy of $\Delta E = \alpha E_0$ such that the energy of the particle is $E_n = E_0(1+\alpha)^n$ after n cycles. Averaged over all directions, the fractional

[1] A cosmic-ray particle with an energy above 1 EeV is denoted as ultra-high-energy cosmic ray (UHECR).

[2] Second order Fermi acceleration is a different process, which is not related to shock fronts and less efficient.

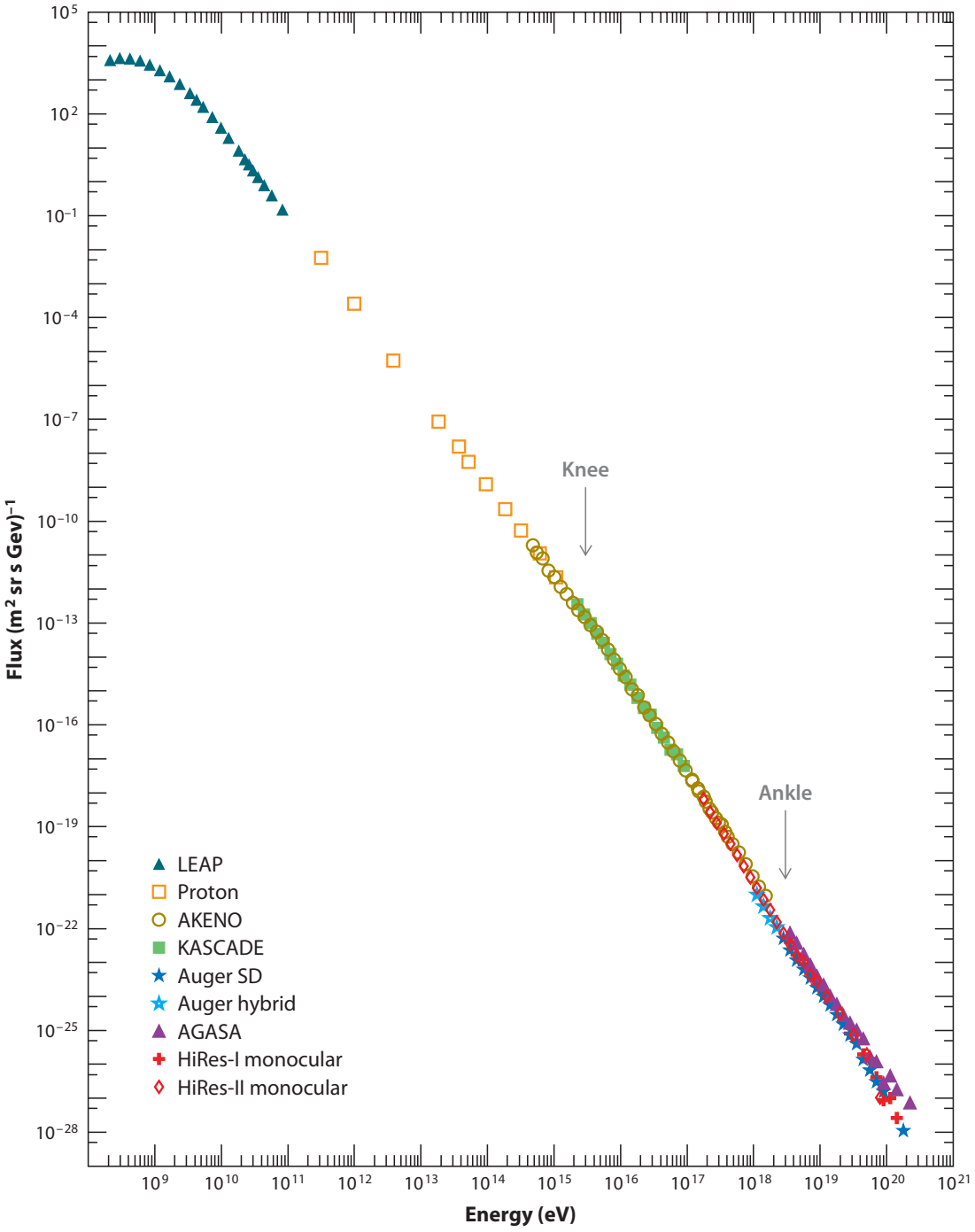

Figure 2.2: The all-particle cosmic-ray flux as a function of the energy per nucleus. Data points are from LEAP [82], Proton [83], AKENO [84], KASCADE [85], the Auger surface detector [86], Auger hybrid [87], AGASA [88], and HiRes-I/-II monocular [89]. The spectral breaks referred to as the "knee" and "ankle" are indicated by arrows. Figure reproduced from [90].

energy gain depends linearly on the velocity of the moving shock front as given in Equation 2.3 with $\alpha \simeq 4v/3c$. It is only possible for the particle to gain energy if it crosses the shock front from the unshocked into the shocked medium and back. The number of cycles through which the particle can go depends on the escape probability $p_{esc} = 4(u - v)/c$ that the particle leaves the shock region. It is calculated by dividing the flux of particles which escape the acceleration region by moving away from the shock front through the shocked medium by the flux of particles which cross the shock front into the unshocked medium. The escape probability is therefore proportional to the velocity difference of the shock front and the shocked medium. It follows that the differential energy spectrum of N particles accelerated to an energy E is given by

$$\frac{dN}{dE} \sim \left(\frac{E}{E_0}\right)^{-\gamma}, \tag{2.4}$$

where $\gamma \simeq 1 + p_{esc}/\alpha = 1 + 3(u - v)/v$. For non-relativistic shocks that move faster than the speed of sound in the medium, this yields $\gamma \simeq 2.1$ [94]. Note that the spectral index only depends on the velocities of the shock front and the shocked medium. The steeper observed $\sim E^{-2.7}$ cosmic-ray spectrum can be reasonably explained by energy-dependent diffusion in magnetic fields [95, 96]. An extension to the first oder Fermi acceleration model is the consideration of relativistic shock fronts [97, 98]. Other acceleration mechanisms have been proposed in recent years such as magnetic reconnection [99] and plasma wakefield acceleration [100].

In general, acceleration only works efficiently if the shock region is much larger than the gyro-radius of the scattered particle which would otherwise escape the acceleration process too quickly. Anthony Hillas used this requirement to classify possible source candidates of cosmic rays by relating the necessary extension and magnetic field of a source to the maximum attainable energy of a particle [101]. The **Hillas criterion** for this energy is

$$\left(\frac{E_{max}}{10^{18}\,\text{eV}}\right) = \frac{3}{20}\beta z \left(\frac{B}{\text{G}}\right)\left(\frac{R}{10^{17}\,\text{cm}}\right), \tag{2.5}$$

where R is the extension and B the magnetic field of the source, $\beta = v/c$ the velocity of the shock front in units of the speed of light and z the charge number of the cosmic-ray particle. In Figure 2.3, this relation is depicted in comparison with several source classes. The diagonal lines indicate a threshold below which a source is not capable of confining a particle with energy E and charge z. Because the disk of the Milky Way is not thicker than 1 kpc [102] and its magnetic field strength is of the order of a few μG [103], the Hillas diagram illustrates that UHECRs must be accelerated in extra-galactic sources. In contrast, galactic **supernova remnants (SNR)** are prime source candidates for low-energy cosmic rays. They eject an expanding shock wave from the explosion of a massive progenitor star which interacts with the interstellar medium. Although the galactic supernova rate is not well-known, the translation of a few percent of the shock wave energy to particle acceleration would suffice to explain the flux of cosmic rays up to an energy of $\sim z \cdot 100$ TeV below the "knee" [94]. While the origin of cosmic rays in the intermediate region is still uncertain [104], the sources of UHECRs are likely extra-galactic. The acceleration might occur in large magnetic fields which are generated by massive bulk flows of relativistic charged particles and powered by immense gravitational forces in the vicinity of neutron stars or black holes. Conceivable source candidates for these highest-energy cosmic rays are **active galactic nuclei (AGN)** [105] and **gamma-ray bursts (GRB)** [106]. AGNs are very luminous compact regions in the center of a galaxy and powered by a supermassive black hole. Ambient matter forms an accretion disk and converts gravitational into electromagnetic energy by emitting a broad electromagnetic spectrum from radio to gamma radiation. Some AGNs form relativistic beams of intense radiation (*jets*), which can terminate in lobes (*hot spots*). AGN accretion disk, jets, and hot spots could potentially accelerate cosmic rays up to ∼100 EeV [107].

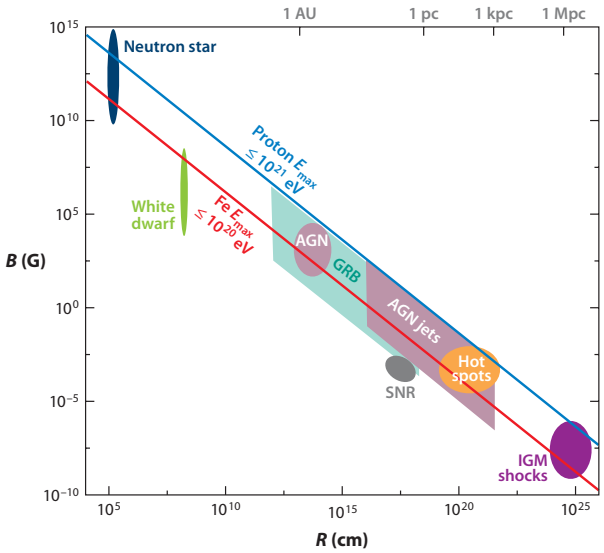

Figure 2.3: Hillas diagram relating the magnetic field strength B and size R of a source. The diagonal lines indicate the threshold region above which a source would be capable of confining protons up to a maximum energy of 10^{21} eV (blue line) and iron nuclei up to 10^{20} eV (red line). Contours are shown for the most promising source candidates for cosmic-ray acceleration. See text for description of source classes. Neutron stars, white dwarfs and, shocks of the intergalactic medium (IGM) are not considered in this context. Figure reproduced from [108].

GRBs are extremely bright transient flashes of gamma radiation which typically last from milliseconds to several minutes. In their short emission time they are more luminous than any other steady gamma-ray source in the universe [109]. GRBs are described theoretically by the fireball shock model [110], which predicts an initial short burst of highly energetic gamma radiation and a longer lasting after-glow emitting a broad waveband from x-ray to radio. Long GRBs with a duration above 2 s are thought to be associated with the core-collapse of a supermassive progenitor star [111], whereas shorter GRBs are likely caused by the merging of two neutron stars or a neutron star with a black hole [112, 113]. Both scenarios are assumed to form highly relativistic jets with multiple shock fronts, thereby accelerating cosmic rays.

2.2 Extensive Air Showers

Highly energetic cosmic rays do not reach the surface of the Earth but rather interact in the atmosphere. While penetrating the atmosphere, the cosmic-ray primary particle collides with an atomic nucleus in the air. The interaction produces a cascade of countless secondary particles through subsequent collisions, which share the initial energy of the primary particle. This process stops when the energy per particle falls below the production threshold for new particles. It is called an *extensive air shower* (EAS) and can be several kilometers wide when it reaches the surface of the Earth. The principle of an EAS and suitable detection techniques are illustrated in Figure 2.4. The dominant fraction of an air shower contains charged and neutral pions. The $\pi^0 \rightarrow 2\gamma$ decay feeds the electromagnetic component of the shower, which can be readily detected by radio emission and fluorescence or Cherenkov light. The $\pi^{\pm} \rightarrow \mu^{\pm} + \overset{(-)}{\nu}_{\mu}$ decay produces muons and neutrinos. Muons generally arrive at the surface, where they can be detected by large arrays of particle detectors. They can also penetrate deep into the ground if their energy is large enough. The illustrated detection techniques are not sensitive to neutrinos. However, a large underground detector like IceCube (see Chapter 3) is capable of detecting the highest-energy atmospheric muons and neutrinos from cosmic-ray-induced air showers.

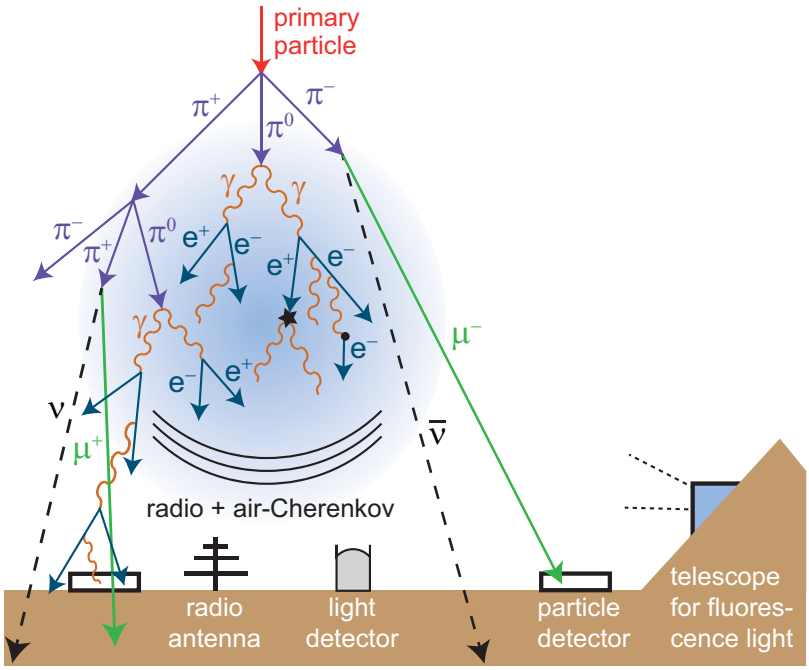

Figure 2.4: Sketch of an extensive air shower and suitable detection techniques. A primary cosmic-ray particle interacts with an atomic nucleus in the atmosphere and produces a cascade of particles. The decay of π^0 feeds the electromagnetic component of the shower which can be readily detected by radio emission and fluorescence or Cherenkov light. The decay of $\pi^{\pm}$ produces muons and muon-neutrinos. Muons generally reach the surface, where they can be detected by large arrays of particle detectors. Neutrinos cannot be detected with the displayed techniques but rather with large-volume detectors constructed deep underground, such as IceCube. The sketch is simplified, because a real shower contains significantly more particles and involves more complicated processes. Figure reproduced from [114].

2.2.1 Atmospheric Muons

Muons are unstable particles with a lifetime of 2.2 μs and a mass of 105.7 MeV/c^2 [78]. In air showers, they are typically produced at an altitude of $10 - 15$ km and generally reach the surface of the Earth due to relativistic effects. For example, a muon with an energy of 2.4 GeV has a decay length of 15 km, which reduces to 8.7 km if its continuous energy losses due to ionization in the atmosphere are taken into account [78]. More energetic muons not only reach the surface of the Earth but also penetrate deep into the ground. They are an important atmospheric background in underground neutrino detectors.

The atmospheric muon flux depends on the energy and zenith angle of a muon. The flux follows the parent cosmic-ray spectrum of $\sim E^{-2.7}$ in the energy range between $10-100$ GeV, becomes increasingly steeper towards higher energies, and can be approximated by an $\sim E^{-3.7}$ spectrum above 10 TeV [78]. The reason is that charged pions are more likely to decay than interact at lower energies, thus preserving the cosmic-ray spectrum. However, with increasing energy, pions can interact several times before they decay and transfer a substantially smaller amount of energy to the muon. Atmospheric muons are less energetic for vertical showers and more energetic if coming from the horizon. This is mostly explained by the much longer propagation length of a few hundred kilometers of horizontally arriving muons compared to a few kilometers for vertical muons. As the decay length of a muon is energy-dependent, most horizontally arriving muons have already decayed, leaving only the highest-energy muons to be detected. In addition, nearly horizontal showers produce more high-energy muons, because the atmosphere is less dense and, consequently, secondary pions are more likely to decay than interact.

Another important spectral feature is caused by the different production mechanisms of atmospheric muons. The decays of charged pions and kaons, which occur frequently in air showers, produce **conventional atmospheric muons**. Because charged pions and kaons have a comparably long lifetime, they likely interact before decaying, thereby steepening the muon spectrum. Depending on energy, conventional muons can occur in bundles of up to hundreds or even thousands of muons per shower. In contrast, **prompt atmospheric muons** are thought to be produced much less frequently in the decay of very short-lived hadrons. These come either from the leptonic decays of heavy charmed mesons (D, D_s) or from the di-muon decays of light vector mesons (η, ρ, ω) [115]. They typically have much shorter lifetimes than charged pions and kaons ($\sim 10^{-4}$ times shorter [78]). Consequently, they almost always decay before interacting and transfer a large fraction of the initial primary energy to a single secondary muon. Therefore, prompt muons do not occur in bundles but rather emerge as a single highly energetic muon from the air shower and produce a significantly harder spectrum than $E^{-3.7}$. Due to the higher production threshold of charmed mesons, the prompt muon flux is also much lower than the conventional muon flux and only detectable at energies well above a few hundred TeV.

The IceCube detector is located $1.5 - 2.5$ km deep below the surface such that the ice sheet in between absorbs a large fraction of the atmospheric muons. The vertical intensity of muons is reduced by a factor of $\sim 10^3 - 10^4$ compared to the surface [116]. Nevertheless, IceCube is a very large detector and records ~ 3000 muons per second (see Section 3.2.3). Naturally, the muon spectrum shifts towards higher energies, because low-energy muons are less likely to survive propagation through the thick ice sheet than high-energy muons.

The energy spectrum of the atmospheric muon flux has been measured up to ~ 100 TeV with detectors at sea level, underground, and underwater [116] and up to ~ 1 PeV with IceCube [117]. The result of the latter measurement is shown in Figure 2.5 in comparison to conventional and prompt muon flux predictions from the GaisserH3a cosmic-ray composition model [118]. As mentioned above, the flux is well described by an $E^{-3.7}$ spectrum and shows indication for a prompt component at the highest energies, albeit with large uncertainties.

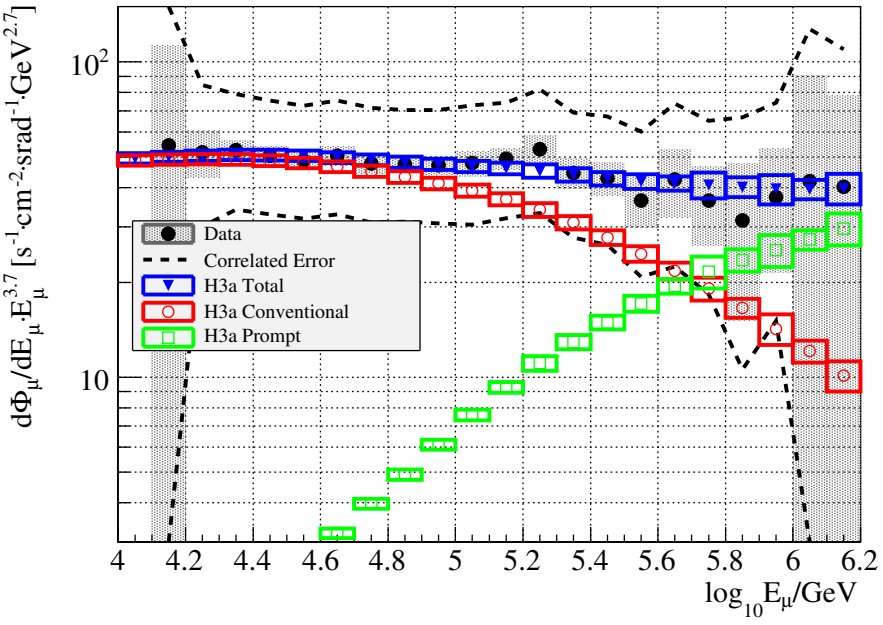

Figure 2.5: Measurement of the all-sky atmospheric muon spectrum above 10 TeV obtained from single muon events in the IceCube detector. It is compared to the prediction of the conventional and prompt muon fluxes from the GaisserH3a cosmic-ray composition model [118]. The flux is scaled by $E_\mu^{-3.7}$ to enhance the visibility of spectral features. Figure reproduced from [117].

2.2.2 Atmospheric Neutrinos

Atmospheric neutrinos are generated numerously in cosmic-ray-induced air showers, and mostly appear in conjunction with atmospheric muons. Relevant production processes vary depending on energy. The dominant source of **conventional atmospheric neutrinos** is due to the decays of charged pions and kaons

$$\pi^{\pm} \rightarrow \mu^{\pm} + \overset{(-)}{\nu}_{\mu}, \tag{2.6}$$

$$K^{\pm} \rightarrow \mu^{\pm} + \overset{(-)}{\nu}_{\mu}, \tag{2.7}$$

$$K^{\pm} \rightarrow \pi^{0} + e^{\pm} + \overset{(-)}{\nu}_{e}, \tag{2.8}$$

$$K^{0}_{L} \rightarrow \pi^{\pm} + e^{\mp} + \overset{(-)}{\nu}_{e}. \tag{2.9}$$

Almost all conventional atmospheric electron-neutrinos are produced in the decay of kaons.[3] At energies well above 100 GeV, charged pions no longer significantly contribute to the production of atmospheric muon-neutrinos (unlike for atmospheric muons) [120]. Consequently, conventional atmospheric neutrinos are predominantly produced in the decay of kaons in the relevant energy region accessible with IceCube. Due to the different production efficiency and branching ratios of Equations 2.6 to 2.9, muon-neutrinos are produced in much higher numbers than electron-neutrinos. The flavor ratio $\nu_{\mu} : \nu_{e}$ is strongly energy-dependent and ranges between $\sim 20 - 30$ from $\sim 1\,\text{TeV} - 1\,\text{PeV}$ for conventional atmospheric neutrinos [120].[4]

In contrast, **prompt atmospheric neutrinos** are produced in the decays of charmed mesons

$$D^{0}, D^{\pm} \rightarrow e^{\pm} + \overset{(-)}{\nu}_{e} + X, \tag{2.10}$$

$$D^{0}, D^{\pm} \rightarrow \mu^{\pm} + \overset{(-)}{\nu}_{\mu} + X, \tag{2.11}$$

where X stands for *anything* in the inclusive decay mode.[5] Because the branching ratios of the inclusive decays into electron- and muon-neutrinos are almost identical, the expected flavor ratio is $\nu_{\mu} : \nu_{e} \simeq 1 : 1$ for prompt atmospheric neutrinos alone [78]. The production of atmospheric tau-neutrinos is strongly suppressed and effectively expected to occur only via

$$D^{\pm}_{s} \rightarrow \tau^{\pm} + \overset{(-)}{\nu}_{\tau} \quad \text{and the subsequent decay} \quad \tau^{\pm} \rightarrow \mu^{\pm} + \overset{(-)}{\nu}_{\mu} + \overset{(-)}{\nu}_{\tau}. \tag{2.12}$$

The tau-neutrino contribution to the total prompt flux is $\sim 5\%$ and is generally negligible [121]. The resulting atmospheric flavor composition is $\nu_{e} : \nu_{\mu} : \nu_{\tau} \simeq 1 : 1 : 0.1$ for prompt neutrinos between $\sim 1\,\text{PeV}$ and $\sim 100\,\text{PeV}$. The energy spectrum of the atmospheric neutrino flux can be approximately described by two power-laws

$$\frac{dN}{dE} \sim \begin{cases} E^{-3.7} & \text{for conventional atmospheric } \nu \text{ (above } \sim 100\,\text{GeV)}, \\ E^{-2.8} & \text{for prompt atmospheric } \nu \text{ (below } \sim 100\,\text{TeV)}. \end{cases} \tag{2.13}$$

It is steeper for conventional neutrinos, because the parental charged pions and kaons are likely to interact multiple times before they decay. Prompt neutrinos are produced in the immediate decay of short-lived hadrons without prior interaction and do not lose energy on their propagation

[3] A recent study found a significant contribution of $K^{0}_{S} \rightarrow \pi^{\pm} + e^{\mp} + \overset{(-)}{\nu}_{e}$ to the atmospheric electron-neutrino flux above 100 TeV. Although the branching ratio is very small, the lifetime of the K^{0}_{S} is so short that its negligence underestimated the previously modeled flux by $\sim 30\%$ [119].

[4] Note that the muon decay does not contribute to the ν_{e}-fraction in this energy range, because it only occurs after the muon has lost a substantial amount of energy.

[5] Unlike for prompt atmospheric muons, the decay of light vector mesons, such as η, ρ, ω, cannot produce prompt atmospheric neutrinos.

path from the production point in the shower to the interaction point in the detector. Therefore, the prompt neutrino flux approximately follows the same spectrum as the primary cosmic-ray flux. The conventional neutrino flux additionally depends on the zenith angle and is largest for neutrinos coming from the horizon. As explained in the previous section, this is due to the longer propagation of air showers through less dense parts of the atmosphere. This increases the interaction length for charged pions and kaons and thus the probability that they decay before they interact. Consequently, the vertically down-going conventional neutrino flux is suppressed in comparison. Because charmed mesons decay immediately and independently of the atmospheric density, the prompt neutrino flux is constant in zenith angle. See Figure 2.7 in Section 2.3.2 for an illustration of the energy and zenith dependence of the atmospheric neutrino flux, where it will be discussed in the context of searching for a diffuse astrophysical neutrino flux.

The energy spectrum of the conventional atmospheric neutrino flux has been measured up to a few hundred GeV with underground neutrino experiments such as Super-K [122] and the *Fréjus Nucleon-Decay Detector* [123] and up to a few hundred TeV with IceCube [124]. The result of the latter measurement is shown in Figure 2.6 for the conventional atmospheric electron- and muon-neutrino fluxes and agrees well with model predictions [125]. A prompt atmospheric neutrino flux has yet to be observed, because the predicted normalization resides below the currently accessible detection threshold [121].

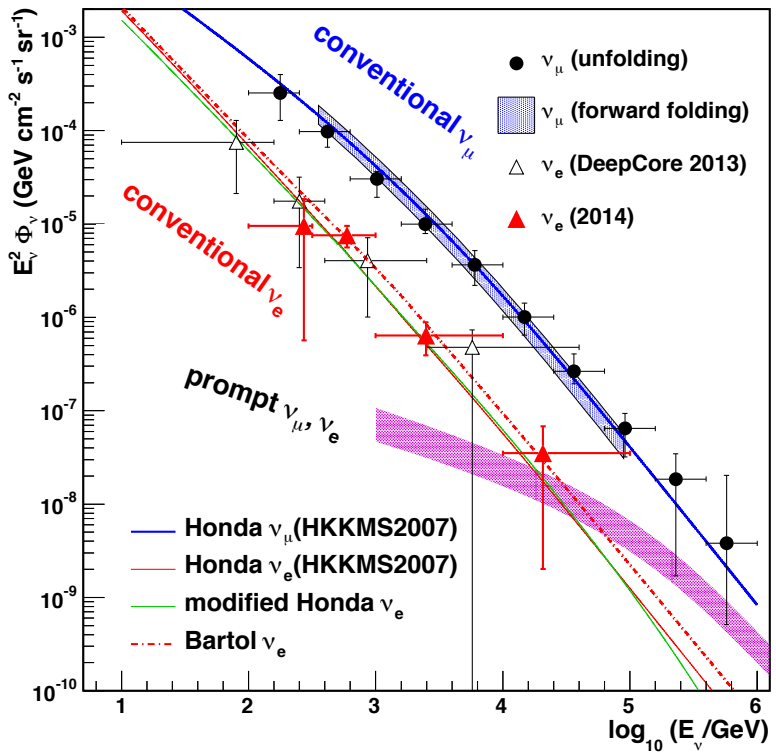

Figure 2.6: Measurement of the conventional atmospheric neutrino flux with the IceCube detector. The muon-neutrino flux was obtained in [126, 127] and the electron-neutrino flux in [124, 128]. Predictions are shown for conventional neutrinos based on the HKKMS model [125] and the Bartol [129] model and for prompt neutrinos based on the ERS model [121]. The HKKMS model is shown as baseline and as a modified version which incorporates corrections of the "knee"-region in the GaisserH3a cosmic-ray composition model [118, 130] and an additional contribution of the K^0_S decay to the ν_e flux [119]. Figure reproduced from [124].

2.3 Astrophysical Neutrinos

Neutrinos of astrophysical origin are expected to be produced in conjunction with cosmic rays. Suitable sources must be capable of accelerating particles up to extremely high energies and have ambient matter or radiation fields nearby. Cosmic rays could then interact before they escape the source environment and thereby produce neutrinos in the subsequent decay of secondary particles. Neutrinos are excellent messenger particles, because they propagate from the acceleration site in the cosmos to the detector on Earth without being deflected. Hence, the sources of cosmic rays could potentially be identified by finding neutrino point sources and by characterizing the energy spectrum and flavor composition of a diffuse neutrino flux.

2.3.1 Production Mechanisms and Source Candidates

Production mechanisms of astrophysical neutrinos are typically divided into two classes, which differ by the environment of source candidates ("beam dump"). In the **hadronuclear scenario**, cosmic rays interact with surrounding matter close to the acceleration site. As cosmic rays are mostly protons (c.f. Section 2.1) and interstellar gas or plasma clouds typically consist of neutral or ionized hydrogen, this is also called the pp-scenario (or pn-scenario if neutrons are involved). In contrast, the **photohadronic scenario** is characterized by the interaction of cosmic rays with ambient radiation fields and is thus also called the pγ-scenario.

In the pp-scenario, the inelastic scattering of a highly energetic proton from the acceleration process with a thermal proton from the beam target creates a particle shower similar to cosmic-ray-induced air showers in the atmosphere (c.f. Section 2.2). Among other particles, numerous neutral and charged pions are produced in the process. They are also produced in the pγ-scenario in which a proton interacts with a photon of the ambient radiation field predominantly via

$$\mathrm{p} + \gamma \;\rightarrow\; \Delta^{+} \;\rightarrow\; \begin{cases} \mathrm{p} + \pi^{0}, \\ \mathrm{n} + \pi^{+}. \end{cases} \tag{2.14}$$

The process is similar to Equation 2.2, with the difference that the photon from the source can be much more energetic than a photon from the cosmic microwave background. Consequently, the proton can be much lower in energy to reach the production threshold of the Δ^{+}-resonance. In addition to this resonant production, pions can be generated via inelastic scattering of $\mathrm{p} + \gamma$ if the center-of-mass energy is larger than the rest mass of the pion.

Neutrinos are generally produced in both the hadronuclear and photohadronic scenarios through the production of secondary pions. While the decay $\pi^{0} \rightarrow 2\gamma$ contributes to potentially observable gamma radiation of the source, neutrinos are produced via

$$\pi^{\pm} \;\rightarrow\; \mu^{\pm} + \overset{(-)}{\nu}_{\mu} \qquad \text{and the subsequent decay} \qquad \mu^{\pm} \;\rightarrow\; \mathrm{e}^{\pm} + \overset{(-)}{\nu}_{\mathrm{e}} + \overset{(-)}{\nu}_{\mu}. \tag{2.15}$$

In contrast to the production of atmospheric neutrinos, the density of the source environment is generally assumed to be low enough for the muon to decay without losing energy. This implies that all neutrinos in Equation 2.15 share a similar fraction of the initial energy. On average, each neutrino receives $\sim 1/20$ of the initial energy of the primary cosmic-ray particle if it is a proton and all secondary particles decay without previous interactions or energy losses [131]. Consequently, the neutrino energy spectrum is expected to follow a power-law similar to the parent cosmic-ray spectrum, depending on the production mechanism and source class (c.f. Section 2.1). This production scenario yields a flavor composition of $\nu_{\mathrm{e}} : \nu_{\mu} : \nu_{\tau} = 1 : 2 : 0$ at the source, however, other flavor compositions that depend on the source environment and cosmic-ray energy are also conceivable [59]. This will be discussed further in Section 2.3.3.

There are many conceivable source candidates for astrophysical neutrino emission which have been increasingly constrained by the IceCube and ANTARES experiments, in particular. A summary of the current status of neutrino astronomy is given in [132]. The most important theoretical production mechanisms and experimental results are briefly sketched in the following.

An upper limit on the astrophysical neutrino flux called the **Waxman-Bahcall-bound** has been derived by Eli Waxman and John Bahcall [76, 133]. The idea is that the entire UHECR flux produces the astrophysical neutrino flux and regenerates itself in the process, without exceeding measurements. The original derivation is based on a few prerequisites. First, the cosmic-ray flux is generated by Fermi acceleration of protons with an E^{-2} spectrum (c.f. Section 2.1). Second, all protons undergo $p\gamma$-interactions, thereby producing protons and neutrons as well as gamma rays and neutrinos from the decay of π^0 and π^+, respectively (c.f. Equation 2.14). Third, the acceleration site is optically thin for neutrons, allowing their escape and subsequent β-decay, which produces more neutrinos and regenerates the highest-energy protons of the cosmic-ray spectrum. Constrained by the observed cosmic-ray spectrum above the "ankle", the Waxman-Bahcall-bound for an all-flavor astrophysical neutrino flux is $E_\nu^2 \Phi_\nu^{\mathrm{W.B.}} \leq 3.4 \cdot 10^{-8}\,\mathrm{GeV\,cm^{-2}\,sr^{-1}\,s^{-1}}$ [76]. This updated limit also accounts for the possibility that neutrinos are produced in the pp-scenario in the vicinity of the sources. However, it can be considerably weaker if the observed cosmic-ray energy spectrum $E^{-2.8}$ instead of a generic E^{-2} spectrum is used [134]. A diffuse astrophysical neutrino flux of the order of the Waxman-Bahcall-bound, albeit with a steeper spectrum, has been measured in the range of a few TeV to a few PeV with IceCube (see Section 2.3.2). Neutrinos in this energy range are assumed to be produced near the acceleration sites of cosmic rays, and therefore have the same source candidates (c.f. Section 2.1).

While **galactic neutrino source candidates** are conceivable, they are experimentally disfavored. Although gamma-ray measurements of galactic SNR predict a few sources that are potentially resolvable in neutrinos, the estimated diffuse flux from the galaxy is well below current measurements [135]. A dedicated search for sources within the galactic plane has seen no excess in neutrinos [60]. A similar class of sources is a specific type of core-collapse supernovae, which is expected to produce neutrinos in the collision of the supernova ejecta with massive circumstellar material [136]. However, a recent search has seen no associated clustering of high-energy neutrinos around the direction of known core-collapse supernovae [57].

In contrast, **extra-galactic neutrino source candidates** such as AGNs and GRBs are more favorable. Neutrino emission has been modeled from the accretion disk of AGNs [73–75] and from associated jets [137]. A dedicated search for neutrino emission from populations of Fermi blazars found that these sources cannot account for more than $10-20\%$ of the diffuse neutrino flux observed with IceCube [55]. GRBs have been proposed as prime candidates for cosmic-ray and associated neutrino production for a long time. Neutrinos may be emitted during different phases of a GRB, such as the pre-burst of the progenitor star [138], the prompt gamma-ray emission during the burst [76], and potentially in conjunction with the afterglow [139]. However, an initial search with IceCube produced no evidence for high-energy neutrinos associated with gamma-bright GRBs [140], and an extended search tightened these constraints by finding that they cannot account for more than $\sim 1\%$ of the diffuse neutrino flux detected by IceCube [141]. Hence, the origin of these neutrinos is currently unclear.

Extremely energetic **cosmogenic neutrinos** are expected due to the GZK-cutoff [142]. They are hypothesized to be produced in the decay of the π^+ through the interaction of propagating cosmic-ray protons above 50 EeV with the CMB (c.f. Section 2.1). The additional observation of the diffuse extra-galactic gamma-ray background by Fermi LAT (expected from the associated decay of π^0) tightens the constraints on the cosmogenic neutrino flux and places an upper limit of the order of $E_\nu^2 \Phi_\nu \lesssim 10^{-8}\,\mathrm{GeV\,cm^{-2}\,sr^{-1}\,s^{-1}}$ for neutrinos near 1 EeV energy [77]. However, no neutrinos close to this energy have been observed with IceCube so far [143].

The simultaneous production of gamma rays and neutrinos implies a tight connection between these messengers within the context of studying cosmic-ray acceleration. A coincidental observation through *multi-messenger astronomy* and the clear establishment of the connection between the diffuse gamma-ray and neutrino fluxes would be the key ingredients for identifying the sources of cosmic rays. However, some of the aforementioned models rely on simplified assumptions, while the reality may be more complicated. In particular, neutrino emission from the pγ-scenario is significantly reduced if UHECRs are heavier nuclei than protons. In this case, *photo-disintegration* becomes the dominant process in which the interaction with a photon causes the nucleus to be split into smaller fragments without emitting a neutrino [144]. This significantly reduces the predicted flux of cosmogenic neutrinos [77]. Furthermore, the neutrino emission expected from such sources can be significantly altered when not only considering the full reaction chain of the pγ-scenario but also *proton synchrotron radiation*, *synchrotron self-Compton scattering*, and cascades from electron-positron-pairs [145].

2.3.2 Observation of a Diffuse Astrophysical Neutrino Flux

A diffuse neutrino flux is produced by a sum of neutrino-emitting sources, none of which is strong enough to be individually detectable. Because neutrinos should be produced in association with cosmic rays via pp- or pγ-interactions in the "beam dump"-scenario, it is reasonable to assume a power-law spectrum $\mathrm{d}N/\mathrm{d}E \sim E^{-\gamma}$ for the **astrophysical neutrino flux model** as well. As long as no individual point sources or source regions (such as the galactic plane) are resolvable, it is also reasonable to model the arrival directions of the flux isotropically. The ratio of neutrinos to antineutrinos is generally fixed to $\nu : \bar{\nu} = 1$ for any flavor. This assumption does not necessarily hold for each individual source. The ratio is generally dependent on the excess of π^+ over π^- (or heavier mesons) produced in the interaction of cosmic rays with the "beam dump". While pp-interactions produce charged pions in approximately equal numbers (with a slight overburden of π^+ due to the fact that both cosmic rays and target material are protons), pγ-interactions produce fewer π^-, most of which through multi-pion production. Due to the lack of π^-, the Δ^+-resonance would predominantly emit ν_μ and ν_e but no antineutrinos as can be deduced from Equation 2.14 and Equation 2.15. Consequently, the model assumption $\nu : \bar{\nu} = 1$ is motivated by averaging over many conceivable sources. It is not critical, because neutrino and antineutrino interactions are indistinguishable in the IceCube detector in any case. An exception, however, is the resonant production of a W^- in the interaction of a $\bar{\nu}_e$ with a shell-electron of the detector material, named *Glashow-resonance* (see Section 3.1.1). It is only observable for $\bar{\nu}_e$ at 6.3 PeV and is sensitive to the production mechanisms at the source [146], however, has many caveats and is challenging under realistic assumptions [147]. The last model assumption is that the flavor composition is fixed to $\nu_e : \nu_\mu : \nu_\tau = 1 : 1 : 1$ unless it is an explicit measurement quantity. This will be discussed in greater detail in Section 2.3.3.

In the search for astrophysical neutrinos, even deep-underground detectors like IceCube need to manage a **large background of atmospheric muons and neutrinos** from cosmic-ray-induced air showers. As mentioned in Section 2.2.1, IceCube detects $\sim$3000 muons per second at trigger level, whereas typical event selections yield between $\sim 10 - 100$ astrophysical neutrinos per year, of which only few are at energies above a few hundred TeV (see e.g. [46]). Hence, the main aim of any event selection is to reduce atmospheric backgrounds to a level where astrophysical neutrinos become detectable. This is more efficiently realized for atmospheric muons than for atmospheric neutrinos. Atmospheric muons leave a detectable signature in the outer parts of the detection volume, because they are charged particles and always enter from outside. This is employed in the *high-energy starting event selection* (see Section 4.2) in which the outer detector boundary is defined as *veto region* for the detection of incoming muons. In contrast, neutrinos may pass the veto region without detection and interact in the

inner part of the detector. The signature of an atmospheric neutrino is, in principle, identical to an astrophysical neutrino. However, the combined set of all observed neutrinos can distinguish the two cases on a statistical basis, when proxies for the neutrino energy and zenith angle are fully employed. The dependence of the flux on these observables is depicted in Figure 2.7. It can be seen that the conventional atmospheric neutrino flux is much steeper than the observed astrophysical neutrino flux. Consequently, neutrinos at particularly high energies cannot be explained by assuming an atmospheric origin. In addition, the zenith angle distribution differs for conventional atmospheric and astrophysical neutrinos. While the flux of the latter peaks around the horizon (c.f. Section 2.2.2), the astrophysical neutrino flux is assumed to be isotropic.

Evidently, the modeled prompt atmospheric neutrino flux is similar to the astrophysical neutrino flux in both energy spectrum and zenith dependence. This makes it experimentally challenging to disentangle prompt atmospheric from astrophysical neutrinos. Many searches, such as the high-energy starting event selection, employ the **self-veto effect** in which a discarded muon simultaneously reduces accompanying atmospheric neutrinos from the same air shower [148]. The self-veto efficiency is highest for small zenith angles and large energies. Hence, the down-going region $\cos\theta \simeq 1$ at energies above 100 TeV in Figure 2.7 is most sensitive to astrophysical neutrinos if atmospheric muons can be discarded efficiently. A more conservative upper limit on the prompt neutrino flux was derived for a maximal intrinsic charm contribution to the forward-scattering region of an air shower [149]. It might significantly increase the contribution of the atmospheric neutrino flux in the TeV energy region but cannot explain the highest-energy neutrinos observed between a few hundred TeV and a few PeV by IceCube.

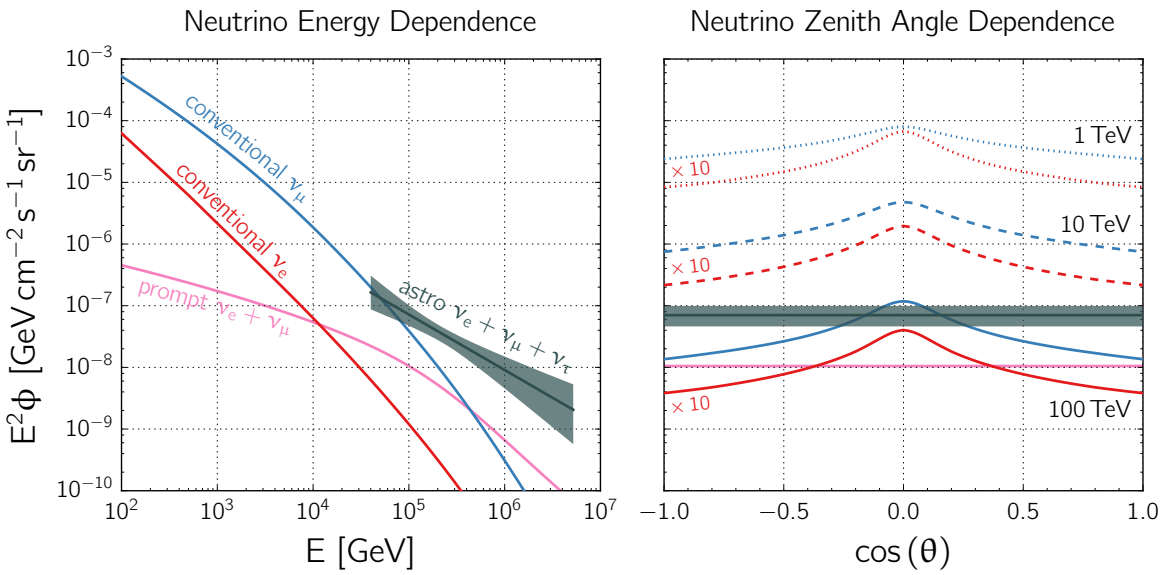

Figure 2.7: Dependence of the atmospheric and astrophysical neutrino fluxes on the energy and zenith angle. In the left plot, the flux is depicted as a function of the neutrino energy while being averaged over all zenith angles. The conventional atmospheric flux based on the HKKMS model [125] is shown for muon-neutrinos (blue) and electron-neutrinos (red), along with the prompt neutrino flux based on the ERS model [121] for the sum of electron- and muon-neutrinos (magenta) with a composition of $\nu_e : \nu_\mu = 1 : 1$. In addition, the recently updated measurement of the astrophysical neutrino flux is shown for the sum of all flavors (gray) with a composition of $\nu_e : \nu_\mu : \nu_\tau = 1 : 1 : 1$ [4]. In the right plot, the flux is depicted as a function of the zenith angle for three different energies at 1 TeV (dotted lines), 10 TeV (dashed lines) and 100 TeV (solid lines). The conventional electron-neutrino flux is scaled by a factor of 10 for comparison, and the prompt and astrophysical flux contributions are only depicted at 100 TeV. The flux is scaled by E^2 to enhance the visibility of spectral differences.

Strong evidence for the existence of astrophysical neutrinos was first found with the IceCube detector in 2013 [43]. The discovery was confirmed with consecutive updates of the initial search utilizing more detector data [4, 44, 50]. While point source searches [4, 52, 54], specific source class stacking searches [53, 55–57], and source region searches such as the galactic plane [60] have not found significant over-fluctuations, the diffuse flux has been measured with increasing precision [45, 46, 48, 49, 150]. An overview of the most important results are given in Table 6.4 in Section 6.3.4. A recent measurement yielded a per-flavor flux of $\phi_{\nu+\bar{\nu}} = (2.46 \pm 0.8) \cdot 10^{-18} (E/100\,\mathrm{TeV})^{-2.92^{+0.33}_{-0.29}}\,\mathrm{GeV}^{-1}\,\mathrm{cm}^{-2}\,\mathrm{sr}^{-1}\,\mathrm{s}^{-1}$ [4], which is of the order of the Waxman-Bahcall-bound but has a steeper spectrum. The flavor composition was assumed to be $\nu_e : \nu_\mu : \nu_\tau = 1 : 1 : 1$ in most of these measurements, which will be motivated and discussed in the context of the measurement goal of this thesis in the next section.

2.3.3 Neutrino Oscillations and Flavor Composition

The phenomenon that neutrinos transition between flavors during the propagation between production and detection point is commonly known as **neutrino oscillations**. It was first suggested by Bruno Pontecorvo that neutrino oscillations would be possible if neutrinos had mass [25]. This proposal was revolutionary, as it contradicted the standard model of particle physics in two respects. First, lepton flavor had been thought to be conserved and, second, neutrinos had been assumed to be massless. While neutrino oscillations have been well-studied for decades [151], the individual neutrino masses are still unknown [152]. An upper limit on the sum of neutrino masses of $\Sigma_i m_{\nu_i} < 0.23\,\mathrm{eV/c^2}$ could be derived from the observed cosmological power spectrum of the large structures in the universe [153]. Future experiments aim at a direct measurement of the neutrino mass via the electron energy spectrum of single $\beta-$decay or neutrino-less double β-decay, with an estimated sensitivity of the order of $\sim 0.1\,\mathrm{eV/c^2}$ [152].

In the following, the theoretical foundation of neutrino oscillations in vacuum is outlined for the three-flavor scenario as derived in [154].[6] Although there are models of *sterile neutrinos* which do not actively take part in electroweak interactions (see Section 2.3.4), the existence of no more than three weakly interacting neutrino families at the aforementioned mass scale is well constrained by precision measurements of the Z-decay [155]. Furthermore, neutrinos are assumed to be of *Dirac-type*, i.e. the neutrino is not its own antiparticle.

A fundamental requirement for neutrino oscillations is that the *flavor eigenstates* $|\nu_e\rangle$, $|\nu_\mu\rangle$, $|\nu_\tau\rangle$ are not identical to the *mass eigenstates* $|\nu_1\rangle$, $|\nu_2\rangle$, $|\nu_3\rangle$, but rather quantum superpositions

$$|\nu_\alpha\rangle = \sum_{k=1}^{3} U^*_{\alpha k}\,|\nu_k\rangle\,, \tag{2.16}$$

where $\alpha = e, \mu, \tau$ and $k = 1, 2, 3$. The mixing strength between eigenstates is given by the elements $U_{\alpha k}$ of the unitary **PMNS-matrix**, named after Bruno Pontecorvo, Ziro Maki, Masami Nakagawa, and Shoichi Sakata [156]. It is conventionally parametrized via

$$\begin{pmatrix} U_{e1} & U_{e2} & U_{e3} \\ U_{\mu 1} & U_{\mu 2} & U_{\mu 3} \\ U_{\tau 1} & U_{\tau 2} & U_{\tau 3} \end{pmatrix} = \begin{pmatrix} c_{12}c_{13} & s_{12}c_{13} & s_{13}e^{-i\delta_{CP}} \\ -s_{12}c_{23} - c_{12}s_{23}s_{13}e^{i\delta_{CP}} & c_{12}c_{23} - s_{12}s_{23}s_{13}e^{i\delta_{CP}} & s_{23}c_{13} \\ s_{12}s_{23} - c_{12}c_{23}s_{13}e^{i\delta_{CP}} & -c_{12}s_{23} - s_{12}c_{23}s_{13}e^{i\delta_{CP}} & c_{23}c_{13} \end{pmatrix}, \tag{2.17}$$

where $c_{jk} := \cos\theta_{jk}$ and $s_{jk} := \sin\theta_{jk}$ with $j, k = 1, 2, 3$. With this choice, there are three mixing angles $0 \leq \theta_{12}, \theta_{23}, \theta_{13} \leq \pi/2$ and one Dirac-type CP phase $0 \leq \delta_{CP} \leq 2\pi$. The measured

[6] Note that natural units $\hbar = c = 1$ are used in the derivation. This means that in the relativistic limit, frequencies and mass are given in units of energy and time is given in units of distance.

values of these parameters are listed in Table 2.1. It can be seen that mixing is strongest between $|\nu_1\rangle$ and $|\nu_2\rangle$ as well as between $|\nu_2\rangle$ and $|\nu_3\rangle$, whereas δ_{CP} is largely unconstrained. Because $\mathbf{U}$ is unitary, the sum of all neutrino eigenstates is conserved.

The temporal evolution of a mass eigenstate is determined by the *free Schrödinger equation*

$$\mathrm{i}\frac{\mathrm{d}}{\mathrm{d}t}\,|\nu_k(t)\rangle = H\,|\nu_k(t)\rangle\,, \tag{2.18}$$

where t is the time and H the *Hamiltonian operator* in vacuum. In this case, the solution is given by the complex plane wave

$$|\nu_k(t)\rangle = \mathrm{e}^{-\mathrm{i}E_k t}\,|\nu_k\rangle\,, \tag{2.19}$$

where E_k is the energy of the mass eigenstate $|\nu_k\rangle$. The amplitude for the state $|\nu_\beta\rangle$ given an initial state $|\nu_\alpha\rangle$ after a time period t is

$$\langle\nu_\beta|\nu_\alpha(t)\rangle = \left(\langle\nu_j|\sum_{j=1}^{3}U_{\beta j}\right)\left(\sum_{k=1}^{3}U^*_{\alpha k}\mathrm{e}^{-\mathrm{i}E_k t}\,|\nu_k\rangle\right) = \sum_{k=1}^{3}U^*_{\alpha k}U_{\beta k}\mathrm{e}^{-\mathrm{i}E_k t}, \tag{2.20}$$

where the orthogonality $\langle\nu_j|\nu_k\rangle = \delta_{jk}$ of the mass eigenstates was used. The corresponding **flavor oscillation probability** is defined as the amplitude squared, which yields

$$P_{\alpha\to\beta} = \left|\langle\nu_\beta|\nu_\alpha(t)\rangle\right|^2 = \sum_{j=1}^{3}\sum_{k=1}^{3}U^*_{\alpha j}U_{\beta j}U_{\alpha k}U^*_{\beta k}\mathrm{e}^{-\mathrm{i}(E_j-E_k)t}. \tag{2.21}$$

As mentioned above, the neutrino mass scale is below 1 eV, whereas the relevant energy range for astrophysical neutrinos is above 100 TeV. Consequently, the energy $E_k = \sqrt{p_k^2 + m_k^2}$ with momentum p_k and mass m_k can be approximated as $E_k \simeq p_k + m_k^2/2p_k$ in the ultra-relativistic limit $p_k \gg m_k$. Accordingly, the differences in individual energies can be attributed to the mass difference with a common energy $E \simeq p_1 \simeq p_2 \simeq p_3$, which yields $E_k \simeq E + m_k^2/2E$. It follows that the phase in Equation 2.21 can be approximated as

$$E_j - E_k \simeq \frac{\Delta m^2_{jk}}{2E} \qquad \text{with} \qquad \Delta m^2_{jk} := m_j^2 - m_k^2. \tag{2.22}$$

The squared mass differences are very small and have been measured as $\Delta m^2_{21} \simeq 7.5\cdot 10^{-5}\,\mathrm{eV}^2$ and $\Delta m^2_{32} \simeq \Delta m^2_{31} \simeq 2.5\cdot 10^{-3}\,\mathrm{eV}^2$ [151]. The ordering of the mass hierarchy is still unknown. In normal ordering $m_1 < m_2 < m_3$, it follows that $\Delta m^2_{32} > 0$ while the inverted ordering $m_3 < m_1 < m_2$ implies $\Delta m^2_{32} < 0$. Assuming that all neutrinos travel at the speed of light, the propagation time t can be expressed by the propagation distance $L \simeq t$. A substitution of Equation 2.22 into a rewritten form of Equation 2.21 yields

$$P_{\alpha\to\beta}(L,E) = \sum_{k=1}^{3}|U_{\alpha k}|^2\,|U_{\beta k}|^2 + 2\,\mathrm{Re}\left(\sum_{j=1}^{3}\sum_{k>j}^{3}U_{\alpha j}U^*_{\beta j}U^*_{\alpha k}U_{\beta k}\mathrm{e}^{\mathrm{i}\frac{\Delta m^2_{jk}L}{2E}}\right). \tag{2.23}$$

The dependence of the oscillation probability on the neutrino energy E and the propagation distance L appears as a phase factor L/E in the oscillation term in Equation 2.23. The L/E phase space is important for characterizing precision experiments which are capable of measuring flavor oscillations using terrestrial neutrino sources. The *baseline* denotes the distance between the neutrino source and detector. Ideally, the neutrino source and baseline are chosen such that the experiment with a specific L/E is capable of measuring the maximal oscillation effects, either via *flavor appearance* $P_{\alpha\to\beta}$ $(\alpha \neq \beta)$ or *flavor disappearance experiment* $P_{\alpha\to\alpha}$.

Parameter	Normal Hierarchy (NH)		Inverted Hierarchy (IH)	
	Best-Fit $\pm 1\,\sigma$	$3\,\sigma$ Range	Best-Fit $\pm 1\,\sigma$	$3\,\sigma$ Range
θ_{12} [°]	$33.5^{+0.8}_{-0.8}$	31.3 . . . 36.0	$33.5^{+0.8}_{-0.8}$	31.3 . . . 36.0
θ_{23} [°]	$42.3^{+3.0}_{-1.6}$	38.2 . . . 53.3	$49.5^{+1.5}_{-2.2}$	38.6 . . . 53.3
θ_{13} [°]	$8.5^{+0.2}_{-0.2}$	7.9 . . . 9.1	$8.5^{+0.2}_{-0.2}$	7.9 . . . 9.1
δ_{CP} [°]	306^{+39}_{-70}	0 . . . 360	254^{+63}_{-62}	0 . . . 360

Table 2.1: Neutrino oscillation parameters from a three-flavor global fit [151]. The best-fit mixing angles θ_{12}, θ_{23}, θ_{13} and Dirac-type CP phase δ_{CP} are listed with $1\,\sigma$- and $3\,\sigma$-uncertainties. The inverted ordering of the neutrino mass hierarchy ($m_3 < m_1 < m_2$) is slightly preferred over the normal ordering ($m_1 < m_2 < m_3$), although poorly constrained experimentally [151].

Short-baseline experiments such as the *Double Chooz* experiment [157], the *Kamioka Liquid Scintillator Antineutrino Detector* (KamLAND) [158], and the *Daya Bay Reactor Neutrino Experiment* [159] use neutrinos from nuclear reactors and probe oscillation distances from $\sim 100\,\text{m}$ to $\sim 100\,\text{km}$. Neutrino beams produced in particle accelerators are used in long-baseline experiments such as the *Main Injector Neutrino Oscillation Search* (MINOS) [160], the *Tokai to Kamioka* experiment (T2K) [161] and the *Neutrinos at the Main Injector Off-Axis ν_e Appearance* experiment (NOνA) [162], with oscillation distances of hundreds of kilometers. Atmospheric neutrinos have been measured with detectors such as Super-K [163] and IceCube [164], with baselines as large as the diameter of the Earth. The baseline for neutrinos from the acceleration sites of cosmic rays is significantly longer than that. For an energy of 100 TeV, the required distance, which places the phase term L/E at maximal oscillation effect, would be shorter than the distance to the Sun ($L \lesssim 1\,\text{AU}$). Even the highest-energy neutrinos above 100 EeV would still require a distance, which is much smaller than the galactic disk ($L \lesssim 10\,\text{pc}$). Because these neutrinos are likely of extra-galactic origin, they can be assumed to have propagated across baselines much larger than that. In any case, they may be produced incoherently in multiple sources at different energies. Therefore, $P_{\alpha\to\beta}(L, E)$ must be averaged over L/E, which eliminates the oscillation term in Equation 2.23. This yields the **averaged flavor oscillation probability**

$$\langle P_{\alpha\to\beta}\rangle = \sum_{k=1}^{3} |U_{\alpha k}|^2 \left|U_{\beta k}\right|^2 , \tag{2.24}$$

which is completely independent of Δm^2_{jk}, E and L. Hence, any expected astrophysical neutrino flavor composition at Earth is fully determined by the emitted composition at the source and the mixing parameters θ_{12}, θ_{23}, θ_{13} and δ_{CP} as given in Table 2.1.

The **pion-production scenario** for astrophysical neutrinos associated with cosmic-ray acceleration was discussed in Section 2.3.1. It was argued that pp- and pγ-interactions yield charged pions whose subsequent decays produce neutrinos, as stated in Equation 2.15. If the source environment is such that both charged pions and secondary muons decay before they interact, the expected neutrino flavor composition at the source would be $\nu_e : \nu_\mu : \nu_\tau = 1 : 2 : 0$.

In the vicinity of sources with strong radiation or magnetic fields, charged pions and muons from pp- and pγ-interactions may suffer energy losses due to synchrotron radiation that are $(m_p/m_{\pi,\mu})^3 \sim 10^3$ times stronger than for protons [165]. Muons are more likely to interact before they decay than are charged pions, as they have a $\tau_\mu/\tau_{\pi^\pm} \sim 10^2$ times longer lifetime. These sources are therefore opaque to muons, which eliminates the contribution of muon decay to the generated neutrino flux. Consequently, this **muon-damped scenario** alters the flavor composition at the source to $\nu_e : \nu_\mu : \nu_\tau = 0 : 1 : 0$ in the same energy range. Because the interaction probability of the muon increases with energy, a more realistic source is modeled with an energy-dependent shifting flavor composition $1 : 2 : 0 \to 0 : 1 : 0$. The transition occurs over $1 - 2$ decades in neutrino energy and is expected at $\sim 100\,\text{TeV}$ for GRBs [166].

Sources with dominant $p\gamma$-interaction and extremely strong magnetic fields may produce a flavor composition of $\nu_e : \nu_\mu : \nu_\tau = 1 : 0 : 0$ in this **neutron-beam scenario** [167]. It is determined by the production of highly energetic neutrons, either through Equation 2.14 or from the photo-disintegration of heavy cosmic-ray nuclei. The source environment must be optically thin for neutrons to escape and decay via $n \to p + e^- + \bar{\nu}_e$. The electron-antineutrinos from this decay are generally lower in energy than neutrinos from the decay of charged pions or muons. Consequently, the magnetization of the source must be sufficiently strong for charged pions and muons to be efficiently cooled via synchrotron losses, such that their decays do not contribute to the high-energy neutrino flavor composition.

At very high energies, sources with dominant pp-interaction may produce much heavier mesons that pions or kaons. In this **charm-production scenario**, the expected flavor composition is $\nu_e : \nu_\mu : \nu_\tau = 1 : 1 : 0$ [121], similar to the generation of prompt atmospheric neutrinos (c.f. Section 2.2.2). The decay of the charmed D-mesons produces electron- and muon-neutrinos in equal numbers, as stated in Equation 2.10 and Equation 2.11. As argued in Section 2.2.2, the tau-neutrino contribution is of the order of $\sim 5\%$ and can be neglected. Although heavier mesons could be included, the production rate for bottomed mesons is ~ 10 times smaller than for charmed mesons [59]. A flavor composition of $\nu_e : \nu_\mu : \nu_\tau = 1 : 1 : 0$ may also be caused by an energy-dependent secondary acceleration of muons and pions at the source [168].

As mentioned above, it seems reasonable that more realistic source scenarios have varying flavor compositions that depend on the energy and source environment [169]. In fact, these four production scenarios are recovered as specific cases of a more generally constructed model, in which the flavor composition is parameterized as a function of the size and magnetic field of the acceleration site in the Hillas phase space [170]. By additionally including synchrotron cooling and other higher energy processes, this generalized picture consists of strongly varying flavor compositions, with possible energy-dependent transitions between individual cases.

Due to neutrino oscillations, the **flavor composition changes between source and observer**. Astrophysical neutrinos are likely produced incoherently in the aforementioned scenarios, with varying energies at different positions near the source, and traveling over cosmic baselines before they are detected on Earth. Hence, the averaged oscillation probability given in Equation 2.24 applies. Using the best-fit oscillation parameters for the inverted mass hierarchy as listed in Table 2.1, the flavor compositions $\nu_e : \nu_\mu : \nu_\tau$ change as follows:

Pion-production scenario:	$1 : 2 : 0 \to 0.31 : 0.35 : 0.34$
Muon-damped scenario:	$0 : 1 : 0 \to 0.19 : 0.43 : 0.38$
Neutron-beam scenario:	$1 : 0 : 0 \to 0.55 : 0.19 : 0.26$
Charm-production scenario:	$1 : 1 : 0 \to 0.37 : 0.31 : 0.32$

Although there is a large range of conceivable neutrino flavor compositions that could be produced in association with cosmic rays, the altered compositions that would be detectable on Earth is restricted to a very narrow phase space. This is illustrated in Figure 2.8. In fact, any possible flavor composition $\nu_e : \nu_\mu : \nu_\tau = x : 1 - x : 0$ with $x \in [0, 1]$ lies within a thin sliver which is approximately connected by the four depicted production scenarios. The gray region represents production scenarios with fewer restrictions for *any* possible flavor composition $\nu_e : \nu_\mu : \nu_\tau = x : y : 1 - x - y$, also allowing tau-neutrino contribution with $x, y \in [0, 1]$ and $x + y \leq 1$. In addition, the region covers the uncertainties of the mixing parameters at $3\,\sigma$ confidence level. This result has two striking implications. First, the expected phase space of detectable flavor compositions at Earth is so small that high-precision measurements are likely required to exclude specific source models. Second, *any* production scenario predicts the astrophysical tau-neutrino fraction detectable at Earth to be significantly larger than zero.

Note that the derivation is only sketched for neutrino oscillations in vacuum. This is evidently true for the dominant fraction of the propagation between the source and Earth. However, the flavor composition at the source can be significantly altered by neutrino propagation through ambient matter [171]. In this case, a matter potential V changes the Hamiltonian $H \to H_{\text{vac}} + V$ in Equation 2.18 and makes the solution more complicated. This is known as the **MSW-effect**, named after Stanislav Mikheyev, Alexei Smirnov, and Lincoln Wolfenstein, which may resonantly enhance flavor oscillation in the presence of a changing matter density [172–174]. Although this is a conceivable scenario, the alteration of the flavor composition detectable at Earth is likely small in comparison to the phase space indicated by the gray region in Figure 2.8.

The pion-production scenario is typically chosen as a **benchmark model**, with a detectable flavor composition of $\nu_e : \nu_\mu : \nu_\tau \simeq 1 : 1 : 1$ on Earth. Therefore, measurements of the astrophysical neutrino spectrum with IceCube are obtained by assuming equal flavor contributions and quoted as per-flavor flux normalizations (c.f. Section 2.3.2). Also in the context of this thesis, a benchmark flavor composition of $\nu_e : \nu_\mu : \nu_\tau = 1 : 1 : 1$ is used to test the performance of the analysis. The most recent measurement result using multiple IceCube data samples in a global fit has yielded $\nu_e : \nu_\mu : \nu_\tau \simeq 1 : 1 : 0$ [46]. The uncertainties of the electron- and tau-neutrino fractions are large, as can be seen in Figure 2.8. However, the neutron-beam scenario with $\nu_e : \nu_\mu : \nu_\tau = 1 : 0 : 0$ at the source has been disfavored with a significance of $3.6\,\sigma$.

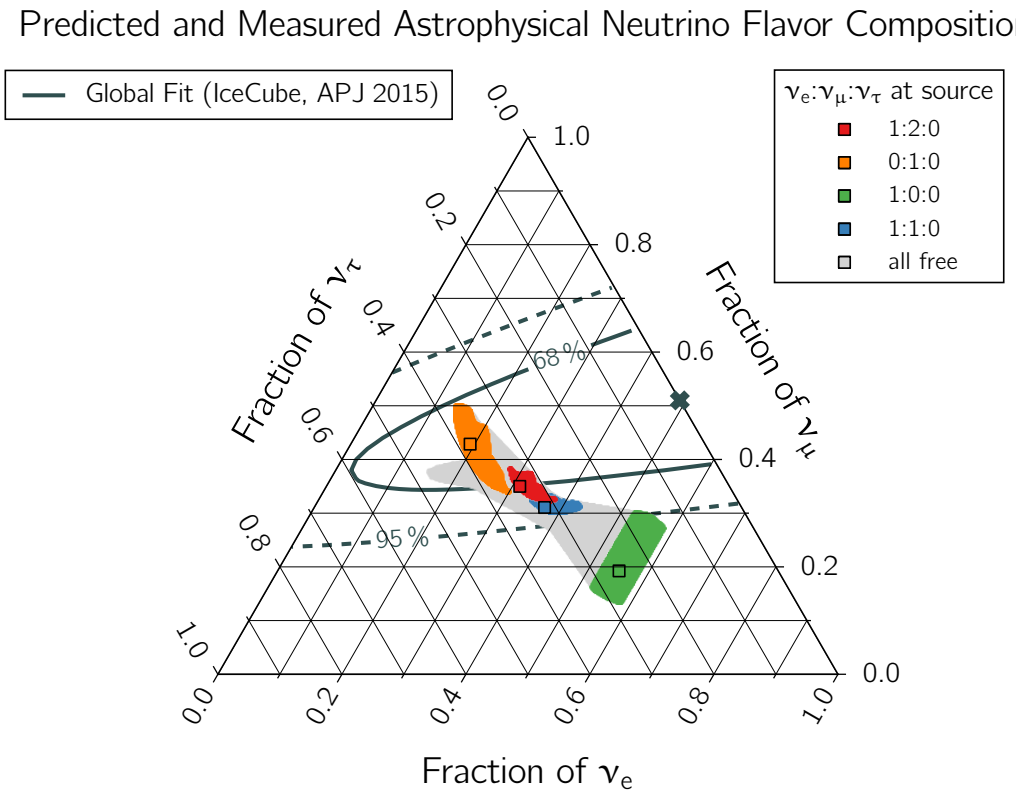

Figure 2.8: Theoretically possible astrophysical neutrino flavor compositions at Earth. Each point in the triangle plot corresponds to a flavor composition $\nu_e : \nu_\mu : \nu_\tau$ which is read off the corresponding axes along the direction of the ticks. Different production scenarios as discussed in the text are marked with '□' using the oscillation parameters for inverted mass hierarchy from Table 2.1. The colored regions correspond to the variation of each composition within the $3\,\sigma$-uncertainties of the mixing parameters. The gray area represents the composition expected at Earth for any possible production scenario ($\nu_e : \nu_\mu : \nu_\tau = x : y : 1 - x - y$) including the aforementioned uncertainties of the oscillation parameters. The most recent measurement is shown in comparison, for which the best-fit result is marked with '×' and the 68% and 95% confidence regions are indicated by solid and dashed lines, respectively [46].

2.3.4 Sterile Neutrinos, Neutrino Decay, and Other More Exotic Phenomena

The explications in the previous section are all based on the standard model of particle physics with the extension of three-flavor neutrino oscillations. However, various exotic phenomena collectively known as *beyond-standard-model* (BSM) theories can also alter the expected astrophysical neutrino flux at Earth. In this section, a few select BSM-theories are briefly outlined in the context of the expected flavor composition.

Independent fits of the mixing parameters without invoking the unitarity constraints of the PMNS-matrix seem to agree well with the existence of only three active neutrino families [175]. However, anomalies were observed with radiochemical neutrino experiments [176, 177] and with experiments using neutrinos from particle accelerators [178, 179] and nuclear reactors [180]. These could be explained by the addition of **sterile neutrinos**, which do not participate in weak interactions but mix with standard active neutrinos. The most simple extension of standard neutrino oscillations is the 3+1 model, in which one additional sterile neutrino is incorporated into the theoretical framework [181]. This implies that the PMNS-matrix as given in Equation 2.17 is expanded to 4×4 and contains three additional mixing angles $0 \leq \theta_{14}, \theta_{24}, \theta_{34} \leq \pi/2$ (as well as additional δ_{CP}-phases which are not considered here). The averaged oscillation probability given in Equation 2.24 is extended accordingly and reads

$$\langle P_{\alpha \to \beta} \rangle = \sum_{k=1}^{4} |U_{\alpha k}|^2 \left|U_{\beta k}\right|^2 . \tag{2.25}$$

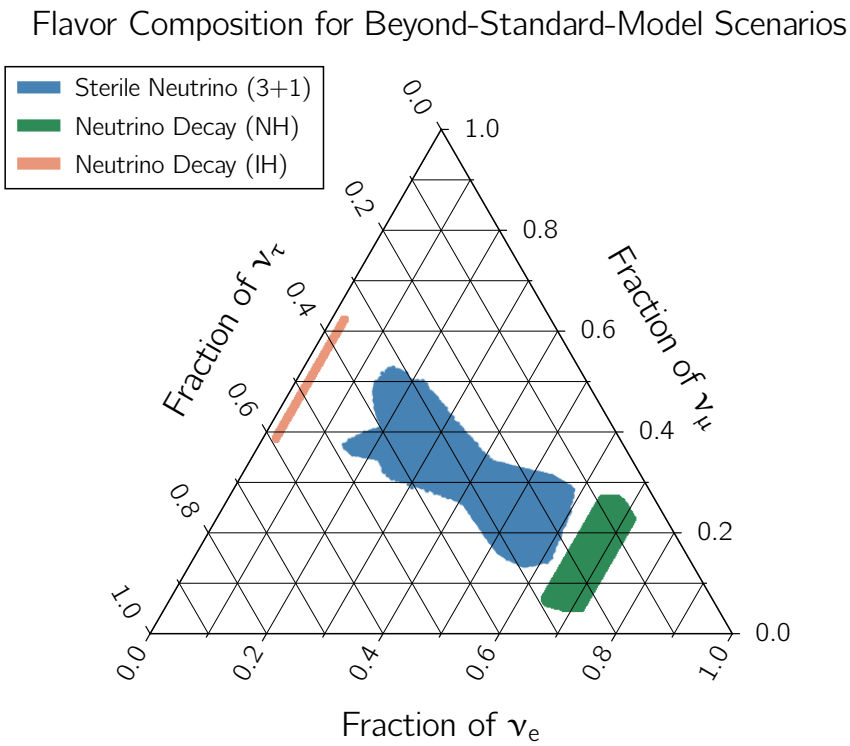

Figure 2.9: Astrophysical neutrino flavor compositions at Earth for select beyond-standard-model scenarios, as discussed in the text. The blue region corresponds to the $3+1$ sterile neutrino model, with constraints on the additional mixing angles from [182, 183]. The green and pink regions correspond to a neutrino decay model with a single stable mass eigenstate m_1 for a normal hierarchy (NH) and m_3 for an inverted hierarchy (IH), respectively, where the other mass eigenstates have decayed entirely. The colored regions cover any possible production scenario at the source including the $3\,\sigma$-uncertainties of the mixing parameters from Table 2.1.

Using the 90% upper limits on θ_{14}, θ_{24} from [182] and on θ_{34} from [183] (assuming an inverted neutrino mass hierarchy) yields the allowed region depicted in Figure 2.9 for any flavor composition at the source. It can be seen that it is slightly larger than the corresponding gray region in Figure 2.8, but not significantly different. Consequently, the $3+1$ sterile neutrino model cannot be constrained by a measurement of the astrophysical neutrino flavor composition.

Another scenario is that some neutrino mass eigenstates could be unstable and thus decay during propagation over cosmic distances [184–186]. The maximum possible effect expected due to **neutrino decay** is illustrated in Figure 2.8 as well. The allowed regions are obtained by assuming that only the lightest neutrino mass eigenstate is stable, into which all other mass eigenstates have decayed entirely. The lightest mass eigenstate is m_1 in the normal ordering of the neutrino mass hierarchy and m_3 in the inverted hierarchy. It can be seen that the expected flavor composition accesses a different phase space than that in standard model scenarios. Hence, various neutrino decay models could be constrained with IceCube, in principle.

Other exotic scenarios include the interaction of neutrinos with *dark matter* [187], a violation of *Lorentz invariance*, and a symmetry breaking of the *charge conjugation*, *parity transformation*, and *time reversal* (CPT) [188]. An overview of the effect of non-standard neutrino production, propagation, and detection on the astrophysical neutrino flavor composition at Earth is given in [189]. While the possible phase space of flavor compositions is much larger than depicted in Figure 2.9 for some BSM theories, it is particularly interesting that most do not allow a vanishing astrophysical tau-neutrino fraction [189]. These exotic scenarios are therefore not relevant within the context of the search for tau-neutrinos presented in this thesis.

3 The IceCube Neutrino Observatory

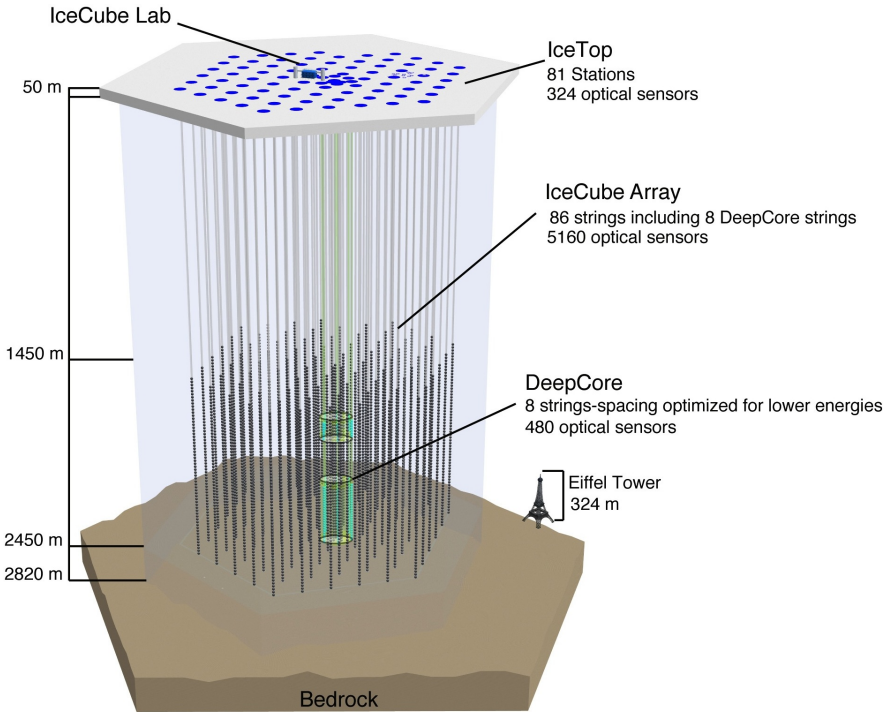

Figure 3.1: Schematic view of the IceCube detector. The main array consists of 5160 digital optical modules on 86 strings embedded in the Antarctic ice at a depth of 1450 m to 2450 m. It includes a more densely instrumented sub-array called DeepCore for low-energy events. A surface array called IceTop is used for air shower detection. Figure reproduced from [42].

The first suggestion that a kilometer-scale neutrino detector would be necessary to detect a flux of high-energy astrophysical neutrinos was published in 1960 [36]. The idea was to transform a large volume of water or ice into a Cherenkov detector. Pioneering work in the design and construction of such a neutrino detector was achieved with the DUMAND experiment that was supposed to be constructed in the sea off the main island of Hawaii [37] and during the deployment of a smaller instrument in Lake Baikal [38]. The first large-volume neutrino detector was the AMANDA experiment, for which a few hundred optical modules were deployed into the Antarctic ice at the South Pole [41]. It was the precursor to the km^3-scale IceCube experiment, which is also located at the South Pole [42]. IceCube is the largest neutrino detector in the world and complemented in the Northern Hemisphere by the ANTARES experiment, which is located in the Mediterranean Sea and is one order of magnitude smaller than IceCube [39].

In Section 3.1, the general detection principle of neutrinos in Cherenkov detectors is covered. The components of the IceCube detector, including the data acquisition and optical properties of the South Pole ice, are described in Section 3.2. Last, the different event topologies in IceCube and the simulation and reconstruction of such events are explained in Section 3.3.

3.1 Neutrino Detection

Neutrinos are elementary particles that do not carry an electrical charge. They only interact weakly and cannot be detected directly but rather via charged secondary particles only. Secondaries emit Cherenkov radiation while propagating through a dielectric medium if they are energetic enough. The emitted Cherenkov light can then be detected with photomultipliers. Large-volume neutrino detectors like IceCube require a target mass of the order of gigatons. Due to resource limitations, only natural target material can be considered for the construction of such a neutrino detector. Ice is a good detection medium, because it can be found in large quantities in Antarctica and is mostly transparent to Cherenkov radiation.

3.1.1 Neutrino Interaction Channels

The weak force is mediated by the W-bosons for *charged-current* (CC) and by the Z-boson for *neutral-current* (NC) interactions. At energies above the hadronic binding energy of $\sim 10\,\mathrm{MeV}$, the relevant interaction process is the **deep-inelastic neutrino-nucleon scattering**

$$\overset{(-)}{\nu}_\mathrm{l} + \mathrm{N} \rightarrow \mathrm{l}^\pm + \mathrm{X} \qquad \text{for CC} \tag{3.1}$$

$$\text{and} \quad \overset{(-)}{\nu}_\mathrm{l} + \mathrm{N} \rightarrow \overset{(-)}{\nu}_\mathrm{l} + \mathrm{X} \qquad \text{for NC.} \tag{3.2}$$

Here, N is a nucleon bound in an atom in the ice, $\overset{(-)}{\nu}_\mathrm{l}$ is the (anti)neutrino of lepton flavor $\mathrm{l} = \mathrm{e}, \mu, \tau$, and X is a hadronic particle shower. The corresponding Feynman diagrams are sketched in Figure 3.2. In the CC interaction, the neutrino is transformed into a charged lepton of the same flavor. In the process, a W-boson is emitted and interacts with a quark. This breaks up the nucleon and creates a hadronic shower. In the NC interaction, a neutrino scatters off the nucleon without transforming into a charged lepton. The process is mediated by the Z-boson which also interacts with a quark inside the nucleon and creates a hadronic shower.

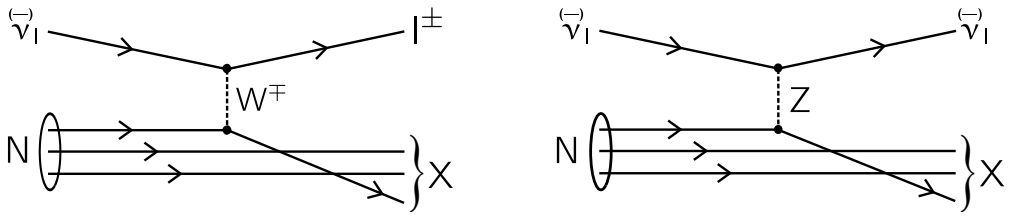

Figure 3.2: Feynman graphs of deep-inelastic neutrino-nucleon scattering for CC (left) and NC (right).

For the charged-current interaction $\nu_\mathrm{l}(k) + \mathrm{N}(p) \rightarrow \mathrm{l}(k') + \mathrm{X}$, given the initial momenta k and p and the final momentum k', the differential neutrino-nucleon cross section is given by

$$\frac{\mathrm{d}^2\sigma}{\mathrm{d}x\,\mathrm{d}y} = \frac{2{G_\mathrm{F}}^2}{\pi} m_\mathrm{N} E_\nu \left(\frac{m_\mathrm{W}^2}{Q^2 + m_\mathrm{W}^2}\right)^2 \left(q(x, Q^2) + (1-y)^2 \bar{q}(x, Q^2)\right), \tag{3.3}$$

where G_F is the Fermi constant, m_N is the mass of the nucleon, E_ν is the neutrino energy, and m_W is the mass of the W-boson [190]. The invariant momentum transfer of the scattering process is $Q^2 = -q^2$ with $q = k - k'$. The *Bjorken scaling variable* $x = Q^2/(2p \cdot q)$ denotes the momentum fraction of the scattered quark inside the nucleon. The *Bjorken inelasticity variable* $y = (p \cdot q)/(p \cdot k)$ is a measure of the amount of energy transferred to the hadronic shower X. Last, $q(x, Q^2)$ and $\bar{q}(x, Q^2)$ are the **parton distribution functions** (PDF) which correspond to the probability density of a quark or antiquark, respectively, to have a momentum fraction x of the nucleon at the energy scale Q^2 of the interaction.

If $Q^2 \ll m_W^2$, the PDFs are approximately independent from Q^2 and the cross section scales linearly with neutrino energy. For higher energies, the PDFs strongly depend on the momentum transfer as scattering on *sea quarks* becomes increasingly dominant in addition to scattering on *valence quarks*. The **neutrino-nucleon cross sections** have been measured at the *Hadron-Electron Ring Accelerator* (HERA) up to 54 TeV neutrino energy, and they have been extrapolated to higher energies [190–192]. Above 1 PeV, the PDFs also include heavy sea quarks and are calculated using *perturbative quantum chromodynamics* [193].

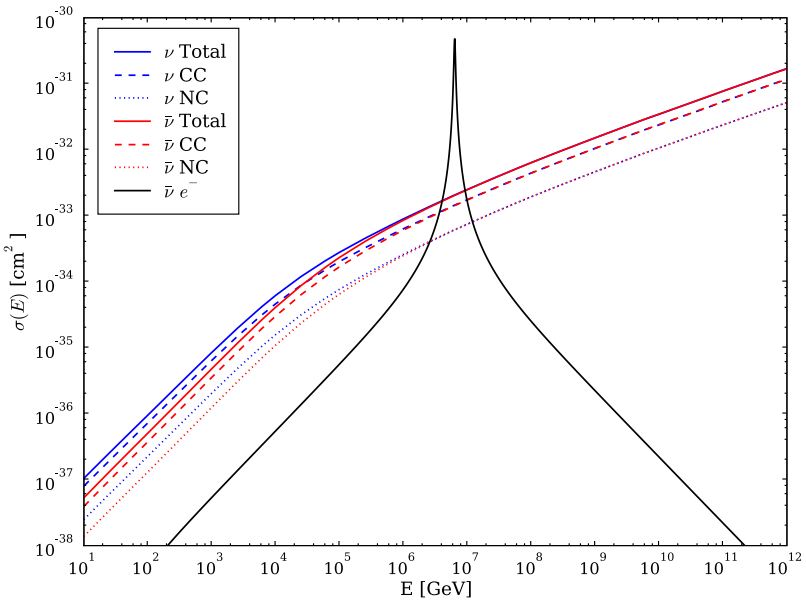

Figure 3.3: Neutrino-nucleon cross sections as a function of the neutrino energy for neutrinos (blue) and antineutrinos (red). The total (solid) and individual cross sections for CC (dashed) and NC (dotted) interactions are shown separately. The cross section for inelastic $\bar{\nu}_e\, e^-$ scattering is shown as well, as it is the dominant neutrino interaction around 6.3 PeV, known as the *Glashow resonance*. Figure reproduced from [194].

The cross section for deep-inelastic neutrino-nucleon scattering is depicted in Figure 3.3. The contributions are shown separately for CC and NC interactions and for neutrinos and antineutrinos. It can be seen that the CC cross section is generally larger than the NC cross section due to a stronger coupling of the W-boson compared to the Z-boson. Furthermore, the cross sections for neutrinos and antineutrinos are only different up to an energy of $\sim$1 PeV, above which they become equal, as the scattering on sea quarks becomes increasingly likely with higher energy. In addition, Figure 3.3 contains the cross section for inelastic $\bar{\nu}_e\, e^-$ scattering in which an electron-antineutrino scatters off a (practically resting) shell electron of an atomic nucleus and produces a resonant W-boson. This process is known as **Glashow resonance**. It is occurs at $\sim$6.3 PeV neutrino energy, where the center-of-mass energy is equal to the rest mass energy of the W-boson, which decays into leptons ($W \to \nu_l + l$ with $l = e, \mu, \tau$) or hadrons.

3.1.2 Lepton Propagation in Ice

The most important secondary particles for the detection of neutrinos are the charged leptons $l = e, \mu, \tau$ which are produced in the CC interaction $\nu_l + N \to l + X$. Depending on the kinematics of the interaction, these may carry a significant amount of the initial neutrino energy. It is important to understand how these leptons propagate in ice and how likely they are to either **decay or interact** on their path. The different behavior of each lepton in ice is the basis for flavor discrimination in IceCube.

Decay The electron is a stable particle and does not decay. Both the muon and the tau are unstable and have a lifetime of $\tau_\mu = 2.2 \cdot 10^{-6}\,\mathrm{s}$ and $\tau_\tau = 290.3 \cdot 10^{-15}\,\mathrm{s}$, respectively [78]. The decay time in the lab frame depends on the energy of the lepton due to the time dilation described in the theory of special relativity. The corresponding propagation length before the lepton decays (called *decay length*) is $\lambda_{\mathrm{dec}} = c\beta\gamma\tau$, where c is the speed of light, $\beta = v/c$ is the speed of the lepton, $\gamma = 1/\sqrt{1-\beta^2}$ is the Lorentz factor, and τ is the lifetime of the lepton in the center-of-mass frame. In the energy range of IceCube, all secondary leptons effectively travel at the speed of light, thus approximating $\beta \simeq 1$. The decay length can then be written as $\lambda_{\mathrm{dec}} = (E\tau)/(mc)$, using $E = \gamma mc^2$ where E is the energy of the lepton and m is its mass. The decay length gives the distance after which the survival probability of a lepton decreases to $1/e \simeq 36.8\%$. This is based on the exponential decay law $p(L) = \exp(-L/\lambda_{\mathrm{dec}})$ which gives the survival probability for a lepton with the decay length λ_{dec} after the propagation length L. For example, a 1 TeV muon has a decay length of $\lambda_{\mathrm{dec},\,\mu} = 6242\,\mathrm{km}$, whereas a tau of the same energy has a much smaller decay length of $\lambda_{\mathrm{dec},\,\tau} = 4.9\,\mathrm{cm}$ using $m_\mu = 105.7\,\mathrm{MeV/c^2}$ and $m_\tau = 1776.9\,\mathrm{MeV/c^2}$ for the muon and tau masses, respectively [78].

Interaction Charged leptons undergo constant interactions while propagating in the ice, which may cause them to change direction and/or lose energy. The energy loss profile $\mathrm{d}E/\mathrm{d}X$ is a measure of how much energy $\mathrm{d}E$ the lepton loses while traversing the amount of ice $\mathrm{d}X$, commonly given in units of $\mathrm{g/cm^2}$. Four processes are generally considered: continuous energy losses due to *ionization* as well as radiative losses due to *bremsstrahlung*, *pair production*, and *photonuclear interactions*. Ionization is caused by the collision of the traversing lepton with shell electrons of the target atoms. The corresponding energy loss is continuous and only scales logarithmically with energy. In the energy range of IceCube, it can be approximated as constant $\langle \mathrm{d}E/\mathrm{d}X\rangle_{\mathrm{ion}} \simeq 2\,\mathrm{MeV/(g/cm^2)}$ for leptons with $\beta\gamma \gg 1$ [94]. Hence, in ice with a density of $\rho_{\mathrm{ice}} \simeq 0.9\,\mathrm{g/cm^3}$, a lepton continuously loses $\sim 180\,\mathrm{MeV/m}$ along its propagation path. Neglecting radiative losses, it requires at least $\sim 180\,\mathrm{GeV}$ in order to traverse $\sim 1\,\mathrm{km}$ through the IceCube detector. At energies above 1 TeV that are relevant to the analysis presented in this thesis, radiative interactions dominate and energy losses due to ionization are negligible.

Radiative energy losses occur randomly along the propagation path of the lepton. An important quantity to describe this process is the *radiation length* X_0

$$\frac{1}{X_0} = \frac{4\alpha^3\hbar^2}{c^2 m^2}\frac{N_A}{A}\left(Z^2\Big(\ln\left(184.15Z^{-1/3}\right) - f(Z)\Big) + Z\ln\left(1194Z^{-2/3}\right)\right), \tag{3.4}$$

which is defined as the average propagation length after which the lepton has lost $1/e$ of its initial energy due to radiative processes [78]. Here, α is the electromagnetic fine-structure constant, $\hbar$ the reduced Planck constant, c the speed of light, and N_A the Avogadro constant. The formula is valid for a lepton with mass m traversing matter with an atomic number Z and a mass number A with a polynomial function $f(Z)$ as given in [78]. Bremsstrahlung is emitted when the traversing lepton undergoes Coulomb scattering and is deflected by either the shell electrons or the nucleus of the target atom. The energy loss due to bremsstrahlung is stochastic and scales linearly with energy. Its average is given by $\langle \mathrm{d}E/\mathrm{d}X\rangle_{\mathrm{brems}} \simeq -E/X_0$ [94]. Pair production is a secondary process where a photon creates an electron-positron pair in the vicinity of the nuclear Coulomb field. A requirement is that its energy is above the production threshold of $E_\gamma \geq 2m_e$. The energy loss due to pair production is also stochastic and scales linearly with energy. Above a few GeV, its average is given by $\langle \mathrm{d}E/\mathrm{d}X\rangle_{\mathrm{pair}} \simeq -E/(\frac{9}{7}X_0)$ [94]. Photonuclear interaction is a process where a high-energy photon interacts with an atomic nucleus and causes its disintegration into smaller fragments. The energy threshold is above the binding energy of the nucleus at a few MeV. Energy losses due to photonuclear interactions are $\sim 50\%$ smaller than bremsstrahlung and pair production [195].

The processes described above are generally valid in the energy range of IceCube. However, at very high energies above 10 PeV, the **LPM-effect**, named after Lev Landau, Isaak Pomeranchuk, and Arkady Migdal [196–198], significantly reduces the cross sections for bremsstrahlung and pair production. Consequently, leptons may propagate much farther. At even higher energies above 100 EeV, energy losses are predominantly due to photonuclear interactions [199].

The radiation length as defined in Equation 3.4 depends on the mass of the traversing lepton via $X_0 \sim m^2$. Consequently, it is very different for each lepton in the same medium. In ice it is $X_0 \simeq 36\,\text{cm}$ for electrons, $X_0 \simeq 15\,\text{km}$ for muons and $X_0 \simeq 4353\,\text{km}$ for taus. It follows that electrons lose their entire energy on a very short path (a few meters) whereas muons can on average propagate much farther (a few kilometers) before losing energy. Although taus could in principle cover an even greater distance without interacting, they have a much shorter lifetime than muons and usually decay before they lose a significant amount of energy.

3.1.3 Particle Showers

When an electron passes through matter, it emits photons from bremsstrahlung which in turn may create electron positron pairs. This is an iterative process where a primary particle creates secondary particles which create more particles. Hence, this is called a **particle shower** or **cascade** and is important for neutrino detection in IceCube. The main features can be explained in a simplistic model formulated by Walter Heitler, in which photons, electrons, and positrons are the only involved particles interacting via the electromagnetic force [200]. A primary electron with energy E_0 interacts via bremsstrahlung after one radiation length X_0 and produces a high-energy photon. In this simple model, the number of particles is doubled after each propagation length, and the energy is split equally among all particles. This multiplication process stops when the energy per particle crosses the critical energy E_c, below which the radiative energy losses due to bremsstrahlung become smaller than the ionization losses. For electrons in ice, this is $E_c \simeq 72\,\text{MeV}$, which can be obtained by setting $\langle \mathrm{d}E/\mathrm{d}X \rangle_{\text{brems}} = \langle \mathrm{d}E/\mathrm{d}X \rangle_{\text{ion}}$.

In this model, the number of particles is given by $N(t) = 2^t$ and the energy by $E(t) = E_0/2^t$ with $t = X/X_0$. The maximum number of particles is $N_{\text{max}} = E_0/E_c$ at the maximum shower depth $t_{\text{max}} = \log_2(E_0/E_c)$. Although the Heitler model has simplistic assumptions, it shows two important features that are phenomenologically true for all particle showers. First, the maximum number of shower particles increases linearly with the primary energy $N_{\text{max}} \sim E_0$. This is important in IceCube as all charged particles of the shower emit Cherenkov light (in the limit $\beta \simeq c$, see Section 3.1.4). Consequently, the Cherenkov light yield scales linearly with the primary energy. Second, the maximum shower depth scales logarithmically with the primary energy $t_{\text{max}} \sim \log E_0$. This is important in IceCube because it means that all particle showers over a wide energy range are extremely small (a few meters) with respect to the dimensions of the detector (one kilometer). This feature causes the event topologies in IceCube to be very different for secondary electrons and muons (see Section 3.3.1).

In a more realistic model than the one by Heitler, the **longitudinal energy loss profile** of a particle shower is parametrized by

$$\frac{\mathrm{d}E}{\mathrm{d}t} = E_0 b \frac{(bt)^{a-1} \mathrm{e}^{-bt}}{\Gamma(a)}, \tag{3.5}$$

describing a steeply rising edge and a slow decrease after the maximum [78]. The shower maximum can be calculated via $t_{\text{max}} = (a-1)/b$. The dimensionless parameters a and b are determined experimentally and depend on the target material (see below). The transversal energy loss profile is characterized by the *Molière radius* $R_M \simeq 21\,\text{MeV}\, X_0/E_c$, which on average contains 90% of the total deposited shower energy.

In IceCube, there are two distinct types of particle showers: **electromagnetic cascades** and **hadronic cascades**. An electromagnetic cascade can generally be described more precisely, because the interactions only involve electrons, positrons, and photons interacting via the electromagnetic force. In contrast, calculations for hadronic cascades are more complex, because many different secondary particles can be produced and the cross sections involved have larger uncertainties. Secondaries can be baryons or mesons and interact via the strong, electromagnetic, or weak forces. The production of neutral pions is an important feature of hadronic cascades as the immediate decay $\pi^0 \to 2\gamma$ feeds an electromagnetic subpart of the shower.

Both electromagnetic and hadronic showers can be approximately described in the same way in IceCube. The longitudinal energy loss profile in Equation 3.5 is used for both electromagnetic and hadronic cascades with different values for the shower parameters a and b. Originally, they were determined experimentally for electromagnetic cascades in water [201]. In a more recent study using `GEANT4` simulations, these shower parameters have been fitted for different primary particles inducing electromagnetic or hadronic showers [202]. For an electromagnetic cascade induced by an electron, they are $a = 2.02 + 0.63 \log(E_0/\mathrm{GeV})$ and $b = 0.63$, and for a hadronic cascade induced by a charged pion, they are $a = 1.81 + 0.39 \log(E_0/\mathrm{GeV})$ and $b = 0.34$. Note that the electromagnetic radiation length in Equation 3.4 is used for both showers, although the nuclear interaction length for hadronic showers is generally larger than that. However, only the parts of the shower that emit Cherenkov light are detectable in IceCube. The light yield of hadronic cascades is lower than that of electromagnetic cascades. One reason is that a considerable fraction of neutral particles or slowly moving charged particles do not emit Cherenkov light. Furthermore, the production threshold of hadrons is higher than of electrons, positrons, and photons. The amount of energy that is proportional to the Cherenkov light yield is called the **visible energy**. It is calculated by convolving the energy of the primary particle with the *relative light yield* of hadronic cascades compared to electromagnetic cascades. The relative light yield is parametrized by

$$f = 1. - (E_0/0.399\,\mathrm{GeV})^{-0.130}(1. - 0.467), \tag{3.6}$$

and increases with the primary energy due to the growing ratio of π^0. It is between $\sim 60 - 95\,\%$ within the energy range of IceCube [203].

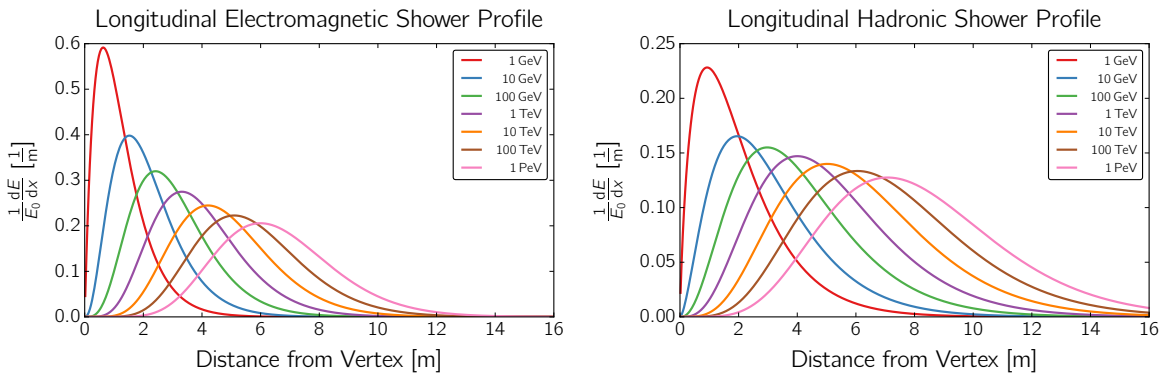

Figure 3.4: Longitudinal shower profiles for visible energy losses of an electromagnetic cascade (left) and a hadronic cascade (right). Shown is the relative differential deposition of visible energy for different primary energies as a function of the distance from the shower vertex using the radiation length in Equation 3.4, the longitudinal shower parametrization in Equation 3.5, and the light scale factor for hadronic cascades in Equation 3.6. Note the different scale of the axes due to the substantially lower light yield of hadronic cascades.

As an example, the longitudinal energy loss profiles for electromagnetic and hadronic cascades are shown in Figure 3.4 for different primary energies. It can be seen that the shower maximum is displaced from its origin by a few meters, depending on energy. The shower elongation extends with increasing energy, whereas hadronic cascades are more elongated than electromagnetic cascades. It can also be seen that the relative amount of visible energy in a hadronic cascade is generally lower than in an electromagnetic cascade due to the neutral particles in the shower not being visible. However, the visible energy increases with the shower energy due to the light scale factor that accounts for a larger contribution of electromagnetic subshowers.

3.1.4 Cherenkov Radiation

When a charged particle passes through a dielectric medium, it excites the molecular dipoles of the medium, which then return to their ground state by emitting light. If the particle is slower than the phase velocity of light in the medium, then the light emission is isotropic and interferes destructively (see Figure 3.5). Only when the particle travels at a speed that is faster than the phase velocity of light does the limited response velocity of the medium cause a coherently interfering shockwave known as *Cherenkov radiation* [204].

From simple geometric considerations as depicted in Figure 3.5, it can be deduced that the Cherenkov radiation is emitted as a light cone with an opening angle given by

$$\cos\theta_{\mathrm{Ch}} = \frac{1}{n\beta}, \tag{3.7}$$

where $n = \mathrm{c}/v_{\mathrm{phase}}$ is the refractive index of the medium and $\beta = v/\mathrm{c}$ the particle velocity in units of the speed of light c. Cherenkov radiation is only emitted if $v \geq v_{\mathrm{phase}}$ or equivalently $n\beta \geq 1$. The refractive index depends on the wavelength and has a value of $n = 1.31$ in ice for a wavelength of 400 nm [205], which corresponds to the peak sensitivity of the optical modules in IceCube (see Section 3.2.2). Consequently, the emission threshold for Cherenkov radiation is $\beta_{\mathrm{Ch}} \gtrsim 0.76$, which corresponds to a lower energy of 0.28 MeV for electrons and 58.09 MeV for muons well below the energy threshold of $\sim$200 GeV in IceCube. With the usual approximation $\beta \simeq 1$ for high-energy particles in IceCube, the opening angle of the Cherenkov cone is $\theta_{\mathrm{Ch}} \simeq 40.2°$ at the peak sensitivity wavelength.

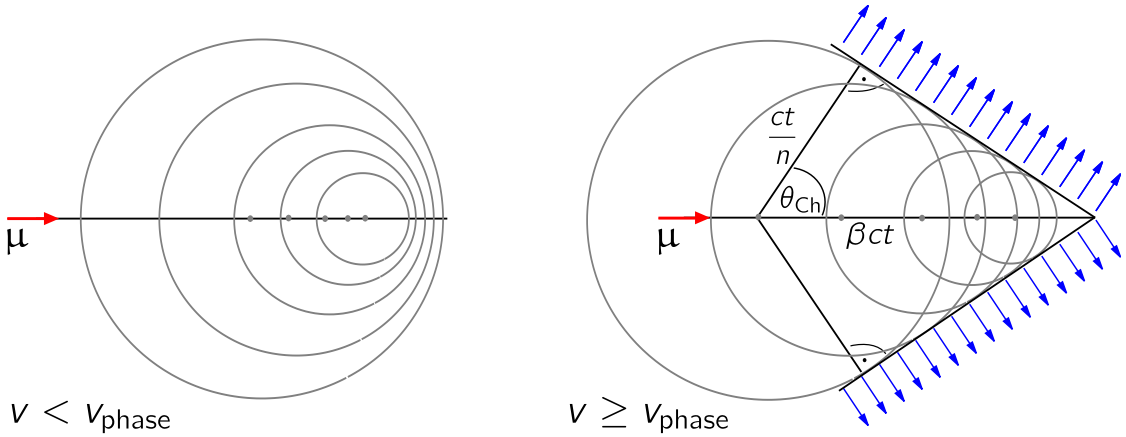

Figure 3.5: A sketch of the Cherenkov effect is depicted for a muon with a velocity $v = \beta c$ traversing a dielectric medium with a refractive index n. The phase velocity of light in the medium is $v_{\mathrm{phase}} = \mathrm{c}/n$. The circles represent wavefronts with equal phase shifts and illustrate isotropic emission if the muon velocity is smaller than the phase velocity (left) and a coherent emission at an angle θ_{Ch} if the muon velocity is greater than the phase velocity (right).

The number of Cherenkov photons that are emitted within a waveband $d\lambda$ by a particle with charge ze within the propagation length dx is given by the *Frank-Tamm-formula*

$$\frac{d^2N}{dxd\lambda} = \frac{2\pi\alpha z^2}{\lambda^2}\left(1 - \frac{1}{\beta^2 n^2(\lambda)}\right), \tag{3.8}$$

where α is the fine-structure constant [78]. For a high-energy particle with $\beta \simeq 1$ passing through ice, this gives approximately 250 photons/cm in the wavelength band of 300 nm to 500 nm, in which the optical modules in IceCube are most sensitive [206].

As discussed in the previous sections, neutrino interactions in IceCube can only be detected indirectly via Cherenkov radiation emitted by charged secondary particles. These can be single leptons from the primary interaction, most importantly muons due to their long radiation length, or electromagnetic or hadronic particle showers. At an energy above 1 TeV, the Cherenkov light emitted directly by a muon is negligible. Such a muon is predominantly detected via light emitted by secondary particle showers that are initiated by stochastic losses along its propagation path. All other neutrino interactions at these energies are detected via Cherenkov light from electromagnetic and hadronic cascades (see Section 3.3.1). The amount of Cherenkov light emitted by a cascade is proportional to the total propagation length of all charged particles above the Cherenkov threshold in the shower.

3.2 Detector Components

The IceCube neutrino observatory is located at the Amundsen-Scott South Pole station in Antarctica. The detector instrumentation is based on the *digital optical module* (DOM), which combines a *photomultiplier tube* (PMT) with digital readout electronics. Thousands of these DOMs are deployed deep below the surface of the ice, thereby transforming approximately one gigaton of the ultra-transparent glacial ice into a giant Cherenkov detector. In the following Sections 3.2.1 to 3.2.3, only the most important detector properties are summarized. The information is based on [42], where a more detailed description can be found.

3.2.1 IceCube, DeepCore, and IceTop

The layout of the IceCube detector is shown schematically in Figure 3.1. It consists of three detector parts: *IceCube*, *DeepCore* and *IceTop*. The main array comprises IceCube and DeepCore and consists of 5160 DOMs arranged on 86 strings. Each string has 60 DOMs attached at a depth between 1450 m to 2450 m below the ice surface. IceCube is the main detector and instruments a total volume of $\sim 1\,\mathrm{km}^3$ of ice using 78 strings. DeepCore is an infill-array in the center of IceCube with a much smaller volume but denser instrumentation using 8 strings. IceTop is a surface detector which consists of 162 ice-filled tanks instrumented with two DOMs each. The detector was built by drilling 2.5 km deep holes with a customized hot water drill. After the deployment of a string, the water inside the drill hole refroze and sealed the DOMs irreversibly inside the ice. Each IceTop station was constructed by filling two tanks with water and inserting two DOMs into each tank. The water inside the tanks froze and the tanks were covered up with snow. Construction lasted from January 2005 to December 2010 and data collection has been ongoing with the full detector configuration ever since.

The strings are arranged on a hexagonal grid as depicted in Figure 3.6. It shows the position of IceCube and DeepCore strings and IceTop tanks. The vertical spacing of the DOMs is ~ 125 m and the horizontal spacing is ~ 17 m for the 78 IceCube strings. The instrumentation density limits the energy threshold to ~ 200 GeV (c.f. Section 3.1.2). The 8 additional DeepCore strings

have an average vertical spacing of 72 m. On each string, 10 DOMs are mounted every 10 m between a depth of 1750 m to 1850 m, and 50 DOMs are mounted every 7 m between 2100 m to 2450 m. The intermediate region is not instrumented due to a *dust layer* which is almost opaque to light (see Section 3.2.4). The denser instrumentation and higher quantum efficiency of those DOMs lowers the energy threshold of DeepCore to $\sim$10 GeV (see Section 3.2.2).

The main goal of IceCube has been the discovery of astrophysical neutrinos. Current topics of research span a wide range, including the search for neutrino point sources and the characterization of the spectral shape and flavor composition of the observed diffuse neutrino flux. The purpose of DeepCore is the characterization of the atmospheric neutrino flux while making use of a lower energy threshold. IceTop is used to characterize the cosmic-ray flux by measuring extended cosmic-ray-induced air showers. In addition, all three detector components can be used jointly for *veto-based searches* of neutrino interactions. A signal from a neutrino interaction in IceCube that is in coincidence with a signal in IceTop from a cosmic-ray-induced air shower is most likely of atmospheric origin. Furthermore, IceCube strings can be used as a veto region for incoming events in a search for interactions that start inside DeepCore. Although neither DeepCore nor IceTop are explicitly used in the work presented in this thesis, the veto-based approach is an important part of the event selection described in Section 4.2.

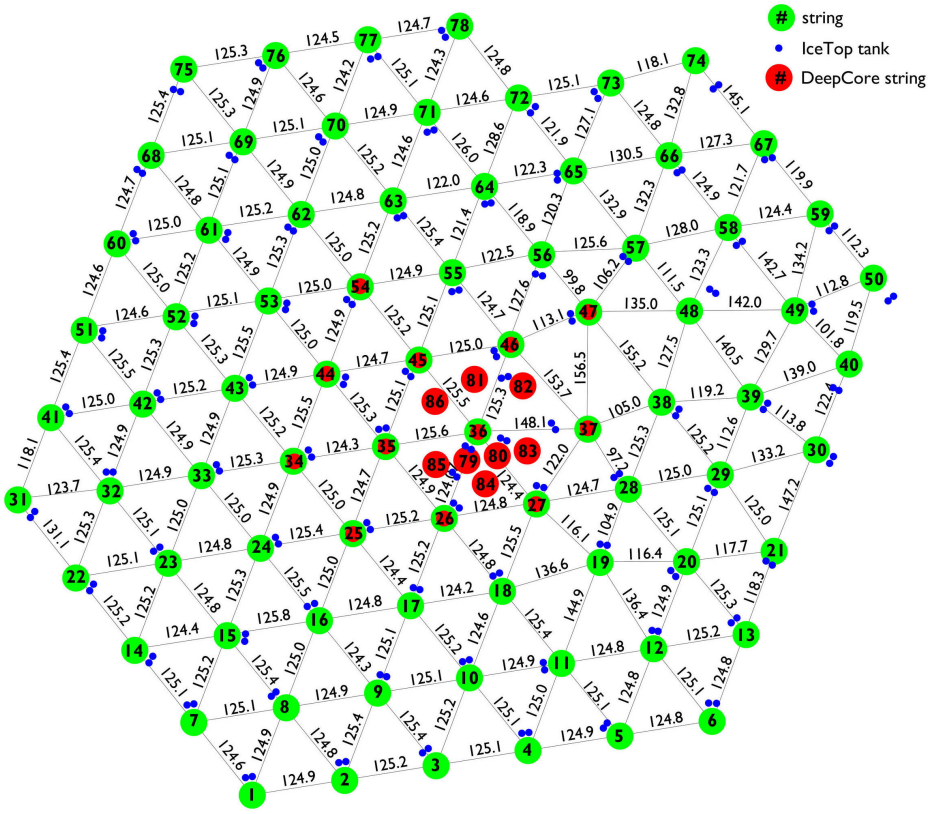

Figure 3.6: Schematic view of the hexagonal IceCube detector layout. It consists of 78 IceCube strings (green) and 8 DeepCore strings (red). The numbers between strings are the corresponding distances in meters. The average spacing between IceCube strings is $\sim$125 m, and the average spacing between DeepCore strings is $\sim$72 m with a larger variation. The locations of 162 IceTop tanks (blue) on the surface of the ice are marked. Figure reproduced from [207].

3.2.2 Digital Optical Modules and Flasher LEDs

The light sensor of IceCube is an autonomous detection unit combining a photomultiplier tube with digital readout electronics. The **digital optical module** is shown in Figure 3.7. It contains a 10″-diameter downward facing *Hamamatsu R7081-02* PMT with a peak quantum efficiency of about 25%. DeepCore DOMs use the same sized model *Hamamatsu R7081-02MOD* with a peak quantum efficiency of 34%. The PMTs are sensitive to light in a wavelength range of 300 nm to 650 nm with the peak quantum efficiency near 390 nm. They are operated at a maximum high-voltage of 2047 V and at a gain of 10^7. The PMT signal is split into a delay line and a discriminator, with a trigger threshold set to 0.25 pe (photoelectrons). A signal above this trigger threshold is called a *hit*, and the pulse shape is called a *waveform*. The waveform of a triggered hit is sampled from the delay line by two digitizers with different sampling speeds and overlapping dynamic range. The first is an *analog transient waveform digitizer* (ATWD) and the second is a continuously sampling *fast analog-digital-converter* (fADC). Depending on the amount of light, the digitizers typically record waveforms above 1 mV and beyond the PMT linearity limit at ∼2 V. The maximum duration is 427 ns at a resolution of 3.3 ns for the ATWD and 6.4 µs at a resolution of 25 ns for the fADC. A system of three ATWDs is operated at different gains to enhance the resolution of recorded waveforms. All digitizers and readout electronics are located on the DOM mainboard.

The DOM has a spherical glass vessel with 1.25 cm thick walls and a diameter of 33 cm as an outer layer. It consists of borosilicate and is resistant to the high pressure and cold temperatures of the deep glacial ice. Although the potassium content of the glass is purposely low, the β-decay of the ^{40}K still generates noticeable noise. Along with other noise sources, such as thermionic emission and electronic noise, the total average dark noise hit rate is 560 Hz (780 Hz) for IceCube (DeepCore) DOMs. The cable for the high-voltage supply and the readout of the digitized PMT signal is connected through a socket in the glass vessel. The cable and the DOM are mounted on a harness that keeps it fixed on the string. The cable is attached to the outside of a DOM and covers a small fraction of about 1% of the photo-sensitive area. The PMT is covered by a *mu-metal cage* to compensate the Earth's magnetic field, which increases the collection efficiency and resolution of a single photoelectron. The photo-sensitive area of the PMT is optically coupled to the glass pressure housing by matching the refractive indices with a *room temperature vulcanizing* (RTV) gel.

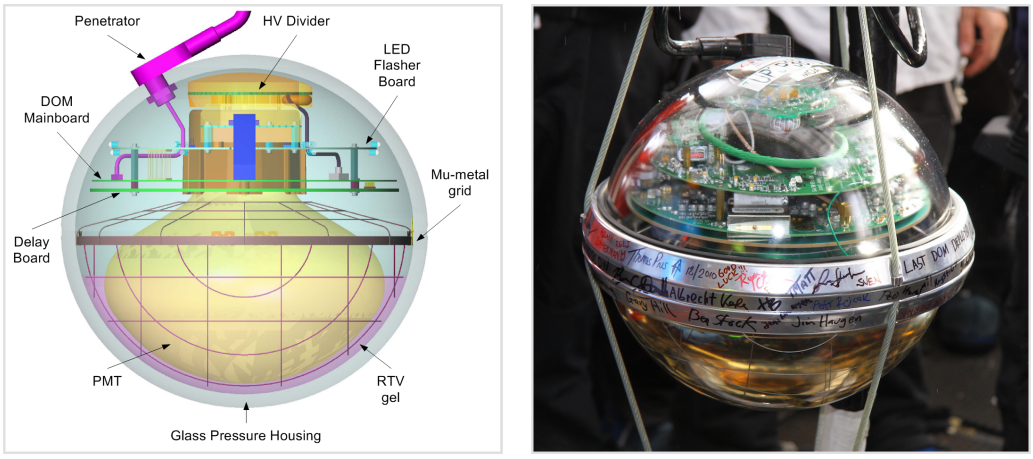

Figure 3.7: Schematic view (left) and photo (right) of the digital optical module. The photo-sensitive area of the PMT is located at the bottom of the DOM and the high-voltage divider and readout electronics at the top. The DOM is surrounded by a glass pressure housing that is optically connected to the PMT surface with a gel. The metal grid surrounds the PMT to compensate for the Earth's magnetic field. Figures reproduced from [207].

Each DOM has 12 **flasher LEDs** that are mounted onto a separate circuit board. They are used as in-situ light sources for calibration purposes and for measuring the ice properties (see Section 3.2.4). The LEDs are aligned in pairs of six in a circular pattern. One is tilted downward at an angle of 10.7° and one is tilted upward at an angle of 51.6° with respect to the horizontal plane. After the light is refracted through the glass of the DOM into the ice, the first LED emits light horizontally into the ice and the second at an upward angle of 48°. The horizontal angular spacing between each LED pair is approximately 60°. They can be flashed individually or simultaneously in any combination. The wavelength distribution of the light output is very narrow, with a central value of (405 ± 5) nm.[1] The angular emission profile has a *full width at half maximum* (FWHM) of 30° in air. After the light refraction into the ice, the emission is modeled using a *Gaussian profile* with $\sigma = 9.7°$ ($\sigma = 9.2°$) in the polar direction and $\sigma = 9.8°$ ($\sigma = 10.1°$) in the azimuthal direction for the tilted (horizontal) LEDs. The duration of a flasher pulse can be adjusted from 6 ns to 70 ns at the FWHM with a 10% afterglow decaying over 15 ns to 20 ns. The brightness can be adjusted via the driving voltage from 4.5 V to 15 V. The total light output depends on both the width and brightness of a single flasher pulse as well as the number of flashed LEDs. A single DOM can generate a light output of $\sim 10^6 - 10^{11}$ photons, which corresponds to an electromagnetic equivalent energy of $\sim 10\,\text{GeV} - 1\,\text{PeV}$.

3.2.3 Triggering, Data Acquisition, and Event Filtering

In IceCube, DeepCore, and IceTop, it is not feasible to read out every single DOM continuously. Instead, **triggers** are defined as algorithms which look for clusters of hit DOMs in time and space. Unlike randomly distributed hits from dark noise and radioactive decay, clusters of hits indicate light from a particle interaction in the detector. In its most basic form, this is implemented as a *hard local coincidence* (HLC) which is met when at least two neighboring DOMs on the same string detect hits within a time window of 1 µs. The fundamental trigger in IceCube requires at least eight HLC hits in a sliding time window of 5 µs without any requirement for the spatial correlation of the HLC hits. This is called the *simple multiplicity trigger* (SMT). Each sub-detector has different values for the number of required HLC hits and for the sliding time window, which are based on the geometry of the detector and on the travel time of light in ice. Longer time windows are added before and after the trigger to also read out early and late hits in the event. In addition, there are other triggers that look for slowly moving particles or that trigger at a fixed rate, for example. Consequently, multiple triggers run in parallel, and overlapping time windows are merged for events that fulfill more than one trigger. The total trigger rate of all sub-detectors varies between 2500 Hz to 2900 Hz depending on the season.

A triggered event is read out by the **data acquisition system** (DAQ) which is located in the IceCube laboratory on the surface of the ice. It handles the recorded information from 86 DOM hubs, each managing 60 DOMs per string, and uses the digitized waveforms of all DOMs to build a full event in space and time. Multiple reconstruction algorithms obtain first estimates of event properties, such as the direction or deposited energy. Depending on the event topology or other criteria, the algorithms and computing time may vary. Computational resources are very limited at the South Pole and these algorithms are thus mostly simple in nature and only applied where necessary. Various **event filters** run online at the IceCube laboratory to collect all information and sort events into different data streams. The processed data from the *online filtering* is saved and transmitted to the Northern Hemisphere via satellite. With much larger computational resources available there, the *offline filtering* uses more sophisticated reconstruction algorithms. All events from the various data streams are collected at the *Level 2* of the offline filtering, which is the basis for the event selection used in this work (see Section 4.2).

[1] There are also a few DOMs which carry LEDs with light output at different wavelengths. This is important for studying the wavelength dependence of scattering and absorption in ice (see Section 3.2.4).

3.2.4 Optical Properties of the South Pole Ice

The deep Antarctic ice is the most important detector component as it is the detection target and light propagation medium in IceCube. Unlike the DOM hardware, which has been calibrated and studied in the laboratory, the glacial ice can only be measured in-situ and is therefore more difficult to describe. The optical properties arise from the dust concentration and the amount of air bubbles in the ice as well as the crystalline and molecular structure of ice. The first data was obtained using ice cores of the deep regions below a depth of 2000 m from drill sites approximately 1000 km away from the South Pole [208]. The deep South Pole ice was first measured with the LED calibration system of AMANDA [209]. During the construction of IceCube, direct measurements of the dust concentration in the glacial ice were obtained by a dust logger that had been deployed into some drill holes [210]. In addition to the dust-logger data, the flasher LED calibration system of the IceCube detector has been used for fitting a detailed **South Pole Ice Model** (SPICE). It is the default ice model of IceCube, for which multiple iterations (SPICE1, SPICE2, SPICEMie, SPICELea) have been developed so far [211, 212].

The optical properties described by each ice model are the **scattering** and **absorption** of light in ice. They are quantified by the *scattering length* l_s and *absorption length* l_a, respectively, as well as an average scattering angle. The scattering length is the average propagation distance after which a photon is scattered and the absorption length after which the survival probability of a photon decreases to 1/e. In practice, only an *effective scattering length* $l_s^{\text{eff}} = l_s/(1-\langle\cos\theta\rangle)$ is experimentally accessible, for which the average scattering angle $\langle\cos\theta\rangle$ is taken into account. The effective and geometric scattering lengths are equal ($l_s^{\text{eff}} = l_s$) if the light is scattered isotropically. Measurements with the in-situ LED calibration system of IceCube have yielded $l_s^{\text{eff}} \simeq 6\,\text{m} \ldots 90\,\text{m}$ and $l_a \simeq 20\,\text{m} \ldots 300\,\text{m}$, depending on depth [211]. Consequently, the deep ice is so clear that photons may travel for hundreds of meters before being absorbed. However, the much shorter scattering lengths cause the light to diffuse relatively quickly, with the result that a point-like light source looks nearly isotropic at a distance of $\sim 100\,\text{m}$.

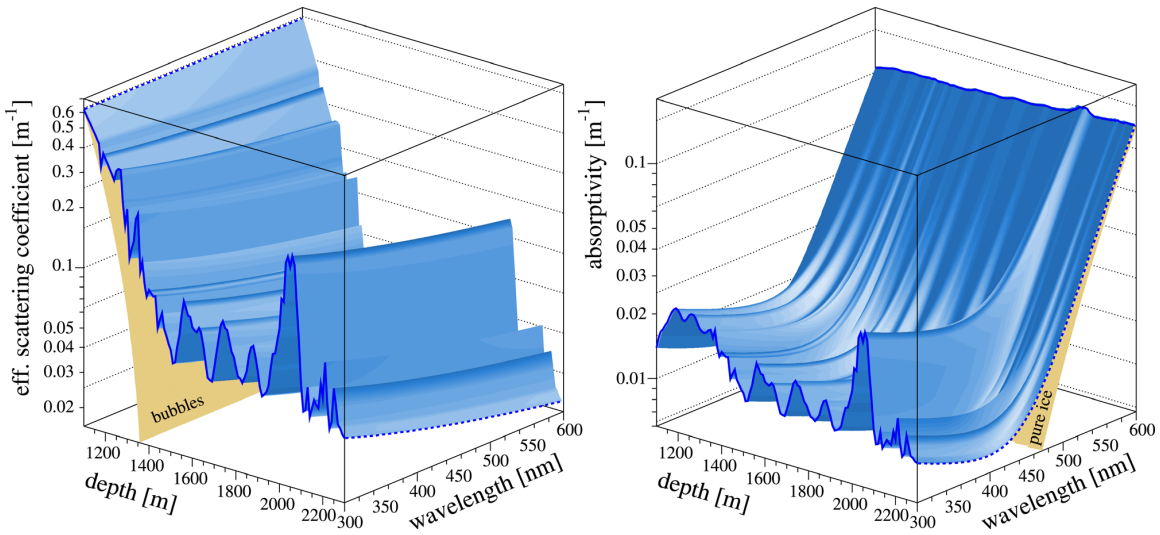

Figure 3.8: Effective scattering coefficient (left) and absorption coefficient (right) of light in South Pole ice as a function of depth and wavelength. Scattering in the shallow ice is large due to bubble columns. In contrast, the deep ice is very clear and absorption is minimal around a wavelength of 400 nm. The region of high absorption and scattering around a depth of 2000 m is called *dust layer* and likely due to volcanic ash. Figure reproduced from [209].

Both scattering and absorption depend on the wavelength of the light and on the depth of the ice as shown in Figure 3.8. Here, the measured and modeled effective scattering and absorptions coefficients are shown. They are defined as the reciprocal values of the effective scattering and absorption length, respectively. These measurements were obtained by the in-situ LED calibration system of AMANDA [209]. Down to a depth of $\sim 1300\,\mathrm{m}$, light scattering is dominated by residual air bubbles. At larger depths, the increasing pressure leads to a compression of the air bubbles, and dust becomes the dominant source of scattering. The dust concentration changes with depth due to variations in climate and volcanic activity as snow accumulates on the South Pole glacier over time [213]. Near a depth of $\sim 2000\,\mathrm{m}$, scattering and absorption is significantly increased due to a high dust concentration, potentially from a major volcanic eruption in the past. This region is called *dust layer*. Light absorption is caused by dust particles in the ice and therefore follows the same depth dependence as scattering for the ice below 1400 m. Light scattering decreases with its wavelength. It is larger for ultraviolet light and smaller for infrared light. Absorption of light is also dependent on its wavelength. The intrinsic properties of ice cause a strong attenuation of infrared light. The absorption is minimal for light with a wavelength around 400 nm and, again, larger for light with a shorter wavelength.

The SPICE1 ice model was fitted using full brightness LED flasher data and describes the effective scattering and absorption coefficients at a wavelength of 400 nm for ice layers between a depth of 1098 m to 2798 m in bins of 10 m. The width of the ice layers is limited by the vertical distance between two DOMs. Unlike the newer generation ice models, SPICE1 was completely symmetric and isotropic within one ice layer. In SPICEMie, the ice model fit was extended to include numerical calculations based on Mie theory [214]. Also, evidence arose that the ice layers are not exactly horizontal but rather tilted [211]. This **ice tilt** most likely related to an uneven surface of the rock at the bottom of the glacier on which the ice layers accumulated over time. The effect was parametrized symmetrically along an axis that is approximately perpendicular to the glacial flow and also dependent on depth. With the extension of an ice tilt, the scattering and absorption coefficients have effectively become dependent on the full three-dimensional position in the ice instead of just the depth. In the latest ice model, SPICELea, the isotropy assumption has been lifted and an **ice anisotropy** of the scattering coefficient depending on the direction of the photon propagation has been introduced [212]. The modulation of the nominal scattering coefficient was fitted to -8% along the horizontal direction of the glacial flow, $+4\%$ along the horizontal direction of the ice tilt and $+4\%$ along the vertical direction towards the surface of the ice. There has been no evidence that the modulation is also dependent on the position in the glacier. The ice anisotropy is an asymmetry of the model which is important for tau-neutrino reconstruction in IceCube. This will be discussed in greater detail in Chapter 5.

3.3 (Re)construction of an IceCube Event

A highly energetic particle interaction in the IceCube detector can produce enough Cherenkov light to trigger hundreds of DOMs. Each DOM records a digitized waveform that carries information of both the arrival time and the amount of detected light. Together with the position of the DOM, the four-dimensional distribution of Cherenkov light in the detector is determined. The entirety of all triggered DOMs make up an event in IceCube. It can be visualized to display different hit patterns which are classified into various event topologies. Event properties such as the direction, energy, or interaction type can be derived by reconstruction algorithms and used to define event selections. In order to study the performance of reconstruction algorithms, hundreds of thousands of events are simulated in IceCube by Monte Carlo methods, and the true simulation parameters are compared to the reconstructed results.

3.3.1 Event Topologies

The visualization of an event in IceCube is commonly shown as in Figure 3.9. It shows the IceCube detector as an array of strings where each colored sphere corresponds to a triggered DOM. The size of the sphere scales with the amount of detected light. The color indicates the arrival time going from early hits marked in red to late hits marked in blue. The hit pattern that is caused by the light distribution in the ice is a footprint of the particle interaction. In most cases, it is not possible to directly identify the interaction type itself but only deduce it from the hit patterns. Similar hit patterns are categorized into event topologies. The three most important topologies are *single cascade*, *double cascade*, and *track* (see Figure 3.9).

A **single cascade** is caused by the NC interactions of (anti)neutrinos of all flavors and the CC interaction of electron-(anti)neutrinos. In any NC interaction, the primary neutrino scatters off a nucleus in the ice, causes a hadronic cascade from the recoil, and leaves the detector without further interaction (c.f. Section 3.1.1). In addition to a hadronic cascade, the CC interaction of an electron-(anti)neutrino also produces an electron (positron). Due to the short radiation lengths of electrons and positrons, they produce an electromagnetic cascade (c.f. Sections 3.1.2 to 3.1.3). Both hadronic and electromagnetic cascades are contained within a few meters. Hence, the Cherenkov light emission is effectively reduced to a point-like source when comparing it to the kilometer-scale of the detector. Due to the light scattering over longer distances (c.f. Section 3.2.4), the hit pattern for a cascade looks almost spherical.

A **double cascade** is only caused by the CC interaction of a tau-(anti)neutrino ("double bang"). The primary neutrino interaction produces a hadronic cascade and a tau (antitau). Depending on its energy E, the tau propagates an average distance $L \simeq 50\,\mathrm{m} \cdot E/\mathrm{PeV}$ before it decays (c.f. Section 3.1.2). Due to its high mass, the tau has little stochastic energy losses and therefore emits a negligible amount of Cherenkov light along its propagation path. The tau decay produces another cascade or a track depending on the decay channel. The branching ratios are 17.83% for $\tau^{\pm} \to e^{\pm} + \overset{(-)}{\nu}_e + \overset{(-)}{\nu}_\tau$, 17.41% for $\tau^{\pm} \to \mu^{\pm} + \overset{(-)}{\nu}_\mu + \overset{(-)}{\nu}_\tau$, and 64.76% for $\tau^{\pm} \to X + \overset{(-)}{\nu}_\tau$ where X stands for a hadronic cascade [78]. Hence, both the electronic and hadronic decays produce another cascade. The double cascade topology therefore consists of a first (interaction) cascade linked by a subsequent second (decay) cascade and makes up approximately 83% of all CC tau-neutrino interactions. The various other event topologies involving a tau-neutrino interaction will be discussed in Section 4.1.

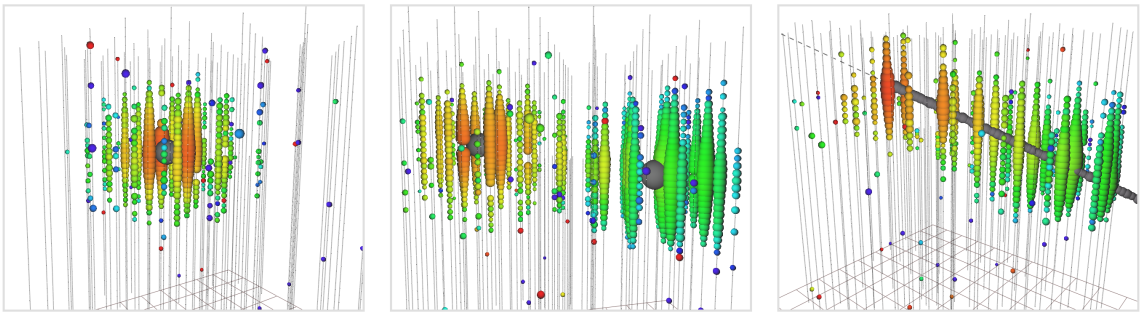

Figure 3.9: Event topologies in IceCube: single cascade (left), double cascade (center), and track (right). Colored spheres indicate hit DOMs. The size of the sphere scales with the amount of detected light, and the color indicates the photon arrival times going from red (early) to blue (late). Single cascades are described by a spherical light pattern and are caused by electromagnetic and hadronic showers which are point-like in comparison to the kilometer-scale size of the detector. Double cascades are described by the light pattern from two subsequent cascades linked to the production and decay of a tau lepton. Tracks are described by an elongated light pattern caused by muons traversing the entire detector.

A **track** occurs whenever a highly energetic muon traverses the detector. Most abundantly, these are atmospheric muons from cosmic-ray-induced air showers that are energetic enough to reach the detector. Tracks are also caused by the CC interaction of a muon-(anti)neutrino producing a hadronic cascade and a muon (antimuon). If the neutrino interaction vertex is outside the detector volume, atmospheric muons and neutrino-induced muons are indistinguishable (without considering the energy and direction of the track). These events are called *through-going tracks*. If the vertex is inside the detector volume, both the hadronic cascade from the primary interaction and the emerging track from the produced muon are visible. These events are called *starting tracks* and can only be caused by neutrino interactions and not by atmospheric muons, as they cannot enter the detection volume without being visible. This property is exploited in the high-energy starting event selection used in the context of this thesis (see Section 4.2).

3.3.2 Monte Carlo Event Simulation

The search for astrophysical neutrino interactions in the IceCube detector is conducted in a *blind* manner. All expected signal and background components to this search are modeled in simulation and then used for the development of reconstruction algorithms, event selections, and analysis designs. If available, every step of this process is validated against a small subset of the experimentally available data (usually 10%). Event simulation in IceCube is based on commonly used Monte Carlo methods. The simulation framework contains all steps, starting with the generation and propagation of a primary particle, the interaction and subsequent production and propagation of secondary leptons, the emission and propagation of Cherenkov light, and ending with the digitized waveforms that are recorded by all hit DOMs in IceCube.

Primary particle generation The simulation chain starts with the generation of a primary particle which can be a neutrino or a cosmic-ray particle. Neutrinos are the only primary particles that can reach the detector, whereas cosmic rays interact in the atmosphere well above the surface of the ice and create atmospheric particle showers. Only muons from these cosmic-ray-induced air showers can propagate through the ice and penetrate the detector volume. The software that generates atmospheric muon simulation in IceCube is an adaption of `CORSIKA` (*Cosmic-Ray Simulations for Kascade*) [215], where only muons from the shower are propagated into the deep ice. Because this process is computationally expensive, a parametrized version of muons from air showers called `MuonGun` has been developed that allows for atmospheric muons to be generated more effectively [216]. However, only single muons can be simulated with this software. In a veto-based event selection, as it is used in the context of this thesis, muon bundles are rejected extremely efficiently, such that the dominating background is single muons.

The software that generates neutrinos is called `NuGen` (*Neutrino Generator*) and is based on `ANIS` (*All Neutrino Interaction Simulation*) [217]. The neutrino generation can be anywhere inside or below the ice to account for Earth absorption. The interaction is forced into a region from which charged secondaries can reach the detector volume. In simulation production, there is no difference between atmospheric and astrophysical neutrinos. It is only when a specific flux model is used and a generated event is weighted accordingly that the difference is expressed in the expected event rate (see Equation 3.11 and explanation below). The correlation of atmospheric neutrinos and atmospheric muons from the same cosmic-ray-induced air shower is taken into account via a parametrization that characterizes the self-veto effect, in which a discarded muon simultaneously reduces accompanying atmospheric neutrinos (c.f. Section 2.3.2). Neutrinos and antineutrinos as well as neutrinos of all flavors are commonly generated in equal amounts, i.e. in simulation production $\nu : \bar{\nu} = 1 : 1$ and $\nu_e : \nu_\mu : \nu_\tau = 1 : 1 : 1$.

Lepton propagation Both atmospheric muons from air showers and secondary leptons, such as electrons, muons, and taus from CC neutrino interactions, are propagated through the ice after they are produced. The software used for lepton propagation is called PROPOSAL (*Propagator with optimal precision and optimized speed for all leptons*) and is based on the previous implementation MMC (*Muon Monte Carlo*) [195, 218]. The lepton production is simplified by assuming that the emission angle is aligned with the incident angle of the primary particle and that it travels at the speed of light which are both reasonable assumptions above the energy threshold of 100 GeV. The various propagation effects of different particle types and energies as described in Section 3.1.2 is taken care of by PROPOSAL. In particular, highly energetic muons are simulated to have long tracks that are predominantly characterized by stochastic energy losses. Electromagnetic and hadronic cascades as described in Section 3.1.3 are simulated by CMC (*Cascade Monte Carlo*) [194]. It generates individual particle showers by randomly sampling energy losses from the energy-dependent shower parametrization and also takes the LPM-effect into account. The shower parametrizations have been determined by fitting the Cherenkov light yield for a full shower simulation using GEANT4 (*Geometry And Tracking*) [202, 219].

Light emission and propagation After all primary and secondary particles have been propagated through the detector, their energy losses are recorded in a Monte Carlo *tree*. The next step of the simulation chain is the Cherenkov light emission and propagation from all particles or energy losses that are considered visible (c.f. Section 3.1.2). The number of photons scale with the total track length of all charged particles and the emission angle varies around 41° depending on the refraction index (c.f. Section 3.1.4). The individual photon propagation is executed by an *OpenCL*-based photon-tracking simulation CLSIM. It propagates a photon through the ice and tracks its scatter path until it is either absorbed or detected by hitting the PMT of a DOM. The scattering and absorption lengths are tabulated as a function of the position and direction of the photon (c.f. Section 3.2.4). The currently used ice models are SPICEMie [211] and SPICELea [212]. CLSIM uses GPUs for photon propagation, because they are optimal for running hundreds of simple operations (like photon scattering) in parallel [220].

The light yield of a generalized source is parametrized by *photo spline tables*, which will be discussed in greater detail in Section 5.2.1. The idea is to simulate a light source (cascade, track, or flasher) at a specific depth and direction multiple times and track the photon yield around the source. The simulation is repeated for all possible combinations of depth and direction and then recorded in a large table. Photo spline tables can be useful for simulating highly energetic events for which direct photon propagation would be computationally too expensive. With a photo spline table, the expected light yield of a source can simply be looked up for any DOM. Most importantly, however, these tables are required for reconstructing events where multiple source hypotheses must be tested very quickly (see Section 3.3.3). They were originally produced with PHOTONICS using CPUs for direct photon propagation [221] and have been generated with CLSIM using GPUs instead for a few years. Because the resulting tables are binned, they are fitted with a smooth *spline interpolation* that has been developed for this purpose [222].

Detector response The last step of the simulation chain is the response of the detector. Aside from its quantum efficiency, the PMT sensitivity depends on the wavelength and the incident angle of the photon. Whether a hit PMT is actually triggered therefore varies from photon to photon, which is considered in simulation. The angular photon acceptance is parametrized such that local scattering variations of the hole ice are taken into account. The PMT hardware has been calibrated and studied in the laboratory [223] and the results have been modeled in simulation. Specifically, the transit time and jitter of the PMT are important to model in simulation as they affect the time and width of a pulse, respectively. Finally, every trigger that runs online at the South Pole is also implemented in simulation. It is the last step of the simulation chain and completes the construction of a simulated event.

Weighting The majority of Monte Carlo simulation in IceCube is generated with a spectrum that may not reflect a realistic physical model. For example, if a search is focused on highly energetic neutrinos, it can be more useful to simulate an E^{-1} spectrum rather than the softer observed spectrum between E^{-2} and E^{-3}. The available number of simulated events required at the highest energies is thereby artificially increased and the usage of computational resources is optimized. This procedure is valid as long as the simulated events are later *reweighted* to represent a flux that is realized in nature.

Typically, a search for neutrino interactions in IceCube is just a counting experiment of N events over a certain exposure time Δt. Commonly, the rate $R = N/\Delta t$ is of interest and is given by

$$R = \int \mathrm{d}\Omega \int \mathrm{d}E \, A_{\mathrm{eff}}(E, \Omega) \, \frac{\mathrm{d}\Phi}{\mathrm{d}E} \tag{3.9}$$

in its most general form. Here, Ω is the solid angle and $\mathrm{d}\Phi/\mathrm{d}E$ the differential neutrino flux with energy E. The neutrino interaction probability is described by the *effective area* $A_{\mathrm{eff}}(E, \Omega)$. It depends on the direction and energy of the neutrino and on the detector properties. Whereas the effective area characterizes the experiment, the differential neutrino flux

$$\frac{\mathrm{d}\Phi}{\mathrm{d}E} = \frac{\mathrm{d}N}{\mathrm{d}t \, \mathrm{d}A \, \mathrm{d}\Omega \, \mathrm{d}E} \tag{3.10}$$

with N neutrinos per time t, unit area A, solid angle Ω, and energy E is model-dependent and the quantity of interest. The generation spectrum is given by a differential fluence which is the total number of generated events per unit area, solid angle, and energy. The *weight* of a simulated event is the ratio

$$w = \frac{\mathrm{d}N_{\mathrm{expected}}/\mathrm{d}t \, \mathrm{d}A \, \mathrm{d}\Omega \, \mathrm{d}E}{\mathrm{d}N_{\mathrm{generated}}/\mathrm{d}A \, \mathrm{d}\Omega \, \mathrm{d}E} \tag{3.11}$$

which is in units of s^{-1}. The expected *event rate* for a physical model is simply the sum over all weights and its *statistical error* the square root of the sum over all weights squared [224]

$$R = \sum_i w_i \quad \text{and} \quad \sigma_R = \sqrt{\sum_i w_i^2}. \tag{3.12}$$

The weights can also be used to determine the *effective livetime*

$$T_{\mathrm{eff}} = \frac{\sum_i w_i}{\sum_i w_i^2}, \tag{3.13}$$

which is defined as the detector exposure time after which the statistical error of simulation and experimental data have become equal. Weighted neutrino simulation usually has an effective livetime of the order of hundreds of years, because neutrinos rarely interact in reality but can be forced to interact frequently in simulation. In contrast, atmospheric muon simulation usually has an effective livetime that is less than the detector exposure time, because thousands of muons are measured experimentally every second but cannot be simulated in the same frequency due to limited computational resources. A critical component in a search for neutrino interactions in IceCube therefore is the limited statistics of available atmospheric muon simulation to properly describe an important background component. The effective area as given in Equation 3.9 is directly calculated from the simulation weight of the generated event. It is used to quantify the signal efficiency of an event selection as will be discussed in Chapter 4.

3.3.3 Maximum Likelihood Event Reconstruction

An event in the IceCube detector is reconstructed by using the detected number and arrival time distribution of Cherenkov photons at each DOM in a **maximum-likelihood estimation**. The observed data are individual pulses with a charge (given in units of photoelectrons) at a certain time. Pulses are deconvolved from the digitized waveforms using known *single-photoelectron pulse templates*. The likelihood is defined as a product of probabilities, each comparing the observed data to the expected data of a certain source hypothesis. For each event, the parameters of a source hypothesis are varied until they maximize the likelihood. The resulting best-fit parameters then reflect the best knowledge of the particle interaction. They can be used to construct observables which estimate properties of the initial neutrino.

The likelihood is generally defined as a product over individual probabilities [225]

$$\mathcal{L}(\mathbf{d}|\mathbf{s}) = \prod_i p(d_i|\mathbf{s}), \tag{3.14}$$

where $\mathbf{s}$ is the parameter set that describes the source hypothesis and $\mathbf{d}$ is the observed data. For an IceCube event, a light source is given by $\mathbf{s} = (x_\mathrm{s}, y_\mathrm{s}, z_\mathrm{s}, t_\mathrm{s}, \theta_\mathrm{s}, \phi_\mathrm{s}, E_\mathrm{s})$ with cartesian coordinates $x_\mathrm{s}, y_\mathrm{s}, z_\mathrm{s}$, emission time t_s, polar angles θ_s and ϕ_s, and energy E_s. However, an event can also be more complex and contain multiple light sources (see below). The observed data $\mathbf{d} = \{(x_o, y_o, z_o, t_{oi}, \Delta t_{oi}, n_{oi}) \,|\, i \in \text{time bins}, o \in \text{DOMs}\}$ is the entirety of all digitized waveforms, characterized by the number of photoelectrons n_{oi} at the position x_o, y_o, z_o in a time bin with the central value t_{oi} and the width Δt_{oi}. Because each bin of the digitized waveform is simply a counting experiment of photoelectrons, the **Poisson probability** $p(n|\mu) = \frac{\mu^n}{n!}\mathrm{e}^{-\mu}$ for observing $n \in \mathbb{N}$ photoelectrons with an expectation of $\mu \in \mathbb{R}^+$ is used in Equation 3.14. Including the photon arrival times, the likelihood becomes

$$\mathcal{L}(\mathbf{d}|\mathbf{s}) = \prod_{\substack{o \in \text{hit} \\ \text{DOMs}}} \prod_{i \in \text{time bins}} \frac{\mu_{oi}^{n_{oi}}}{n_{oi}!}\mathrm{e}^{-(\mu_{oi}+\rho_{oi})} \prod_{\substack{o \in \text{unhit} \\ \text{DOMs}}} \mathrm{e}^{-(\mu_o+\rho_o)}, \tag{3.15}$$

where a term $\mu_o = \sum_i \mu_{oi}$ is included for all DOMs that did not detect any photoelectrons and $\rho_o = \sum_i \rho_{oi}$ is the time-integrated noise term. The time-dependent noise term $\rho_{oi} = \nu \Delta t_{oi}$ is simply given by the approximately constant noise frequency $\nu \simeq 560\,\mathrm{Hz}$ (c.f. Section 3.2.2) multiplied by the width of the time bin. The expected number of photoelectrons μ_{oi} for each arrival time t_{oi} is taken from the photo spline table of a source hypothesis (c.f. Section 3.3.2). While the observed data $\mathbf{d}$ remains fixed, the source parameters $\mathbf{s}$ are varied numerically until the likelihood in Equation 3.15 is maximal.[2]

A generalized multiple source likelihood fit in the **millipede framework** is used for the work presented in this thesis [226]. The main idea is that a track must be described by different source hypotheses depending on its energy. At energies below $\sim 1\,\mathrm{TeV}$ muons are minimum-ionizing and a continuous approximation of energy losses is valid. In this case, a track is a single muon moving through the detector at the speed of light and continuously emitting Cherenkov light. The expected number of photoelectrons is taken from a photo spline table which is generated by repeatedly simulating a low-energy muon traversing the entire detector. However, above $\sim 1\,\mathrm{TeV}$, stochastic losses of the muon induce secondary particle showers which dominate the total Cherenkov light yield of the track. The light emission pattern for showers is different, as they are approximately point-like and appear in irregular intervals along the track. In this case, the expected number of photoelectrons is a superposition of multiple showers each taken from a photo spline table which is generated by repeatedly simulating a cascade.

[2] In practice, the negative logarithm of the likelihood is minimized, as it is computationally more feasible.

Consequently, a high-energy track hypothesis for a `millipede` reconstruction is segmented into spatial bins, each containing a single cascade. This is sketched in Figure 3.10. The expected light yield at each DOM is then given by the linear superposition of all light sources (and noise). In a first iteration of the fit, the timing information is omitted and only the total number of observed photoelectrons $n_o = \sum_i n_{oi}$ and expected photoelectrons $\mu_o = \sum_i \mu_{oi}$ are compared for each DOM $o = 1 \dots m$. This is called an **amplitude fit**. The expectation values μ_o are determined by the *linear equation system* (LES)

$$\begin{pmatrix} B_{11} & \dots & B_{1k} & \dots & B_{1l} \\ \vdots & \ddots & \vdots & \ddots & \vdots \\ B_{o1} & \dots & B_{ok} & \dots & B_{ol} \\ \vdots & \ddots & \vdots & \ddots & \vdots \\ B_{m1} & \dots & B_{mk} & \dots & B_{ml} \end{pmatrix} \begin{pmatrix} E_1 \\ \vdots \\ E_k \\ \vdots \\ E_l \end{pmatrix} = \begin{pmatrix} \mu_1 \\ \vdots \\ \mu_o \\ \vdots \\ \mu_m \end{pmatrix}, \tag{3.16}$$

in which the superposition of all cascade energies E_k per track segment $k = 1 \dots l$ is scaled with the tabulated light yield B_{ok} [226]. The matrix elements $B_{ok} = B(x_k, y_k, z_k, \theta_k, \phi_k, x_o, y_o, z_o)$ are normalized to a cascade of 1 GeV energy and account for light scattering and absorption in the ice between a source k and receiver o. Because $l \neq m$ in general, the linear equation system in Equation 3.16 cannot be solved analytically. Instead, the unfolded energy losses $\{E_k \,|\, E_k \geq 0\}$ are determined by minimizing $|\mathbf{BE} - \boldsymbol{\mu}|$ via a *non-negative least-squares algorithm* [227].

After the first amplitude fit, more iterations of a **timed fit** are performed. Incorporating the photon arrival time distributions, the LES in Equation 3.16 becomes $\sum_k B_{oik} E_k = \mu_{oi}$ with $B_{oik} = B(x_k, y_k, z_k, t_k, \theta_k, \phi_k, x_o, y_o, z_o, t_{oi})$. Inserting into Equation 3.15 yields the `millipede` likelihood to be maximized during the event reconstruction

$$\mathcal{L} = \prod_{\substack{o \in \text{hit} \\ \text{DOMs}}} \prod_{\substack{i \in \text{time} \\ \text{bins}}} \frac{1}{n_{oi}!} \left(\sum_{\substack{k \in \text{light} \\ \text{sources}}} B_{oik} E_k + \rho_{oi} \right)^{n_{oi}} \mathrm{e}^{-\left(\sum_k B_{oik} E_k + \rho_{oi}\right)} \prod_{\substack{o \in \text{unhit} \\ \text{DOMs}}} \mathrm{e}^{-\left(\sum_k B_{ok} E_k + \rho_o\right)}. \tag{3.17}$$

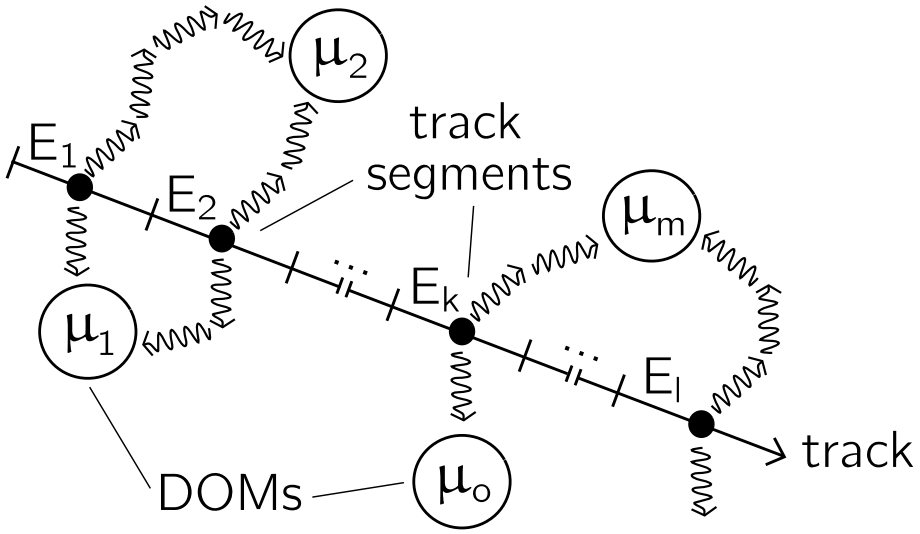

Figure 3.10: Sketch of the `millipede` unfolding. A muon track is divided into segments, each containing a cascade with energy E_k to fit the stochastic losses of the muon. The expected number of photoelectrons μ_o at every DOM o is determined by the superposition of all sources E_k along the track scaled with the tabulated light yield as stated in Equation 3.16.

This framework allows the reconstruction of **single cascade**, **double cascade**, and **track** source hypotheses (c.f. Section 3.3.1) with the respective algorithms `monopod`, `taupede`, and `millipede`. They are based on the same likelihood as defined in Equation 3.17 but use different source parametrizations. The hypothesis which fits the observed data best can be identified by comparing maximum likelihood values. It is an estimate of the interaction type in the detector.

Monopod is the single cascade source reconstruction algorithm which considers a cascade hypothesis as a special case of the track hypothesis. Consequently, the sum in Equation 3.17 reduces to a single expectation value $\mu_{oi} = B_{oi} E_\mathrm{s}$. The single cascade source is parameterized as $\mathbf{s} = (x_\mathrm{s}, y_\mathrm{s}, z_\mathrm{s}, t_\mathrm{s}, \theta_\mathrm{s}, \phi_\mathrm{s}, E_\mathrm{s})$. The vertex $(x_\mathrm{s}, y_\mathrm{s}, z_\mathrm{s})$ and time t_s correspond to the shower maximum (c.f. Section 3.1.3). The vertex can be used to exclude certain regions like the dust layer or the outer rim of the detector in which reconstruction works less reliably. The direction $(\theta_\mathrm{s}, \phi_\mathrm{s})$ can be useful to distinguish atmospheric and astrophysical neutrinos (c.f. Section 2.3.2) but is generally not well constrained. The deposited energy $E_\mathrm{dep} = E_\mathrm{s}$ is associated with the visible energy deposition of the shower. It is an important estimator of the initial neutrino energy.

Taupede is the double cascade source reconstruction algorithm. It is the intermediate case between a single cascade and a track by causally connecting two cascades. Instead of a fixed segment spacing, it is implemented to have one more additional free fit parameter which is the distance L between the two cascades. The double cascade source is fully determined with $\mathbf{s} = (x_\mathrm{s}, y_\mathrm{s}, z_\mathrm{s}, t_\mathrm{s}, \theta_\mathrm{s}, \phi_\mathrm{s}, L, E_1, E_2)$. In this case, E_1 and E_2 can be associated with the cascade energy of the neutrino interaction and the tau decay, respectively, and L can be identified with the tau decay length. The deposited energy is $E_\mathrm{dep} = E_1 + E_2$. The reconstruction of double cascade events will be discussed in greater detail in Section 4.3 as this is a central part of the search for tau-neutrino interactions presented in this thesis.

Millipede is the reconstruction algorithm for track sources. As described above, the track hypothesis is parameterized via multiple subsequent cascade sources and is fully determined by $\mathbf{s} = (x_\mathrm{s}, y_\mathrm{s}, z_\mathrm{s}, t_\mathrm{s}, \theta_\mathrm{s}, \phi_\mathrm{s}, \Delta L, \{E_k\})$, where ΔL is the length of the equally-spaced track segments. The position, time, and direction of each secondary cascade with energy E_k is fully defined by knowing an arbitrary starting (or "anchor") point $(x_\mathrm{s}, y_\mathrm{s}, z_\mathrm{s}, t_\mathrm{s})$ in space and time and the length of the track segments. This is valid under the assumption that the track moves with the speed of light and that all secondary cascades are aligned with the direction of the track. While the reconstructed spatial distribution of all energy losses E_k can be an estimate of the muon energy, the deposited energy $E_\mathrm{dep} = \sum_k E_k$ is not a well-suited measure of the primary neutrino energy. In contrast, the commonly well-reconstructed direction $(\theta_\mathrm{s}, \phi_\mathrm{s})$ can be used in conjunction with the time t_s to search for neutrino point sources and correlated optical sources.

The parameter set $\mathbf{s}$ of any source hypothesis is given with respect to the right-handed Cartesian **IceCube coordinate system**. The center is located at 46 500 ft E and 52 200 ft N in the *Universal Transverse Mercator* (UTM) coordinate system at an elevation of 2900 ft (corresponding to a depth of 1948.07 m below the surface of the ice). The x-axis points Grid East, the y-axis points Grid North towards Greenwich, UK, and the z-axis points towards the surface of the ice. A vertex is given in Cartesian coordinates with respect to the coordinate center. The boundaries of the instrumented detector volume are approximately $(-500\,\mathrm{m}, 500\,\mathrm{m})$ in each dimension. A time is given with respect to the beginning of the detector readout and can be transformed into the *Modified Julian Date* (MJD) using the time offset from the detector calibration. A direction is given as a set of polar angles (θ, ϕ) or (zenith, azimuth). The former correspond to the propagation direction of a particle and the latter point back to its origin. The transformation is zenith $= 180° - \theta$ and azimuth $= \phi + 180°$, where zenith and θ are bounded by $[0°, 180°]$, and azimuth and ϕ are bounded by $[0°, 360°)$.

4 Development of Tau-Neutrino Identification

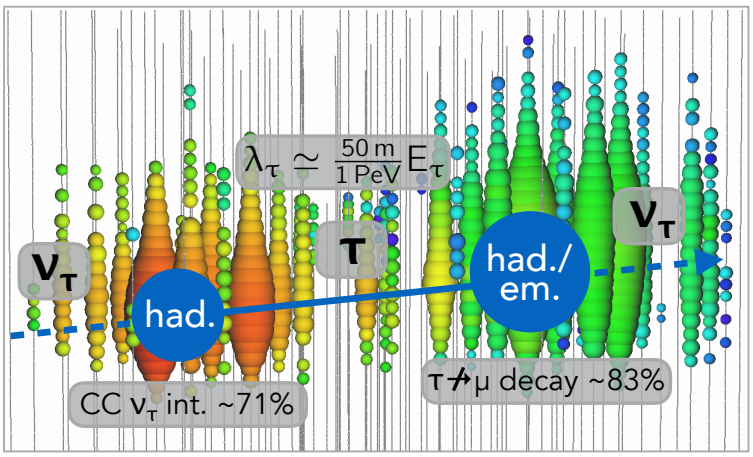

Figure 4.1: A simulated "double bang" event in the IceCube detector. A charged-current tau-neutrino interaction produces a hadronic cascade and a tau lepton. The tau travels an average distance of approximately 50 m per PeV energy until its decay produces a hadronic or an electromagnetic cascade (excluding the muonic decay channel). About 59% of all tau-neutrino interactions are "double bang" events, which makes it the most promising event topology for a first detection. However, the identification is only possible at the highest energies where the tau decay length is long enough for the interaction and decay cascades to be separable. The simulated event shown here has a neutrino energy of ~ 10 PeV.

The idea of observing tau-neutrino interactions in a large-volume neutrino detector via the "double bang" event topology was initially proposed in [228]. It is characterized by a charged-current tau-neutrino interaction with a nucleus in the ice which produces a hadronic cascade and a tau lepton. After propagating a certain distance, the tau decays and produces a second hadronic or electromagnetic cascade. This double cascade event topology excludes the muonic decay of the tau and is unique to the tau flavor. The two cascades are only distinctly resolvable if the distance between them is large enough. The decay length of the tau scales linearly with its energy due to relativistic effects. The work presented in this chapter focuses on the explicit reconstruction of the double cascade event topology as a means for direct detection of tau-neutrino interactions in IceCube. It is a continuation of an initial study presented in [229] and is concluded such that, for the first time, a search for tau-neutrino interactions via the double cascade topology is experimentally realizable.

In Section 4.1, an overview of tau-neutrino signatures in IceCube is given and the uniqueness of the double cascade method is explained. In Section 4.2, the high-energy starting event selection, which is used in the context of this thesis, is summarized. In Section 4.3, the implementation of the double cascade event reconstruction and the construction of tau-neutrino-related observables are described. A method for neutrino flavor discrimination is developed, and the resulting distributions and resolution of event properties are discussed. In Section 4.4, the tau-neutrino identification efficiency is studied with respect to the observable phase space.

4.1 Tau-Neutrino Interactions in IceCube

Tau-neutrino interactions have a variety of signatures in IceCube. Aside from neutral-current interactions where only the hadronic cascade of the neutrino-nucleon scattering is observable, the charged-current interaction produces a tau lepton that causes different event topologies. These are determined by the neutrino interaction vertex, the energy-dependent tau decay length, the decay vertex, and the decay channel. A summary of all tau-neutrino topologies in IceCube is sketched in Figure 4.2. They are shown as a function of the tau energy E_τ and the tau decay length λ_τ, which are connected via $\lambda_\tau \simeq \frac{50\,\mathrm{m}}{1\,\mathrm{PeV}} E_\tau$ (c.f. Section 3.1). Cascades are visualized as circles and tracks as lines. The line of a tau is drawn thinner than that of a muon, because a tau track emits much less light than a muon track. A general distinction between different topologies is the decay channel of the tau. The muonic decay of the tau $\tau^\pm \to \mu^\pm + \overset{(-)}{\nu}_\mu + \overset{(-)}{\nu}_\tau$ has a branching ratio of $\sim 17\%$ and produces an outgoing muon track from the tau decay vertex. All other decay channels of the tau produce another cascade with an inclusive branching ratio of $\sim 83\%$. Multiplied by the fraction $\sim 71\%$ of the charged-current cross section over the total cross section, about 59% of all tau-neutrino interactions are "double bang" events.

The majority of topologies can only be seen at very high energies where the tau is able to propagate over a sufficiently large distance before it decays. A high-energy tau track that enters the detector from the outside and decays into a cascade on the inside, or one that starts inside and stops somewhere outside the detector, is very hard to distinguish from a low-energy muon that stops or starts in the detector, respectively. It is also difficult to identify a high-energy tau which enters the detector from the outside and decays into a muon inside the detector, because the transition from a very dim to a very bright track is extremely challenging to reconstruct. All three topologies only occur at very high energies above $\sim 10\,\mathrm{PeV}$, where the average tau decay length is above $\sim 500\,\mathrm{m}$ and therefore long enough to be seen as a track. Events at these energies are most likely down-going in the detector as the absorption of neutrinos inside the Earth is strong enough to significantly reduce the flux of up-going neutrinos. Hence, the field of view for these events is quoted as 2π. At energies below $\sim 100\,\mathrm{TeV}$, the tau decay length is too short to be resolved. Events where the tau decays into a muon cannot be distinguished from charged-current muon-neutrino interactions, and events where the tau decay produces a cascade cannot be distinguished from a single cascade produced by charged-current electron-neutrino interactions and neutral-current interactions of all neutrino flavors.

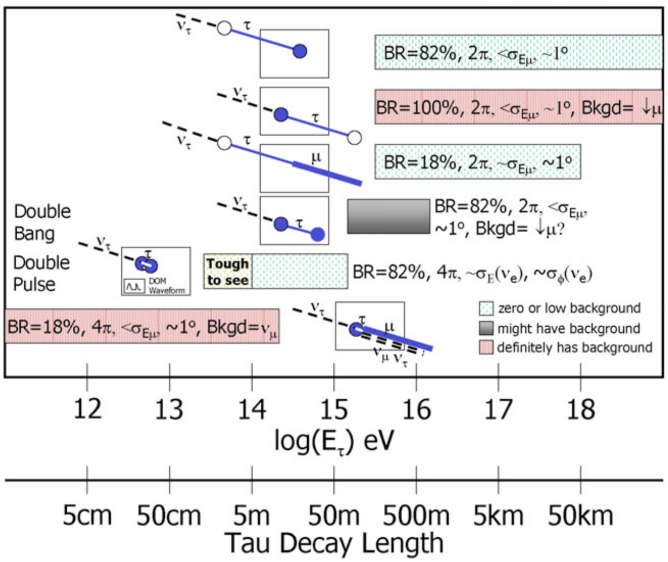

Figure 4.2: Tau-neutrino topologies in IceCube mainly depend on the energy, decay length, and decay channel of the tau. See text for explanation. Figure adapted from [230].

Tau-neutrino interactions may be identifiable via the "double bang" event topology for a tau energy between $\sim 100\,\text{TeV} - 10\,\text{PeV}$, for which both vertices of the interaction cascade and the decay cascade are contained inside the detector volume. Note that there is an upper limit of the tau energy for this topology, as the decay vertex is less likely to be contained with increasing energy. The field of view ranges from 2π to 4π depending on the energy, due to Earth absorption. Historically, the name "double bang" has been used to refer to a highly energetic tau-neutrino interaction that produces a separation of the interaction and decay cascades that would be visible to the eye as shown in Figure 4.1. The name *double pulse* has been used for events that are lower in energy where no clear separation of the cascades is visible to the eye but might appear as two distinct pulses in the waveform of a single DOM. In this thesis, however, the name "double bang" is used to refer to the interaction channel where two subsequent cascades are produced, independently of the tau energy. The names *double pulse* and *double cascade* are used to describe two different detection methods of "double bang" events.

The **double pulse** detection method has been used in the most recent search for tau-neutrino interactions in IceCube [68]. The idea is that a "double bang" event located close to a string would produce two peaks in the waveform of at least one nearby DOM. The first peak is caused by the Cherenkov light from the interaction cascade, and the second peak corresponds to the decay cascade. The time difference between the two peaks corresponds to the propagation time of the tau (which travels approximately at the speed of light and is faster than the emitted light in ice) and the distance of each cascade to the receiving DOM. The phase space for observing "double bang" events via the double pulse method is very small, and irreducible background is dominated by atmospheric muons that mimic a double pulse due to stochastic losses. In the tau-neutrino search published in [68], an algorithm has been developed to identify a double pulse structure in individual waveforms. An event selection based on parameters from this algorithm has yielded an event expectation of ~ 0.55 identifiable tau-neutrino events on a total background of ~ 0.35 events for three years of data under the assumption that the astrophysical neutrino flux is described by an E^{-2} spectrum. No tau-neutrino event has been observed in this search.

The **double cascade** detection method was initially developed in [229] and has been further extended in the scope of this thesis. The idea is to use the entirety of all digitized waveforms and explicitly reconstruct the hypothesis of two subsequent cascades with a maximum-likelihood fit based on the `millipede` framework (c.f. Section 3.3.3). The possible phase space of identifiable "double bang" events is thereby increased, because all available information is used instead of just one waveform from a single DOM.[1] Reconstruction is limited by light scattering and absorption in the ice and by the geometry of an event. Hence, there is a fundamental threshold in the energy and decay length of the tau, below which the interaction and decay cascades become inseparable. This will be discussed in greater detail in Section 4.3.

4.2 High-Energy Starting Event Selection

The data sample used for the work presented in this thesis is obtained by applying the high-energy starting event selection (HESE) as described in [43] to all triggered events that are processed to the offline level 2 (c.f. Section 3.2.3). The main idea is to define a veto region on the outer edges of the detector in order to only select starting events where the first Cherenkov photons are detected inside the fiducial volume. The veto region is sketched in Figure 4.3 for the top view (left) and the side view (right) of the detector. It is comprised of the outer strings as well as a top layer of 90 m and a center layer of 80 m around the dust layer (c.f. Section 3.2.4), each containing four to five DOMs per string and a bottom layer of 10 m containing one DOM per string. The veto region is much thicker at the top of the detector, because atmospheric

[1] An illustration of this will be discussed in the context of double flasher events in Section 5.3.2.

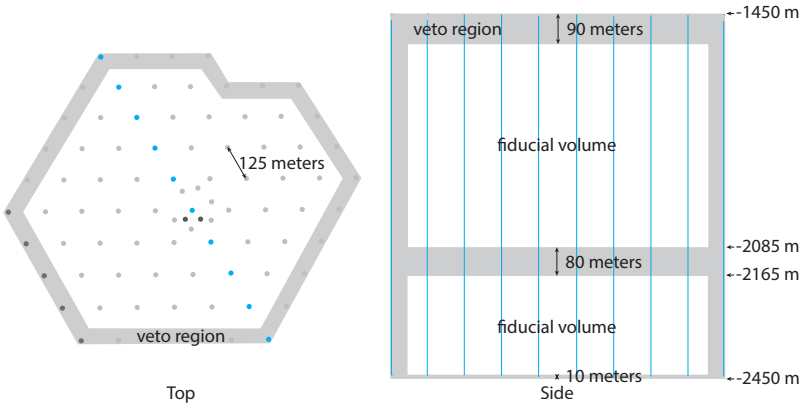

Figure 4.3: Sketch of the veto region and fiducial volume of the high-energy starting event selection. The veto region is comprised of the outer strings as shown in the top view of the detector (left) and of three layers at the top, around the dust layer and at the bottom as shown in the side view (right). An event is discarded if the first light is detected in the veto region, thereby selecting events that start inside the fiducial volume. Figure reproduced from [43].

muons predominantly enter the detector from above. The veto region at the bottom of the detector is necessary for discarding muons that are produced in muon-neutrino interactions and enter the detector from below. As there are no up-going atmospheric muons, it can be much smaller. Muons that enter the detector through the dust layer at a large zenith angle can mimic a starting event, because light emitted in the dust layer is heavily absorbed. Therefore, another veto region around the dust layer is necessary to discard these events. Starting events are selected by requiring fewer than 3 pe of the first 250 pe observed in the event to be detected within the veto region. In addition, a total observed charge of at least 6000 pe is required per event, above which statistical fluctuations in the light yield decrease and highly energetic muons are less likely to pass the veto region undetected.

The high-energy starting event selection rejects at least 99.999% of the atmospheric muon background [43]. Because both atmospheric muons and atmospheric neutrinos are produced in the same cosmic-ray-induced air showers, the event selection also rejects a large fraction of atmospheric neutrinos that accompany the vetoed muons. The self-veto effect depends on the neutrino energy and zenith angle (c.f. Section 2.3.2). The passing fraction of atmospheric neutrinos in this event selection increases with larger zenith angles, because it becomes more likely that muons from the same shower die out due to the longer propagation distance through the atmosphere and the ice. There is no self-veto effect for up-going atmospheric neutrinos. The passing fraction increases on average with decreasing neutrino energy, because it is correlated with the muon energy. A generalized calculation of the self-veto probability is used separately for conventional and prompt atmospheric neutrino fluxes [148].

While rejecting a large fraction of the atmospheric background, the high-energy starting event selection retains a majority of astrophysical neutrino events within the fiducial volume. It is similarly efficient for all neutrino flavors, as the selection criteria are independent of the topology of the event as long as it starts inside the fiducial volume. This can be seen in Figure 4.4, in which the neutrino effective areas (c.f. Section 3.3.2) of the high-energy starting event selection are shown. The effective areas increase with neutrino energy, as more visible energy is deposited inside the fiducial volume. There is a soft lower energy threshold of ~ 30 TeV, which is related to the selection requirement that the observed charge must be larger than 6000 pe. Above a few hundred TeV, the effective areas are approximately equal for all flavors, with the exception of the Glashow resonance for electron-antineutrino interactions at 6.3 PeV (c.f. Section 3.1.1). In the lower energy range, the effective areas are slightly different for each flavor, because

the fraction of the neutrino energy that is deposited as visible energy in the charged-current channel varies. It is highest for electron-neutrino interactions, as almost all of the neutrino energy is deposited in an electromagnetic and a hadronic cascade. Muon-neutrino interactions produce muons which only deposit some of their energy until they leave the detector. Therefore, the detection threshold is a little higher. For the same reason, tau-neutrino interactions have an effective area that is between electron- and muon-neutrino interactions, as the decay of the tau produces a muon in about 18% of the cases (with a higher detection threshold) and a cascade in the remaining cases (with a lower detection threshold). In addition, the decay of the tau-neutrino produces secondary neutrinos which further reduce the deposited energy. Looking at the other two plots for different zenith angle bands, it can be seen in addition that the effective areas decrease for all flavors with increasing zenith angle. The effect is particularly visible in the up-going region for the highest energies. This is due to Earth absorption, which becomes significant for neutrino energies above $\sim 1\,\text{PeV}$. The difference between tau-neutrino interactions compared to the other flavors at the highest energies is due to an effect called *tau regeneration*. A highly energetic tau-neutrino that travels through the Earth is likely to interact at some point. The interaction produces a tau, and its subsequent decay produces a second tau-neutrino that continues to propagate through the Earth. Because this secondary tau-neutrino is lower in energy, it is more likely to reach the detector. Therefore, primary tau-neutrinos at the highest energies can still be detected in principle via these secondary tau-neutrinos at lower energies, as long as they are above the threshold of $\sim 30\,\text{TeV}$.

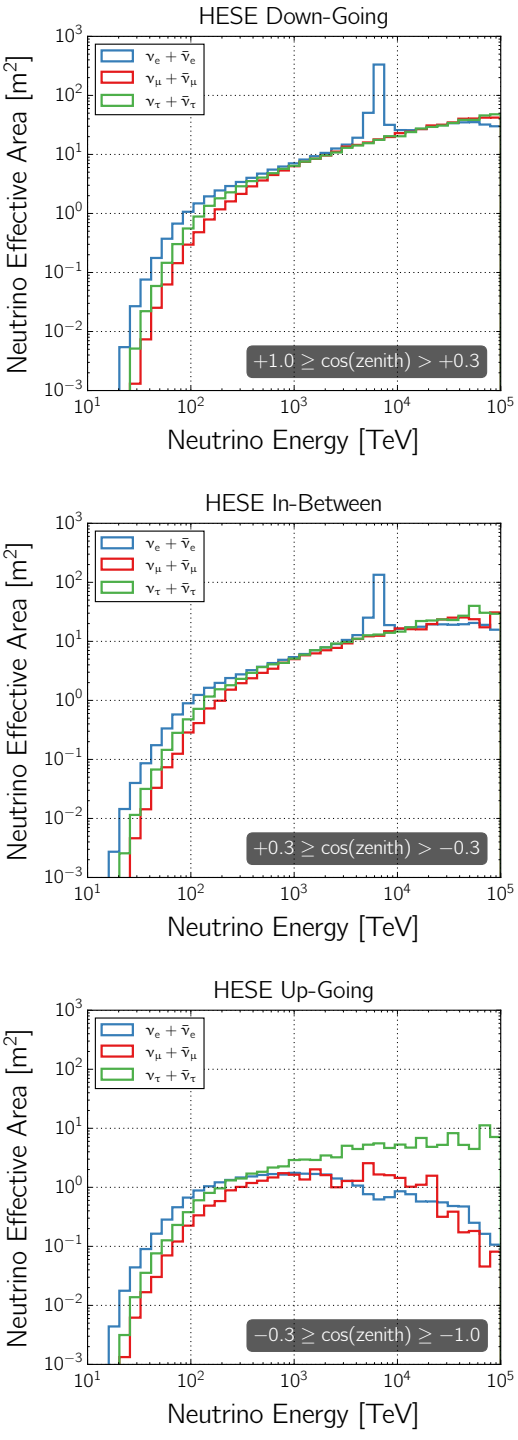

Figure 4.4: Neutrino effective areas for the high-energy starting event selection as a function of the neutrino energy. Distributions are shown for all flavors and for different zenith bands.

Experimental results of the high-energy starting event selection were continuously reported with an increasing number of IceCube operating years [4, 43, 44, 50]. The current data sample consists of 82 events in the energy range between $\sim 30\,\text{TeV}$ and $\sim 3\,\text{PeV}$ collected between 2010 and 2016. The expected number of atmospheric muons is 25.2 ± 7.3 and the expected number of atmospheric neutrinos is $15.6^{+11.4}_{-3.9}$, where the uncertainty includes the upper limit of an unknown prompt atmospheric neutrino component [130]. The observation corresponds to an exclusion of the atmospheric-only hypothesis and the discovery of the astrophysical neutrino flux at a significance level that is of the order of $\sim 8\sigma$. The results of the spectral fit of the diffuse astrophysical neutrino flux will be discussed in comparison with the results presented in this thesis in Section 7.1.

4.3 Double Cascade Event Reconstruction

The double cascade event hypothesis is unique to tau-neutrino interactions. The primary neutrino interaction is represented by the first cascade and the tau decay by the second cascade. Events are reconstructed using the `millipede` framework as described in Section 3.3.3. In the context of this thesis, the three event topologies single cascade, double cascade, and track are fitted assuming the corresponding hypotheses with `monopod`, `taupede`, and `millipede`, respectively. The hypotheses for tracks and cascades have been established for years [226], whereas the double cascade hypothesis has only been developed recently [229]. In an initial study, the performance of the double cascade event reconstruction was tested using simulation data where the seed of the minimizer was the smeared simulated value. In the work presented in this thesis, the reconstruction algorithm is upgraded to work with experimental data and to optimize the performance without the need for a specific seed. The reconstructed observables are used to discriminate different neutrino flavors. For the first time, the double cascade event reconstruction is sensitive to the identification of a tau-neutrino interaction in the experiment.

4.3.1 Implementation and Tau-Neutrino-Related Observables

The **double cascade event hypothesis** is constructed by extending a single cascade source described by the vertex (x_1, y_1, z_1), time t_1, direction (θ, ϕ), and energy E_1 by two additional parameters, the length L and the second energy E_2. In total, this yields nine fit parameters $\mathbf{s} = (x_1, y_1, z_1, t_1, \theta, \phi, L, E_1, E_2)$. The length L is the distance between the two cascades and can be interpreted as the tau decay length for double cascade events. The energy of the second cascade E_2 corresponds to the visible energy that is deposited in the tau decay. Note that the number of fit parameters is not double the number of a single cascade fit, as the second cascade is assumed to be causally connected to the first. It is constructed by assuming that the tau travels at the speed of light and that it has the same direction as the initial neutrino. Both are reasonable assumptions considering the resolution limit and energy scale in IceCube. The vertex and time of the second cascade are fully determined by the first cascade and the length via

$$x_2 = x_1 + L \sin\theta \cos\phi, \tag{4.1}$$
$$y_2 = y_1 + L \sin\theta \sin\phi, \tag{4.2}$$
$$z_2 = z_1 + L \cos\theta, \tag{4.3}$$
$$t_2 = t_1 + L/c. \tag{4.4}$$

All reconstruction algorithms based on the `millipede` framework use the same **configuration** to make them comparable. The configuration is similar to the prior analysis of the high-energy starting event selection [43]. DeepCore DOMs and *bright DOMs* are excluded from the likelihood fit since they may introduce a bias. These DOMs typically carry a large fraction of the total observed charge. The PMT of a DeepCore DOM has a $\sim$35% higher quantum efficiency than an IceCube DOM. A bright DOM may be caused by a source which is highly energetic and/or close to a string and is empirically defined to contain at least ten times the average observed charge of the event. The underlying reason for the exclusion of high-charge DOMs is that the corresponding statistical uncertainty of the digitized waveforms is smaller than the systematic uncertainty. However, the systematic uncertainty cannot be incorporated into the likelihood fit because it is not known for individual DOMs. Furthermore, saturated DOMs are excluded, as the digitized waveform is incomplete. DOMs that are marked as "bad" due to various reasons and DOMs with an erroneous calibration are also excluded. The time bins of the `millipede` likelihood are constructed by requiring each bin to contain a minimum of five pulses. DOMs without any observed pulses are included in the likelihood as described in Section 3.3.3.

The single cascade hypothesis is reconstructed with `monopod` and is used as a **seed** for the double cascade hypothesis, which is reconstructed with `taupede`. The track hypothesis is reconstructed using a specific track reconstruction algorithm that only takes the first detected photo electron of each DOM and then iteratively fits a track. In principle, it could also be reconstructed using the `millipede` algorithm. However, this is computationally too expensive. Instead, `millipede` is only used for the deconvolution of the energy losses along the track obtained by the faster reconstruction algorithm. The likelihood is thus comparable between all three source hypotheses. A better scheme of using the `taupede` fit is developed in order to account for the difficulty in reconstructing double cascade events. It is effectively turned into a **"brute-force" fitter** where multiple hypotheses are tested and compared. The main need for this is based on the fact that it is hard to find a reliable seed for the length. Different attempts to construct a seed were tested, but none came close to the results obtained from the "brute-force" approach. The changes and extension to the `taupede` fit are:

1. The evaluation of the length phase space of the `taupede` fit is adjusted by the step size `StepL` and the bounds `LengthBounds`. The former tells the minimizer how densely to vary the value of the length during the minimization, and the latter are its boundaries. The default step size is 15 m and the default bounds are (0 m, 2000 m). It was found that the step size must be configured to a much smaller value to evaluate the rapidly changing likelihood landscape in a sufficiently dense grid. It is therefore set to 1 m, instead. Furthermore, limiting the length parameter to positive values prohibits the minimizer to look "behind" the seed cascade, because a negative value of L switches the order (in time) of the two cascades. Therefore, the bounds are set to $(-800\,\mathrm{m}, 800\,\mathrm{m})$ in order to allow negative values. The maximum absolute value is decreased to improve fit performance, because only a more realistic phase space inside the fiducial volume is considered.

2. The length parameter must be seeded for the fit. In principle, this can be done with the first guess $L = 50\,\mathrm{m/PeV} \cdot E_{\mathrm{dep}}$. However, this only holds on average but not for individual events. Instead of estimating a seed, the parameter space is coarsely scanned by sampling different length values. They are empirically set to $L = 10\,\mathrm{m}, 25\,\mathrm{m}, 50\,\mathrm{m}, 100\,\mathrm{m}$.

3. The remaining seed parameters are obtained from the single cascade `monopod` fit. Depending on the kinematics of the interaction, the best-fit single cascade vertex can reside close to the neutrino interaction or to the tau decay or somewhere between. It depends on the amount of deposited energy in each cascade, as `monopod` effectively fits an energy-weighted mean vertex position. The best-fit vertex of the `monopod` fit is used to construct the event hypothesis with varying ordering for each length seed to account for these cases. It is used as a seed for the first cascade or the second cascade or for a central location between both cascades, each placed at $L/2$ in opposite directions.

4. The best-fit result of either cascade energy may be zero. Although this is technically a permitted solution, it simply returns the single cascade hypothesis. Therefore, zero-energy solutions are to be avoided during the fit. The quality of the fit result for each constructed hypothesis is assessed by requiring each cascade to be "softly" contained and to have a reconstructed energy greater than 1 TeV. Soft containment means that the vertex is not farther away than 50 m outside of the detector. The required minimum energy of 1 TeV per cascade corresponds to $\sim 6\%$ of the energy threshold of the high-energy starting event selection. The three best-fit results of all tested hypotheses are obtained by comparing the corresponding likelihood values in addition to the aforementioned requirements.

5. The `taupede` fit is executed in an iterative way. First, all constructed hypotheses are fitted using only the integrated charge per DOM (amplitude fit). The three best-fit results are then refitted using the entire digitized waveform of each DOM (timed fit), and out of those the best-fit result is determined.

The final best-fit result is accepted as a **successful double cascade event reconstruction** if

- the `taupede` fit converged,
- each cascade has a reconstructed energy larger than 1 TeV,
- each cascade vertex is not farther away than 50 m from the detector,
- and the opening angle between the `taupede` and `millipede` results is not larger than 30°.

The first requirement accounts for the evident exclusion of fits that did not converge. A minimum energy is required to enforce non-zero solutions to be preferred in the likelihood comparison of different fit hypotheses of a double cascade source. A soft vertex containment is required, because the reconstruction performance degrades outside the detector volume as the available amount of observed light decreases. The last requirement is a quality criteria of the reconstruction in order to decrease the amount of misidentified tracks.

Important observables in a search for a diffuse astrophysical neutrino flux are the *zenith angle* and the *total deposited energy*. They are necessary in order to distinguish atmospheric from astrophysical neutrinos (c.f. Section 2.3.2). In the analysis presented in this thesis, the zenith angle and total deposited energy are used similarly as for the previously published spectral fit using the high-energy starting event selection [43]. In addition, observables sensitive to tau-neutrino interactions are obtained from the double cascade fit. These are the *length* L, the *vertices* (x_1, y_1, z_1) and (x_2, y_2, z_2), and the *deposited energies* E_1 and E_2 of the two cascades. Furthermore, two topology estimators are constructed: the *energy asymmetry* E_A, which was introduced in [229], and the *energy confinement* E_C, which is new (see Figure 4.5). All aforementioned observables are briefly described in the following.

The **direction** of a particle is given by the zenith angle and the azimuth angle. The zenith angle gives the direction of particle origin with respect to the vertical axis that points towards the surface of the ice and upward from the South Pole. A zenith angle of 0° means that a particle is straight down-going in the detector, an angle of 90° means that it is propagating horizontally, and an angle of 180° means it is straight up-going. The azimuth angle gives the direction of particle origin with respect to the horizontal x-axis of the IceCube coordinate system (c.f. Section 3.3.3). It is usually not interesting in terms of separation power between an atmospheric and a diffuse astrophysical neutrino flux, as both are expected to be azimuthally isotropic. However, the azimuth angle is particularly important with respect to systematic uncertainties of the reconstructed length due to an anisotropy of the light scattering in ice, as will be discussed in Chapter 5. Both zenith and azimuth angles are implicitly used for modeling the systematic uncertainty of the reconstructed length due to the ice anisotropy (see Appendix A). The zenith angle is also used as direct observable in the likelihood fit described in this thesis for measuring the astrophysical neutrino flavor composition (see Section 6.2.2). The reconstructed direction is a very good estimate for the initial neutrino direction, because the energy in IceCube is high enough for the kinematic opening angle to be negligible. The direction can be reconstructed more precisely for tracks than for cascades and depends on the length for double cascade events, as will be discussed in Section 4.3.3.

The **total deposited energy** E_tot is the electromagnetic-equivalent energy that is visible in IceCube. It is obtained by the sum of all "softly" contained energy losses from the `millipede` energy deconvolution along the direction of the best-fit hypothesis. As described above, a "softly" contained energy loss is not farther away than 50 m from the detector. The spacing of secondary cascades along the thought track is 5 m (c.f. Section 3.3.3). Zero energy solutions are possible, which means that the deposited energy is compatible for different source hypotheses. In particular, the reconstructed energy of a single cascade hypothesis is the same as the sum of all deconvolved energy losses along its direction as the former is a subset of the latter with all remaining secondary energy losses being fit to zero. The total deposited energy is used as

direct observable in the likelihood fit, as well (see Section 6.2.2). It is always a lower limit of the neutrino energy, because not all energy is deposited in the detector or visible. Some energy can be carried away by secondary neutrinos (e.g. in the tau decay) or by muons that leave the detector, and some energy is simply not visible like a fraction of hadronic showers. Hence, the sensitivity of the total deposited energy to the primary neutrino energy depends on the event topology. With the single cascade and double cascade topologies, the initial electron- and tau-neutrino energy, respectively, can be much better constrained with the total deposited energy than the muon-neutrino energy using the track topology.

The **length** L is the most important observable that is directly related to tau-neutrino interactions. As described above, it is a fit parameter of the double cascade event reconstruction which can also be calculated via $L = \sqrt{(x_1 - x_2)^2 + (y_1 - y_2)^2 + (z_1 - z_2)^2}$. The length is used as a direct observable in the likelihood fit in order to measure the flavor composition as described in this thesis (see Section 6.2.2). It corresponds to the tau decay length for tau-neutrino interactions that produce a double cascade event. The **cascade vertices** (x_1, y_1, z_1) and (x_2, y_2, z_2) are only indirectly used for the containment selection and for constructing the energy confinement. Similarly, the **cascade energies** E_1 and E_2 are also not used as direct observables but only indirectly for constructing the energy asymmetry and the energy confinement.

The **energy asymmetry** E_A is a measure of how the relative amount of deposited energy in each cascade is distributed. It uses the cascade energies and is defined by

$$E_A = \frac{E_1 - E_2}{E_1 + E_2}. \tag{4.5}$$

This quantity allows a convenient determination of the distribution of the total energy in each cascade. If $E_A = 1$, it means that all of the energy is in the first (hadronic) cascade, if $E_A = -1$, it means all of the energy is in the second (decay) cascade, and if $E_A = 0$, it means that both cascades have an equal amount of energy. A true single cascade event has $E_A = 1$ by definition, because there is no second cascade. A true double cascade event, however, can have any value from $E_A = -1 \ldots 1$ depending on the kinematics of the deep-inelastic neutrino-nucleon scattering and the tau decay channel. The energy asymmetry is a good estimator to separate single cascades from double cascades, as will be shown in Section 4.3.2.

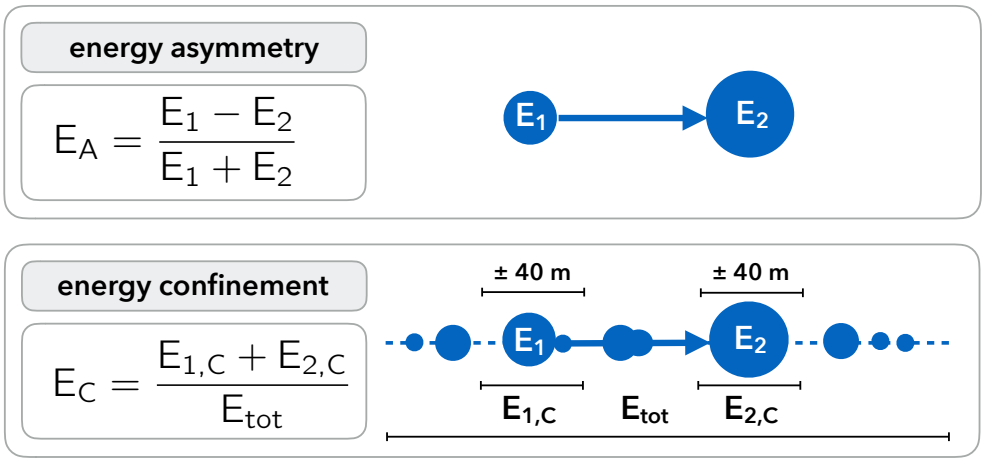

Figure 4.5: Sketch of the topology estimators. The energy asymmetry is a measure of how the relative amount of deposited energy in each cascade is distributed. The energy confinement is a measure of how much of the total deposited energy is confined to the reconstructed vertex positions of the double cascade event hypothesis.

The **energy confinement** E_C is a measure of how much of the total deposited energy is confined to the reconstructed vertex positions of the double cascade event hypothesis. It uses the cascade vertex positions and the deconvolution of the energy losses and is defined by

$$E_C = \frac{E_{1,C} + E_{2,C}}{E_{tot}}, \tag{4.6}$$

where $E_{1,C}$ and $E_{2,C}$ are the sum of all energy depositions of the deconvolution that are within 40 m distance of the first and second double cascade vertex, respectively. E_{tot} is the total deposited energy as defined above. Note that $E_{tot} = E_{1,C} + E_{2,C} = E_1 + E_2$ only holds for a tau-neutrino-induced double cascade event. Hence, for unambiguous tracks, it always follows that $E_C < 1$. The distance threshold of 40 m is chosen conservatively, because it retains any event with a tau decay length smaller than 80 m. Since the tau is not completely invisible between the two cascades, this value ensures that no event in the sensitivity region of $L < 100$ m is discarded. The energy confinement is sensitive to apparent tracks, which have energy depositions outside the region around the double cascade vertices. It is therefore a suitable estimator to separate single cascades and double cascades from tracks, as will be discussed in Section 4.3.2.

The **main observables** for determining the event topology are the energy asymmetry, the energy confinement, the length, and the total deposited energy. These observables are the most sensitive to tau-neutrino interactions in the "double bang" channel. They are discussed in greater detail in the following. If an observable is named *true*, it is represented by the known event properties from the Monte Carlo simulation (c.f. Section 3.3.2). If an observable is named *reconstructed*, it is represented by the best-fit result of the reconstruction algorithms without any knowledge of the true event properties.[2] Any figure showing an expected distribution of an astrophysical neutrino flux is weighted to a **benchmark spectrum** of $E_\nu^{-2.3}$ and a **benchmark flavor composition** of $\nu_e : \nu_\mu : \nu_\tau = 1 : 1 : 1$. The choice of this flux model will be discussed in Section 6.2.1. It is consistent throughout this thesis except for in Section 6.3.4, where different spectral shapes will be studied. True and reconstructed topologies are compared in order to study the performance of the developed method for flavor discrimination. A reconstructed event topology is estimated using various event properties (see next section). A true event topology is determined using Monte Carlo information via the following selection criteria.

A **true single cascade** event is selected by requiring only one cascade to be produced within the detector volume or in the vicinity of the detector edges.[3] This is predominantly caused by CC electron-(anti)neutrino events and by all NC events. In addition, Glashow resonance events produce a single cascade if the W-boson decays hadronically or into a positron (electron) and an electron-(anti)neutrino. Also, tau-(anti)neutrinos can produce a single cascade topology if the tau-(anti)neutrino interacts inside the Earth and produces secondary neutrinos that interact within the detector volume accordingly. A tau (antitau) from a CC tau-(anti)neutrino interaction that leaves the detector and only decays far away is considered a single cascade, because neither the decay cascade nor the (negligibly small) energy losses of the tau are detectable. This is a minor contribution to the topology, as it only occurs well above 10 PeV neutrino energy.

A **true double cascade** event is selected by requiring two causally connected cascades to be produced within the detector volume or in the vicinity of the detector edges. This is exclusively caused by CC tau-(anti)neutrino events where the secondary tau (antitau) decays hadronically or into a positron (electron) and neutrinos. No minimum decay length of the tau is required for an event to be counted towards the double cascade topology.

[2] If an observable is not further specified as *true* or *reconstructed* (e.g. in plot labels), it corresponds to the reconstructed observable. If a true observable is depicted, this is always explicitly included in the label. As the neutrino energy is not reconstructed, it is always given by the simulated value.

[3] In this context, the vicinity is defined as a cube around the detector center of length 1300 m, which on average means that a vertex may not be farther away than 100 m to 150 m outside of the detector.

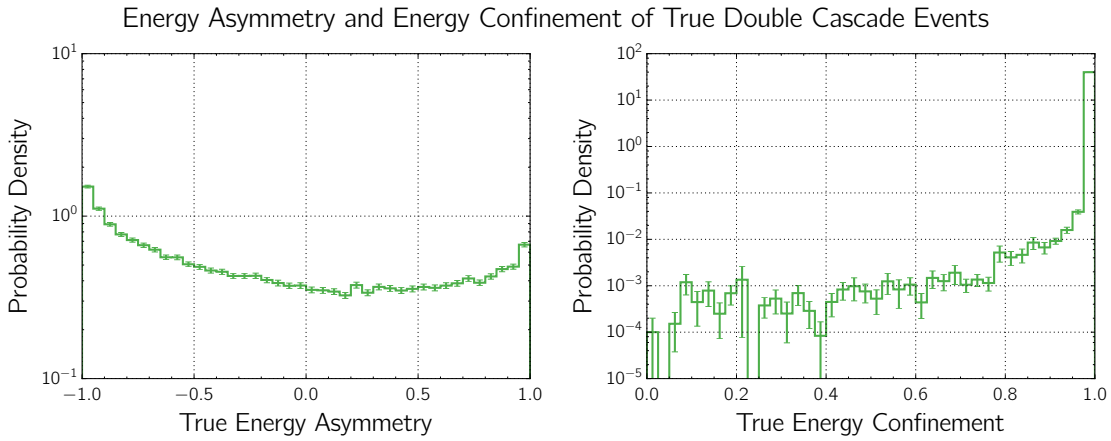

Figure 4.6: Probability density distribution of the true energy asymmetry (left) and true energy confinement (right) for true double cascade events passing the high-energy starting event selection.

A **true track** event is selected by requiring at least one muon to propagate through the detector volume. This is predominantly caused by CC muon-(anti)neutrino events and atmospheric muons. In addition, Glashow resonance events can produce a muon in the leptonic decay of the W-boson. Furthermore, if a tau lepton is produced (either via a CC tau-neutrino interaction or a W-boson decay) the muonic decay of the tau produces a muon, as well.

In Figure 4.6, the probability density distributions of the true energy asymmetry and energy confinement are shown for true double cascade events passing the high-energy starting event selection. The distribution of the energy asymmetry strongly increases towards $E_A = -1$, meaning that for a majority of events, the dominant fraction of the total available energy is deposited in the second (decay) cascade rather than the first (interaction) cascade. The shape of the distribution strongly depends on the neutrino energy. In particular, for neutrinos below 10 TeV energy, the distribution is approximately mirrored around $E_A = 0$, i.e. the dominant fraction of events increases towards $E_A = 1$. For neutrinos above 100 TeV, it is more likely to have a large energy deposition in the decay cascade, as shown Figure 4.6. This is due to the decreasing inelasticity of the neutrino interaction at large neutrino energies. The Bjorken inelasticity variable y is small, because the W-boson from the neutrino interaction couples to the sea quarks and transfers a smaller amount of energy to the hadronic cascade (c.f. Section 3.1.1). Therefore, most of the tau-neutrino energy is transferred to the tau lepton, and the first cascade generally contains less energy than the second cascade for the high-energy starting event sample. The distribution of the energy confinement sharply peaks at 1. This is expected due to the construction of the energy confinement, for two reasons. First, the length distribution follows a steep exponential decay law, which causes a majority of events to have $L < 80\,\text{m}$ and consequently $E_C = 1$. Second, the tau lepton rarely undergoes stochastic energy losses due to its high mass. The probability of stochastic losses increases with energy, and the median energy for events at $L > 80\,\text{m}$ is much higher than for shorter decay lengths. The amount of energy deposited by the tau before it decays is very little compared to the amount of energy deposited in the interaction and decay cascades. Only in very rare cases is the tau extremely bright, making up more than half of the total deposited energy. This only occurs in less than $\sim 0.05\%$ of all cases, as can be deduced from Figure 4.6.

The survival probability of a tau lepton follows an exponential decay law $p(L) = \exp(-L/\lambda_\tau)$, where the decay length λ_τ is the propagation distance L, after which the survival probability decreases to $\sim 36.8\%$. As discussed in Section 3.1.2, the decay length λ_τ and the energy E_τ of the tau lepton scale linearly via $\lambda_\tau \simeq \frac{50\,\text{m}}{1\,\text{PeV}} E_\tau$. Consequently, the probability density distribution as a function of the propagation length of the tau is a convolution over all tau energies, which strongly depends on the assumed neutrino spectrum (see Section 6.3.4).

The tau energy E_τ is not a direct observable and can only be estimated as a lower limit via the second cascade energy. Neglecting minor stochastic losses of the tau propagation, a fraction of the energy deposited in the tau decay is invisible due to the secondary tau-neutrino, which is produced in all decays. In addition, the visible fraction of hadronic cascades is energy-dependent and further reduces the amount of detectable energy deposited in the tau decay cascade (c.f. Section 3.1.3). Taking the most important decay channels into account,[4] the aforementioned correlation between E_τ and λ_τ also holds for E_2 and λ_τ, because the dominant fraction of the tau energy is deposited as visible energy in the decay cascade. This can be seen in Figure 4.7, where the probability density distribution for the true tau decay length is shown in correlation with the true second cascade energy. It is clearly visible that the expected correlation $E_\tau \simeq \frac{1\,\mathrm{PeV}}{50\,\mathrm{m}}\lambda_\tau$ between the energy and decay length of the tau is only shifted in energy compared to the second cascade energy. As described, this is reasonable, because E_2 is a lower limit to E_τ. Furthermore, it can be seen that both the energy and decay length follow steeply falling distributions. Consequently, a majority of events cluster around low energies and short decay lengths. In fact, the fraction of tau-neutrino interactions with $L \leq 10\,\mathrm{m}$ is $\sim$69% of all true double cascade events, assuming the $E_\nu^{-2.3}$ benchmark spectrum. It is only $\sim$31% for $L > 10\,\mathrm{m}$, $\sim$18% for $L > 20\,\mathrm{m}$, $\sim$8% for $L > 50\,\mathrm{m}$, $\sim$4% for $L > 100\,\mathrm{m}$, and less than 1% for $L > 500\,\mathrm{m}$. Evidently, the chance of observing an unambiguous tau-neutrino interaction where the separation of both cascades is visible to the eye (c.f. Figure 3.9) is extremely low, as this would correspond to a decay length of a few hundred meters. Hence, an integrated identification efficiency of $\sim$50% above the lower resolution threshold of the reconstructed double cascade length of $\sim 10\,\mathrm{m}$ (see Section 4.3.3) would only allow for the identification of $\sim$15% of all tau-neutrino interactions in the "double bang" channel.

The probability density distribution for the true tau decay length in correlation with the true total deposited energy is shown in Figure 4.8. Again, the expected correlation $E_\tau \simeq \frac{1\,\mathrm{PeV}}{50\,\mathrm{m}}L$ is shown in comparison. Similarly, the correlation between the decay length and the total deposited energy holds, as well. On average, it is only shifted in energy. This can be understood with respect to the distribution of the energy asymmetry shown in Figure 4.6. As explained above, neutrinos with sufficiently high energy ($\sim$100 TeV) transfer most of their energy to the secondary lepton due to the small inelasticity of the interaction. Consequently, E_1 of the first (interaction) cascade generally makes up a small fraction of the total deposited energy. Hence, E_tot effectively scales with E_2 and the correlation between E_tot and L is very similar to E_2 and L, as can be seen by comparing Figure 4.7 and Figure 4.8. However, this is specific to the high-energy starting event selection, as these relations rapidly change at neutrino energies below $\sim$10 TeV. In practice, E_tot, E_2, and L cannot be used simultaneously, as the available Monte Carlo simulation data is limited in statistics and too sparse to generate the probability density distribution for a three-dimensional histogram. Instead, it is more feasible to use E_tot instead of E_2 for two reasons. First, it does not introduce a disadvantage, as there is no loss in sensitivity to tau-neutrino interactions due to the similar correlation with the decay length. Second, E_tot is more sensitive to the spectral index γ of the astrophysical neutrino flux than E_2 due to a stronger correlation with the neutrino energy.

In summary, only few tau-neutrino events are expected to be identifiable at $L \gtrsim 10 - 20\,\mathrm{m}$ due to the steep decay distribution of the tau. The approximate scaling $E_2 \sim E_\mathrm{tot}$ is specific to the high-energy starting event sample and the resulting correlation $E_\mathrm{tot} \sim L$ expected from $E_\tau \sim \lambda_\tau$ can be employed in order to identify tau-neutrino interactions. E_tot is a preferred choice over E_2, because it is more sensitive to the spectral index as an additional fit parameter of the flavor composition measurement presented in this thesis (see Section 6.2.1).

[4] In the "double bang" channel, the dominating decays are $\tau^\pm \to \overset{(-)}{\nu}_\tau \overset{(-)}{\nu}_e e^\pm$, $\tau^\pm \to \overset{(-)}{\nu}_\tau \pi^\pm$, $\tau^\pm \to \overset{(-)}{\nu}_\tau \pi^\pm \pi^\pm \pi^\mp$, $\tau^\pm \to \overset{(-)}{\nu}_\tau \pi^\pm \pi^0$, $\tau^\pm \to \overset{(-)}{\nu}_\tau \pi^\pm \pi^0 \pi^0$ and $\tau^\pm \to \overset{(-)}{\nu}_\tau \pi^\pm \pi^0 \pi^0 \pi^0$, which cover $\sim$75% of the total branching ratio of the tau decay [78].

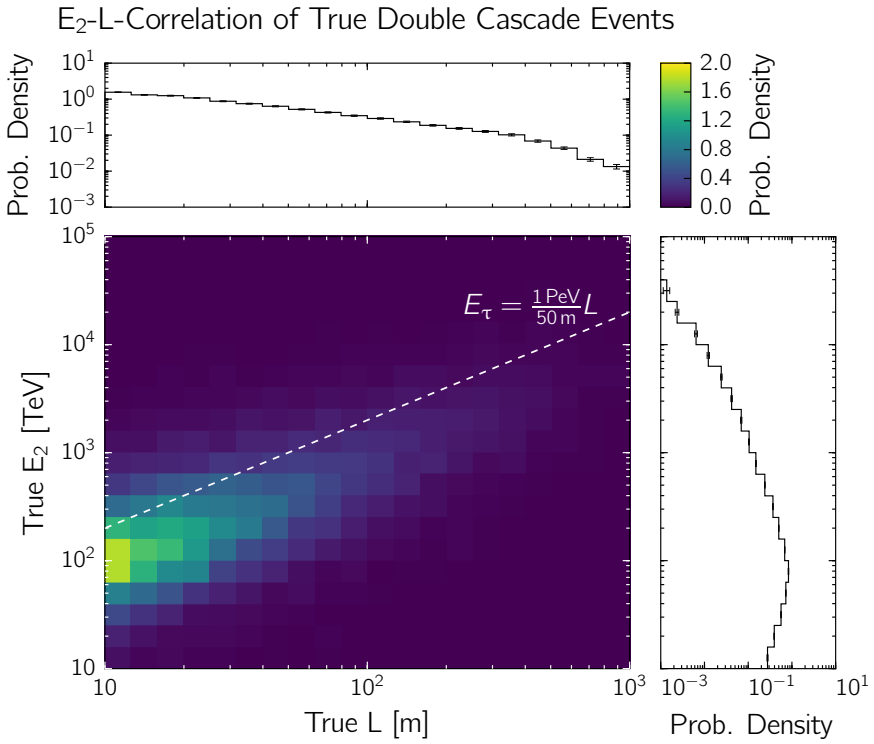

Figure 4.7: Probability density distribution of the true second cascade energy and the true tau decay length for true double cascade events passing the high-energy starting event selection. The diagonal line indicates the expectation for the tau energy $E_\tau = \frac{1\,\mathrm{PeV}}{50\,\mathrm{m}} L$. The distribution of E_2 is smeared and shifted compared to E_τ, but the correlation $E_2 \sim L$ remains. The shift is due to the reduced visible fraction of the tau energy that is deposited in the decay cascade.

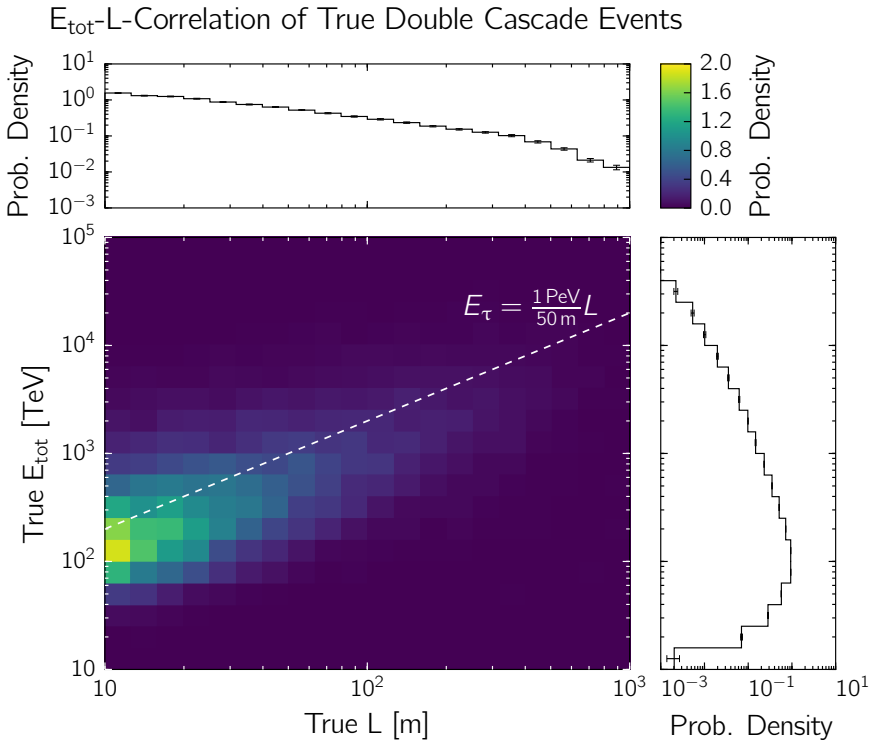

Figure 4.8: Same as in Figure 4.7, but for the true total deposited energy E_{tot}. Unlike the second cascade energy, the total deposited energy also contains the visible energy of the neutrino interaction cascade. The correlation $E_{\mathrm{tot}} \sim L$ remains, as discussed in the text.

4.3.2 Neutrino Flavor Discrimination

The focus of the work presented in this thesis is the development of a tau-neutrino identification via the observables obtained from the double cascade event reconstruction. A measurement of the neutrino flavor composition, however, must be based on a discriminator which is sensitive to all flavors. Therefore, an ad-hoc classification is developed to distinguish between single cascades, double cascades, and tracks through the use of the same observables.

A **particle identifier** (PID) is a quantity that assigns a probability to the reconstructed particle to be of a certain type. It is not possible to construct such a PID for neutrino interactions in IceCube, because multiple particles may cause the same event topology (c.f. Section 3.3.1). Instead, a **ternary topology identifier** on the basis of the three event topologies single cascade, double cascade, and track is developed, and the contributing fractions of each neutrino flavor are obtained from the underlying Monte Carlo templates. The optimization of the topology ID is based on the comparison between reconstructed and true event topologies, as described in Section 4.3.1. Because the double cascade event topology is unique for tau-neutrino interactions, it is considered the signal. Single cascade and track events are considered background. Distributions are generated by assuming the benchmark astrophysical $E_\nu^{-2.3}$ spectrum and flavor composition $\nu_e : \nu_\mu : \nu_\tau = 1 : 1 : 1$, and by including conventional and prompt atmospheric neutrinos as well as atmospheric muons (see Section 6.2.1).

The topology ID is obtained by a combination of **selection criteria** using the different tau-neutrino-related observables as sketched in Figure 4.9. The first level of the topology ID is based on requirements of the reconstruction quality as described in Section 4.3.1. The `taupede` fit should have converged and should be generally consistent with the direction of the `millipede` fit. In addition, each cascade is required to have a minimum energy of 1 TeV and to be "softly" contained in the detector volume. The second level of the topology ID is a selection of the reconstructed length. The minimum required length of 10 m corresponds to a threshold, below which the distinct vertices of an average double cascade event can no longer be resolved due to light scattering in the ice. The threshold value is found empirically and can be compared to the resolution of the length, as will be discussed in Section 4.3.3. The distribution of the reconstructed length above this threshold is also used as a direct observable in the likelihood fit for measuring the flavor composition (see Section 6.2.2). Further levels of the topology ID are based on the energy asymmetry and energy confinement topology estimators. The reconstructed distributions are depicted in Figure 4.10 for events passing the high-energy starting event selection and the preselection (first and second level) of the topology ID. Each distribution for true single cascade, double cascade, and track events is a superposition of the individual astrophysical and atmospheric flux components. The energy asymmetry is useful for distinguishing between single cascades and double cascades, and the energy confinement is useful for distinguishing tracks from everything else. The distributions and selection criteria are explained in greater detail in the following.

The distribution of the **energy asymmetry** (Figure 4.10, left) has a few interesting features. A single cascade can only formally be reconstructed as a double cascade if the reconstructed energy of either cascade or the reconstructed length is very small. This effect can indeed be seen for the energy asymmetry distribution of single cascades. They are predominantly reconstructed towards $E_A = \pm 1$, which corresponds to a very small energy in either cascade. There is another accumulation of events around $E_A = 0$. These can be explained by a best-fit solution of the double cascade event hypothesis with a reconstructed length close to the resolvable threshold. In this case, the single cascade and double cascade solution are degenerate, and the reconstruction algorithm can no longer distinguish between one cascade with energy E and two cascades close together with $E_1 = E_2 = E/2$. In fact, this effect is much more pronounced for single cascade events reconstructed at $L < 10$ m, which is not shown here. In general, a misreconstructed single

cascade is most likely explained by either a very short reconstructed length or by a very small energy of either cascade. A double cascade is only successfully reconstructed as such, if the tau decay length is above the threshold. Therefore, an increase of the distribution towards $E_A = +1$ is caused by misreconstructed events that effectively look like single cascades, because the two cascades cannot be individually resolved. The increase towards $E_A = -1$, however, is mostly due to successfully reconstructed events. This can be deduced by comparing the distribution of double cascades to single cascades for $E_A \lesssim 0$ as well as by comparing to the expected true distribution in Figure 4.6. The distribution for tracks is less important, because the dominant fraction can be distinguished from single and double cascades by using the energy confinement.

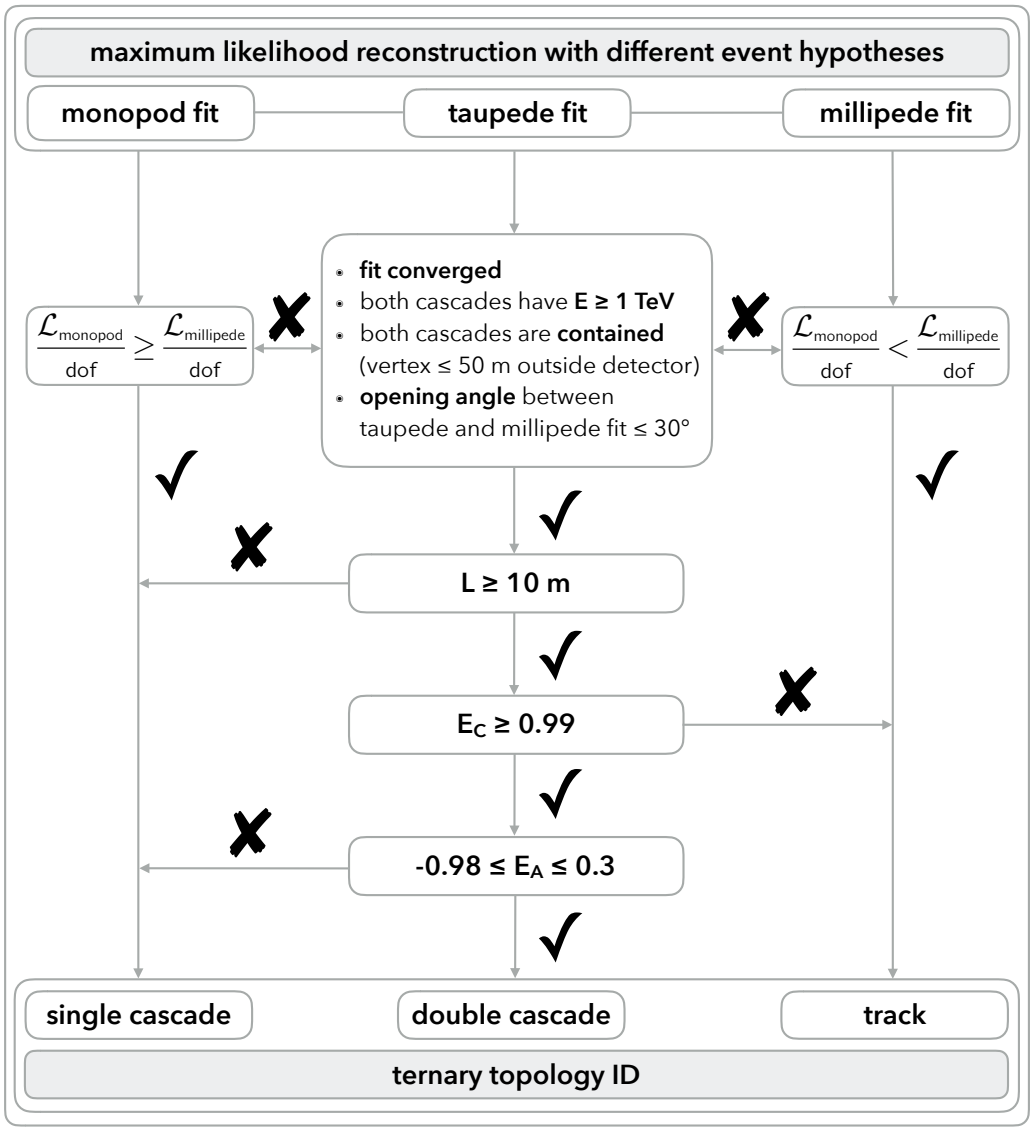

Figure 4.9: Event classification scheme of the topology ID. The first level is defined by selection criteria based on the reconstruction quality. If any requirement is not fulfilled, the event is classified as a single cascade or as a track by comparing the likelihood values $\mathcal{L}_{\text{monopod}}$ and $\mathcal{L}_{\text{millipede}}$ for the `monopod` and `millipede` fits, respectively, reduced by the degrees of freedom (dof). The second level is a selection based on the reconstructed length. It corresponds to a threshold below which the distinct vertices of an average double cascade event can no longer be resolved and effectively look like a single cascade. The third and fourth levels are selections based on the energy confinement and energy asymmetry, respectively, as described in the text.

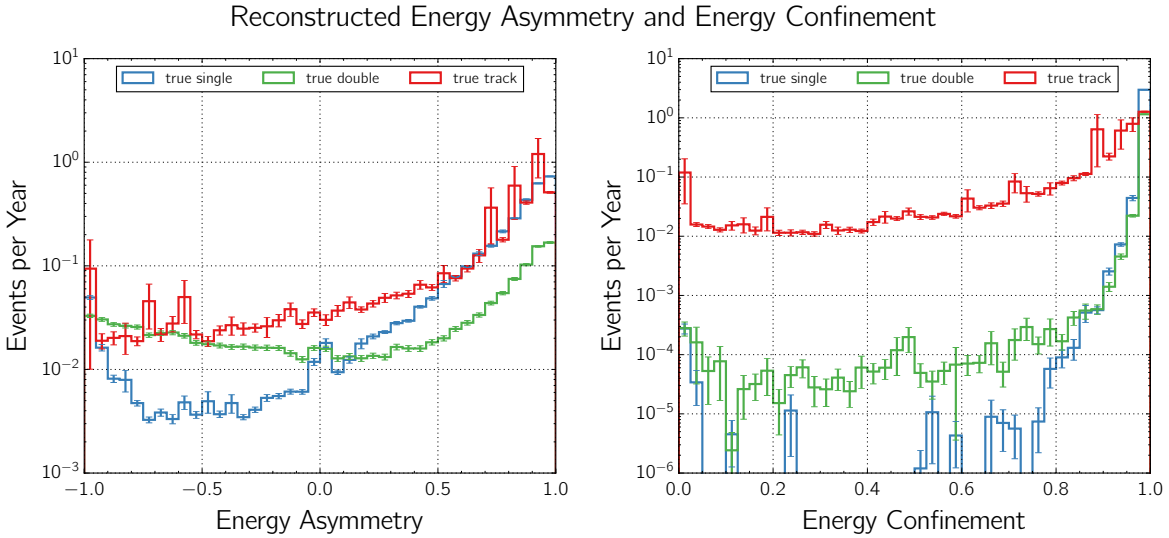

Figure 4.10: Expected event rate distribution of the reconstructed energy asymmetry (left) and reconstructed energy confinement (right) shown for the true event topologies. Each distribution is a sum of all astrophysical and atmospheric components passing the high-energy starting event selection and preselection (first and second level) as sketched in Figure 4.9.

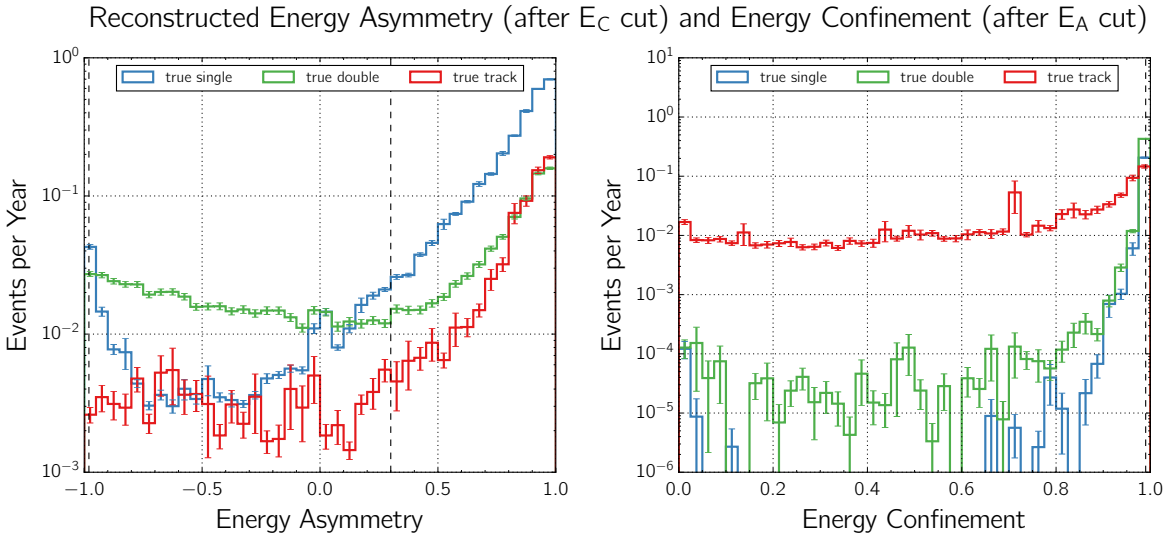

Figure 4.11: Same as Figure 4.10, but after additional selections on the energy confinement $E_C \geq 0.99$ (left) and energy asymmetry $-0.98 \leq E_A \leq 0.3$ (right) on the respective other distribution. Cut values are indicated by vertical dashed lines.

The distribution of the **energy confinement** (Figure 4.10, right) sharply peaks at $E_C \simeq 1$ for double cascade events, because the dominant fraction with a tau decay length $L \lesssim 80\,\mathrm{m}$ is left invariant by construction. The distribution for single cascades looks very similar, as these events also do not have large energy depositions far away from the cascade vertex. It can be seen that the energy confinement is useful to distinguish tracks from other event topologies, as the distribution is much broader for tracks. This is reasonable, because tracks typically have multiple energy depositions that are located outside the region of the reconstructed double cascade vertices. However, there is also a large fraction of track events that are indistinguishable in terms of the energy confinement. This is due to the hadronic cascade of the neutrino interaction being contained in the detector volume, as the events start inside the fiducial volume. Consequently, a true track event is usually not only a muon but instead a starting muon emerging out of a hadronic cascade. Depending on the kinematics of the neutrino scattering, the hadronic cascade might contain much more energy than the muon. However, this effect becomes less important at higher energies, as described for tau-neutrino interactions in Section 4.3.1. A true track might also look like a cascade if the starting vertex is close to the edge of the detector and the muon propagates outward. In this case, the track might be too short to be resolvable. The small accumulation of events at $E_C \simeq 0$ are events that are not well reconstructed, as the `millipede` energy deconvolution found dominant energy losses far away from the cascade vertices which are in contradiction to the best-fit result of the double cascade reconstruction.

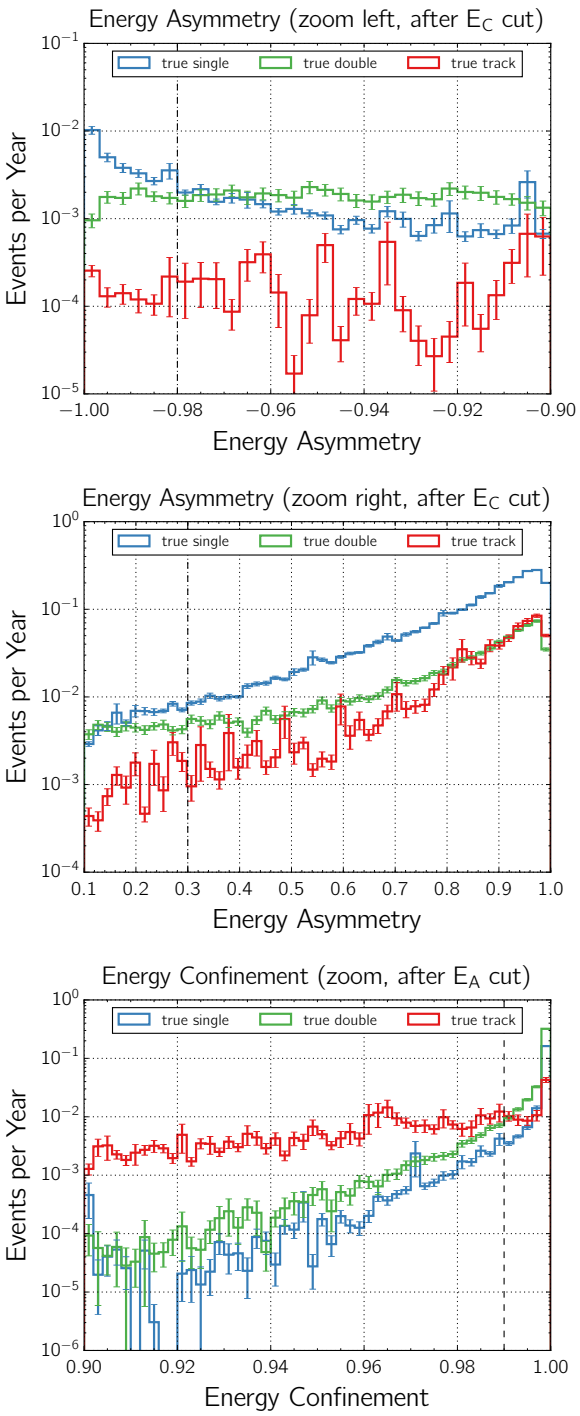

Figure 4.12: Same as Figure 4.11 but zoomed in near the boundaries of the energy asymmetry at $E_A = -1$ (top) and $E_A = +1$ (center) and near the boundary of the energy confinement at $E_C = 1$ (bottom).

The energy asymmetry and energy confinement are not correlated. The respective selections are thus applied consecutively. A selection of the energy confinement mostly leaves the energy asymmetry distributions of single cascade and double cascade events invariant, and a selection of the energy asymmetry mostly leaves the energy confinement distribution of track events invariant. This can be seen for each distribution after the selection of the respective other. In Figure 4.11, the full distributions are shown, and in Figure 4.12, they are zoomed in to the regions around the cut values in order to enhance the visibility of differences.

As displayed in Figure 4.9, the **cut values** are chosen such that

- events with $E_C < 0.99$ are classified as track,
- events with $E_C \geq 0.99$ and $-0.98 \leq E_A \leq 0.3$ are classified as double cascade,
- events with $E_C \geq 0.99$ and $E_A < -0.98$ or $E_A > 0.3$ are classified as single cascade.

There are a few remarks with respect to these values. First, they are not numerically optimized, but rather manually chosen through the use of the *signal-to-background ratio* as an estimator. Second, the cut values are placed rather loosely in order to let more background into the final sample of double cascade candidate events. The reason is that the analysis presented in this thesis is not a pure counting experiment. Instead, the shape of the correlation between the reconstructed length (corresponding to the tau decay length) and the total deposited energy (scaling with the tau energy) is employed, because it is more sensitive to tau-neutrino interactions (see Section 4.4). Therefore, a sufficiently large amount of background events must be allowed into the double cascade sample in order to describe the shape of the background in that parameter space. Third, the dependence of the cut values on the assumed astrophysical spectrum is weak. The reason is that all atmospheric backgrounds drop quickly with increasing energy. Consequently, the dominant background is of astrophysical origin, because the sensitivity region for tau-neutrino interactions is at very high energies due to the energy-dependent resolution threshold. After applying these selection criteria, the construction of the topology ID as sketched in Figure 4.9 is complete. Note that none of the events in the high-energy starting event sample are discarded. Instead, they are separated into three different event topology samples: a single cascade sample, a double cascade sample, and a track sample.

In Figure 4.13, the **neutrino effective areas** are shown for the reconstructed single cascade, double cascade, and track samples as a function of the primary neutrino energy. The different distributions in each sample are shown separately for the true event topologies and neutrino flavors. It is evident why a unique PID cannot be constructed by comparing the neutrino effective areas for each topology and flavor. The color code is chosen such that the neutrino flavor is marked in the same color as the event topology it dominantly causes, i.e. single cascade and ν_e, double cascade and ν_τ, track and ν_μ. The remaining fraction of events with a certain topology are caused by a mixture of the other neutrino flavors. For example, the neutrino effective areas of the reconstructed single cascade sample (top row) look similar for true single cascades and for ν_e. The scale difference is explained by the NC interactions of ν_μ and ν_τ, which causes the distribution for true single cascades to shift upward and the distributions for ν_μ to shift downward. The distribution of ν_τ behaves differently, because the double cascade topology is unique to the tau-neutrino flavor and has a strong dependence of the selection efficiency on the energy. Another example can be seen for the occurrence of true tracks by comparing the peak of the Glashow resonance at 6.3 PeV (c.f. Section 3.1.1) for the distributions of the reconstructed track sample (bottom row). These events are exclusively caused by $\bar{\nu}_e$, but they are visible as true single cascades and as true tracks due to the different decay channels of the W-boson.

The **reconstructed single cascade sample** (Figure 4.13, top row) dominantly contains true single cascade events, as desired. The distribution for true tracks is lower by a factor ~ 10. These misidentified events are tracks which are either too dim or too short to be distinguishable from single cascade events. The distribution for true double cascade flattens with increasing neutrino energy. This is a desired behavior, as it implies that the misidentification fraction of true double cascades as single cascades decreases with increasing energy. This is expected, because the average tau decay length scales with energy. Hence, double cascade events are more efficiently identified at high energies (see Section 4.4). Consequently, the distribution of misidentified true double cascades misidentified pose an irreducible contribution to the single cascade sample. These events have a tau decay length that is too short to be resolved. Hence, they effectively look like single cascade events.

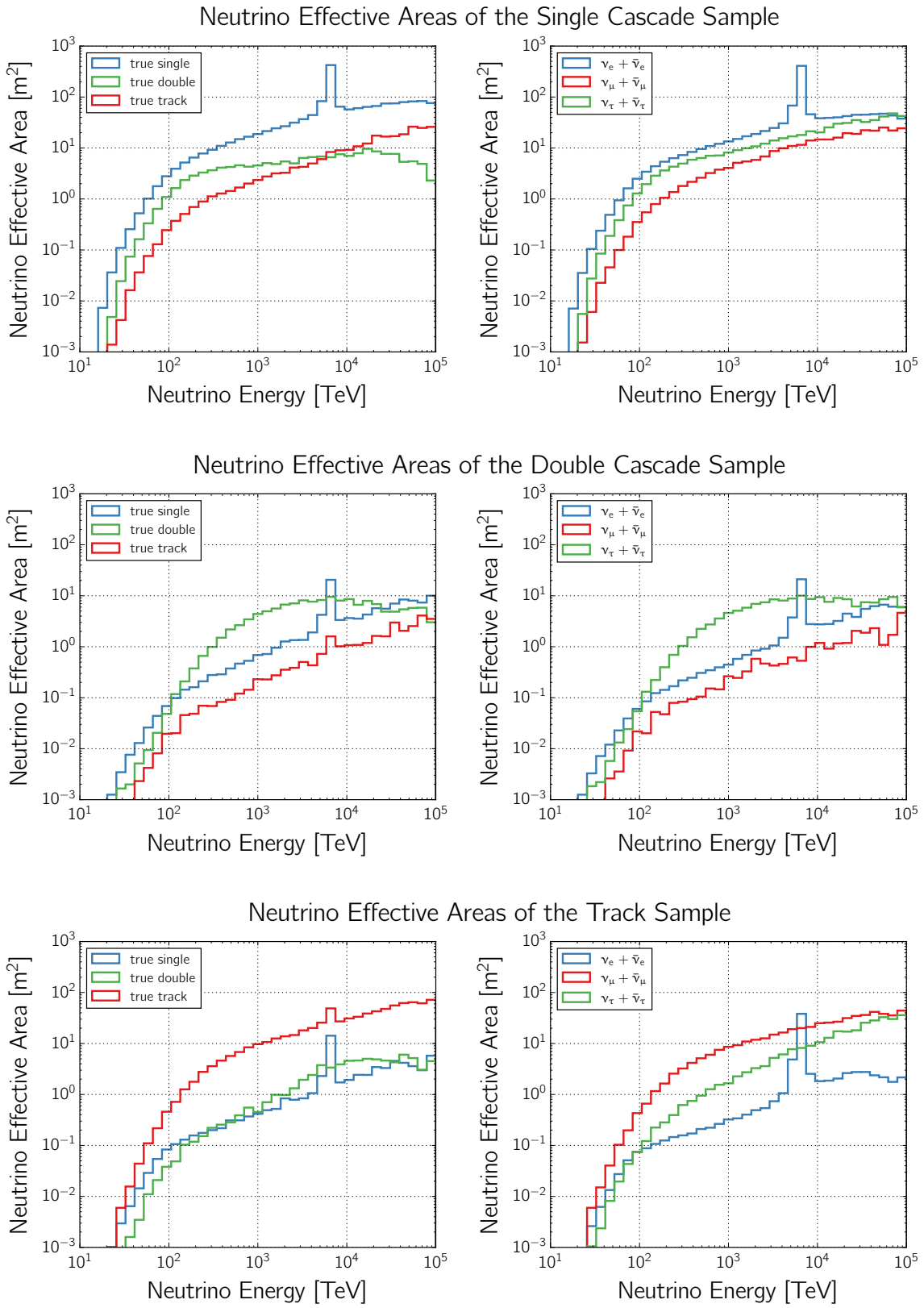

Figure 4.13: Neutrino effective areas of the reconstructed event topology samples as a function of the primary neutrino energy. In the top row of plots, the neutrino effective area is shown for the reconstructed single cascade sample, in the center row for the double cascade sample, and in the bottom row for the track sample. In the left column of plots, the effective areas are shown for the true event topologies and in the right column for the neutrino flavors.

The distributions for the **reconstructed double cascade sample** (Figure 4.13, center row) are most important, as they yield an estimate of the tau-neutrino selection efficiency. It can be seen that, in fact, true double cascade events have the dominant fraction of the total neutrino effective area in that sample. The distribution for true single cascades is larger at low energies where the tau decay length is too short for a resolvable double cascade events, at the Glashow resonance where the abundance of single cascades is simply large enough, and above 10 PeV to 20 PeV where the effective area for true double cascade events decreases again. This is caused by the requirement that both the first (interaction) and the second (decay) cascade be contained in the detector volume (c.f. Section 4.3.1). At the aforementioned energy region, the average tau decay length is of the order of 500 m to 1000 m which means that the decay cascade of a (starting) double cascade event is on average no longer contained. A decrease of the effective area at these energies is acceptable, because no neutrinos above 10 PeV have been observed so far. The fraction of misidentified tracks is much lower across a wide range of energy. It can be deduced that misidentified single cascade events are the dominant background and misidentified tracks only have a minor contribution in this analysis.

The **reconstructed track sample** (Figure 4.13, bottom row) predominantly contains true tracks as desired. The fraction of misidentified single cascades is lower than in the double cascade sample, because they are more likely distinguished from tracks. The contamination of true double cascades is slightly larger around 10 PeV, which is caused by extremely energetic taus with a decay length of a few hundred meters. They may deposit significant energy losses along their propagation path, although this is very rare. Note that the effective area for ν_τ in the reconstructed track sample increases more steeply in comparison, because this distribution also contains the muonic decay channel of the tau which counts towards the true track distribution.

The integrated **(mis)identification fractions** of all true event topologies in each reconstructed event topology sample are summarized in Table 4.1. The *purity* of a sample is defined as the integrated rate of the targeted true topology over all contributions. The single cascade sample has a purity of $\sim$72%, the double cascade sample $\sim$65%, and the track sample $\sim$91%. The track sample has the lowest contamination due to misidentified events. Note that the purity of the single cascade sample only seems low, as misidentified true double cascade events mostly have a tau decay length that is too short to be resolvable. In fact, the purity of the single cascade sample increases to $\sim$85% if true double cascade events with a tau decay length smaller than 10 m are effectively counted as single cascade events. The purity of the double cascade sample is a direct measure of the tau-neutrino sensitivity, because a true double cascade is exclusively induced by a tau-neutrino interaction. Consequently, this sample corresponds to a signal-to-background ratio of $\sim$1.8. This would only reflect an actual estimate of the tau-neutrino sensitivity if the analysis were a simple counting experiment. Because it is based on a likelihood fit which employs the correlation of the total deposited energy and the double cascade length in addition to the topology ID, the sensitivity is significantly higher. The underlying details will be discussed in Section 4.4, and the final sensitivity will be presented in Section 6.3.

	Reco Single	**Reco Double**	**Reco Track**
True Single	$(72.1 \pm 0.3)\%$	$(24.9 \pm 0.5)\%$	$(5.5 \pm 0.3)\%$
True Double	$(18.3 \pm 0.1)\%$	$(64.8 \pm 1.0)\%$	$(3.7 \pm 0.2)\%$
True Track	$(9.6 \pm 0.2)\%$	$(10.3 \pm 0.7)\%$	$(90.8 \pm 5.8)\%$

Table 4.1: Fractions of true event topologies in each reconstructed event topology sample. Each column adds up to 100%. The purity of each sample is given by the fractions on the diagonal axis whereas the off-axis values in each column give its misidentification fraction. The values are calculated for astrophysical and atmospheric neutrinos as well as atmospheric muons passing the high-energy starting event selection above $E_{\text{tot}} \geq 60$ TeV. The errors are statistical.

In Figure 4.14, the neutrino effective areas of the double cascade sample and the previously published double pulse sample are compared (c.f. Section 4.1). An improvement of the signal effective area is clearly visible over a wide energy range up to $\sim 20\,\mathrm{PeV}$. Above this energy, it is smaller for the double cascade sample due to the required vertex containment. Although the total effective area of the neutrino background is also larger, it is important to keep in mind a few differences. First, the overall signal neutrino effective area is larger, which is particularly important for analyses with very low event expectations. Second, the signal-to-background ratio (in terms of effective area) is either the same or better in the relevant energy range between $\sim 100\,\mathrm{TeV} - 10\,\mathrm{PeV}$. Third, the energy threshold of the double cascade method could be lowered in comparison to the double pulse method. In addition, the different analysis methods (likelihood fit versus counting experiment) and the varying atmospheric background suppression (veto technique versus observable selections) cause a further increase in sensitivity. A comparison of the results achieved with both methods will be discussed in Section 7.2.

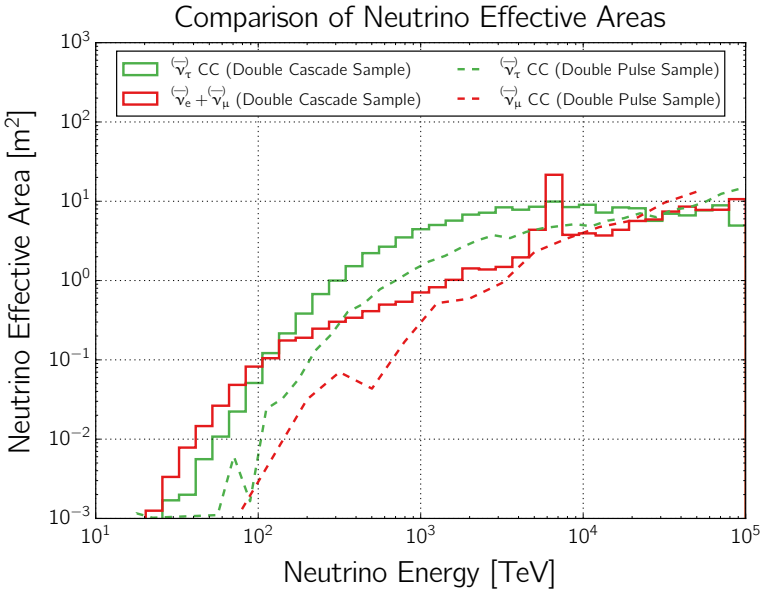

Figure 4.14: Neutrino effective areas for the double cascade (solid) and double pulse (dashed) samples shown as a function of the primary neutrino energy. The former is obtained in the context of thesis and the latter is based on the previously published method [68]. The CC tau-neutrino contribution is the signal (green) in both cases. In this analysis, the neutrino background (red) consists of both electron- and muon-neutrinos, whereas for the double pulse method only the CC muon-neutrino contribution was considered to be the dominant background.

4.3.3 Distributions and Resolution of Event Properties

The resolution of an event property is obtained by comparing its reconstructed value with the true value known from Monte Carlo simulation. It is presented as an absolute value, which means that the median of the cumulative resolution distribution can be interpreted as estimator of the width of the distribution rather than its bias. The energy resolution is given in terms of visible energy losses that are deposited inside the detector volume or not farther away than 50 m from the outer detector edge. It is calculated via $|E_{\mathrm{reco}} - E_{\mathrm{true}}|/E_{\mathrm{true}}$, the zenith resolution via $|\mathrm{zenith}_{\mathrm{reco}} - \mathrm{zenith}_{\mathrm{true}}|$ and the length resolution via $|L_{\mathrm{reco}} - L_{\mathrm{true}}|$. Note that the resolution discussed in this section only represents the statistical error of the relevant event properties. The systematic uncertainties of these observables will be discussed in greater detail in Section 6.2.3 and in particular with respect to the tau-neutrino identification in Chapter 5. The relevant deposited energy region for the work presented in this thesis is between $\sim 60\,\mathrm{TeV} - 10\,\mathrm{PeV}$.

The distributions are shown separately for the true event topologies, because the resolution of an observable depends on the topology. The directional resolution is better for a track than for a cascade, but the energy resolution of a cascade is better than that of a track [226]. The former effect is due to the long lever arm of a track, which constrains the direction much better than an almost spherically-shaped light distribution of a cascade. The latter is due to the relative amount of visible deposited energy compared to the total energy of the particle. A major fraction of the initial particle energy is deposited as visible energy in an electromagnetic or hadronic cascade, but a muon (represented by a track) only deposits some of its energy via continuous and stochastic energy losses. Consequently, the uncertainty of estimating the muon energy via the observable deposited energy is much larger. Therefore, the total deposited energy (either by cascades or by tracks) is considered as energy estimator in the analysis presented in this thesis instead of estimating the muon energy. The total deposited energy is a good estimator of the neutrino energy for cascades, but poor for tracks (c.f. Section 4.3.1). Including systematic errors, it was found that the total deposited energy can be resolved to $\sim 15\,\%$ for both cascades and tracks and the direction to $\sim 10^\circ - 15^\circ$ for cascades and $\lesssim 1^\circ$ for tracks [43, 226].

The main observables that were used for the published spectral fit of the diffuse astrophysical neutrino flux based on the high-energy starting event selection are the total deposited energy and the zenith angle [4]. These are also used in the analysis presented this thesis, with the addition of the topology ID and the double cascade length as tau-neutrino sensitive observables. Keep in mind that each distribution of a true event topology is a superposition of astrophysical and atmospheric neutrinos as well as atmospheric muons. This causes distinct features to appear in the distributions which are easily identifiable when dividing them into the different astrophysical and atmospheric flux components instead of the event topologies.[5]

The distributions of the **total deposited energy** and the **zenith angle** as well as their resolution are summarized in Figure 4.15 for the entire high-energy starting event sample without any flavor discrimination. The sample is dominated by single cascades, because these have the largest effective area. The Glashow resonance is clearly visible at a deposited energy of $\sim 6\,\mathrm{PeV}$, as expected. Note that the Glashow resonance is not visible for tracks, as the deposited energy is different depending on the stochastic losses of the muon. The track component dominates at low deposited energies ($E_{\mathrm{tot}} \lesssim 60\,\mathrm{TeV}$) and in the down-going region ($\cos(\mathrm{zenith}) \gtrsim 0.7$), as the majority of these events are atmospheric muons.[6] The zenith distribution decreases for all topologies towards the up-going region ($\cos(\mathrm{zenith}) \simeq -1$), where high-energy events are less frequent due to increasing absorption in the Earth.

The cumulative distribution of the **energy resolution** shows that events are generally well reconstructed in energy. The median energy resolution is $\sim 4\%$ for single and double cascades and $\sim 6\%$ for tracks. It can clearly be seen that the energy resolution is generally better for cascades than for tracks. Energy losses of a track have more degrees of freedom than the more confined energy depositions of a single or double cascade. Therefore, the energy resolution is slightly worse for tracks. Another effect is visible when the median energy resolution is depicted as a function of the true deposited energy. It can be seen that the resolution stays rather constant until a few PeV above which it deteriorates. This can be explained by different causes. First, the assumption that a cascade is point-like becomes increasingly inaccurate as the shower extension increases and the LPM-effect starts to play a role (c.f. Section 3.1.2). Second, at sufficiently high energies, the light yield is so large that it causes PMTs to saturate. Since DOMs with saturated PMTs are excluded from the reconstruction, the effective light yield used for the reconstruction decreases (c.f. Section 3.3.3). This plays a particular role for highly energetic tracks. These are more likely to pass multiple DOMs near to where they may deposit large

[5] For example, compare Figure 4.15 (top row) to Figure 6.2 in Section 6.2.2.

[6] Note that the statistical error is particularly large in these bins as the available simulation data for atmospheric muons is very limited (order of ~ 50 simulated events). See Section 6.2.3 for details on how this is treated.

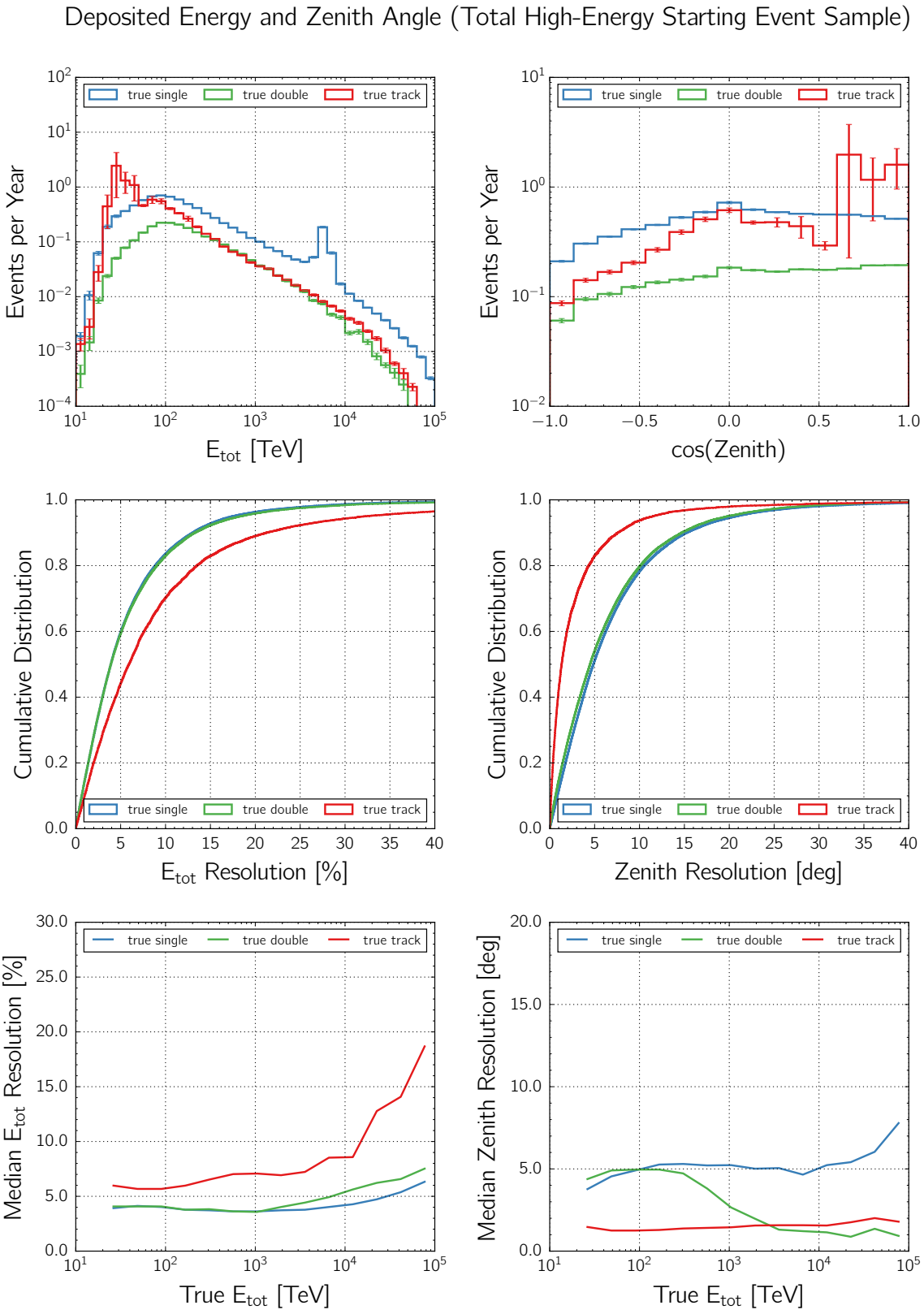

Figure 4.15: Observable and resolution distributions of the total deposited energy (left) and zenith angle (right) for the total high-energy starting event sample. The observable distributions are shown in the top row, the cumulative resolution in the center row, and the median resolution as a function of the true deposited energy in the bottom row. Distributions are shown for true single cascades, true double cascades, and true tracks separately.

stochastic losses. In contrast, a cascade deposits its entire energy in a single location. Third, energy losses that are not deposited inside the detector volume are less reliably reconstructed. Both true and reconstructed energy depositions are discarded for the calculation of the resolution if they are farther away than 50 m from the outer detector edge. This is only relevant for tracks, because uncontained cascade events are discarded by the high-energy starting event selection. Therefore, this boundary effect particularly deteriorates the energy resolution of track events, as the muon may deposit a large fraction of its energy outside the detector volume. The light yield of such energy losses expected at the closest DOM may be too small to be detected.

The cumulative distribution of the **zenith resolution** shows that events are generally well reconstructed in direction. Single cascade and double cascade events have a median zenith resolution of $\sim 4.5°$ and track events have $\sim 1.5°$. It is better for tracks than for cascades due to the long lever arm. This effect is illustrated when the median zenith resolution is depicted as a function of the true deposited energy. It can be seen that the resolution is rather constant over a wide range of energies for single cascades and tracks, but steadily improves for double cascades. This is caused by the correlation of the energy with the tau decay length. The larger the energy deposition, the more likely the tau propagates a longer distance before decaying. If the reconstructed length of the double cascade increases, the lever arm of the event becomes longer as well. Consequently, the median zenith resolution between the two extreme event cases of a single cascade (no lever arm) and a track (long lever arm) is bridged by the double cascade topology (energy-dependent lever arm). The resolution deteriorates for single cascades at very high energies, as the assumed point-like light emission pattern is increasingly inaccurate. Note that the zenith resolution of double cascades is even slightly better at very large deposited energies than it is for tracks. In these cases, a starting track event is likely to have a dim muon that is not identified properly by the reconstruction algorithm due to the overwhelming contribution of the hadronic cascade.

In Figure 4.16 (top row), the distributions of the **total deposited energy** and the **length** as well as their resolution are summarized for events classified as double cascade topology. It is evident that the largest contribution in the sample is caused by true double cascade events, as desired. This is in agreement with the results discussed in Section 4.3.2. The dominating background are single cascades, particularly in the lower energy region and at the Glashow resonance simply due to the enhanced event rate. Signal events are identifiable above $\sim 100\,\mathrm{TeV}$ and have a maximum expected event rate at $\sim 300\,\mathrm{TeV}$. Evidently, this must be seen in correlation with the reconstructed double cascade length. It can be seen that the length distribution continuously drops for double cascade events, as expected from the exponential decay law. The same distribution, however, is much steeper for single cascades, as these are not expected to have a large reconstructed length. It can be seen that already above $\sim 20\,\mathrm{m}$, the signal expectation is well above the background. Note that true tracks generally have a longer reconstructed length of a few hundred meters. Whereas single cascades by definition have a "true double cascade length" of zero, it is ill-defined for starting tracks. The length distribution for tracks can be explained by an artificially constructed "true double cascade length" for tracks. The first cascade of the double cascade reconstruction is defined by the vertex, time, and energy corresponding to the first deposited light inside the detector. It generally corresponds to the hadronic cascade from the neutrino-nucleon interaction or the first major stochastic loss of an entering muon that passes the veto region undetected. The reconstruction algorithm shifts the second cascade along the track until it best explains all stochastic energy losses simultaneously. Due to the detector geometry and the averaged stochasticity of a muon, the resulting length distribution peaks around a few hundred meters. Note that the track background in this length region is only at a similar level as the signal distribution in the projected phase space of the length. Signal and background contributions are more efficiently distinguished in the correlated phase space of the total deposited energy and the double cascade length (see Section 4.4).

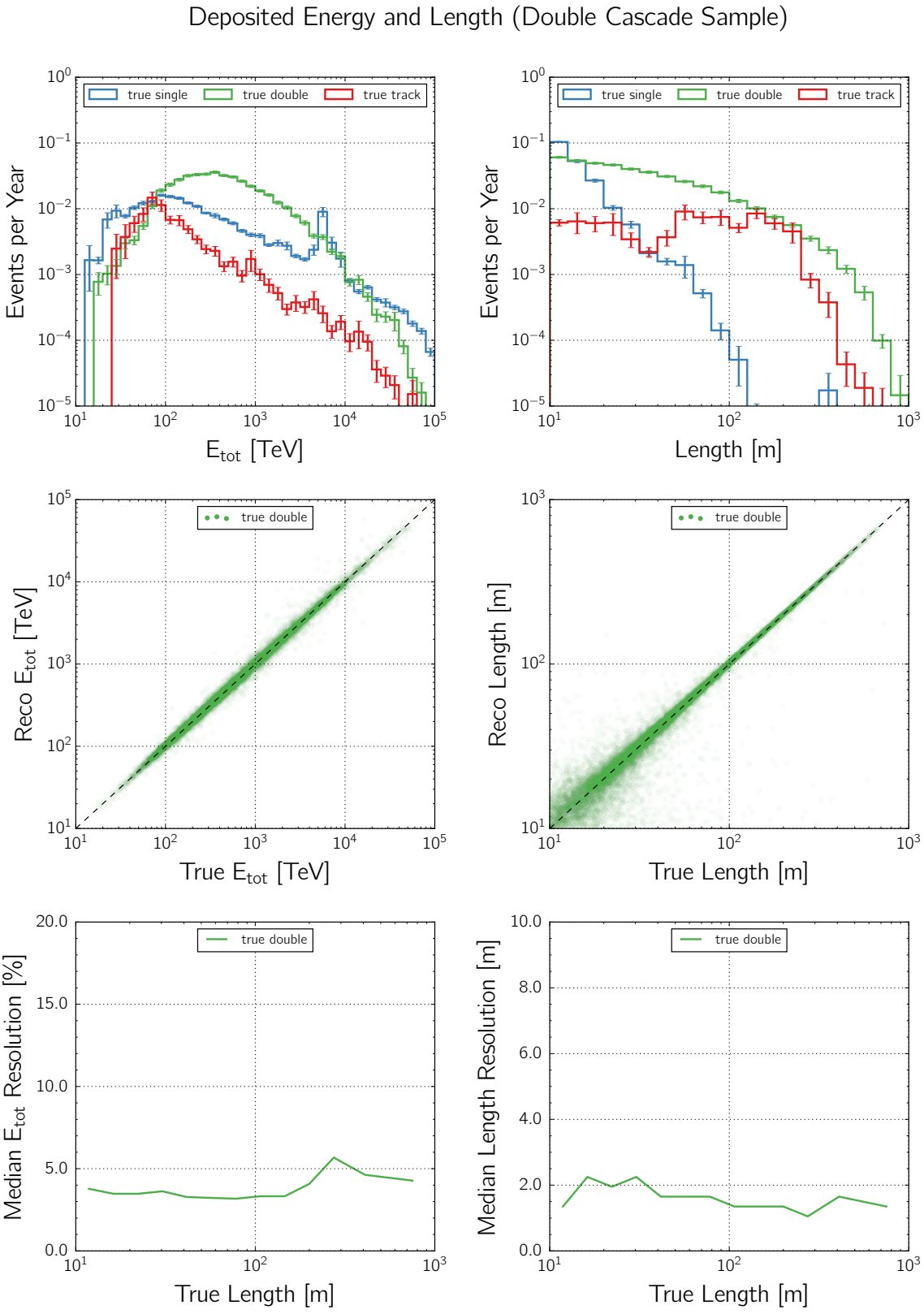

Figure 4.16: Observable and resolution distributions of the total deposited energy (left) and length (right) for the reconstructed double cascade sample. The observable distributions are shown in the top row, a comparison between reconstructed and true observable in the center row, and the median resolution as a function of the true tau decay length in the bottom row. The observable distributions are shown for each true event topology. Resolution plots are only shown for true double cascade events, as the length resolution is not meaningful for other event topologies (see text for further explanations).

The **energy resolution** and the **length resolution** are shown in greater detail only for signal events in Figure 4.16 (center and bottom row). The comparison between reconstructed and true deposited energy, as well as reconstructed and true length, is depicted in these plots. In agreement with the energy resolution without flavor discrimination (c.f. Section 4.15), it can be seen that the total deposited energy is also explicitly well reconstructed for true double cascade events that are identified as such. The plot of the median energy resolution as a function of the true length also consistently shows that the resolution is constant over a wide range and only degrades at large decay lengths where the decay cascade is less likely to be contained inside the detector volume. The comparison of true and reconstructed length illustrates that the relative spread is much smaller at large distances. Equivalently, for short decay lengths close to the boundary of $\sim 10\,\mathrm{m}$, the relative error is much larger. The absolute length resolution is $\sim 2\,\mathrm{m}$ over the entire available phase space.

The **individual energy and directional resolution** of true double cascade events in the reconstructed double cascade sample are summarized in Figure 4.17. It can be seen that the individual cascade energy resolution improves with increasing decay length. This is expected, as the separation between both cascades becomes more likely to be resolvable with longer distance. Additionally, it is also clearly visible that both energies are nearly degenerate (resolution of 15 % to 35 %) close to the boundary of $\sim 10\,\mathrm{m}$, whereas the total deposited energy is still reconstructed well. Due to the kinematics of the deep-inelastic neutrino-nucleon scattering, the second cascade is generally brighter and therefore has a more precisely reconstructed energy (c.f. Section 4.3.1). At decay lengths above a few hundred meters, the fraction of events where the decay cascade is no longer contained inside the detector volume increases and therefore degrades the energy resolution slightly. The opening angle is calculated via $\arccos(|\vec{d}_{\mathrm{true}} \cdot \vec{d}_{\mathrm{reco}}|)$ where $\vec{d}_{\mathrm{true}}$ and $\vec{d}_{\mathrm{reco}}$ are the true and reconstructed normalized directional vectors, respectively. As explained above, the directional resolution improves significantly with increasing decay length due to the longer lever arm (c.f. Figure 4.15). In Figure 4.17, this relationship is shown in direct correlation with the decay length instead of the total deposited energy. It illustrates that the directional resolution of double cascade events matches the resolution of cascade-like events at short and track-like events at long decay lengths.

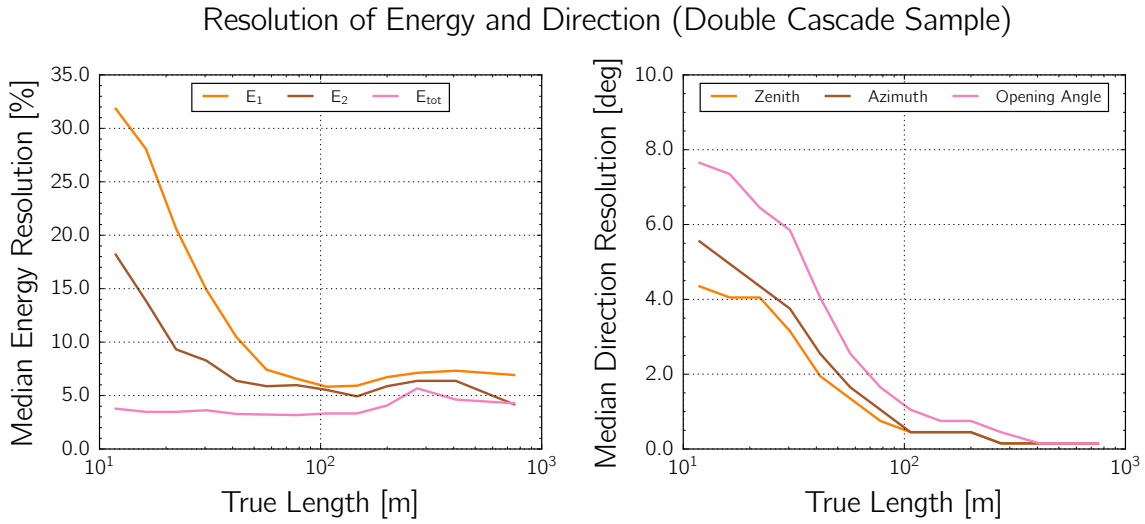

Figure 4.17: Median energy resolution (left) and directional resolution (right) as a function of the true tau decay length for true double cascade events in the reconstructed double cascade sample. The energy resolution is shown for the first and second cascades individually and for the total deposited energy. The directional resolution is shown for zenith and azimuth angles separately and in a combined manner represented by the opening angle.

4.4 Tau-Neutrino Identification Efficiency

The (mis)identification fraction of each event topology sample as listed in Table 4.1 was obtained using the ternary topology ID as sketched in Figure 4.9. The result was a $\sim$65% purity of successfully identified double cascade events on $\sim$35% misidentified background events. In this section, the tau-neutrino identification efficiency and the purity in the double cascade sample is further studied with respect to the length and the total deposited energy as the main observables that are used in the likelihood fit (see Section 6.2.2).

The correlation between total deposited energy and length is shown in Figure 4.18. The event rate distributions clearly illustrate how the maxima shift with deposited energy for an increasing central value of the selected length range. Note how the expected event rate decreases significantly the longer the decay length. The correlation of the length and total deposited energy is depicted by calculating the median value as well as the 68% and 95% percentiles of the energy as a function of the length. As expected, it is approximately linear due to the relation $\lambda_\tau \simeq \frac{50\,\mathrm{m}}{1\,\mathrm{PeV}} E_\tau$ (c.f. Section 3.1). It can be read off that an event with an observed length of $L \simeq 100\,\mathrm{m}$ would correspond to a median total deposited energy of $E_\mathrm{tot} \simeq 1\,\mathrm{PeV}$, which seemingly contradicts the expectation by a factor 2. However, this can be understood by transforming from the total deposited energy to the tau energy. The median ratio of the energy transfer from the tau-neutrino to the tau is $\sim$0.85 at these energies. This means that $\sim$15% of the total deposited energy is contained in the neutrino interaction cascade. The median ratio of the visible light in the decay cascade compared to the tau energy is $\sim$0.6 at these energies. This is due to the reduced light yield of the dominating decay into hadronic cascades compared to electromagnetic cascades. In addition, some of the energy is carried away by the secondary tau-neutrino produced in the decay. Furthermore, λ_τ refers to the decay length after which $1/\mathrm{e} \simeq 37\%$ of a set of tau leptons at the same energy have not decayed yet. However, Figure 4.18 displays the median value of each distribution, i.e. 50%, which gives a conversion factor of $\sim$0.7. Consequently, transforming the observable E_tot to the non-observable E_τ in the median case is obtained via $E_\tau \simeq E_\mathrm{tot} \cdot 0.85 \cdot 1/0.6 \cdot 1/0.7$. For a total deposited energy of $E_\mathrm{tot} = 1\,\mathrm{PeV}$, this yields a tau energy of $E_\tau \simeq 2.02\,\mathrm{PeV}$, thereby recovering the original hypothesis that a tau with $E_\tau \simeq 2\,\mathrm{PeV}$ energy is associated with a decay length of $\lambda_\tau \simeq 100\,\mathrm{m}$.

The phase space region of the total deposited energy and the length that contains 95% of all double cascade events is indicated in Figure 4.18. Although the entire phase space is used in the likelihood fit, the 95% signal containment region can be used to estimate an effective tau-neutrino sensitivity as a function of these two observables. Therefore, a two-dimensional selection is defined as the region between two linear fits through the 95% boundaries. All events that are contained within this region are considered signal-like, and all remaining events are discarded. Note that this selection is only applied to the distributions and numbers presented in the following part of this section in order to study the tau-neutrino identification efficiency. It is not applied anywhere else, in particular not in the analysis presented in Chapter 6.

In Figure 4.19, the **identification efficiency** and **purity** of tau-neutrino events in the double cascade sample are shown as a function of the primary neutrino energy, the total deposited energy, and the length. They are calculated via

$$\text{efficiency} = (\text{selected signal})/(\text{total signal}), \tag{4.7}$$

$$\text{purity} = (\text{selected signal})/(\text{selected signal} + \text{selected background}), \tag{4.8}$$

where *total signal* is the expected rate for all tau-neutrino interactions inducing a double cascade event topology, *selected signal* is the rate of all successfully identified double cascade events, and *selected background* is the total rate of all misidentified single cascade and track events of astrophysical or atmospheric origin.

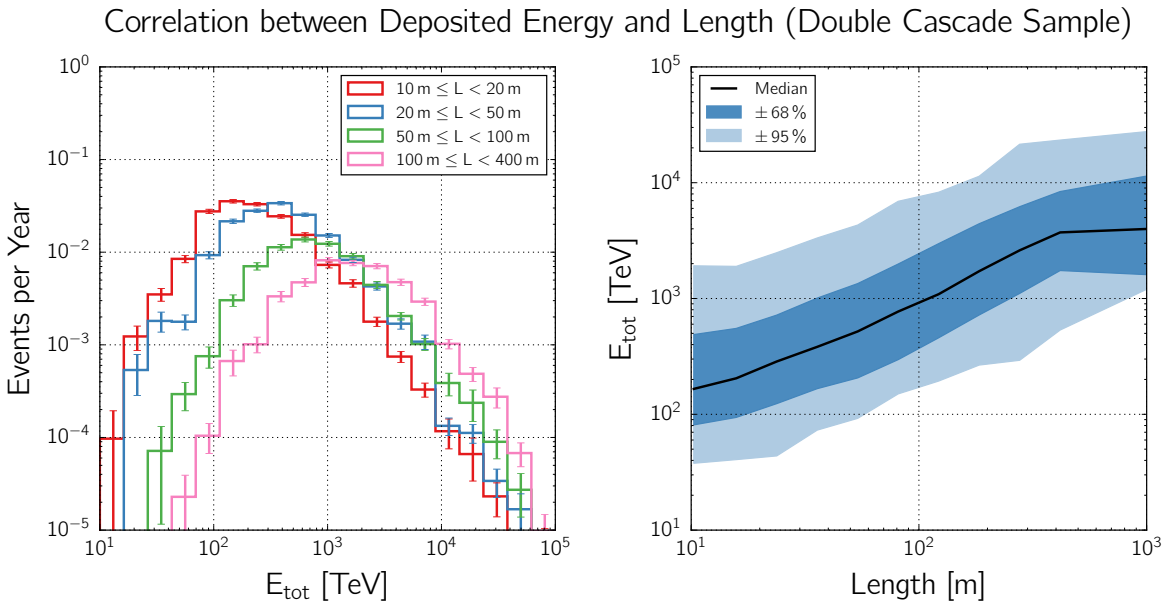

Figure 4.18: Correlation of the total deposited energy and length for true double cascade events in the reconstructed double cascade sample. The event rate is shown as a function of the reconstructed total deposited energy for different ranges of the reconstructed length (left), and the reconstructed total deposited energy is shown as function of the reconstructed length (right). The median value as well as the 68% and 95% percentiles are indicated.

With respect to the **primary neutrino energy** (Figure 4.19, top row) it can be seen that a major fraction of all tau-neutrino interactions cannot be identified. In particular, at energies below a few hundred TeV, the average decay length of the tau is too short to be resolvable. The integrated efficiency over the entire neutrino energy range is only $\sim 18\%$. At ~ 100 TeV, the identification efficiency is $\sim 5\%$, and towards higher energies it becomes increasingly larger and reaches a maximum of $\sim 50\%$ at ~ 2 PeV. Above this energy, the efficiency decreases again due to the requirement that both interaction and decay cascades are "softly" contained within the detector volume (c.f. Section 4.3.1). The neutrino energy range which contains 90% of all signal events is given by a lower limit of 126 TeV and an upper limit of 3981 TeV (for an $E_\nu^{-2.3}$ spectrum). The median neutrino energy is 566 TeV. The background contamination is dominant at low energies and the purity reaches a maximum value of $\sim 90\%$ around a few PeV where the identification efficiency is also largest. Note that the dip in purity around 6 PeV neutrino energy is due to the enhanced single cascade contamination from the Glashow resonance (c.f. Section 3.1.1). Consequently, the double cascade method is only sensitive to tau-neutrino interactions above a few hundred TeV neutrino energy.

The distributions of the **total deposited energy** (Figure 4.19, center row) look similar to those of the neutrino energy. The purity is larger above a few PeV, because the double cascade length is resolved more precisely and background events are less likely to be misreconstructed. Therefore, the misidentification fraction of background events decreases with energy while the identification efficiency increases. The deposited energy range which contains 90% of all signal events is given by a lower limit of 79 TeV and an upper limit of 1995 TeV. The median deposited energy is 357 TeV. Although the identification efficiency has a maximum at ~ 2 PeV, the underlying $E_\nu^{-2.3}$ spectrum causes the maximum rate of identifiable tau-neutrino interactions to be expected around ~ 400 TeV deposited energy. In this energy region, the selection efficiency is only $\sim 35\%$. However, the corresponding purity of $\sim 80\%$ is fairly large, which yields a signal-to-background ratio of ~ 4. Consequently, a successfully identified tau-neutrino interaction (in this analysis) likely only deposits a few hundred TeV energy rather than a few PeV.

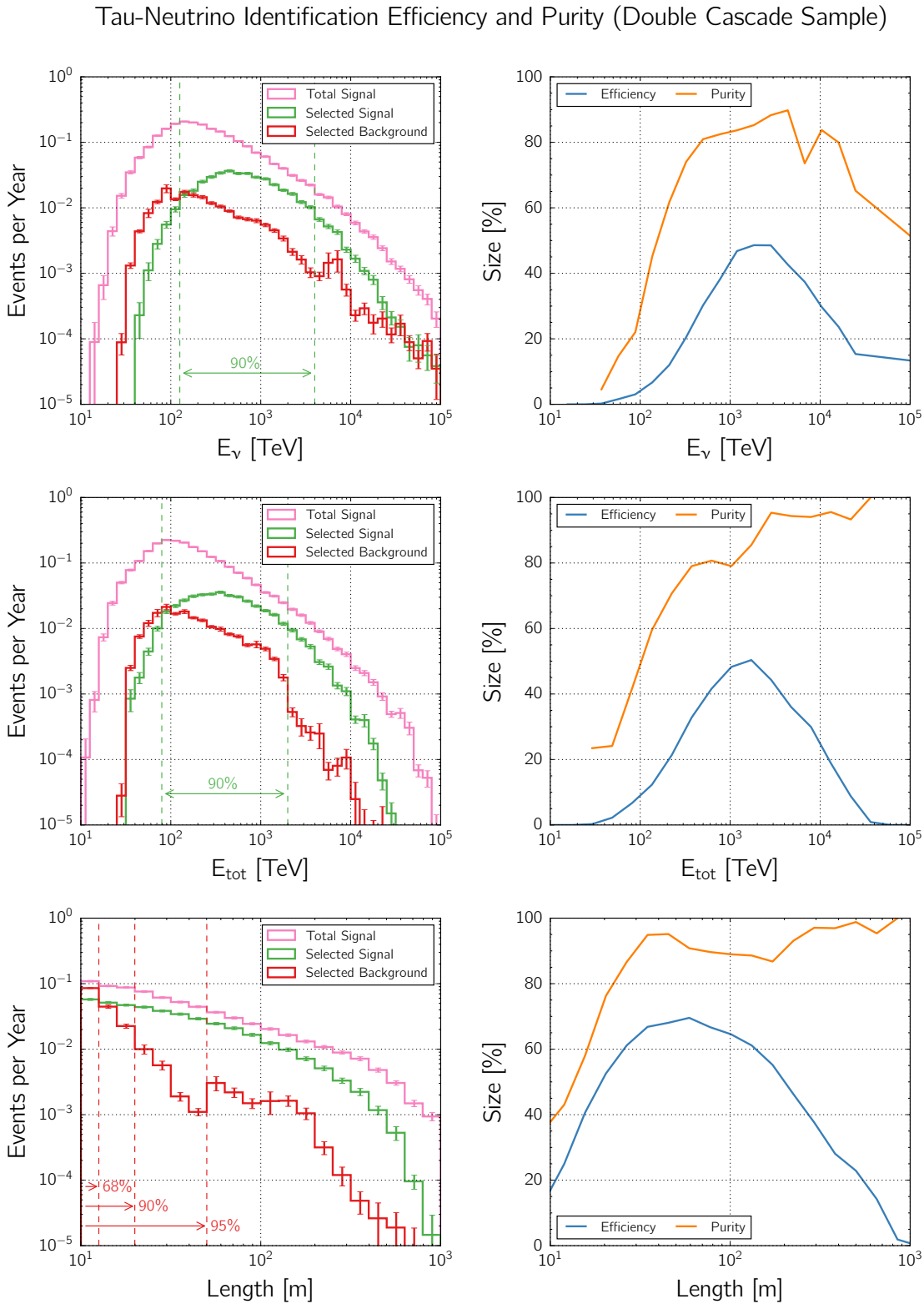

Figure 4.19: Tau-neutrino identification efficiency and purity as a function of the neutrino energy (top), the total deposited energy (center), and the double cascade length (bottom). The expected event rate (left) is shown for all (total signal) and for successfully identified true double cascade events (selected signal) as well as for all misidentified single cascade and track events of astrophysical or atmospheric origin (selected background). The energy ranges which contain 90% of selected signal events (top and center) and the 68%, 90% and 95% percentiles of the length distribution for background events (bottom) are indicated. The efficiency and purity (right) are depicted as a function of the respective quantities. They are calculated via Equation 4.7 and Equation 4.8, respectively.

The **length** distributions (Figure 4.19, bottom row) display the tau-neutrino sensitivity incisively. They are shown above the 10 m threshold of the reconstructed double cascade sample, which discards ∼82% of all true double cascade events, as explained above. The integrated efficiency over the depicted phase space above 10 m is ∼50%. It can be seen that the identification efficiency is just below ∼20% at the threshold and increases to a maximum of ∼70% at a length of ∼60 m. From there on, it decreases steadily as the containment requirement of the decay vertex discards an increasing number of events with larger decay lengths. Note that the purity rapidly reaches an almost constant level of ∼90% above ∼30 m length. It can be deduced from the expected event rate distribution that the background drops by ∼68% at ∼15 m, by ∼90% at ∼20 m and by ∼95% at ∼50 m. The last value is approximately the threshold where the background is no longer dominated by single cascades but by tracks (c.f. Figure 4.16). From the event rate distribution it can be seen that an identifiable tau-neutrino interaction is expected to occur at shorter decay lengths below ∼50 m. Therefore, single cascades are the most important background for the analysis presented in this thesis. Although a tau-neutrino interaction is only half as likely to occur at a decay length of ∼50 m as it is at ∼10 m, if detected, it would be a very clear signature with a purity of ∼95% and a corresponding signal-to-background ratio of ∼19.

The **correlated probability density distributions** of the total deposited energy and length are shown for signal and background events in Figure 4.20 and Figure 4.21, respectively. The 95% signal containment and the 68%, 90%, and 95% percentiles of the background distribution are indicated. It can clearly be seen that energy and length are not correlated for background events, which therefore occupy a different phase space than signal events. Assuming the astrophysical and atmospheric benchmark flux models used in this analysis (see Section 6.2.1), a total of ∼3.05 tau-neutrino interactions per year are expected for the high-energy starting event selection. Of these, only ∼2.26 interactions per year produce a double cascade event topology and of those, only ∼0.70 and ∼0.41 interactions per year have decay length longer than 10 m and 20 m, respectively. The expected event rate of identifiable tau-neutrino interactions is ∼0.43 signal on ∼0.29 background events per year for the entire phase space depicted in Figure 4.20 and Figure 4.21. This corresponds to a signal-to-background ratio of ∼1.5. In the indicated 95% signal containment region, the expected rates decrease to ∼0.41 signal and ∼0.18 background events per year, which increases the signal-to-background ratio to 2.3. In the same region, but above a length of 20 m, the expected rates are further reduced to ∼0.25 signal and 0.03 background events per year. This corresponds to a much higher signal-to-background ratio of ∼8.3. As mentioned above, the indicated signal containment and background exclusion regions are only to guide the eye and obtain these estimates of the signal-to-background ratio. They are not used as selection criteria in the likelihood fit.

In conclusion, the tau-neutrino sensitivity is determined by the ternary topology ID and by the correlation of the total deposited energy and length in particular. An identifiable double cascade event is expected to occur within ∼100 TeV and ∼2 PeV total deposited energy and with a decay length below ∼50 m (assuming an $E_\nu^{-2.3}$ spectrum). In a six-year high-energy starting event sample, ∼2.6 signal and ∼1.7 background events are expected in the entire double cascade sample. In the most sensitive 95% signal containment region above a length of 20 m, the expectation decreases to ∼1.5 signal and ∼0.2 background events.

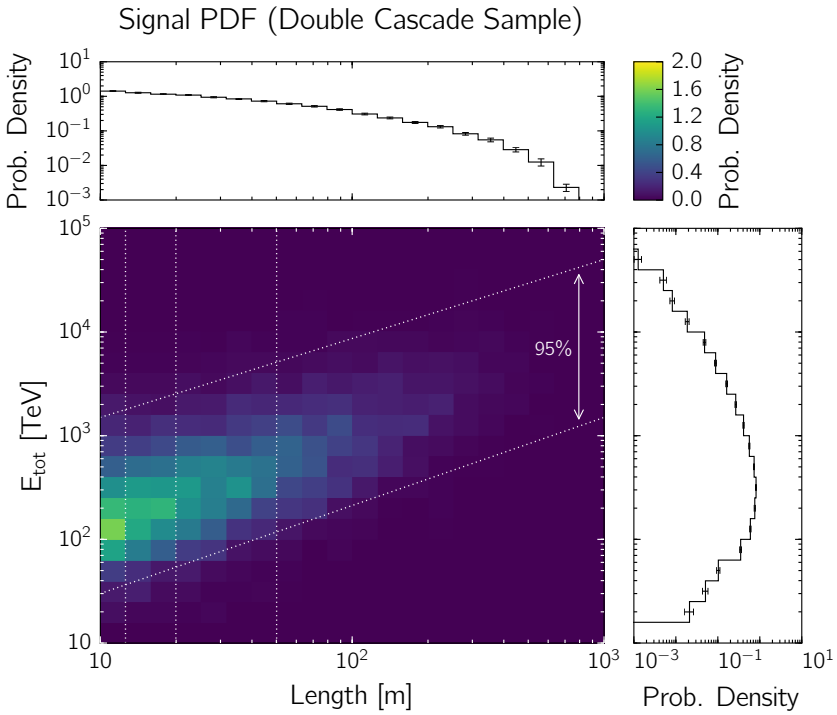

Figure 4.20: Signal probability density distribution for the reconstructed double cascade sample. A signal event is a tau-neutrino interaction inducing a double cascade. The observables are the total deposited energy and the double cascade length, which are correlated due to the scaling $E_\tau \sim \lambda_\tau$ of the tau energy and decay length. The diagonal lines are for visual guidance and indicate the 95% signal containment. The vertical lines are the same as in Figure 4.21.

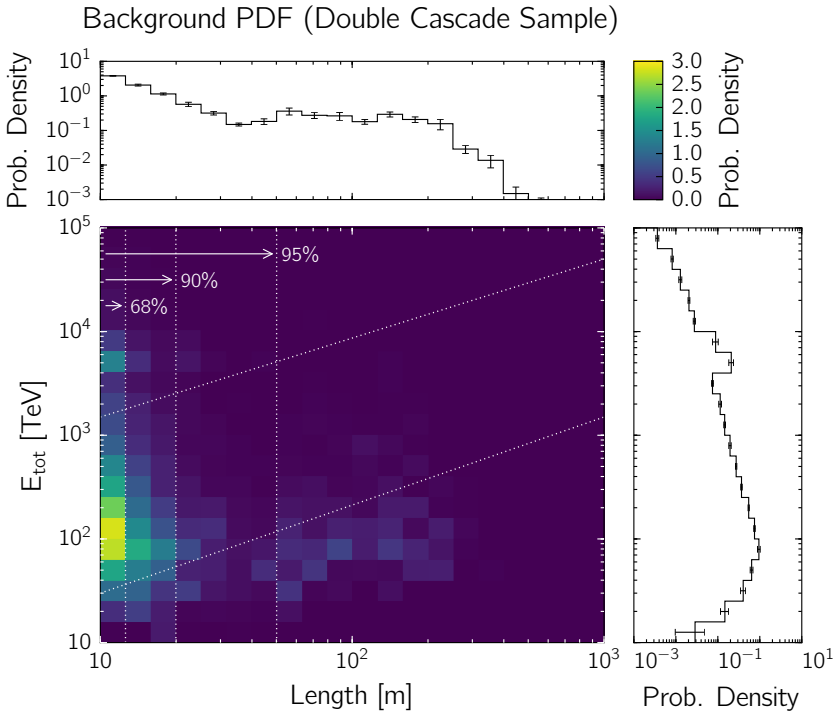

Figure 4.21: Background probability density distribution for the reconstructed double cascade sample. A background event is a single cascade or a track induced from a particle interaction of atmospheric or astrophysical origin. The observables and the diagonal lines are the same as in Figure 4.20. The vertical lines are for visual guidance and indicate the 68%, 90%, and 95% percentiles. Single cascades are the dominant background near the threshold of 10 m.

5 Systematic Treatment of the Ice Anisotropy

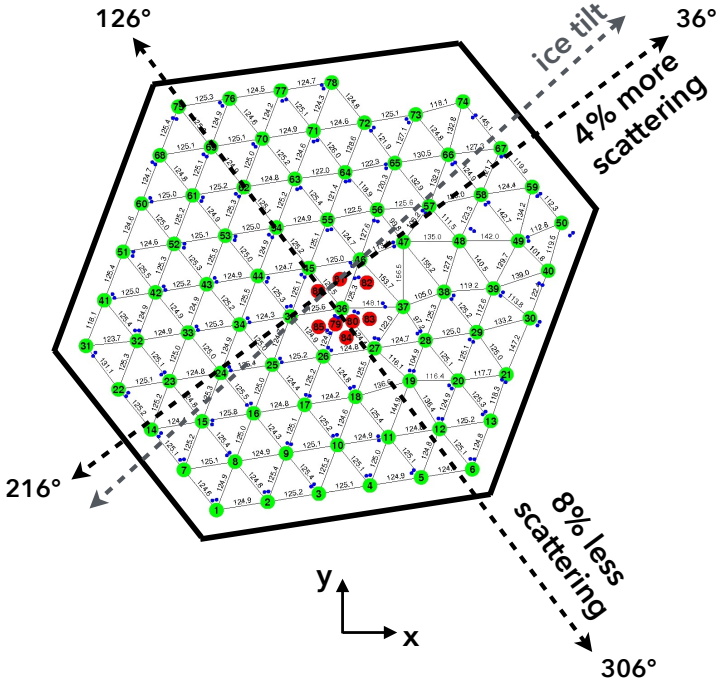

Figure 5.1: Sketch of the ice anisotropy and tilt in the top view of the IceCube detector. The ice anisotropy is a direction-dependent change of the light scattering within an ice layer. It is characterized by a modulation of the scattering coefficient by -8% along the glacial flow of the Antarctic ice (126°), by $+4\%$ along the direction that is orthogonal to the flow (36°) and by $+4\%$ along the positive z-axis that points out of the figure plane. The ice tilt is a position-dependent change of the light scattering in which entire ice layers are tilted. It is characterized by a modulation of the scattering coefficient according to an effective depth along a horizontal axis that is approximately parallel to the minor anisotropy axis (216°).

The optical properties of the Antarctic ice are described by the light scattering and absorption coefficients. For years, these properties have been repeatedly measured and assembled into different ice models. In the process, the effect of their uncertainties on reconstructed observables such as the deposited energy has also been studied. A completely new effect in this context was the introduction of an anisotropy of the scattering coefficient. The expected light pattern in the detector was suddenly dependent on the propagation direction of the photon. This was not incorporated in established event reconstruction algorithms which became a significant problem for tau-neutrino identification via the double cascade method.

In Section 5.1, the ice anisotropy is introduced and its effect on tau-neutrino identification is described. In Section 5.2, the incorporation of the ice anisotropy into reconstruction algorithms is explained and tested. In Section 5.3, a novel approach of artificially constructing double flasher events using in-situ LEDs of the detector is presented. In Section 5.4, the results are summarized and the implications of the ice anisotropy on tau-neutrino identification concluded.

5.1 Effect of the Ice Anisotropy on Tau-Neutrino Identification

The Antarctic ice is mainly modeled by the scattering and the absorption coefficients as a function of the depth below the surface of the ice (c.f. Section 3.2.4). The early ice models in the first operating years of IceCube assumed that the Antarctic ice can be described well by horizontal and isotropic layers which are binned with a thickness of 10 m, corresponding to the vertical DOM spacing of $\sim$17 m. Within each layer the scattering and absorption coefficients were assumed to be equal at all positions and in all directions. However, these assumptions contradict experimental data that has been obtained over time using the in-situ flasher LED calibration system (c.f. Section 3.2.2). Both assumptions have been abandoned with the introduction of the **ice tilt** and the **ice anisotropy** into recent ice models (see Figure 5.1).

First, it became apparent that the flasher LED data can be better described by introducing a tilt of all ice layers. It is modeled as an *effective shift in depth* along an axis of $\phi = 216°$ which is approximately orthogonal to the direction of the glacial flow. This shift in depth is equivalent to a modulation of the scattering coefficients as a function of the position. In the shallow ice, it can be a few meters and in the deep ice it can reach up to $\sim$40 m. The ice tilt was first introduced with the SPICE2 ice model, which was later superseded by SPICEMie [211]. Second, it was found that the ice is not isotropic, as the observed charge on different strings around a DOM that was horizontally flashing in all directions was systematically imbalanced. This was strong evidence that light scattering depends on the propagation direction of a photon. The ice anisotropy was modeled with a *modulation of the scattering coefficients* by -8% along the glacial flow of the Antarctic ice ($\phi = 126°$), by $+4\%$ along the direction that is orthogonal to the flow ($\phi = 36°$) and by $+4\%$ along the vertical axis pointing towards the surface of the ice. In between these axes the modulation is described by a sinusoidal function. The ice anisotropy was first introduced with the SPICELea ice model [212].

A description of the Antarctic ice should be as precise as possible in order to make valid predictions for observables. For example, a variation of the light scattering and/or absorption changes the expected light yield from a source to a DOM, which in return affects the energy estimation. It also influences the ability to reconstruct the time, vertex, and direction of a light source in the detector. The ice tilt is known to introduce a bias in energy reconstruction of cascades, which is on average small (few percent). In contrast, the ice anisotropy has not been an important systematic error for most neutrino searches as it only redistributes the light yield but does not change the overall amount. However, an initial study of the impact on tau-neutrino identification found that an incorrect description of the ice anisotropy in the double cascade event reconstruction increases the rate of misidentified single cascades [229].

The effect is caused by a mismatch between the ice anisotropy assumed during reconstruction and the ice anisotropy used in simulation (and presumably realized in nature), which is absorbed by the double cascade length as the only free fit parameter that is sensitive to the ice anisotropy. So far, reconstruction algorithms that are based on photo spline tables have been limited to ice models which contained neither the ice tilt nor the ice anisotropy. The reason is that the incorporation of any asymmetry in the ice is not straightforward due to technical limitations of photo spline tables. Consequently, the bias of the reconstructed length caused by the incorrect treatment of the ice anisotropy inevitably deteriorates tau-neutrino identification via the double cascade event reconstruction because it promotes the misidentification of single cascades. In contrast, a proper treatment of the ice tilt does not have a significant impact on tau-neutrino identification and is therefore not considered in the context of this thesis. In order to incorporate the ice anisotropy into the reconstruction algorithms, a new method was developed which overcomes the limitations of photo spline tables. The context, implementation, and impact on tau-neutrino identification will be discussed in the following sections. The results presented in Chapter 4 have been obtained through the use of this new method.

5.2 Incorporation of the Ice Anisotropy into Reconstruction

An event is reconstructed assuming a specific light source such as a cascade, a track, or an LED flasher in the `millipede`-framework (c.f. Section 3.3.3). Each of these fundamental light sources can also be used as building blocks for a more complicated source hypothesis, such as a double cascade or multiple flasher LEDs emitting light simultaneously (c.f. Section 3.2.2). The light emission of a minimum ionizing muon is negligible for the work presented in this thesis due to the high energy threshold of $\sim 30\,\text{TeV}$. The stochastic losses can be described by secondary cascades along the track. Therefore, only point-like light sources (cascades and flashers) are considered for the systematic treatment of the ice anisotropy. The reconstruction algorithm varies the event parameters (vertex, time, direction, energy) of the assumed light source such that the expected light yield best describes the digitized waveforms observed by every DOM. For this purpose, photo spline tables are necessary as they contain the expected light yield from every tabulated source type, position, and direction at any possible DOM position for any given time. Because this is a large amount of information to store, these tables are created under the simplified assumptions that the ice is homogenous and isotropic within each ice layer. The former symmetry is broken by the ice tilt and the latter by the ice anisotropy. Due to technical limitations of photo spline tables, it is not possible to simply add more dimensions to include the ice asymmetries. The incorporation of the ice anisotropy is solved by parametrizing the modulation of the scattering coefficient as a shift in distance between light source and DOM as a function of the emission angle. The important aspect is that this description is decoupled from the light emission of a specific source and generalized for any source direction.

5.2.1 Photo Spline Tables and Technical Limitations

Photo spline tables contain the **light yield** and **photon arrival time distribution** for any possible position and time expected from the emission of any given source. Sources are divided into cascades (electrons), tracks (muons), and flashers (LEDs). The light emission and propagation for a specific source is simulated, and the expected light yield is tabulated as a function of the position and arrival time around the source. The photon propagation and tabulation are realized with `CLSIM`, and the resulting binned tables are fitted with a smooth spline interpolation that has been developed for this purpose (c.f. Section 3.3.2). This allows a prediction of the expected waveforms for any possible pair of emitting light source and receiving DOM.

The content of a photo spline table for a cascade light source is schematically sketched in Figure 5.2. A single source is uniquely defined by its **depth** (z-coordinate) and **zenith angle**. A full set of photo spline tables is created by simulating many cascades at different depths and angles throughout the instrumented volume going from $z = -600\,\text{m} \ldots 600\,\text{m}$ and $\text{zenith} = 0^\circ \ldots 180^\circ$ in bins of $\Delta z = 20\,\text{m}$ and $\Delta\text{zenith} = 10^\circ$, respectively. This means that $60 \cdot 18 = 1080$ cascade sources must be simulated. Note that there is no dependence on the x- and y-coordinates of the vertex position or on the azimuth angle of the source. This is not necessary due to the assumption that each ice layer is homogenous and isotropic. The impact of the loss of these symmetries on the creation of photo spline tables is large (see below).

Typically, a source is set to a **constant energy** of 1 GeV and then simulated repeatedly ~ 1000 times to decrease the statistical fluctuation of the light yield. Because the expected light yield is proportional to the energy, it can simply be scaled for different source energies during reconstruction by using the total light yield of $32582 \cdot 5.21$ photons emitted by a 1 GeV cascade. The first value corresponds to the number of Cherenkov photons per meter in a wavelength range of 300 nm to 600 nm assuming $\beta = 1$ and a wavelength dependent index of refraction. The second value is a scaling factor specific to electromagnetic showers [231]. Note that this

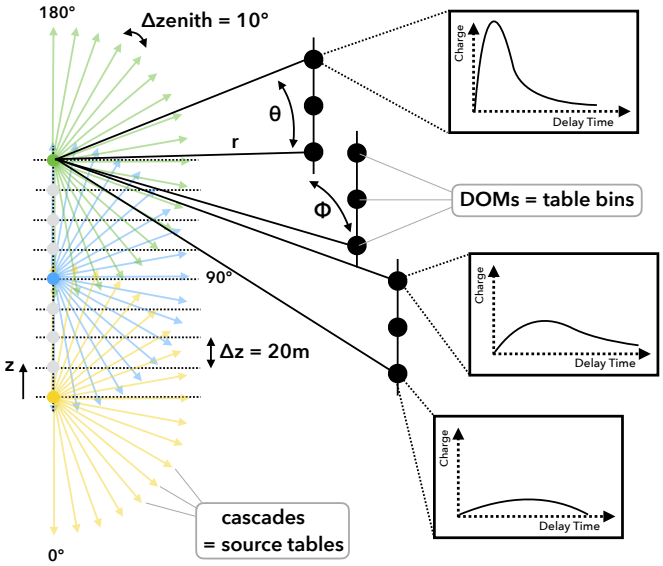

Figure 5.2: Sketch of the content of a cascade photo spline table. Multiple cascade sources at different depths and angles are simulated, and the light propagation is tracked. The surrounding volume is binned, and the expected waveform at a *hypothetical DOM* centered in each table bin is tabulated. The binned tables are fitted with a smooth spline interpolation yielding waveform predictions for any possible combination of a cascade and a DOM.

approach neglects the energy-dependent shower elongation (c.f. Section 3.1.3), as the tabulated light source is effectively point-like. Consequently, the reconstructed vertex position of a realistic cascade is usually close to the shower maximum. This assumption deteriorates the vertex and angular resolution but does not introduce a bias. The loss of information is acceptable, as the necessary number of cascade photo spline tables is greatly reduced by only using a single energy value of 1 GeV instead of tabulating the entire energy-sensitive range of the IceCube detector.

The volume around the cascade source is divided into bins, and every photon is tracked on its propagation path from the point of emission to the point of absorption. Each bin contains a *hypothetical DOM* at its center which includes all PMT effects, such as the quantum efficiency and the angular acceptance. Hence, a distribution of photoelectrons (instead of photons) is recorded. The coordinate system of a source table is centered around the source (not the detector) and aligned with its direction. It uses spherical coordinates (r, ϕ, θ), where r is the distance to the source, ϕ is the azimuthal angle and θ is the polar angle.[1] For each table bin the resulting waveform is recorded, i.e. the expected **charge** q as a function of the **delay time** τ. If t_s is the emission time of a photon at the source, and t_d its detection time at a DOM at the distance r, then the delay time is defined as $\tau = t_d - t_s - r/c$. It is the propagation time of the photon reduced by the geometric time that it would take from the point of emission to the point of detection without being scattered. The full coordinate set for a bin in the cascade photo spline table for each combination of a source and a DOM is given by $(r, \phi, \theta, z, \text{zenith})$, where (r, ϕ, θ) are the relative table coordinates of the DOM with respect to the source and (z, zenith) are the depth and zenith angle, respectively, of the source with respect to the detector coordinate system. The binned photo table is fitted with a smooth spline interpolation over all dimensions. For computational reasons, the spline fit is divided into an **amplitude table**, which contains the expected charge $q(r, \phi, \theta, z, \text{zenith})$, and a **time profile table**, which contains the corresponding delay time distributions $\tau(r, \phi, \theta, z, \text{zenith})$. Note that the former is a single number and the latter is a full (normalized) distribution such that the expected waveform is simply constructed by multiplying q with τ and shifting the entire distribution in time by t_s.

[1] Information on transformation between photo table and detector coordinate systems can be found in [221].

Due to the assumed symmetry of the scattering within an ice layer, a full set of cascade photo spline tables does not contain sources in different x and y-positions or at different azimuth angles. Note that an ice model without tilt or anisotropy is only dependent on the depth. This means that a cascade source must be tabulated as a function of the source depth z but also as a function of the zenith angle, because it is important whether the light is mostly emitted upward or downward into ice layers with more or less scattering, respectively. However, the assumed **homogeneity** of an ice layer causes the scattering coefficient to remain constant if the position of a source is moved horizontally (independence of x and y). Furthermore, the assumed **isotropy** of the ice causes the expected light pattern relative to a source to remain constant if its azimuthal orientation is changed (independence of the azimuth). Both symmetries not only imply that the number of necessary source tables is reduced, but that it is also sufficient to tabulate only a *half-sphere* for each source table, i.e. in the range from $\phi = 0° \dots 180°$ instead of $\phi = 0° \dots 360°$. This has the advantage that the tracked photon propagation of the other half-sphere can be mirrored into the tabulated half-sphere, thereby decreasing the required amount of simulated events by a factor 2. In addition, the computational resources of the time profile spline fit are much easier to manage with the reduced table volume.

The introduction of the ice tilt and the ice anisotropy increases the complexity of photo spline table creation drastically. A naive ansatz would be to simply add all further required dimensions. The ice tilt could be incorporated by tabulating cascade sources for every three-dimensional vertex position in the detector (not only depth), and the ice anisotropy could be incorporated by additionally tabulating every azimuth angle (not only zenith angle) and by extending the table range from a half-sphere to a full-sphere. This approach would certainly cover all symmetry-breaking ice properties. However, the required computational resources are immense:

1. **processing time**: Extending the unique cascade source tables by three more dimensions (x, y, azimuth) would require $60 \cdot 60 \cdot 36$ more source tables. Here, an equivalent binning of $\Delta x, y = 20\,\text{m}$ in the range $x, y = -600\,\text{m} \dots 600\,\text{m}$ and $\Delta\text{azimuth} = 10°$ in the range of azimuth $= 0° \dots 360°$ is assumed. Multiplied with the 1080 source tables from each unique combination of depth and zenith angle, this would yield a total of 139 968 000 source tables. Because the generation of a single source table (including the spline fit) takes $2 - 3$ CPU hours, this approach would be too expensive.
2. **memory consumption**: Extending the range of each source table to a full-sphere consumes vastly more memory during the time profile spline fit of the binned tables. The required memory easily reaches more than 100 GB during a fit, which is highly impractical for a large number of photo tables. Memory consumption is not only increased while a table is produced but also while it is used during reconstruction due to the larger file size.

Consequently, the approach of simply including all necessary dimensions to describe an asymmetric ice model is not feasible. Instead, a new method is developed, in which the ice asymmetries are decoupled from the specific light emission pattern of a cascade source. All other ice properties are kept in the standard photo spline tables which assume a symmetric ice. The ice asymmetries are only parameterized as a function of direction and depth while the assumed translational symmetry in x- and y-position remains. Note that this fully incorporates the ice anisotropy and effectively includes a **local ice tilt** but not a **global ice tilt**. The difference is due to the coordinate system of the ice asymmetry parametrization moving along the z-axis of the detector coordinate system. A source which is located on the z-axis ($x = y = 0$) has a precise description of the surrounding asymmetry due to the ice tilt (local effect). Elsewhere ($x, y \neq 0$), it effectively stays within the same ice layer and is not shifted in depth due to the ice tilt (global effect). Mentions of the ice tilt in the following sections refer to the local effect. An incorporation of the global ice tilt can be realized in principle via a z-shift parameterization. However, this is not critical in the scope of this thesis (c.f. Section 5.1).

5.2.2 Effective Distance Parametrization

The ice anisotropy is incorporated by parametrizing the direction-dependent modulation of the scattering coefficient by an **effective distance** between source and observer. The variation of the light yield at a DOM expected from a source due to the ice anisotropy can thereby be compensated by effectively changing the distance between the source and the DOM. If the source moves closer to a DOM, the expected charge increases, and if it moves farther away, it decreases. Hence, a variation of the scattering coefficient can be translated into a variation of the distance between source and DOM. This effective distance does not mean that either source or DOM are actually moved. Instead, the distance coordinate is transformed to $r \mapsto r_{\text{eff}}$, and the expected light yield is obtained from the tabulated value $q(r_{\text{eff}}, \phi, \theta, \tau, z, \text{zenith})$ in the photo spline table for a specific cascade source.

A crucial point is that the effective distance parametrization must be *completely independent from the orientation of the source* given by the zenith and azimuth angles. Otherwise, there would be no benefit as the problem of the missing azimuth table dimension would remain. Therefore, the effect of the ice anisotropy must be decoupled from the light emission of the source. In fact, this step is natural, because the Antarctic ice is modeled by scattering and absorption coefficients which are evidently independent from the source orientation. The decoupling is achieved by generating an **isotropic light source** that has the same properties of a cascade (point-like light emission in a wavelength range given by the Cherenkov spectrum of an electromagnetic shower) but lacks the dependence on the orientation. Technically, an isotropic light source is realized by a simple two-step trick. The first step is to generate 512 unique source directions which correspond to equally distanced points on a unit sphere (see Figure 5.3). They are obtained by using the algorithm described in [232]. The second step is to place one cascade source (with a standard Cherenkov emission profile of $\sim 41°$) at each of the 512 directions pointing outwards from a single position. Effectively, this is the same as an isotropic light emission after the photons have propagated for a few meters. A photo spline table of an isotropic source has the necessary consequence that the tabulated light yield only depends on the orientation of the ice anisotropy but not on the orientation of the source. The source dependence is thereby decoupled, and only the ice properties are modeled. As a consequence, the orientation of the coordinate system used for the photo spline table of an isotropic source is chosen to be equal to the detector coordinate system. The center of the coordinate system is still placed at the location of the source on the z-axis, and the table coordinates (ϕ, θ) are the same as the polar angles of the detector coordinate system.

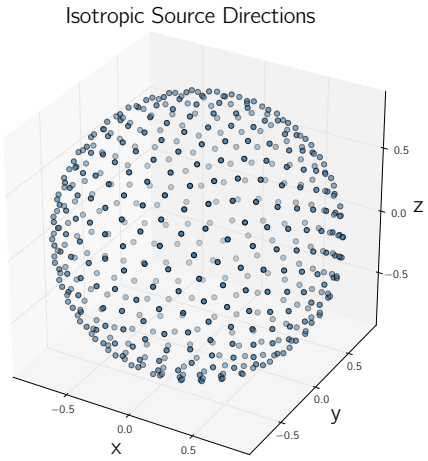

Figure 5.3: Isotropic light source effectively realized by 512 equally distanced points on a unit sphere.

In Figure 5.4 and Figure 5.5, the expected charge is shown as a function of the azimuth angle for two exemplary isotropic sources at depths of $z = 0\,\text{m}$ and $z = -400\,\text{m}$, respectively. These sources have been simulated repeatedly using a **flat ice model** and an **anisotropy/tilt ice model**. A flat ice model is homogeneous and isotropic within each ice layer, and the scattering and absorption coefficients only vary with depth. This is the type of ice model that has exclusively been used for event reconstruction based on photo spline tables so far, due to the aforementioned ice model symmetries and table limitations. An ice model with anisotropy and tilt breaks these symmetries. The expected charge is shown for four specific table bins at

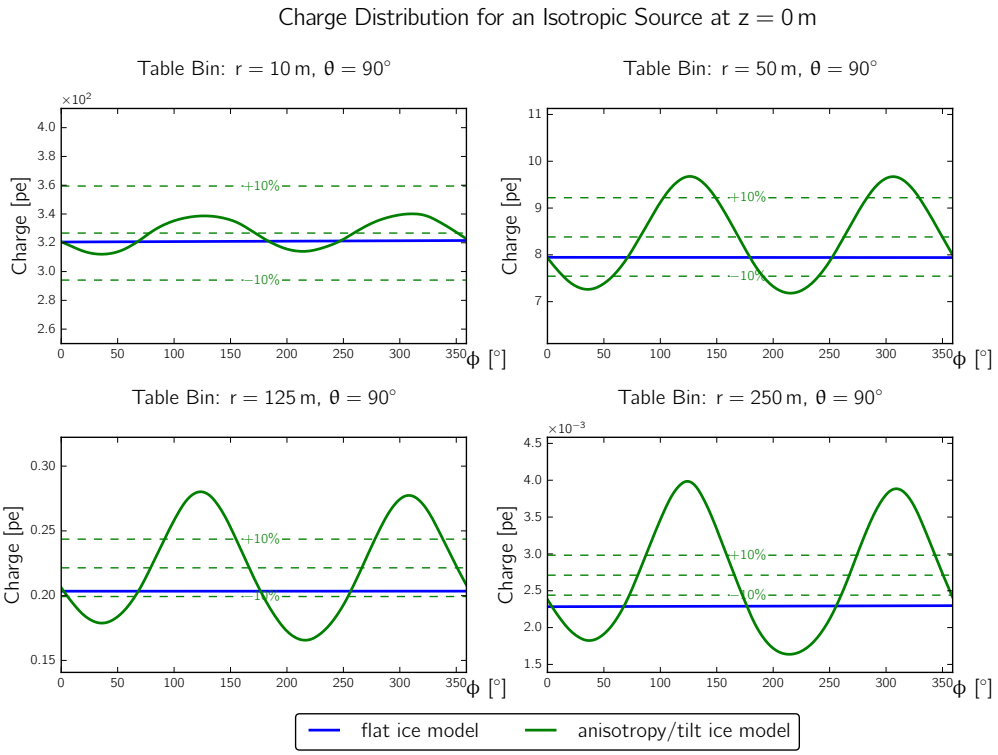

Figure 5.4: Expected charge as a function of the azimuth angle for an isotropic source at $z = 0\,\mathrm{m}$. It is depicted for different distances between source and observer at $r = 10\,\mathrm{m}$ (top left), $r = 50\,\mathrm{m}$ (top right), $r = 125\,\mathrm{m}$ (bottom left) and $r = 250\,\mathrm{m}$ (bottom right) assuming a flat ice model (blue) and an ice model with anisotropy and local tilt (green). The observation bin is chosen to be at the same depth as the source ($\theta = 90°$). The green dashed lines indicate the mean expected charge and the variation of $\pm 10\%$ around it.

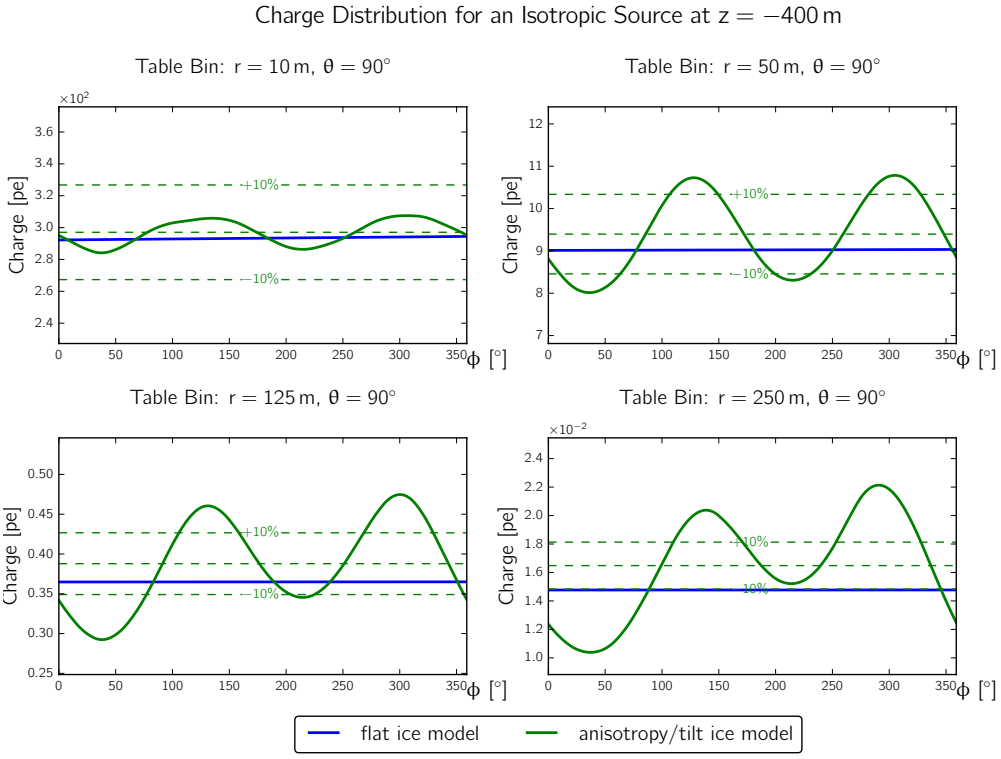

Figure 5.5: Same as in Figure 5.4, but for an isotropic source at $z = -400\,\mathrm{m}$.

different distances between source and observer ($r = 10\,\mathrm{m}, 50\,\mathrm{m}, 125\,\mathrm{m}, 250\,\mathrm{m}$) and at a fixed relative orientation ($\theta = 90°$). Hence, the distributions correspond to a hypothetical DOM moving horizontally around a source at a fixed distance. Whereas 10 m is much closer to the source than would be typical for an event considering the geometry of IceCube, a distance of 50 m would be fairly average for the first detected light of an event. The last two distances 125 m and 250 m correspond to the approximate spacing between neighboring and next-to-neighboring strings, respectively. It is evident that a flat ice model is indeed isotropic within an ice layer, as it shows no dependence on the azimuth angle. For an ice model with anisotropy and tilt, however, the modulation of the scattering coefficient is clearly visible along the two anisotropy axes as indicated in Figure 5.1. Furthermore, it is noteworthy that the effect of the local ice tilt is visible in the asymmetry of the sinusoidal form, which is particularly pronounced at large distances from the source and in the deep ice. This is a *geometric effect* that can be understood by imagining an ice model that only contains the ice tilt and no ice anisotropy. In that model, moving the observation point in a horizontal plane around the source at a large distance still causes the light yield to change as a function of the azimuth angle. This is not caused by a direction-dependent variation of the scattering but simply caused by crossing different ice layers due to the fact that they are tilted. Without an ice tilt, this effect would not be visible, and the sinusoidal variations in Figure 5.4 and Figure 5.5 would be symmetric.

The effective distance is obtained by a bin-wise comparison of the expected charge for an isotropic light source in the flat ice model and in the ice model with anisotropy and local tilt as sketched in Figure 5.6. It is realized by looking up the expected charge $q_{\mathrm{ani}}(r, \phi, \theta, z)$ at a test point with the direction (ϕ, θ) and distance r to an isotropic source at depth z in the photo spline table for an ice model with anisotropy and tilt. It is compared to the corresponding charge $q_{\mathrm{flat}}(r, \phi, \theta, z)$ of the same test point and source from the photo spline table for a flat ice model. The effective distance is obtained by finding a transformation $r \mapsto r_{\mathrm{eff}}$ such that $q_{\mathrm{ani}}(r, \phi, \theta, z) = q_{\mathrm{flat}}(r_{\mathrm{eff}}, \phi, \theta, z)$, i.e. the distance is shifted along the same direction until the expected charge in the flat ice model matches the charge in the ice model with anisotropy and tilt. In a later step, this can be applied by increasing the distance at an angle where the expected light yield is smaller due to more scattering and by decreasing the distance where it is larger due to less scattering. The **effective distance parametrization** is realized over the full phase space of a regular cascade photo spline table. It is $r_{\mathrm{eff}}(r, \phi, \theta, z)$, where $r = 0 \ldots 400\,\mathrm{m}$ is the relative distance between DOM and source at a depth $z = -600\,\mathrm{m} \ldots 600\,\mathrm{m}$. The azimuthal angle $\phi = 0 \ldots 360°$ and the polar angle $\theta = 0 \ldots 180°$ are given with respect to the detector coordinate system. Note that the depth-dependence must also be included, as the third anisotropy axis is aligned with the z-axis and points towards the surface of the ice. As mentioned above, it is important whether photons propagate upward into ice layers with more scattering or downward with less scattering. The parametrization is obtained by a binned calculation of the effective distance corresponding to the original binning of the photo spline tables and a subsequent fit of the binned table with a smooth spline interpolation. The full set of effective distance spline tables is much smaller as only $2 \cdot 60$ photo spline tables must be generated, i.e. 60 isotropic sources (no dependence on the zenith angle of the source) in the range $z = -600\,\mathrm{m} \ldots 600\,\mathrm{m}$ with a binning of $\Delta z = 20\,\mathrm{m}$ and two ice models where one is flat and the other contains the ice anisotropy and tilt.

Two examples of the obtained effective distance parametrization are shown for a source at $z = -400\,\mathrm{m}$ and a hypothetical DOM at $\theta = 10°$ and $\theta = 90°$ in Figure 5.7 and Figure 5.8, respectively. The effective distance is depicted as a function of the azimuthal angle where the hypothetical DOM is located. As discussed above, it is shown for the same distances ($r = 10\,\mathrm{m}, 50\,\mathrm{m}, 125\,\mathrm{m}, 250\,\mathrm{m}$). The setup can be pictured such that the DOM is almost vertically above the source for the case where $\theta = 10°$ and at the same depth for the other case where $\theta = 90°$. The three different anisotropy axes can thereby be visualized (c.f. Section 5.1).

In Figure 5.7, the **vertical anisotropy axis** aligned with the z-axis is illustrated. It has a $+4\%$ modulation of the scattering coefficient. Evidently, the graph of the effective distance as a function of the azimuth angle is nearly circular, i.e. independent of the azimuth angle. This is expected, as the projection of the horizontal anisotropy axes is negligible for nearly vertical directions. However, it is still clearly visible that $r_{\text{eff}} > r$ for the entire phase space, as expected from the increase of the scattering coefficient along the vertical anisotropy axis. Furthermore, it can be seen that the shift increases with distance, because a variation of the scattering coefficient has an even stronger impact with an increasing propagation path of a photon. It can be read off that $r_{\text{eff}}(r = 50\,\text{m}) \simeq 55\,\text{m}$, $r_{\text{eff}}(r = 125\,\text{m}) \simeq 135\,\text{m}$ and $r_{\text{eff}}(r = 250\,\text{m}) \simeq 265\,\text{m}$. Although the effect increases at larger distances, it is important to keep in mind that the expected light yield drastically decreases with distance due to the reduced photon flux per unit area and the light absorption in ice. Hence, for the reconstruction of an event, the intermediate distance range is most critical where the DOMs are close enough that the observed charge makes up a major fraction of the total charge but far away enough that the effect of the ice anisotropy has significantly altered the light yield expected from isotropic photon propagation.

In Figure 5.8, the **horizontal anisotropy axes** aligned with the x-y-plane are illustrated. The major anisotropy axis with a -8% modulation of the scattering coefficient is approximately aligned with the direction of the glacial flow, and the minor axis with a $+4\%$ modulation is approximately orthogonal to the flow direction. In this case, it can be seen that the graph of the effective distance as a function of the azimuth angle is approximately elliptical. This is expected, as the two horizontal anisotropy axes with different amplitudes translate into two different axes of the elliptical shape of the effective distance parametrization. It is clearly visible that $r_{\text{eff}} < r$ along the major anisotropy axis at $\phi = 306°$ with less scattering and that $r_{\text{eff}} > r$ along the minor anisotropy axis at $\phi = 36°$ with more scattering. This is in agreement with the corresponding increase and decrease of the expected light yield, respectively, as shown in Figure 5.4 and Figure 5.5. Furthermore, the elliptical shape becomes more pronounced with increasing distance due to the cumulative effect of the ice anisotropy on the photon path.

In summary, the ice anisotropy is parametrized via an effective distance that is completely independent of the source orientation and can be easily applied to a standard cascade photo spline table. Note that it may seem more sensible to calculate a charge correction factor by the bin-wise comparison between the flat ice model and the ice model with anisotropy and tilt, which is then applied to the light yield expected at a DOM from a source using the standard cascade photo spline tables. However, it is important not only to correct the integrated light yield but also to correct the time profile of the photon arrival distribution. This would not be possible with a simple correction factor but can indeed by realized using an effective distance where the entire time profile is replaced by the expectation from the shifted position. How this is achieved will be discussed in the following section.

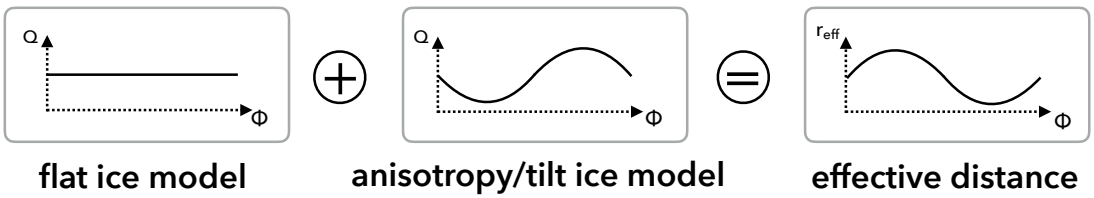

Figure 5.6: Sketch of the effective distance. A bin-wise comparison of the expected charge for an isotropic light source in the ice model without and with anisotropy and local tilt yields the effective distance r_{eff} between a source and a DOM which is obtained via $q_{\text{flat}}(r_{\text{eff}}, \phi, \theta, z) = q_{\text{ani}}(r, \phi, \theta, z)$, where (ϕ, θ) correspond to the polar angles of the detector coordinate system.

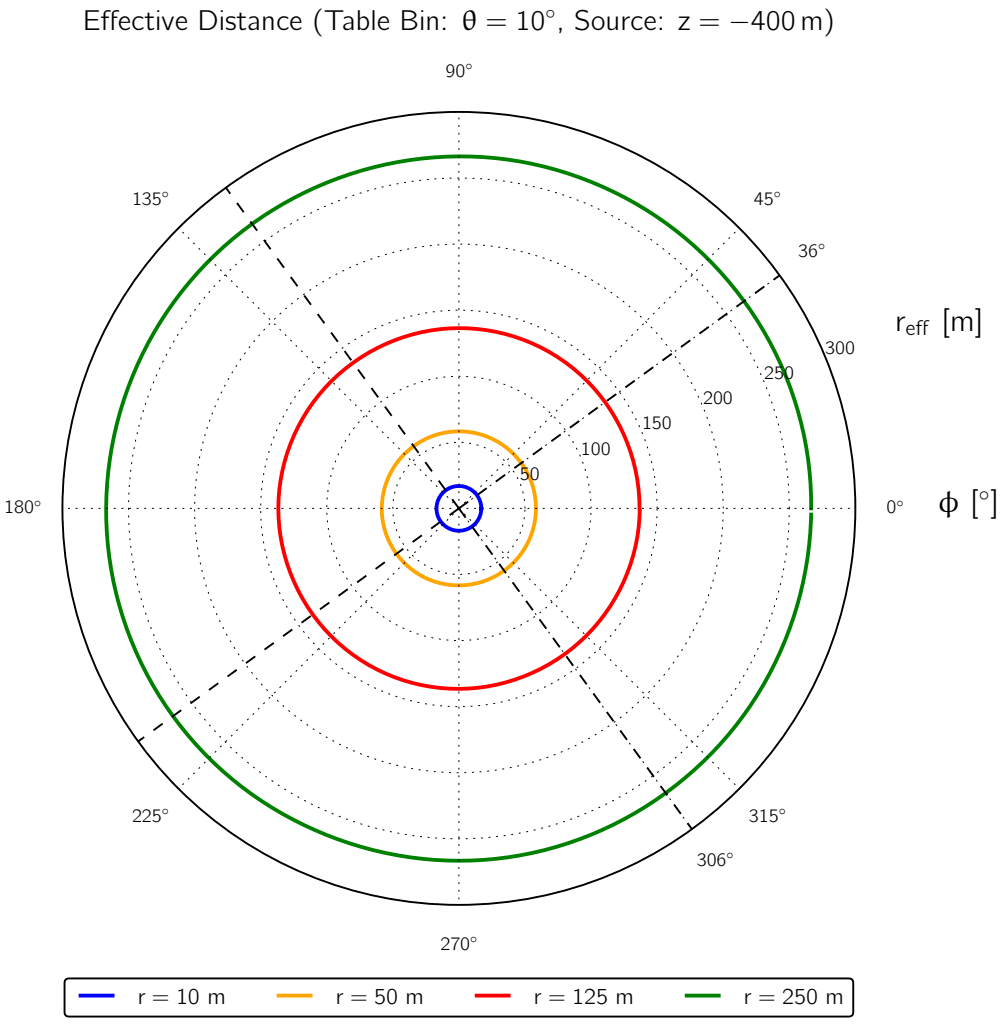

Figure 5.7: Effective distance parametrization for any cascade source at $z = -400\,\mathrm{m}$ and hypothetical DOMs at $\theta = 10°$. The effective distance r_{eff} is depicted as a function of the azimuthal angle ϕ where the hypothetical DOM is located for different distances $r = 10\,\mathrm{m}, 50\,\mathrm{m}, 125\,\mathrm{m}, 250\,\mathrm{m}$ in polar coordinates. This setup can be pictured by a hypothetical DOM which is closely moving around the vertical axis aligned with a cascade source at a fixed distance above it. The dashed lines indicate the major anisotropy axis, with a scattering modulation of -8% along the glacial flow of the Antarctic ice (306°), and the minor anisotropy axis, with a scattering modulation of $+4\%$ along the direction that is orthogonal to the flow (36°).

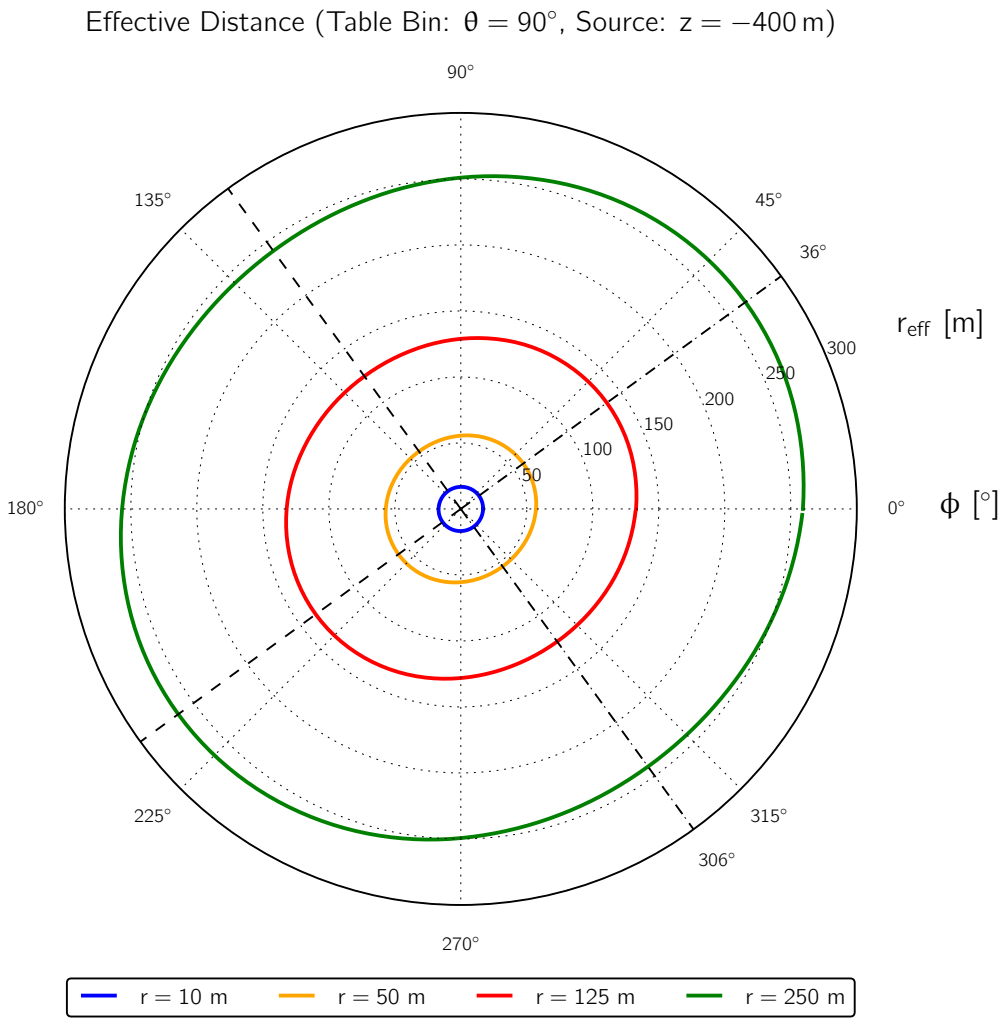

Figure 5.8: Same as in Figure 5.7, but for a hypothetical DOM at $\theta = 90°$. This setup can be pictured by a hypothetical DOM which is horizontally moving around a cascade source at a fixed distance.

5.2.3 Implementation and Simulation Test Results

The effective distance parametrization is a description of the local ice variation due to the ice anisotropy and tilt as a function of the depth below the surface of the ice. It is independent from the source as long as its type is a cascade. The effective distance spline table is to be used in conjunction with a photo spline table of a cascade source, which contains the expectation of the emitted light pattern for a flat ice model. The combination of both gives an effective description of the light pattern expected from the same source for an anisotropy/tilt ice model.

The procedure of **applying the effective distance parametrization** is depicted schematically in Figure 5.9. During the likelihood maximization of an event reconstruction, the standard approach to compare a measured to a predicted waveform follows three steps. First, a cascade source with a position (x_s, y_s, z_s), a direction $(\text{zenith}, \text{azimuth})$, a time t_s, and an energy E_s is chosen. The z-position and zenith angle of the cascade define the source table. Second, a DOM at the position (x_d, y_d, z_d) with a measured waveform starting at the time t_d and the total charge q_d is selected. Both source and DOM coordinates are used to transform to the relative coordinate system $(x_s, y_s, z_s, \text{zenith}, \text{azimuth}, x_d, y_d, z_d) \mapsto (r, \phi, \theta, z_s, \text{zenith})$. Third, the relative coordinates yield the correct bin to look up the expected normalized charge $\hat{q}_e$ in the amplitude photo spline table and the expected delay time distribution τ in the time profile photo spline table. Together with the known emission time t_s and the aforementioned linear scaling $q_e \sim \hat{q}_e E_s$ between light yield and energy, these are used to construct the expected waveform. During the event reconstruction, the expected waveform with charge q_e can then be compared to the measured waveform with charge q_d.

The novel step is introduced before the expected waveform is looked up in the cascade photo spline table, i.e. the **effective distance transformation** is introduced as an intermediate third step. The coordinate transformation $(x_s, y_s, z_s, x_d, y_d, z_d) \mapsto (r, \phi_d, \theta_d, z_s)$ is applied and the effective distance $r_{\text{eff}}(r, \phi_d, \theta_d, z_s)$ is looked up in the effective distance spline table. Then, the waveform is constructed by looking up the charge $q(r_{\text{eff}}, \phi, \theta, z_s, \text{zenith})$ and the delay time distribution $\tau(r_{\text{eff}}, \phi, \theta, z_s, \text{zenith})$ in the cascade amplitude and time profile photo spline tables, respectively. Note the important difference that in general $\phi_d \neq \phi$ and $\theta_d \neq \theta$. The coordinates of a DOM (r, ϕ_d, θ_d) and (r, ϕ, θ) are given with respect to different coordinate systems that are both centered in the source but have different orientations. The coordinates (r, ϕ_d, θ_d) are defined with respect to the detector coordinate system, where (ϕ_d, θ_d) are measured with respect to the detector axes (x, z). The coordinates (r, ϕ, θ) are defined with respect to the photo spline table coordinate system, where (ϕ, θ) are measured with respect to the source axes, i.e. the direction of the zenith angle is defined as z-axis and the orthogonal projection of the azimuth angle as x-axis. Only in the case where the source direction aligns with the detector axes, i.e. zenith $= 180°$ pointing upwards along the z-axis and azimuth $= 180°$ pointing horizontally along the x-axis, are both coordinate systems identical and, consequently, $\phi_d = \phi$ and $\theta_d = \theta$.

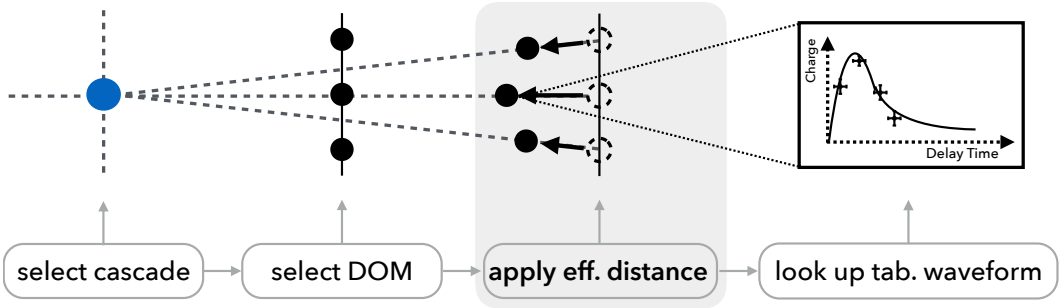

Figure 5.9: Sketch of how the effective distance parametrization is implemented in the standard procedure of predicting the waveform of a source at a DOM using photo spline tables.

In Figure 5.10, an example of the **expected charge** as a function of the azimuthal angle is shown for two different ice models. One prediction is obtained from the standard cascade photo spline table generated by assuming a flat ice model. The other prediction is obtained from the same table in combination with the prior coordinate transformation using the effective distance parametrization. This effectively corresponds to an ice model including anisotropy and local tilt. The example is for a cascade source located at a depth of $z = -400\,\mathrm{m}$, pointing horizontally along the x-axis of the detector. Here, the depicted azimuth range $\phi = 0 \ldots 360^\circ$ and the quoted polar angle $\theta = 90^\circ$ are given with respect to the detector coordinate system such that a hypothetical DOM goes around the source at the same depth. Note that the boundaries $\phi_{\mathrm{min}} = 0^\circ$ and $\phi_{\mathrm{min}} = 360^\circ$ correspond to the forward direction of the cascade and $\phi = 180^\circ$ to its backward direction. As discussed in the previous section, the expected charge distribution is shown at different distances ($r = 10\,\mathrm{m}, 50\,\mathrm{m}, 125\,\mathrm{m}, 250\,\mathrm{m}$). At the closest depicted distance of 10 m, the Cherenkov cone is prominent for the maximum expected charge at angle of $\sim 41^\circ$. The charge distribution has a minimum in the backward direction of the cascade, as photons are less likely to back-scatter. At close distances, there is almost no difference between the flat ice model and the anisotropy/tilt ice model. This is expected, as most photons have not been scattered yet at short distances. The charge distribution stays completely symmetric along the direction of the cascade for the flat ice model. This makes sense, as the emission profile of the Cherenkov light is a symmetric cone around the cascade direction, and the surrounding ice is assumed to be homogenous and isotropic within an ice layer. The difference to the charge distribution using the ice model with anisotropy and local tilt is already visible at short distances. Its asymmetric shape is due to the ice anisotropy, because the emission profile of the Cherenkov light from the cascade naturally does not change. The difference becomes more pronounced with increasing distance from the source, as photons are scattered multiple times before detection. This occurs more or less often along the minor or major axes of ice anisotropy, respectively.

In Figure 5.11, the **delay time distributions** are shown for a hypothetical at the same positions expected from the same source as above. In this case, however, the DOM is fixed at an azimuth angle of $\phi = 306^\circ$ along the major anisotropy axis. In this direction, the effect of the ice anisotropy and thereby the differences between the distributions shown for each ice model are expected to be largest. The general shape of a delay time distribution can be described by a leading edge, a maximum, and a trailing edge. Photons that arrive at a DOM after only few or no scattering processes are described by the leading edge of the distribution. It carries the most valuable information to reconstruct the time, direction, and vertex of an event. The larger the distance between source and DOM, the more a photon is scattered. Therefore, the maximum of the distribution shifts towards larger delay times with increasing distance. At 10 m distance the maximum of the distribution is at a delay time of $\sim 0.5\,\mathrm{ns}$, and at 50 m distance it has already increased to $\sim 25\,\mathrm{ns}$. The trailing edge and the long tail, in particular, are caused by heavily scattered photons that look isotropic and statistically no longer have directional information of the source. As described above, the difference between the two ice models increases with distance, as a larger number of scattering processes causes an increased effect of the ice anisotropy. It can be seen that the delay time distribution for the ice model with anisotropy and local tilt generally has a steeper leading edge and a slightly earlier maximum. This means that photons are scattered less than they are in the flat ice model, which is expected, because source and DOM are aligned with the major anisotropy axis with -8% modulation of the scattering coefficient. The effect is reversed for a hypothetical DOM that is aligned with minor anisotropy axis with $+4\%$ modulation of the scattering coefficient. In that case, the leading edge of delay time distribution is more gradual, and the position of the maximum is shifted towards later times compared to the flat ice model. The delay time distributions of both ice models approximately match if the orientation of the source and DOM are at an azimuthal angle that is $\pm 45^\circ$ away from any anisotropy axis. They would only match exactly if the azimuthal variation were due to the symmetric ice anisotropy without the local ice tilt.

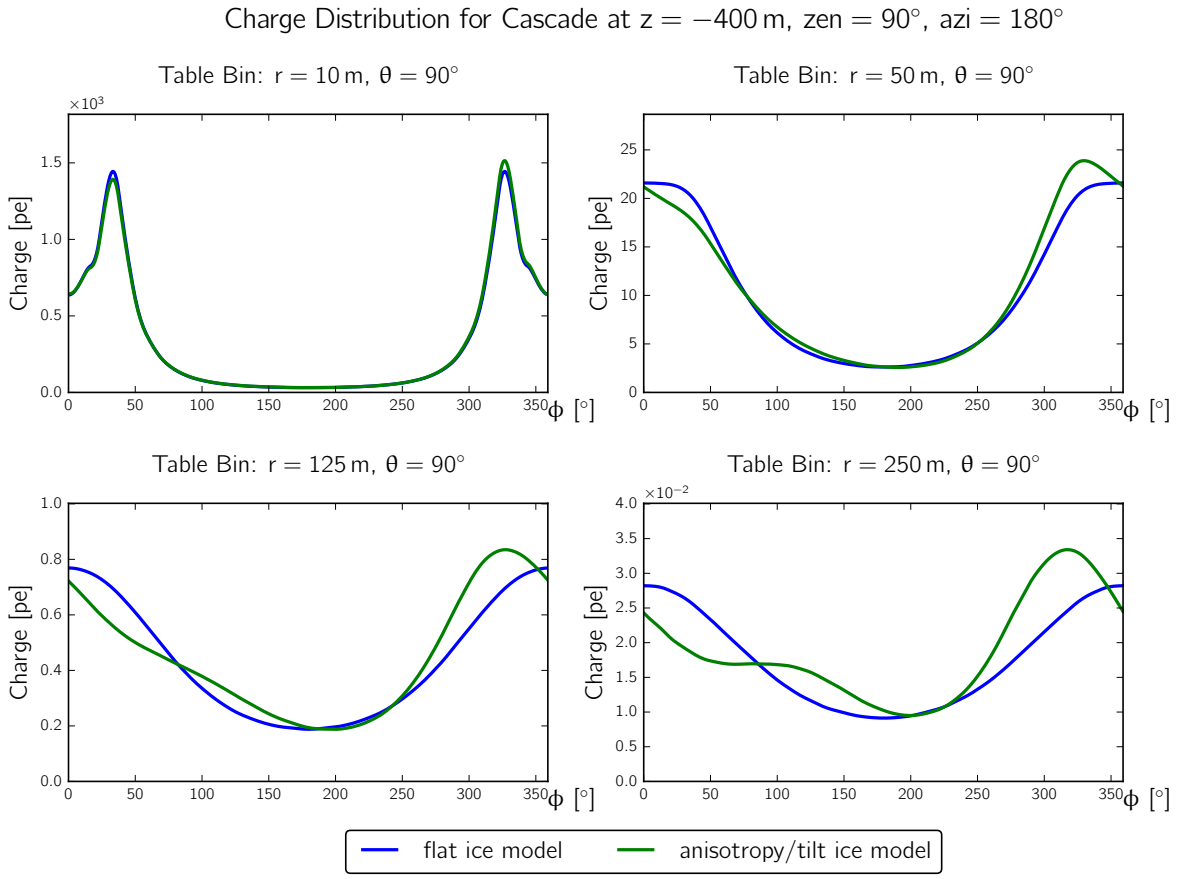

Figure 5.10: Example of the expected charge as a function of the azimuthal angle for a specific cascade source at a depth of $z = -400\,\mathrm{m}$ with an orientation of zenith $= 90°$ and azimuth $= 180°$. This means that the cascade points horizontally along the x-axis of the detector. The expected charge is depicted for a hypothetical DOM located at varying azimuthal angles at the same depth ($\theta = 90°$) for different distances at $r = 10\,\mathrm{m}$ (top left), $r = 50\,\mathrm{m}$ (top right), $r = 125\,\mathrm{m}$ (bottom left) and $r = 250\,\mathrm{m}$ (bottom right). The distributions are shown for a flat ice model (blue) and an ice model with anisotropy and local tilt (green). The former is obtained from the standard cascade photo spline table generated by assuming a flat ice model. The latter is obtained from the same photo spline table in combination with the prior coordinate transformation using the effective distance parametrization. The Cherenkov cone is clearly visible at 41° and 319° in the top left plot. The least charge is observed in the back-scattering region at $\phi = 180°$.

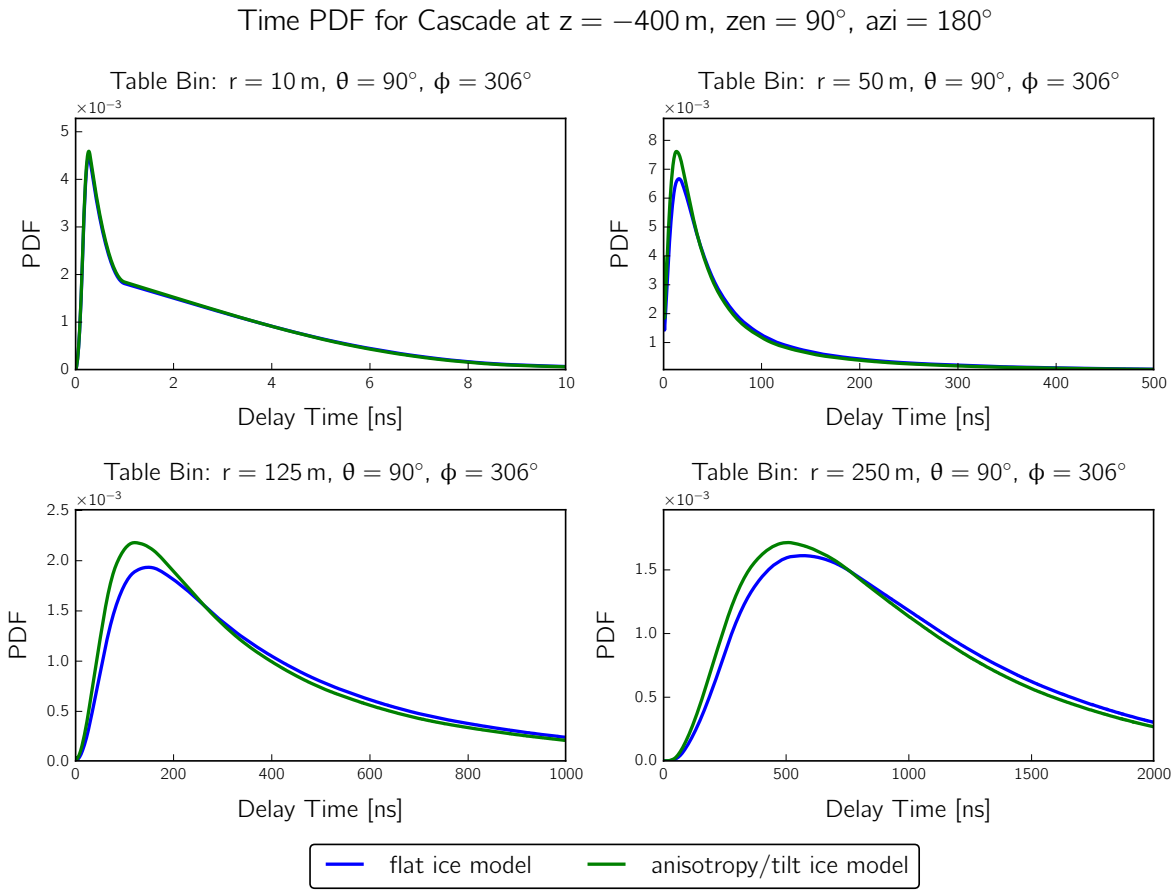

Figure 5.11: Example of expected delay time distributions for the same cascade source as in Figure 5.10. The delay time distributions are depicted for a hypothetical DOM located along the major anisotropy axis ($\phi = 306°$) at the same depth ($\theta = 90°$) for different distances at $r = 10\,\text{m}$ (top left), $r = 50\,\text{m}$ (top right), $r = 125\,\text{m}$ (bottom left) and $r = 250\,\text{m}$ (bottom right). As in Figure 5.10, the distributions are shown for a flat ice model (blue), obtained from the standard cascade photo spline table, and an ice model with anisotropy and local tilt (green), obtained from the same photo spline table in combination with the prior coordinate transformation using the effective distance parametrization. The difference between both distributions is expected to be the largest along the major anisotropy axis as shown here. Note the different scales of the delay time axis in each plot.

These two examples consistently show that the combined use of a standard cascade photo spline table with a prior transformation using the effective distance parametrization indeed yields a different prediction of the light pattern than for a flat ice model. The corrected charge and delay time distributions qualitatively agree with the expected modulation due to the ice anisotropy and local tilt. This is only explicitly shown for two examples but has been tested for numerous combinations of source-DOM-pairs, all of which gave consistent results. In addition, tests have been performed in order to determine whether the general description of a flat ice model and an ice model with anisotropy and tilt is self-consistent (as sketched above), whether the newly generated photo spline tables for a flat ice model are consistent with previously used sets of photo spline tables generated in a different way (not shown), and whether the spline fits to the binned photo tables agree with the bin values and how the fits perform near the edges of the table phase space (not shown). All tests have been successful within known error margins. Nevertheless, cross-checks with simulation data generated with **direct photon propagation** are necessary to quantitatively ensure the validity of the method. Therefore, a controlled test environment is developed using simulation data specifically generated for this purpose. The test is to compare the prediction of the effective distance and cascade photo spline tables to waveforms obtained from direct simulation of cascade events. Events that are simulated using direct photon propagation have the unique property that the expected light patterns can be generated using any ice model – unlike standard photo spline tables which are only valid under the assumption that the ice is homogenous and isotropic within an ice layer (c.f. Section 5.2.1). Therefore, an event is simulated once assuming a flat ice model and once again including the ice anisotropy and tilt, with the goal of performing two comparisons. First, waveforms of direct simulation assuming a flat ice model are compared to the prediction from the standard cascade photo spline table (naturally also assuming a flat ice model) as a cross-check. Second, waveforms of direct simulation assuming an ice model with anisotropy and tilt are compared to the prediction from the combined use of a standard cascade photo spline table with the effective distance spline table as the actual test of the method. A variety of cascade configurations are repeatedly simulated a few thousand times to increase photon statistics. Furthermore, all events are simulated using two different detector geometries, as shown for an exemplary cascade event in Figure 5.12. In addition to the **standard IC86 geometry** (full detector configuration with 86 strings), an **artificial testing geometry** is constructed in a cylindrical way such that the placement of the DOMs recreates a similar structure to the spherical coordinate system of the photo spline tables.[2] Note that the testing detector geometry has a much denser instrumentation in order to properly evaluate the phase space around the source.

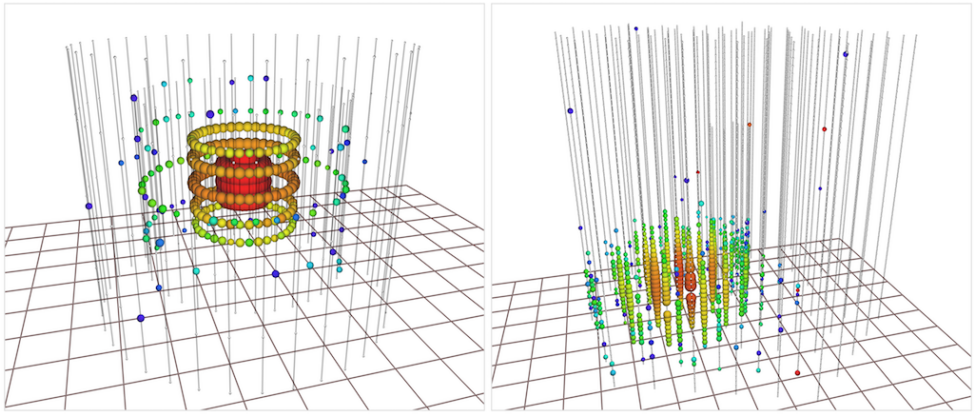

Figure 5.12: Event view of a cascade in the artificial testing detector geometry (left) and the standard IC86 geometry (right).

[2] The artificial construction of a cylindrical detector geometry is chosen because a spherical geometry is not easily realized, as one technical requirement of the IceCube software is that strings must be vertical.

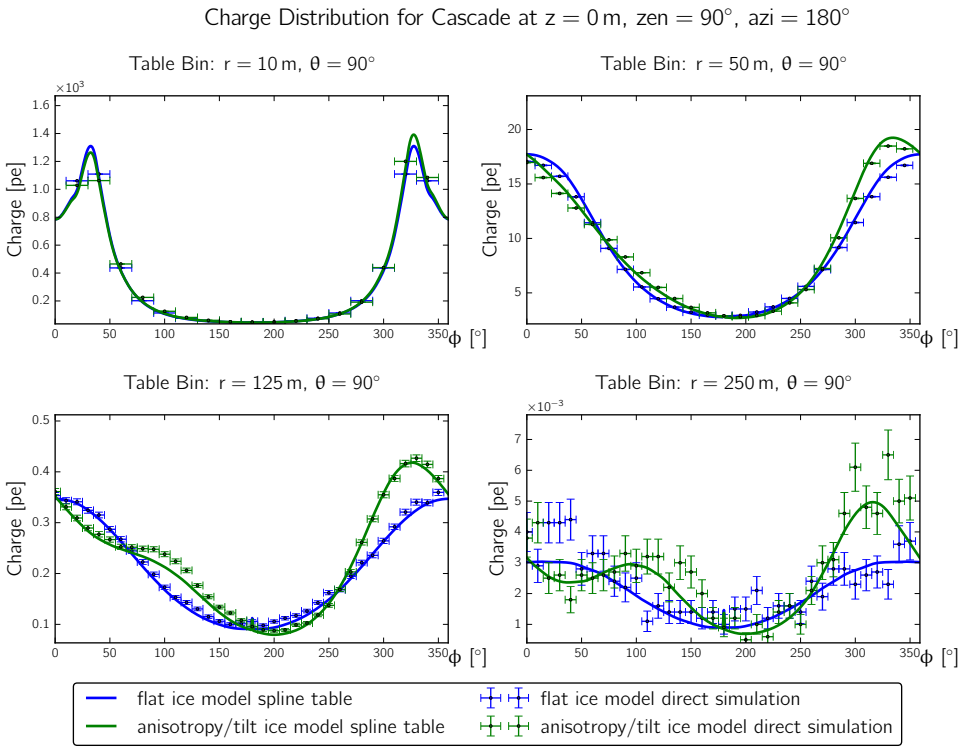

Figure 5.13: Example of the expected charge as a function of the azimuthal angle for a source at $z = 0\,\mathrm{m}$ pointing along the x-axis of the detector and hypothetical DOMs at $\theta = 90°$ in comparison to direct simulation using the testing geometry. It is shown for different distances between source and DOM at $r = 10\,\mathrm{m}$ (top left), $r = 50\,\mathrm{m}$ (top right), $r = 125\,\mathrm{m}$ (bottom left) and $r = 250\,\mathrm{m}$ (bottom right) assuming a flat ice model (blue) and an ice model with tilt and anisotropy (green). The expected charge from the photo spline tables is shown as lines and the observed charge at each hypothetical DOM is shown as marker. The error bars reflect the statistical error in y-direction and the distance between two DOMs in x-direction.

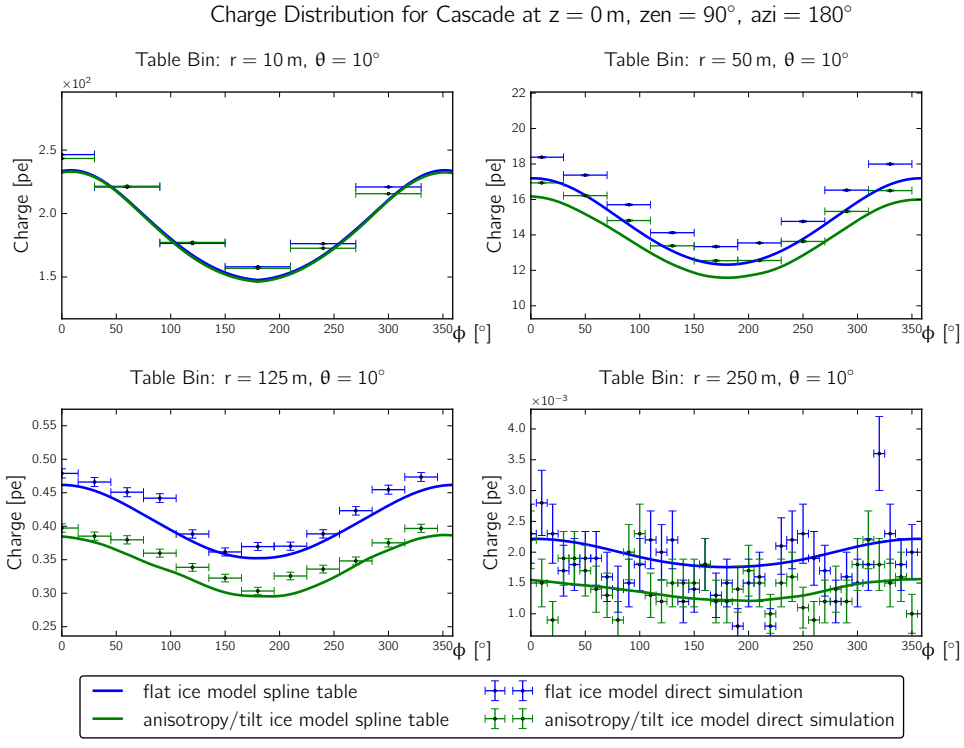

Figure 5.14: Same as in Figure 5.13, but for hypothetical DOMs at $\theta = 10°$.

In Figure 5.13 and Figure 5.14, the expected charge is shown as a function of the azimuthal angle of a hypothetical DOM going around the source at $\theta = 90°$ and $\theta = 10°$, respectively. In both cases, the cascade source is located at a depth of $z = 0\,\text{m}$ and points horizontally along the x-axis of the detector coordinate system. As discussed above, the distributions are depicted at the same distances $r = 10\,\text{m}, 50\,\text{m}, 125\,\text{m}, 250\,\text{m}$ between source and DOM and for a flat ice model and an ice model with anisotropy and local tilt. Additionally, the charge observed at the tightly placed DOMs around the source using the **testing geometry** is shown for the same simulated cascade using direct photon propagation for each ice model. It can be seen that the charge distribution from the photo spline tables and simulation data from direct photon propagation match very well for most DOMs. In particular, the asymmetric shape of the expected charge due to the ice anisotropy and local tilt is also well described in direct simulation. There are, however, a few cases where the shapes differ. This is expected to some extent as the spline fit through a binned photo table is not always able to simultaneously describe every bin equally well. The quality of the fit depends on the number of knots and the smoothing of each dimension of the spline surface. This is optimized in the best possible way but is not expected to perfectly describe every bin of a photo table. Furthermore, in some cases a constant shift between photo spline table and direct simulation is visible. Because it is the same for both ice models, it can be concluded that this is due to general differences between photo spline tables and direct simulation. The shift may be caused by the construction of photo tables by placing a hypothetical point-like DOM in the center of an extended bin. The bin volume increases dynamically with distance to account for the decreasing light yield at larger distances from the source. The extended volume of the bin limits the precision, and the spline interpolation does not necessarily describe the transition phase between large bins correctly. In contrast, the light yield is accurately tracked for a realistic DOM in direct simulation. Therefore, small deviations between the tabulated value and the observed value for a DOM are expected in cases where the bin size of the photo table is comparably large. Note that the depicted error bars with respect to the x-axis reflect the distance between neighboring DOMs in the testing geometry. The original bin size of the photo table is not visible, as only the spline interpolation is shown.

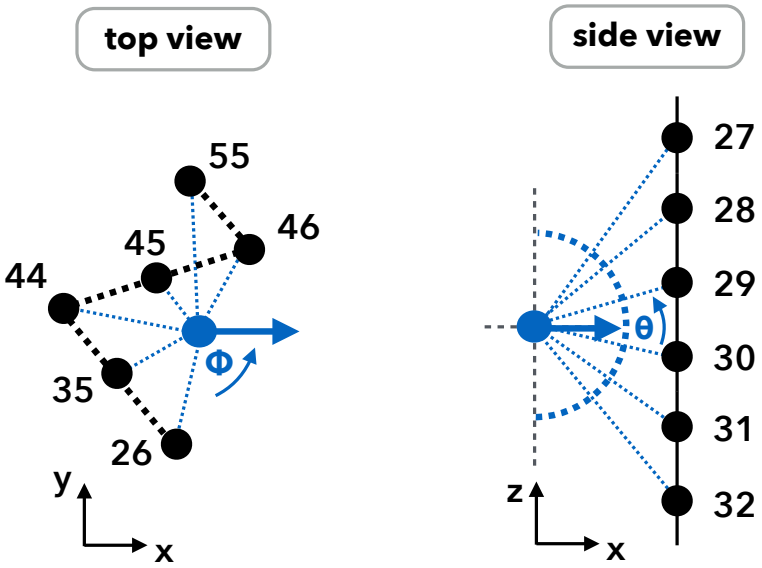

Figure 5.15: Sketch of the relative orientation between cascade and DOMs for which detected waveforms are depicted. The top view represents the x- and y-position of each receiving DOM at the same depth on surrounding strings. Indicated numbers correspond to the same strings as for the horizontal waveforms shown in Figure 5.16. The side view represents the z-position of each receiving DOM on the closest string. Indicated numbers correspond to the same DOMs as for the vertical waveforms shown in Figure 5.17.

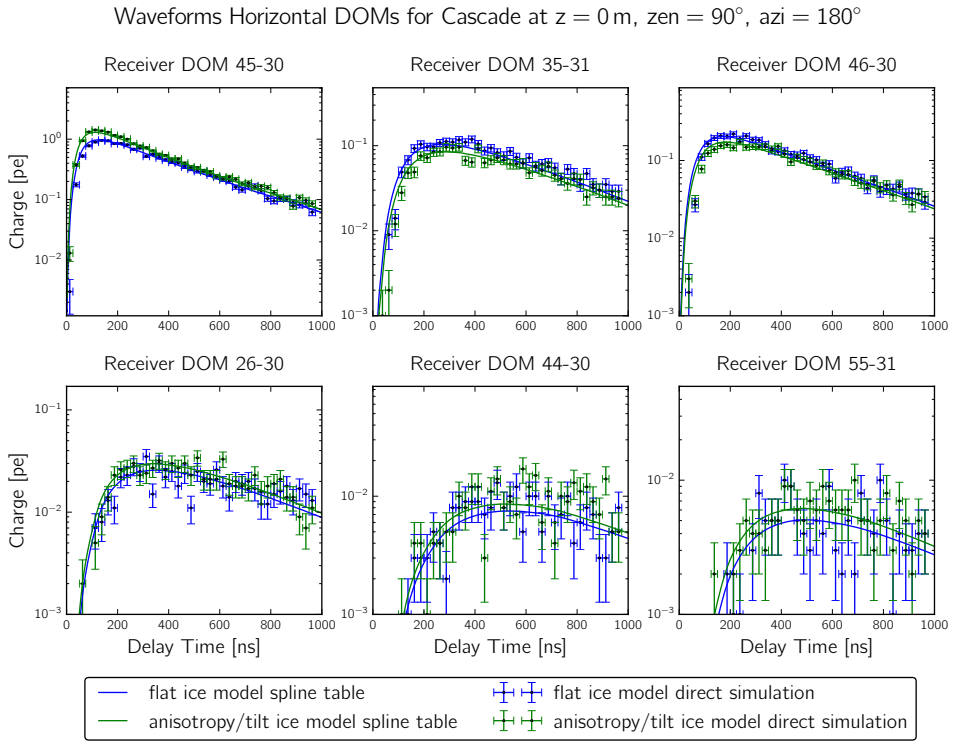

Figure 5.16: Waveforms of horizontally aligned DOMs around an exemplary source at $z = 0\,\mathrm{m}$ pointing along the x-axis of the detector in comparison to direct simulation using the standard IC86 geometry. Receiving DOMs are approximately located at the same depth of the source, at different distances, and along different directions (c.f. Figure 5.15, top view). Waveforms are shown for a flat ice model (blue) and an ice model with anisotropy and local tilt (green), and for photo spline tables (lines) and direct simulation (markers). The error bars reflect the statistical error in y-direction and the time binning in x-direction.

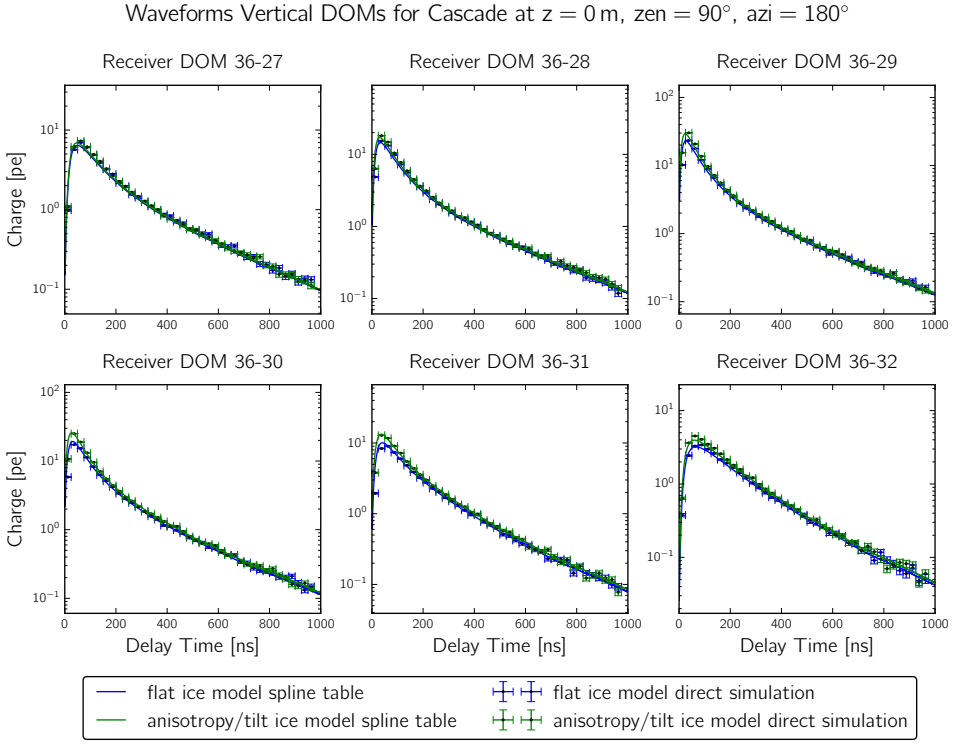

Figure 5.17: Same as in Figure 5.16, but for vertically aligned DOMs which are located on the closest string above and below the source (c.f. Figure 5.15, side view).

In Figure 5.15, the arrangement of receiving DOMs used for the performance test with the standard **IC86 detector geometry** is sketched. Horizontally aligned DOMs are at the same depth as the source but at different distances and along different directions such that both horizontal anisotropy axes can be probed. Vertically aligned DOMs are on the closest string below and above the source such that they approximately align with the vertical anisotropy axis. In Figure 5.16 and Figure 5.17, the expected and observed waveforms of the same simulated cascade as above are shown for these nearby DOMs. It can be seen that not only the observed charge but also the time profile of the waveform are correctly described for an ice model with anisotropy and local tilt through the combined use of the cascade photo spline table and the effective distance spline table. The waveforms of the vertical DOMs also illustrate how the difference between ice models is most pronounced in the horizontal plane (DOMs 36-29 and 36-30) due to the horizontal anisotropy axes. The difference is also evident towards the vertical plane (DOMs 36-27 and 36-32) due to the vertical anisotropy axis pointing along the z-axis.

It can be concluded that the presented method of incorporating the ice anisotropy and the local ice tilt into reconstruction is successful and consistent within all tests that have been performed by comparing waveforms and expected charge and delay time distributions. The new method will be discussed in the following section with respect to double cascade event reconstruction and tau-neutrino identification, as the application for which it was originally intended. A closing remark is that the ice anisotropy is properly described everywhere as it depends only on the direction and not on the position in the ice. As discussed in Section 5.2.1, however, the global ice tilt is not included as it depends on the position in the ice, and the effective distance $r_{\text{eff}}(r, \phi, \theta, z)$ is only parametrized for sources along the z-axis. Consequently, the description of the ice tilt is increasingly inaccurate the farther away a source is from the z-axis. This is not a strong effect and not important for tau-neutrino identification. However, the description of the ice tilt can be improved by introducing an *effective depth* (z-shift), similar to the effective distance for the ice anisotropy. The effective depth would be a global correction, as it depends on the position (x, y, z) in the ice and not on the direction. Due to time restraints, this remains outside the scope of this thesis, but is a proposed future task for the IceCube collaboration.

5.2.4 Double Cascade Reconstruction and Identification

In the previous section, the implementation of the effective distance parametrization was presented as a measure to incorporate the ice anisotropy into reconstruction algorithms. The `millipede`-framework used for event reconstruction in the context of this thesis is based on cascade photo spline tables and applicable for the combined usage with effective distance spline tables. The method has been tested by comparing the expected and observed light patterns and waveforms for different ice models in a controlled test environment. In this section, the application of the effective distance parametrization is tested on a reconstructed subset of realistic neutrino simulation data. The focus is on double cascade event reconstruction and how sensitive the related observables used for tau-neutrino identification are to the ice anisotropy.

The test is conducted with different combinations of ice models used in simulation and in reconstruction. The following cases are compared:

1. **SPICEMie-SPICEMie:** simulation with SPICEMie, reconstruction with SPICEMie,
2. **SPICELea-SPICEMie:** simulation with SPICELea, reconstruction with SPICEMie,
3. **SPICELea-SPICELea:** simulation with SPICELea, reconstruction with SPICELea.

Note that the SPICEMie-SPICEMie case is only used as a cross-check and cannot be used as a reasonable baseline comparison. This is due to the different type of simulation generation as the SPICEMie simulation data samples are much older than the SPICELea data samples. They

were generated using a *hybrid mode* of the photon propagation software `CLSIM`. In this mode, cascades (unlike tracks) are not simulated by direct photon propagation but rather by looking up the expected waveforms in a photo spline table. As discussed in Section 5.2.1, this necessarily means that the ice model used for hybrid simulation did not include the ice tilt.[3] A side effect of this type of simulation is that both measured waveform (simulation) and expected waveform (reconstruction) are sampled from exactly the same probability density functions (PDF). This deviation is important as DOMs are assumed as point-like in photo spline tables which may introduce a small bias for simulation using direct photon propagation (c.f. Figure 5.14). This deviation is important as the cascade vertex resolution is a limiting factor in reducing the single cascade background of the double cascade topology at very short decay lengths. Consequently, the SPICEMie-SPICEMie case corresponds to the best possible scenario, as events are simulated and reconstructed through the use of the exact same photo spline tables. In contrast, the newer SPICELea simulation data samples have been generated using direct photon propagation for all light sources. The extension of the DOM and the ice anisotropy and tilt have been taken into account. It follows that the SPICEMie-SPICEMie and SPICELea-SPICELea cases should only be used for a qualitative comparison of the expected differences due to the ice model. Note that due to the more realistic description, only results that are based on SPICELea simulation are used in the analysis presented in this thesis. The comparison of SPICELea-SPICEMie and SPICELea-SPICELea is essential for testing how big the effect of the ice anisotropy is in reconstruction and how well it is compensated using the effective distance parametrization.

In Figure 5.18, the effect of the ice anisotropy on the reconstructed double cascade length is shown. The **median length bias** $L_{\text{reco}} - L_{\text{true}}$ is depicted as a function of the zenith and azimuth angle for each of the three ice model combinations. There is no bias expected for a well-performing reconstruction algorithm with correct assumptions about the light sources and the ice model. In particular, a potential bias should not depend on the propagation direction of the source, unless there are asymmetries in the ice that are dependent on direction and not modeled correctly in the event reconstruction. That is exactly what is seen for the SPICELea-SPICEMie case in both plots of Figure 5.18. It is clearly visible that the length bias increases towards a zenith angle of 90° as the ice anisotropy is maximal in the horizontal plane. The length bias as a function of the azimuth angle also shows a striking dependence as it increases along the major anisotropy axis at 126° and 306° and decreases along the minor anisotropy axis at 36° and 216°. The effect can be understood by picturing an exemplary double cascade event aligned with the major anisotropy axis and located between two strings. The photons from both light sources are propagated assuming the SPICELea ice model including the anisotropy. The observed waveforms are obtained from the sum of all detected photons at each DOM behind and in front of the double cascade. For the event reconstruction, a double cascade topology is hypothesized, and its parameters are varied until the observed and fitted waveforms match. In this case, however, the waveform templates used for the fit are taken from a photo spline table without ice anisotropy. This means that the observed charge at the DOM from the second cascade in forward direction using the SPICELea ice model is larger than expected using the SPICEMie ice model, because light scattering in that direction is 8% smaller. If the reconstruction algorithm has the freedom to move the cascade, it shifts the vertex closer to the DOM to scale the expected charge up. As the effect is similar for the first cascade and the DOM behind it[4], the intermediate distance is decreased. Consequently, the reconstruction algorithm compensates the unknown effect of the ice anisotropy by its available freedom to increase the length. Hence, the length bias is positive along the major anisotropy axis as observed in the

[3] The ice anisotropy is not part of the SPICEMie ice model, as it was only introduced with SPICELea.

[4] Note that this case is more complicated, because a larger scattering coefficient is necessary in order to increase the probability of photons being back-scattered. As the photon path to the region behind the first cascade leads around the minor anisotropy axis with 4% larger scattering, the back-scattering of photons is actually enhanced.

distribution for the azimuth angle 126° and 306°. Evidently, this is a simplified example. The combined effect of both anisotropy axes in the horizontal plane and the resulting change of all waveforms observed at all DOMs around the source are responsible for the bias. Note the striking difference of the distribution for the SPICELea-SPICELea case. The direction-dependent length bias completely vanishes with the incorporation of the ice anisotropy into reconstruction using the effective distance parametrization. This is also consistent with a flat length bias as expected from the SPICEMie-SPICEMie case. It can be seen, however, that a small constant bias remains in both cases. It is reasonably explained by double cascade events with a short decay length, where the two shower maxima are not fully resolvable and a small bias is introduced as the second cascade tends to be more energetic (c.f. Section 4.3.1).

A similar effect as the length bias is visible in Figure 5.19, where the **misidentification fraction** is shown as a function of the zenith and azimuth angle. It visibly increases towards the horizontal plane and along the anisotropy axes. This dependence is expected, as the misidentification fraction strongly correlates with the length bias. A variation of the reconstructed length around the threshold of 10 m causes the event topology ID to switch between single and double cascade events (c.f. Section 4.3.2). Note that the variation of the event topology ID due to the ice anisotropy is only determined by the length bias and not by the energy confinement or energy asymmetry. This is due to the construction of these topology estimators as a ratio of reconstructed energies. Such a ratio is less susceptible to variations of the ice properties, as the effect cancels if all reconstructed energies are equally affected. The ice anisotropy, if treated incorrectly in reconstruction, is significantly compensated by the length bias. This causes the reconstructed energies, and hence the energy confinement and energy asymmetry used to define the event topology ID, to remain unchanged. Note that the energy asymmetry would indeed show a bias to compensate the effect of the ice anisotropy if the length were fixed in the reconstruction. Again, it is clearly visible how the misidentification fraction is independent of the source direction for the SPICELea-SPICELea case, which includes the ice anisotropy in reconstruction. As mentioned initially, a comparison to the SPICEMie-SPICEMie case is not applicable, as the events are simulated under simplified assumptions which cause the misidentification fraction to be unrealistically low.

It can be concluded that the length of the double cascade reconstruction is very sensitive to the ice anisotropy. If not treated correctly, the reconstruction algorithm introduces a length bias to compensate the skew of the observable light pattern due to the ice anisotropy. It has been shown that the incorporation of the ice anisotropy into reconstruction using the effective distance parametrization also works for realistic neutrino simulation. The correct treatment of the ice anisotropy is significant, as it translates into an increase of the misidentification fraction in the reconstructed double cascade sample. Note that the described method does not include any uncertainty of the size of the ice anisotropy itself. This uncertainty is parametrized with respect to the length bias and included as a nuisance parameter into the likelihood-based measurement of the astrophysical neutrino flavor composition, as described in Appendix A. Also note that all results have been obtained using simulation data, as it is not trivial to test the method using experimental data. An attempt to test the method and probe the uncertainty of the ice anisotropy using experimental flasher LED data will be presented in the next section.

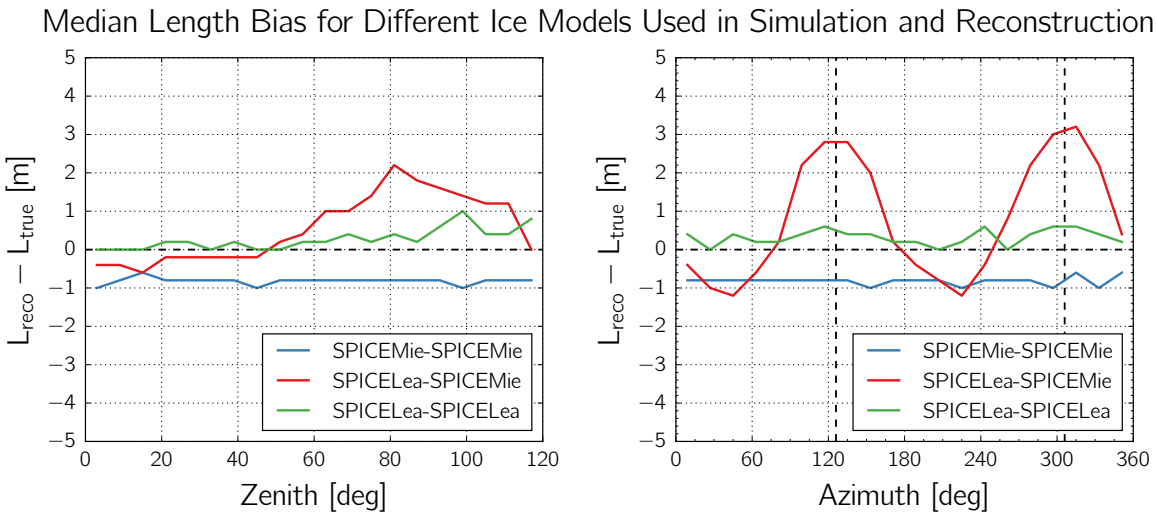

Figure 5.18: Median length bias of reconstructed double cascade events depicted as a function of the reconstructed zenith (left) and azimuth angle (right) for different ice model combinations in simulation and reconstruction. It is shown for successfully identified true double cascade events induced by astrophysical tau-neutrinos assuming an $E_\nu^{-2.3}$ spectrum. The vertical dashed lines in the right plot indicate the direction of the major anisotropy axis.

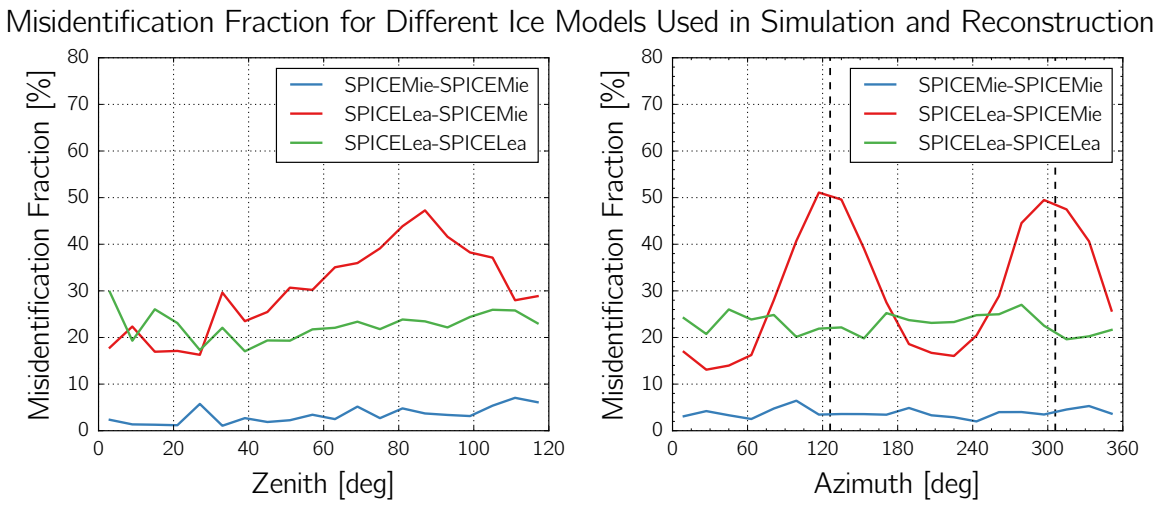

Figure 5.19: Misidentification fraction of reconstructed double cascade events as a function of the reconstructed zenith (left) and azimuth angle (right) for different ice model combinations in simulation and reconstruction. It is calculated via background/(signal+background). As described in Chapter 4, signal is defined as true double cascade events induced by astrophysical tau-neutrinos, assuming an $E_\nu^{-2.3}$ spectrum. In this context, however, background corresponds to the dominant contribution of true single cascade events induced by astrophysical neutrinos of the same spectrum.

5.3 Experimental Test with Flasher LED Data

The development of the double cascade reconstruction as described in Section 4.3 and the incorporation of the ice anisotropy as described in Section 5.2 can be considered successful as tau-neutrino identification performs well and an important systematic error is treated properly. However, there is a drawback in that all methods could only be tested using Monte Carlo methods. Experimentally testing an event topology that has never been observed before is challenging. It seems natural to test the double cascade topology using experimental flasher LED data, i.e. the in-situ calibration system of IceCube (c.f. Section 3.2.2). The idea is to generate a light flash from a single LED on one string and a subsequent flash from another on a neighboring string. The light flashes must be aligned with the propagation direction of a hypothetical tau and delayed by the time it would take from one string to the other, assuming that it travels at the speed of light. Unfortunately, the realization of this idea is not trivial. It is impossible to generate these double flasher events experimentally, because the driving current of flasher LEDs cannot be timed accurately enough to generate two subsequent flashes with the correct time delay.[5] However, it is possible to superimpose two suitable single flasher events to artificially construct an experimental double flasher event. Although flasher events have a few limitations in general, and conclusions are not easily transferable to tau-neutrino identification, this construction of a double flasher event is the only possibility of testing the newly developed reconstruction methods using experimental data. Hence, this is an important test before the double cascade event reconstruction is applied for an attempted measurement of the astrophysical tau-neutrino flux.

5.3.1 Single Flasher LED Anisotropy Data Sample

In January 2015, a high-quality calibration data sample of numerous **single flasher LED** events was collected to specifically study the ice anisotropy. A total of five flasher runs divided into 481 sub-runs each with different flasher locations, directions, and settings were performed for approximately 28 hours. The same detector configuration as for physics runs with the standard IceCube SMT-8 trigger was used (c.f. Section 3.2.3). The decision of which LEDs and DOMs to select for the purpose of studying the ice anisotropy was based on a few **requirements**:

1. flashing LEDs should have a consistent light output and no known instabilities,
2. flashing LEDs should be equally surrounded by receiving DOMs,
3. flashing LEDs should be evenly distributed throughout the detector,
4. flashing LEDs should not be located in the dust layer,
5. flashing LEDs should have a well-known direction,
6. the same LED should be configured with multiple flash durations,
7. the same configuration should be repeated many times.

The first requirement is to ensure a minimum quality of the generated light output. In order to study the optical properties of the ice, it is important to minimize the systematic variation of similar LEDs as the uncertainties of the generated and detected light patterns are entangled with the properties of the LEDs and the ice, respectively. The second requirement means that the position of a flashing DOM should not be at or near a detector edge. This is to ensure that enough data observed in all directions around the light source is available. Because the ice

[5] In fact, flasher data is typically taken by randomly flashing multiple DOMs in the same time window but at different locations. As long as the flasher rate is low enough (usually a few Hz), individual flasher events do not overlap, even if not explicitly timed to do so.

anisotropy is only modeled to be dependent on the direction but not on the depth, the third requirement allows a test of this assumption through the use of flasher LEDs that are evenly distributed throughout the detector. The fourth requirement is to ensure a large enough light yield per flasher event. Because the dust layer heavily absorbs light, flasher LEDs are required to not be located in the dust layer. Furthermore, during the deployment, strings are free to twist, causing each DOM to be arbitrarily rotated with respect to the z-axis of the detector. The DOM rotation is negligible with respect to detecting light, since the angular acceptance of the PMT is azimuthally symmetric (except for the cable shadow). However, the flasher LEDs are located at fixed positions on each DOM and, consequently, point in different directions depending on its rotation. Each DOM can be configured to flash LEDs simultaneously or individually as depicted in Figure 5.20. Hence, the fifth requirement is that the flasher LEDs should have a well-known direction, because any directional study of the ice is useless otherwise. The sixth requirement is an attempt to minimize the experimental uncertainty of a single LED, because the light output is only known statistically but not for individual LEDs. Therefore, the same LED is configured to flash for different durations as the comparison of the observed results is useful for constraining the uncertainties of individual LEDs. The last requirement is necessary in order to generate enough data for one flasher configuration that the statistical error of the observed waveforms is low enough to study the ice properties.

A selection of flashing DOMs that fulfill all necessary requirements was obtained from an all purpose flasher data sample collected over 20 hours in 2012. It contains differently configured flasher events located on six strings and 60 DOMs each. As marked in Figure 5.21, the flashing DOMs are located on strings 19, 24, 57, 62, 80, and 81. This data sample provides numerous single LED flasher events which were used to determine the rotation of each flashing DOM. A total of 73 out of 360 available DOMs were selected for the **anisotropy flasher data sample** using the aforementioned requirements on the basis of the available information. The list of selected DOMs including their rotation is given in Appendix B. Each of those DOMs was configured to flash all six horizontal LEDs simultaneously and, in addition, each LED individually. Furthermore, every LED configuration was used for two flash durations of 10 ns and 70 ns. All LEDs were configured to flash at the maximum available brightness which corresponds to an approximate light output of $1.97 \cdot 10^9$ photons for a 10 ns pulse and $1.17 \cdot 10^{10}$ photons for a 70 ns pulse as determined from laboratory measurements [42]. This gives a total of 1022 flasher configurations (73 DOMs $\times$ 7 LED configurations $\times$ 2 flash durations). About five to six flashing DOMs are run simultaneously on different strings without overlapping in time at a rate of 3 Hz for a total duration of $\sim$ 7 min. This corresponds to $\sim$ 1000 events per flasher configuration.

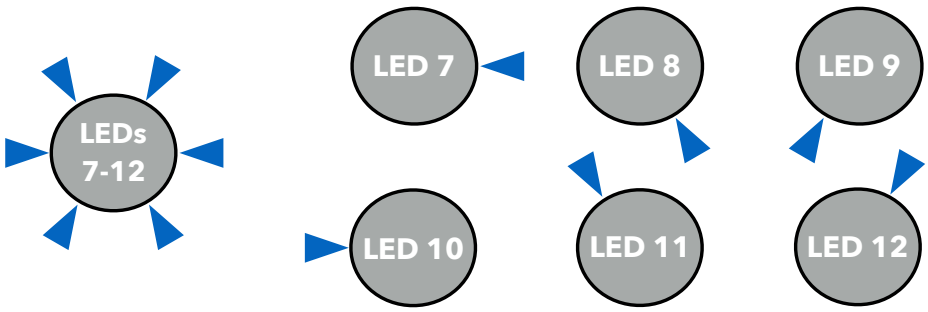

Figure 5.20: Sketch of the different horizontal LEDs and flashing modes used for the anisotropy flasher data sample. DOMs are sketched from the top view, i.e. the z-axis of the detector coordinate system is pointing out of the figure. LED 7 would ideally be aligned with the x-axis, however, during deployment strings are twisted causing the DOM to have an arbitrary horizontal rotation. Individual LEDs are spaced 60° apart, so the directions of all LEDs align periodically with every 60° a DOM is rotated.

5.3.2 Construction of an Experimental Double Flasher

It is impossible to generate a double flasher event experimentally, due to technical limitations of the detector operation. However, a novel method has been developed in the scope of this thesis by artificially constructing such an event through the **superposition of single flasher events**. The approach is to find a pair of independently flashing single LEDs on neighboring strings. The direction of the LEDs must align with the axis that connects both strings. This axis corresponds to the propagation direction of a hypothetical tau traveling from one flasher LED to the other. The individual single flasher events are then superimposed by delaying the second event by the propagation time of the hypothetical tau, assuming that it travels at the speed of light.

The direction of each LED must be known as precisely as possible, because the light emission profile is very narrow (c.f. Section 3.2.2). If the deployed LEDs were able to emit light isotropically, the choice of LED on each DOM would not be important. Because their light emission is beamed, however, the direction of both LEDs must match and they must align with the axis that connects both DOMs. As there are only horizontal and upward tilted LEDs, the possible phase space of double flasher events is limited to two zenith angles at 90° for horizontal and 42° for upward tilted flashers. The azimuth angle is restricted by the string alignment to approximately 11°, 69°, 127°, 188°, 250°, and 311° when flashing LEDs on IceCube DOMs. For horizontal flasher LEDs, both DOMs on neighboring strings must be at the same depth, and for tilted flasher LEDs, the second flashing DOM must be $\sim 112\,\mathrm{m}$ above the first, considering an average string distance of $\sim 125\,\mathrm{m}$. As the vertical spacing between DOMs is 17 m and there is only little variation in depth of same numbered DOMs on different strings, the closest DOMs on the next string would be 10 m below or 7 m above the required depth. Therefore, the construction of a double flasher using tilted LEDs is not applicable.[6]

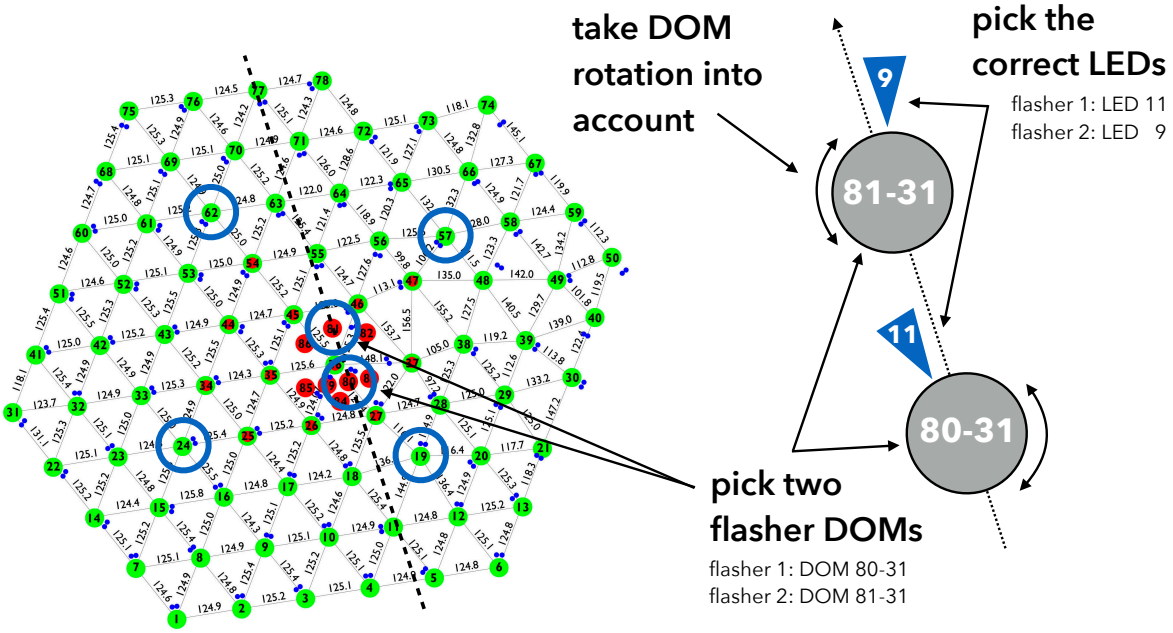

Figure 5.21: Location of selected flasher DOMs in the detector and sketch of the constructed double flasher event. The direction of each LED must be aligned with the connecting axis of the flashing DOM pair, as it corresponds to the propagation direction of a hypothetical tau.

[6] Although a larger phase space would be useful, the construction of double flasher events with horizontal LEDs is more important, as the examinable effect of the ice anisotropy is maximal in the horizontal plane.

The anisotropy flasher data sample as described in the previous section is well suited for the purpose of artificially constructing double flasher events. It contains numerous single flasher events with stable light output, accurately known directions, and different locations in the detector. Unfortunately, out of the 73 available flashing DOMs on six strings, there is only one pair that meets all requirements. That selected pair is DOM 81-31 and DOM 80-31 (see Figure 5.21), which are located at a depth of $z \simeq -300\,\mathrm{m}$. The difference in depth between both flashing DOMs is approximately 2 m, and the location is well below the dust layer. The phase difference of the DOM rotations is approximately 10° and each LED has a maximum deviation from the axis connecting the two strings of no more than 10° (one LED slightly points to the left and the other to the right of the connecting axis). Note that finding one matching pair of LEDs implies that there is another matching pair in the opposite direction due to the circular pattern of LEDs on each DOM with a spacing of 60°. Therefore, the selected DOM pair has a total of four matching horizontal LEDs that allows the construction of two opposite double flasher events which are called (A) and (B), as sketched in Figure 5.22. While **event (A)** is defined via DOM 80-31 with LED 11 as a first flasher and DOM 81-31 with LED 9 as second flasher, **event (B)** is defined via DOM 81-31 with LED 12 as first flasher and DOM 80-31 with LED 8 as second flasher. Each double flasher event has a zenith angle of $\sim 90°$ and an azimuth angle of $\sim 287°$ and $\sim 107°$, respectively. The distance between the two strings is $L \simeq 107\,\mathrm{m}$ which corresponds to the "length" of the double flasher.

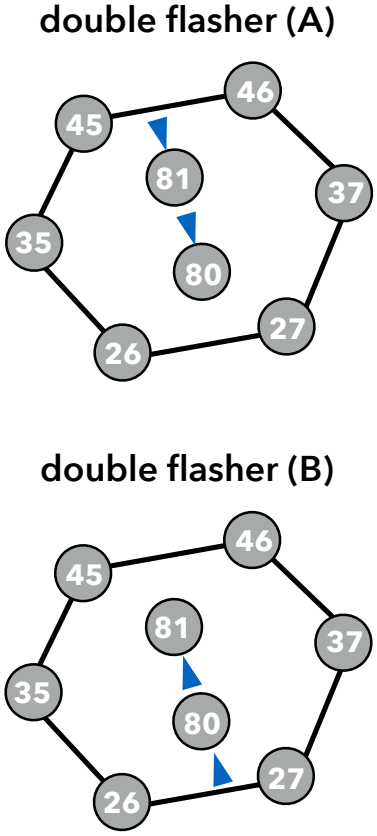

Figure 5.22: Sketch of two double flashers located on DeepCore and surrounded by IceCube strings.

Note that both DOMs are located on DeepCore strings, which has two advantages. First, the distance between both flasher strings is slightly shorter than the average spacing of 125 m between IceCube strings. A more realistic phase space of the reconstructed length can therefore be tested as shorter decay lengths of a tau are naturally more frequent. Second, the distance between flashing and receiving DOMs is more suitable, because events are more likely to start between strings. As DeepCore strings are located in between IceCube strings (c.f. Figure 5.21), the closest distance between flashing DeepCore DOMs and receiving IceCube DOMs is about half the average spacing between IceCube strings. An average event would not be well represented if both flashing and receiving DOMs were located on IceCube strings. Receiving DeepCore DOMs are completely excluded, in particular for the event reconstruction, as will be described in the next section. Otherwise, the results would be distorted, because the distance between flashing and receiving DeepCore DOMs would be too small to reflect a typical event in IceCube.

The **construction of a double flasher event** is realized using the following steps:

1. calibrate waveforms and deconvolve pulses separately for both single flasher events,
2. shift the pulses from the second flasher by the time a hypothetical tau would take from one string to the other, i.e. by $\Delta t = L/c \simeq 357\,\mathrm{ns}$,
3. add the delayed pulses from the second flasher event on top of the pulses of the first flasher event to obtain superimposed waveforms for all receiving DOMs,
4. rebin the superimposed pulses to match the original single flasher calibration.

Furthermore, the joint set of "bad" DOMs and the combined amount of noise is taken into consideration for the following event reconstruction. An experimental double flasher event artificially constructed via this scheme using DOM 81-31 and DOM 80-31 is shown in Figure 5.23. As mentioned above, DeepCore DOMs are excluded from the **visualized hit pattern**, which looks slightly more elongated than a single flasher event might suggest. Two gray spheres indicate wavefronts of (isotropic) unscattered light originating at the time and position of each flasher. It is striking that the latest hits on the far right of the event view cannot be causally connected to the first flasher, as this implies that the emitted photons would have traveled faster than the speed of light in ice. In fact, the first hits at these DOMs are caused by unscattered photons from the second flasher as their arrival time perfectly matches the through-going wavefront.

After thorough consideration, no reason has been identified as to why the artificial superposition of experimental single flasher events should not be a **reasonable representation of an experimental double flasher event**. Only one issue might bias the result in the case where light of each single flashing DOM individually causes the PMTs of neighboring DOMs to nearly go into saturation. The artificial construction using the superimposed waveforms would overestimate the available information as a real double flasher event would probably cause the affected PMTs to saturate. In order to check whether this effect is observable, double flasher events are also simulated using two approaches. First, a double flasher is simulated in a direct way, where two LEDs consecutively flash within one triggered event. Second, the artificial construction is repeated for two simulated single flasher events. The two different simulation methods can thereby be compared with each other to conclude whether saturation plays a role for the superposition of individual waveforms. This check depends on a precise model of the PMT linearity and saturation which is incorporated in simulation [223]. An additional cross-check is to compare the simulated waveforms to the experimentally collected waveforms.

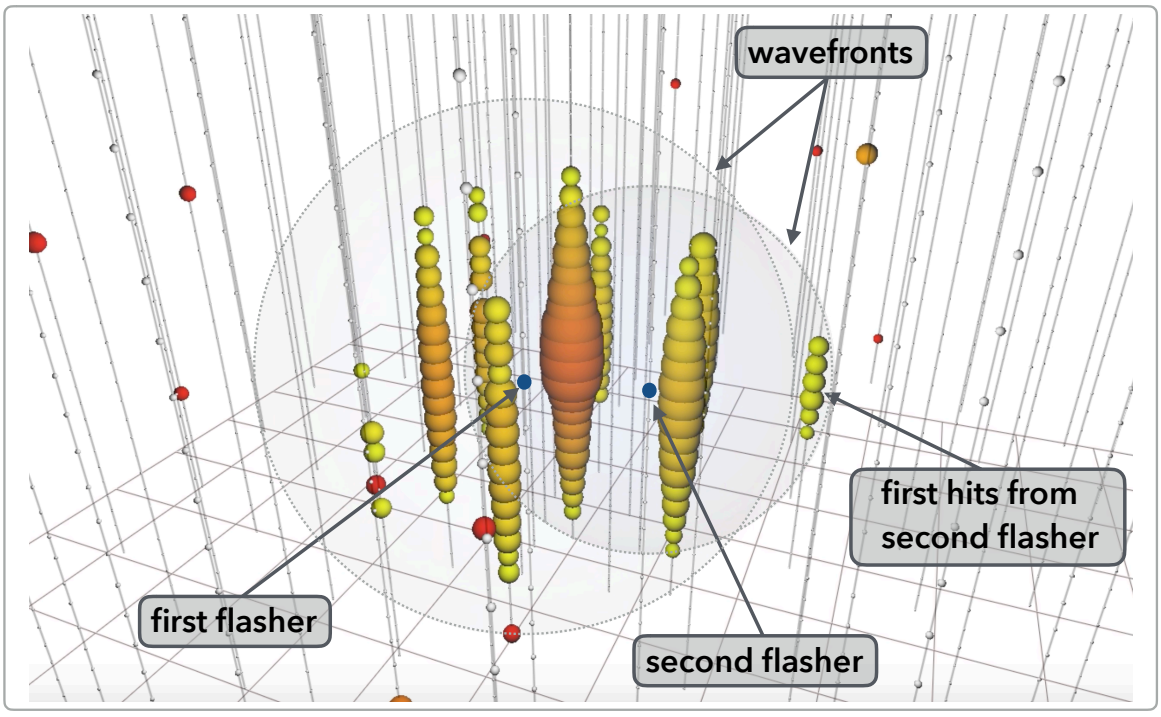

Figure 5.23: Event view of an artificially constructed double flasher using experimental single flasher events. Only triggered IceCube DOMs are shown as DeepCore DOMs are excluded. The dashed lines around two gray spheres indicate wavefronts of isotropically emitted unscattered light originating at the time and position of each marked flasher LED. The triggered DOMs marked on the right can only be causally connected to the second flasher, as photons from the first flasher would otherwise be faster than the speed of light in ice.

In Figure 5.24 and Figure 5.25, the **waveforms of receiving IceCube DOMs** on surrounding strings at approximately the same depth as the light emission are shown for the double flasher events (A) and (B), respectively. Waveforms are depicted for experimental data and for the two aforementioned simulation modes. In general, the amplitude and shape of each waveform is consistent with two successive LED flashes in the same direction. As expected, the largest amount of light is collected on strings 45 and 46 for double flasher event (A) and on strings 26 and 27 for double flasher event (B) in the opposite direction (c.f. Figure 5.22). The waveforms of these DOMs also have the most pronounced peak of the arrival time distribution, as expected for a large fraction of photons which are only scattered a few times before detection.

Waveforms on strings 35 and 37, which are approximately orthogonal to the direction of each double flasher event, have an interesting feature. In these waveforms, a **double pulse structure** is clearly visible and indicates that the reconstruction of double flashers should be possible. In fact, the depicted waveforms clearly illustrate for this particular case that the double cascade method is expected to work much better than the double pulse method (c.f. Section 4.1). The phase space for a double pulse waveform to be visible is rather small, as can be seen by comparing the waveforms of all six receiving DOMs. However, waveforms without a double pulse structure still carry valuable information about the underlying light sources as the leading edge constrains the vertex of the brighter LED (c.f. Figure 5.23). Keep in mind that the depicted waveforms are averaged over ~ 1000 events. Hence, waveforms of individual events have significantly less information and greater fluctuations of the detected light yield.

The time difference between two peaks of a double pulse waveform varies between 350 ns to 650 ns, as expected from the delay time between both flashes and from the light scattering between each flashing LED and receiving DOM. The central position of each of those visible double pulses can be shifted slightly in simulation data compared to experimental data. This is due to the uncertainty of the LED direction that can significantly change the shape of the waveform at a receiver DOM in the forward scattering region due to the narrow emission profile of a flasher LED. The discrepancy of the amplitude between experimental and simulation data of some waveforms is due to large experimental uncertainties of flasher events (see below). It is the same for single flasher events and consequently does not pose an obstacle to the artificial construction of double flasher events. In this respect, the comparison of waveforms obtained from direct and combined simulations is more interesting. Apart from slight deviations in the long tails of two waveforms, both simulation modes yield similar results. Hence, there is no indication that PMT saturation is a problem.

	Single Flasher	**Single Cascade**
Light Source	LED	particle shower
Spatial Profile	point-like	$\sim 2\,\text{m} \ldots 6\,\text{m}$
Time Profile	$\sim 6\,\text{ns}$ (+after − glow) $\ldots 70\,\text{ns}$	$\sim 5\,\text{ns} \ldots 20\,\text{ns}$
Wavelength Profile	delta profile at $\sim 405\,\text{nm}$	Cherenkov profile $\sim \lambda^{-2}$
Angular Profile	Gaussian profile with FWHM $\simeq 30°$	Cherenkov cone with opening angle $\simeq 82°$

	Double Flasher	**Double Cascade**
Phase Space	fixed at $L = 107\,\text{m}$ and $E = 22\,\text{TeV}, 136\,\text{TeV}$	continuous decay law with $L \simeq 50\,\text{m} \cdot E/\text{PeV}$

Table 5.1: Comparison of flasher and cascade light sources as building blocks of the double flasher and double cascade event topologies.

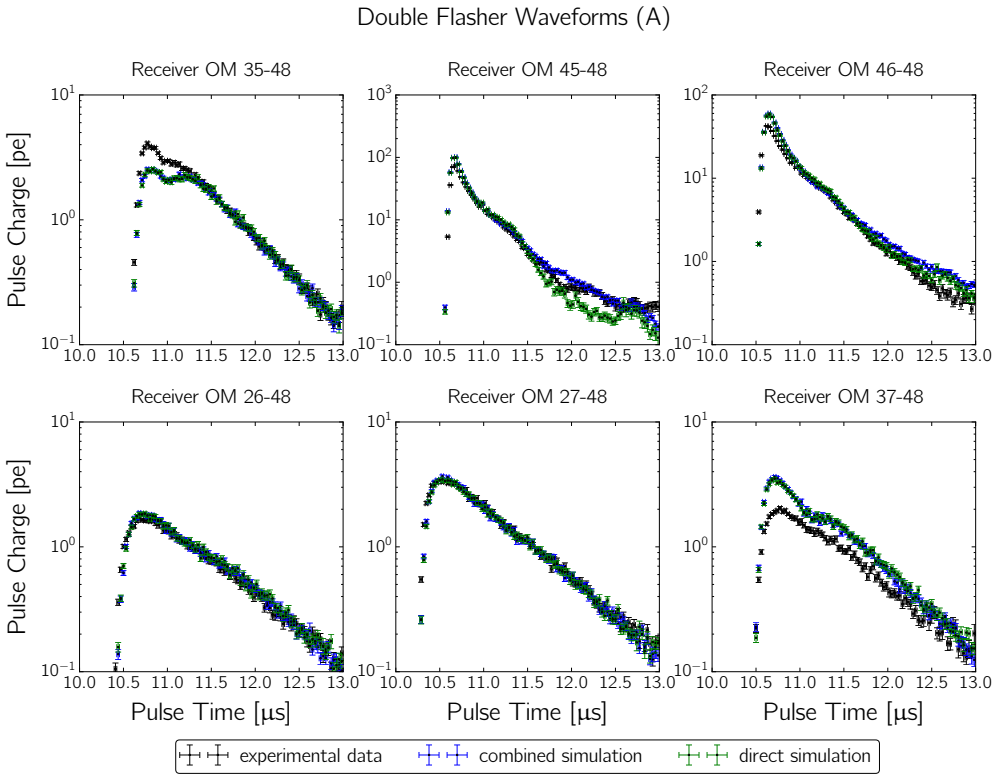

Figure 5.24: Averaged waveforms of the double flasher event (A) at surrounding IceCube DOMs at the same depth as the flasher LEDs. The observed charge is depicted as a function of the detection time for experimental data, combined simulation and direct simulation as described in the text. The receiving DOMs are selected as sketched in Figure 5.22. The waveforms are averaged over $\sim$1000 events, and the error bars represent the statistical error.

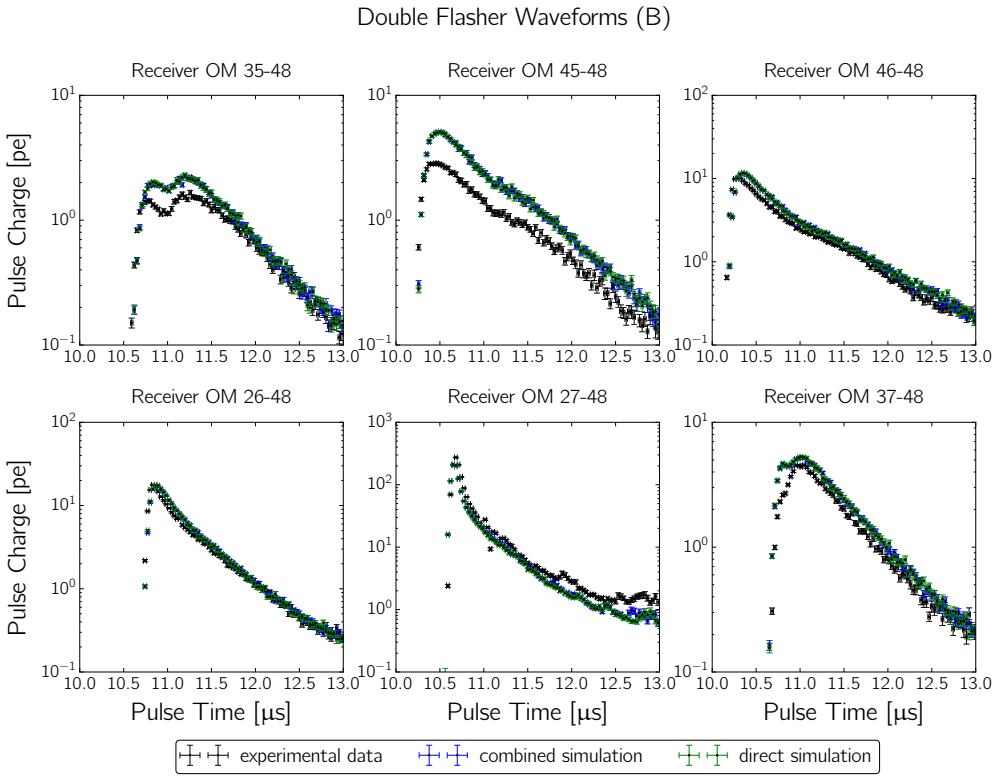

Figure 5.25: Same as in Figure 5.24, but for double flasher event (B).

Consequently, the artificial construction of a double flasher event can be reasonably used in order to test the double cascade event reconstruction with experimental data. Before testing the reconstruction of these double flasher events using the double cascade reconstruction method, there are two caveats that must be addressed. First, the comparison between cascades and flashers is not trivial. Second, flasher LEDs have large experimental uncertainties.

Regarding the first issue, a general **comparison between flashers and cascades** is summarized in Table 5.1. Each light source is very different, in particular and most importantly the angular emission profile. A flasher LED has a two-dimensional Gaussian emission profile with a FWHM of $\sim 30^\circ$ with respect to the forward direction of an LED in ice (c.f. Section 3.2.2). A particle shower emits light at the Cherenkov angle of $\sim 41^\circ$, which corresponds to an opening angle of $\sim 82^\circ$ with respect to the light cone in forward direction (c.f. Section 3.1.4). The emission profile of an LED is therefore much more narrow and beamed compared to a cascade. The emitted wavelength profile is also very different, as an LED is monochromatic at a wavelength of $\sim 405\,\mathrm{nm}$ and the wavelength profile of a cascade is given by a λ^{-2} spectrum. However, the difference is less important, as the detected wavelength profile is folded with the PMT acceptance which ranges from 300 nm to 650 nm and peaks around 390 nm. The spatial profile of a cascade is usually only approximated as point-like, but evidently has an extension parametrized by the shower profile (c.f. Section 3.1.3), whereas an LED is in fact point-like. If the shower parametrization of a cascade is used to define an equivalent of a FWHM, a spatial profile would be in the range of 2 m to 6 m. This directly corresponds to the time profile of a cascade which would approximate to a range of 5 ns to 20 ns. In contrast, the time profile of a flashing LED is much longer. The shortest possible light flash is 6 ns with a dim after-glow at the time scale of 10 ns to 20 ns. The longest possible light flash is 70 ns with a negligible after-glow. The vast difference of the time profile is important, because the reconstructed event hypothesis of either a single cascade or flasher is assumed to be point-like in space and time. A cascade can easily be approximated to be point-like in both space and time, however, a flasher LED is point-like in space but far from point-like in time. This can significantly decrease the reconstruction result as the leading edge of the observed waveforms becomes rather wide. Note, however, that event reconstruction is based on photo spline tables which can be generated for any light source (c.f. Section 5.2.1). Therefore, a set of photo spline tables has been generated in the scope of this thesis for single flasher events with a short flash duration of 10 ns and a long flash duration of 70 ns, specifically to reconstruct the experimental flasher events collected for the anisotropy flasher data sample. Another important issue of the comparison between double flasher and double cascade events is the accessible phase space. The constructed double flasher event is very limited, because the length is fixed by the string distance of $\sim 107\,\mathrm{m}$ and the energy fixed by the total light output of the LEDs at $\sim 22\,\mathrm{TeV}$ for the 10 ns pulses and $\sim 136\,\mathrm{TeV}$ for the 70 ns pulses. In contrast, the phase space of double cascade events is continuous, with the average decay length of the tau scaling with its energy $L \simeq 50\,\mathrm{m} \cdot E/\mathrm{PeV}$. Therefore, the goal cannot be to test the physical region where a tau-neutrino interaction is expected, unfortunately, but to test the performance and reliability of the double cascade event reconstruction using experimental flasher data for a specific configuration.

Regarding the second issue, it is important to keep in mind that flasher events have large **experimental uncertainties**, in particular

- the quoted light output of an LED is an average over many measurements in the laboratory with an uncertainty of $\sim 30\%$,
- although the cable of a DOM cannot affect the light output, because it is fixed between two LEDs, it may alter the detected light by covering the PMT of receiving DOMs,
- the angular emission profile of an LED may deviate significantly from the measurement in laboratory ice, because it is changed by *hole ice* surrounding the flashing DOM,

- the DOM rotation in the ice is generally not known with great precision, nor are the exact orientation and placement of each LED (for well-known LED directions, an average error of $\sim 5^\circ$ is expected),
- the measured time profile of an LED also may deviate significantly from the quoted average (in particular, the after-glow for short flash durations is not well described).

All of these uncertainties can explain deviations between experimental and simulated waveforms as observed in Figure 5.24 and Figure 5.25. Note that most of the quoted uncertainties have an entangled effect on the observable waveforms. In particular, *hole ice* can be a problem for flashing DOMs. It is the part of the ice where holes were drilled with hot water to deploy the strings. The refreezing of the hole encloses a larger amount of air bubbles than the surrounding bulk ice. Although the hole ice is modeled in simulation for receiving DOMs (the angular acceptance profile of the PMT is modulated to account for this effect), it is not modeled for the light emission of a flasher LED. However, it can in principle cause the angular emission profile to spread dramatically and therefore redistribute the observable light pattern at surrounding strings. A similar effect is caused by an imprecisely known rotation of the DOM and consequently the direction of an LED. Furthermore, the after-glow of a flashing LED is also not simulated, as they are not described very well. Therefore, the effect of after-glow is expected to be much more significant for events with a short flashing duration (10 ns) compared to events with a long flashing duration (70 ns). Consequently, it is useful that each configuration is available for two different flasher durations and two opposing directions, as it is possible to estimate the effect of these systematic uncertainties on the reconstruction results.

5.3.3 Double Flasher Reconstruction and Identification

The main goal is to test the double cascade reconstruction method with experimental data to check if there are any systematic errors that are not considered in simulation. The reconstruction of the artificially constructed double flasher events is performed in the same way as described in Section 4.3. In particular, the same settings are applied, and the same set of DOMs are excluded (in particular bright DOMs and DeepCore DOMs). The only difference is that photo spline tables for flashers instead of cascades are used in order to account for the inherent differences in the light sources. Note that the effective distance parametrization is the same, because photo spline tables for both flashers and cascades are based on a spherical coordinate system. Consequently, the underlying ice model assumed in reconstruction includes the ice anisotropy and local effects of the ice tilt. The simulated double flasher events are generated assuming the same ice model with direct photon propagation. Note that the light emission of each LED is also simulated under realistic conditions, where the flashing LEDs are not perfectly aligned with the connecting axis between both strings but point slightly off axis.

	Length Bias		**Length Resolution**	
	Experimental	**Simulated**	**Experimental**	**Simulated**
Double Flasher (A), 10 ns	−4.0 m	−0.6 m	3.1 m	2.2 m
Double Flasher (B), 10 ns	−2.9 m	−0.3 m	3.1 m	2.5 m
Double Flasher (A), 70 ns	−2.0 m	+1.0 m	1.6 m	1.0 m
Double Flasher (B), 70 ns	−0.3 m	−0.1 m	1.3 m	1.3 m

Table 5.2: Reconstructed length bias and resolution of experimental and simulated double flasher events. The length bias corresponds to the central value μ and the resolution to the width σ of a Gaussian fit $f(L|\mu,\sigma) \sim \exp(-(L-\mu)^2/2\sigma^2)$ to the distributions shown in Figure 5.26.

In Figure 5.26, the **reconstructed length** of double flasher events (A) and (B) is shown separately for two different flasher durations 10 ns and 70 ns. Each distribution is based on $\sim$1000 experimental or simulated events and fitted with a Gaussian $f(L|\mu,\sigma) \sim \exp(-(L-\mu)^2/2\sigma^2)$. The central value μ translates to the bias $L_{\text{reco}} - L_{\text{true}}$ and compares to the expected length of 107 m. The width σ corresponds to the resolution of the reconstruction length around its central value. It can be seen that the double flasher length generally reconstructs well. The width of the distribution for the short flasher duration is wider than for the long flasher duration. This is expected, as the flasher events with a shorter pulse duration deposit less light in the detector. Furthermore, the distribution for simulated events is generally more narrow than for experimental events, because uncertainties of flasher LEDs are not modeled in simulation (see below). The fit values for the bias and resolution of each configuration are summarized in Table 5.2. The mean resolution is (2.3 ± 0.8) m for experimental data and (1.8 ± 0.6) m for simulation data. This is in agreement with a median resolution of approximately ± 2 m for double cascades, as presented in Section 4.3.3 using tau-neutrino simulation. The mean length bias is (0.0 ± 0.6) m for simulation data, which is consistent with the expectation that no bias should be observed if the same ice model is used for simulation and reconstruction. However, for experimental data, the mean length bias is (-2.3 ± 1.4) m. This is considered in greater detail in the following. In particular, the individual contributions of experimental flasher uncertainties and of ice anisotropy uncertainties to this bias are estimated.

As discussed in the previous section, there are different sources for **experimental uncertainties** of flasher events, such as the driving current of the LED (related to total light output and timing profile including after-glow for each LED), the position of the LED with respect to the hole ice (related to the emission profile of each LED), and the direction of both flasher LEDs with respect to the connecting axis of the two strings (related to both the emission and timing profile of the combined double flasher source). The latter effect of the deviating direction of a flasher LED with respect to the connecting axis of the two strings cannot be checked with the presented data. In principle, the dependence of the length bias on the angular deviation could be studied systematically for different DOM configurations in both simulated and experimental data. However, this task is beyond the scope of this thesis, but is in fact proposed as a future task for the IceCube collaboration. In contrast, the two former effects of the driving current and position of the LED with respect to the hole ice can be checked with the available data. The motivation for collecting experimental data using two different flasher durations (10 ns and 70 ns) and using LEDs pointing in opposite directions (double flasher events (A) and (B) as sketched in Figure 5.22) was to disentangle the uncertainty of the driving current from the uncertainty due to the position of the LED in the hole ice. Although such a disentanglement is certainly not trivial, the argument for an estimate is the following. On the one hand, a comparison of two flasher durations for the same LED leaves its position in the ice unchanged, and any variation of the observed waveforms and reconstructed length can therefore be attributed to the different driving currents of the LED. On the other hand, a comparison of two opposing LEDs with the same flasher duration approximately leaves the time profile of both LEDs unchanged, and any variation can therefore be attributed to the position of the LED in the hole ice.

A comparison of the length bias for two flasher durations of the same LEDs yields ± 1.0 m for double flasher event (A) and ± 1.3 m for event (B). Adding in quadrature, an estimated length bias of ± 1.6 m due to the uncertainty of the LED driving current is obtained. A comparison of the length bias for the two different double flasher events (A) and (B) with the same flasher durations yields ± 0.6 m for the 10 ns flashers and ± 0.8 m for the 70 ns flashers. Adding in quadrature, an estimated length bias of ± 1.0 m due to the uncertainty of the LED positions in the hole ice is obtained. Consequently, the combined error of the length bias due to experimental uncertainties of the flashers can be estimated to ± 1.9 m. Any remaining error source can most likely not be attributed to the flasher LEDs but rather to uncertainties of the ice model.

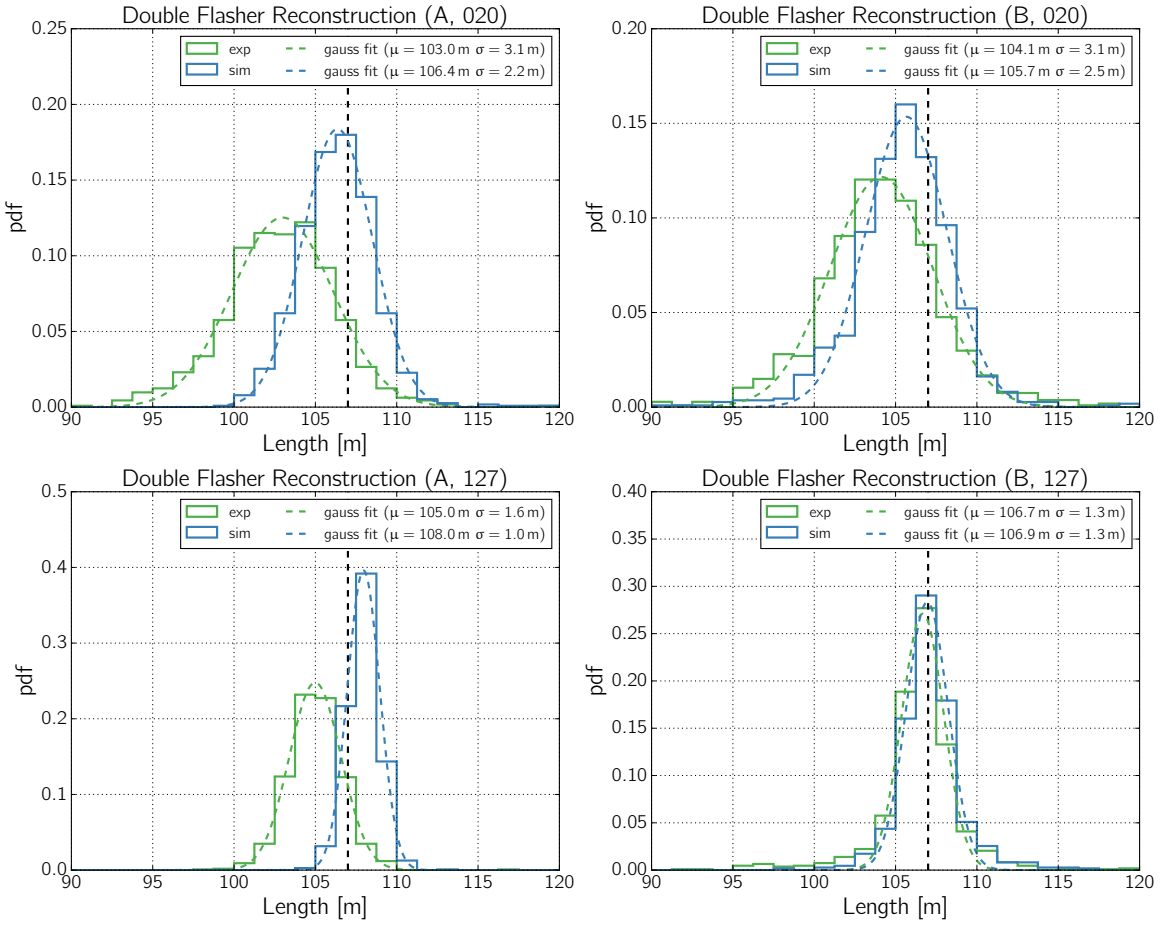

Figure 5.26: Reconstructed length for double flasher event (A) (left) and (B) (right) using a short flasher duration of 10 ns (top) and a long flasher duration of 70 ns (bottom). Distributions are shown for simulation and experimental data on the basis of ~ 1000 available events for each configuration. In addition, a Gaussian of the form $f(L|\mu,\sigma) \sim \exp(-(L-\mu)^2/2\sigma^2)$ is fitted to each distribution. The true length of 107 m is marked with a vertical dashed line.

As presented in Section 5.2.4, an imprecise knowledge of the ice anisotropy translates into a bias of the reconstructed length. Hence, the remaining observed bias in experimental double flashers is indicative of the **uncertainty of the ice anisotropy**. In fact, the size of the modulation of the scattering coefficient along the anisotropy axes has an estimated error of $\sim 30\%$. In Appendix A, the length bias due to this uncertainty of the ice anisotropy is parametrized as a function of the propagation direction of the tau and included in the analysis. Interpreting the $\sim 30\%$ uncertainty of the size of the ice anisotropy as a 1σ variation and using the parametrization for these double flasher events with a zenith angle of 90° and an azimuth angle of 107° and 287°, respectively, the expected length bias solely due to the ice model is $\pm 1.2\,\mathrm{m}$. Adding the uncertainty of the flasher LED obtained above and this ice model uncertainty in quadrature gives a length bias of $\pm 2.2\,\mathrm{m}$. This is in good agreement with the mean bias of $-2.3\,\mathrm{m}$ observed in experimental flasher data. A bias and resolution of the order of $\sim 2\,\mathrm{m}$ is consistent with simulation studies if experimental uncertainties of flasher LEDs and the ice anisotropy are considered. For the first time, the performance of the double cascade reconstruction method could be tested using experimental flasher data with the conclusion that there are no unmodeled systematic error sources that are more significant than the ice anisotropy. Although this is technically only true for this specific setup, it is expected to reveal the largest effect of the ice anisotropy, because events are used that approximately point along the major anisotropy axis.

Another test with experimental data is performed by creating a **binary topology ID** for single flasher and double flasher events that is similar to single cascade and double cascade events. The agreement between experimental data and simulation data can be tested by comparing flasher identification to tau-neutrino identification, as described in Section 4.3.2. Because only the light sources (flashers and cascades) are different and the reconstruction method is the same, the constructed double cascade observables can be applied in an equivalent way. Therefore, the reconstructed length and the reconstructed energy asymmetry are used to define a flasher identification aimed at distinguishing single flasher from double flasher events.

The **length and energy asymmetry distributions** are shown in Figure 5.27 separately for simulated and experimental single flasher and double flasher events. Here, both double flasher events (A) and (B) are combined into the double flasher distributions, and the underlying four different single flasher events are combined into the single flasher distributions. Note that the varying flash durations for each event are also combined into the respective distributions. The expected length of 107 m is marked in the according distributions. As discussed above, it can be seen that it is well recovered by the reconstruction algorithm. In comparison, the reconstructed length of most single flasher events is zero or close to zero, as expected from a single light source. The distribution has a long tail towards larger reconstructed lengths, similar to what is observed for single cascade simulation (c.f. Section 4.4). The energy asymmetry is slightly more complicated than the length. Because all flashing LEDs in a double flasher event are configured to be equally bright, the expected value of the energy asymmetry is $E_{\mathrm{A}} = 0$, as marked in the plots. The distribution of simulated events have a maximum at $E_{\mathrm{A}} \simeq 1$ for single and $E_{\mathrm{A}} \simeq 0$ for double flasher events. Both are expected as double flasher events with equally bright LEDs should be reconstructed to similar energies in each flasher (resulting in $E_{\mathrm{A}} \simeq 0$) and single flasher events are reconstructed as the specific case where the second flasher energy is close to zero (resulting in $E_{\mathrm{A}} \simeq 1$). In this case, the reconstructed length is meaningless, and the double flasher hypothesis is compatible with the single flasher hypothesis, similar to what was described for single cascade simulation. Note that the distribution of experimental double flasher events contains two peaks which are not centered at $E_{\mathrm{A}} \simeq 0$, as naively expected. This is due to the variation of the LED light output and the combined presentation, as one peak corresponds to double flasher event (A) and the other to event (B). As discussed in the previous section, the light output of an LED has an uncertainty of $\sim 30\%$. Because the variation of the LED light output is not modeled in simulation, the central values of the corresponding distributions are

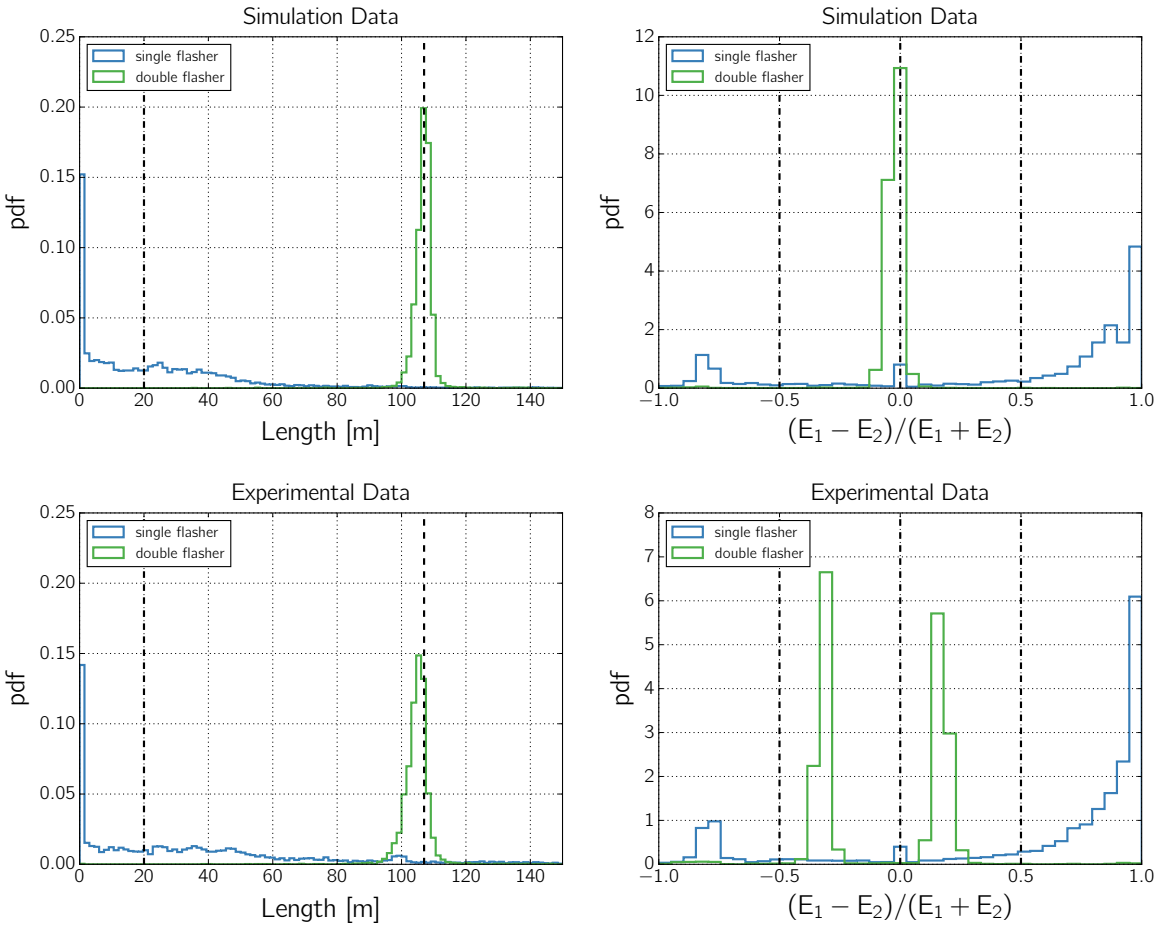

Figure 5.27: Reconstructed length (left) and reconstructed energy asymmetry (right) of single and double flashers shown for simulation data (top) and experimental data (bottom). The distributions contain the sum of all used LED positions and flashing durations. The vertical dashed lines at $L = 107\,\mathrm{m}$ and at $E_\mathrm{A} = 0$ mark the true length and energy asymmetry, respectively, expected for these double flasher events. The vertical dashed lines at $L = 20\,\mathrm{m}$ and at $E_\mathrm{A} = \pm 0.5$ mark cut values on the length and energy asymmetry, respectively, selected to distinguish single from double flasher events.

not expected to match. Assuming a relative variation of the brightness of each LED from the nominal value yields an energy asymmetry of $E_A = \pm 0.3$. This is consistent with the observed deviation in the experimental distribution of the energy asymmetry. The important point is that these distributions can be reconstructed with a very narrow width around the (shifted) central value. The small peaks of the single flasher distributions at $E_A \simeq 0$ and at $E_A \simeq -0.8$ can be explained with numerical reasons of the reconstruction algorithm. The peak around zero is also observed for single cascade simulation. In that case, two cascades are placed closely together which causes a degeneracy in both energies and the minimizer to return two equal energies as the best-fit result. The same effect can be observed for single flasher events. The second peak around $E_A \simeq -0.8$ is another solution of this degeneracy where two sources are placed closely together. This solution is not visible in single cascade simulation and can be attributed to the fact that flashers are not point-like in time as cascades (approximately) are. This is supported by the observation that this effect occurs in both simulation and experimental data. Furthermore, these single flasher events have very short reconstructed lengths, which means that they are not classified as double flasher events in any case, due to the selection criteria (see below).

With respect to the development of a binary topology ID for identifying single flasher and double flasher events, a set of **selection criteria** using the available phase space must be defined. The respective cut values using the reconstructed length and energy asymmetry are marked in Figure 5.27. The selection of the reconstructed length is chosen to be $L > 20\,\text{m}$ for classifying double flasher events. Although an LED is a significantly different light source than a cascade, there is no ad-hoc reason to chose an entirely different cut value for an event topology that consists of two light sources. The cut value of 20 m corresponds to a confidence level of $\sim 90\%$ where background from neutrino simulation is excluded (c.f. Section 4.4). The selection of the reconstructed energy asymmetry is chosen to $-0.5 < E_A < 0.5$, which is slightly different than for neutrino simulation. This is motivated by the different phase space of double flashers which is covered by this region as the experimental uncertainties of LEDs shift the distribution from the expected central value of $E_A = 0$. A single flasher event is classified as such by the inverse of these selection criteria.

In Table 5.3, the resulting **(mis)identification fractions** using the binary topology ID for experimental and simulated single flasher and double flasher events are shown. A true topology is simply given by the knowledge of which flasher LED event is chosen and the reconstructed topology is determined by the aforementioned selection criteria on the reconstructed length and energy asymmetry. The (mis)identification fractions of single and double flasher events are quoted in a similar way as for single cascades, double cascades, and tracks in Table 4.1. It can be seen that the flasher topology ID works very well with a success rate of $\sim 98 - 99\%$. More importantly, however, there is an excellent agreement between experimental and simulation data within the quoted errors. It can be concluded that the reconstruction and identification of double cascade events have been successfully tested using two specific configurations for experimental double flasher events. The results are consistent with both flasher and neutrino simulation and support the assumption that the ice anisotropy is modeled correctly within known uncertainties.

	Reconstructed Single		**Reconstructed Double**	
	Experimental	**Simulated**	**Experimental**	**Simulated**
True Single	$(98.0^{+2.0}_{-2.6})\%$	$(98.8^{+1.2}_{-1.5})\%$	$(2.0^{+2.6}_{-2.0})\%$	$(1.2^{+1.5}_{-1.2})\%$
True Double	$(1.8^{+1.5}_{-1.6})\%$	$(0.9^{+0.9}_{-0.9})\%$	$(98.2^{+1.6}_{-1.5})\%$	$(99.1^{+0.9}_{-0.9})\%$

Table 5.3: (Mis)identification fractions of experimental and simulated single flasher and double flasher events using the binary topology ID as described in the text.

5.4 Summary and Conclusions to Tau-Neutrino Identification

The model of the Antarctic ice is the most important detector component with the largest uncertainties. It determines observable waveforms by the statistical description of photon propagation from a light source to a DOM. Waveform templates are generated assuming a specific ice model and used in the reconstruction of an event hypothesis. Observables that are derived from the reconstructed event can be susceptible to variations of the ice model. The introduction of a scattering anisotropy in the ice model and a novel method to identify tau-neutrino interactions via the double cascade event reconstruction have required a combined treatment. It is based on the finding that the reconstructed double cascade length is sensitive to an uncertainty of the ice anisotropy. In particular, the reconstruction algorithm uses this degree of freedom to compensate a mismatch between observed and expected waveforms due to the ice anisotropy. This is realized by inadvertently decreasing or increasing the distance between a cascade and a DOM depending on the observed charge being greater or smaller than expected, respectively. The incorrect treatment of the ice anisotropy thereby introduces a bias in the reconstructed length. It can be of the order of several meters, in the extreme case where the ice anisotropy is entirely excluded from the event reconstruction. Because the double cascade length is the most sensitive observable to tau-neutrino interactions, but also the most susceptible to background misidentification, a proper treatment of the ice anisotropy has been required.

A major problem of established reconstruction algorithms has been the limited usage of isotropic ice models, due to the technical constraints of photo spline tables in general. An effective distance parametrization was developed to include the ice anisotropy into standard photo spline tables by circumventing these limitations. It is similar in nature to the double cascade length bias. The idea was therefore to parameterize the direction-dependent modulation of the scattering coefficient as a transformation of the distance between source and DOM. It was shown that the combined usage of the effective distance spline tables with standard cascade photo spline tables for an ice model without anisotropy and tilt is equivalent to the SPICELea ice model that contains the ice anisotropy and tilt. The method was successfully tested in multiple ways.

With respect to tau-neutrino identification via the double cascade method, three important results were obtained. First, it was shown that the incorporation of the ice anisotropy into reconstruction causes the length bias to vanish and the fraction of misidentified background events to decrease. Second, a test of the double cascade method using experimental flasher LED data illustrated that the performance is consistent and results obtained from simulation data are transferable to experimental data. Third, the experimental test suggested that there are no further systematic errors that have a similar impact on tau-neutrino-related observables than the ice anisotropy, and that are not modeled in simulation. Furthermore, the comparison between different ice models in simulation and reconstruction allowed for a parametrization of the uncertainty of the ice anisotropy, which is described in Appendix A.

There are, however, some caveats to the discussed results. First, the experimental test using double flasher events is limited to only two specific configurations. In addition, these are in a phase space that is not very likely to contain a potential tau-neutrino interaction. Although different configurations using more closely spaced DeepCore strings may be realized in principle if more flasher data is collected in the future, the present results may be considered a proof of concept. Second, the global ice tilt is not incorporated into reconstruction algorithms. However, this does not pose a problem with respect to tau-neutrino identification. Third, the uncertainty of the direction of the ice anisotropy axes, as well as other model assumptions such as the sinusoidal shape in the horizontal plane, are not considered. Although these contingencies seem possible, they are not essential. As long as the size of the anisotropy axes remains constant, the length bias introduced on average remains unchanged, as well. Hence, a consideration of the size of the ice anisotropy is sufficient in this context.

6 Likelihood-Based Measurement of the Astrophysical Neutrino Flavor Composition

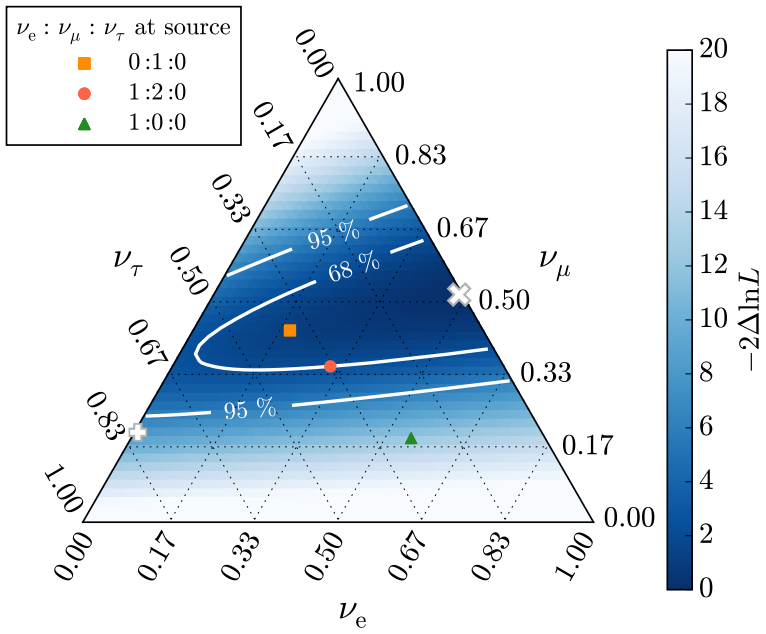

Figure 6.1: Astrophysical flavor composition at Earth measured by using multiple IceCube data samples in a global fit [46]. Each point in the triangle plot corresponds to a flavor composition $\nu_e : \nu_\mu : \nu_\tau$ which is read off the corresponding axes along the direction of the tick labels. The best-fit value of 0.49 : 0.51 : 0 is marked with '×'. The 68% and 95% confidence regions are obtained evaluating the likelihood ratio $-2\Delta \log \mathcal{L}$ in a profile likelihood scan around the best-fit. Three different flavor compositions at Earth are indicated, which are produced in different scenarios at the source (c.f. Section 2.3.3). The best-fit flavor composition of an earlier IceCube analysis is marked with '+' [65]. Figure reproduced from [46].

The astrophysical neutrino flavor composition has been previously measured with IceCube using different analysis methods [46, 48, 65]. The tau-neutrino fraction remains mostly unconstrained, because the methods used for flavor discrimination have been restricted to the cascade and track event topologies. The analysis presented in this thesis aims to measure the flavor composition with the additional constraints from the double cascade event topology.

In Section 6.1, the analysis method is described with respect to the main features of a profile likelihood fit and the construction of confidence regions. In Section 6.2, the model parameters and observables used in the fit are explained and relevant systematic uncertainties are discussed. In Section 6.3, the sensitivity of the analysis to the astrophysical tau-neutrino flux and the astrophysical neutrino flavor composition is presented. The expected number of events is summarized for each topology sample and the dependence of the sensitivity on the spectral shape of the astrophysical neutrino flux is discussed.

6.1 Analysis Method

The analysis is based on a **binned maximum likelihood estimation** where a sum of Monte Carlo templates, each containing the observables for an astrophysical or an atmospheric flux component, is varied until it describes the observed data best. Systematic uncertainties are modeled as *nuisance parameters* into the likelihood fit and are usually constrained by prior knowledge. This construction is also known as a *profile likelihood* [233], and is commonly used for diffuse astrophysical neutrino flux searches in IceCube [46]. It is characterized by a set of

- M physical parameters $\boldsymbol{\theta} = \{\theta_1, \theta_2, \ldots, \theta_M\}$ and
- K nuisance parameters $\boldsymbol{\xi} = \{\xi_1, \xi_2, \ldots, \xi_K\}$ which define
- N expectation values $\boldsymbol{\mu}(\boldsymbol{\theta}, \boldsymbol{\xi}) = \{\mu_1(\boldsymbol{\theta}, \boldsymbol{\xi}), \mu_2(\boldsymbol{\theta}, \boldsymbol{\xi}), \ldots, \mu_N(\boldsymbol{\theta}, \boldsymbol{\xi})\}$ for each of the
- N numbers of observed occurrences $\boldsymbol{n} = \{n_1, n_2, \ldots, n_N\}$.

Because a counting experiment is performed for each bin $i = 1 \ldots N$, the Poisson PDF

$$p\big(n_i|\mu_i(\boldsymbol{\theta}, \boldsymbol{\xi})\big) = \frac{\big(\mu_i(\boldsymbol{\theta}, \boldsymbol{\xi})\big)^{n_i}}{n_i!} \cdot \exp\big(-\mu_i(\boldsymbol{\theta}, \boldsymbol{\xi})\big) \tag{6.1}$$

is a suitable choice for the likelihood, which is defined as the product over all bins

$$\mathcal{L}\big(\boldsymbol{n}|\boldsymbol{\mu}(\boldsymbol{\theta}, \boldsymbol{\xi})\big) = \prod_{i=1}^{N} p\big(n_i|\mu_i(\boldsymbol{\theta}, \boldsymbol{\xi})\big) \prod_{j=1}^{K} \exp\left(-\frac{1}{2}\left(\frac{\xi_j - \bar{\xi}_j}{\sigma_{\xi_j}}\right)^2\right). \tag{6.2}$$

A *penalty term* for each nuisance parameter ξ_j is included in the likelihood where deviations from the central value $\bar{\xi}_j$ in terms of the prior known error σ_{ξ_j} are modeled with a Gaussian PDF. In practice, it is computationally more feasible to minimize the negative logarithm of the likelihood

$$\ln\Big(\mathcal{L}\big(\boldsymbol{n}|\boldsymbol{\mu}(\boldsymbol{\theta}, \boldsymbol{\xi})\big)\Big) = \sum_{i=1}^{N}\Big(n_i \ln\big(\mu_i(\boldsymbol{\theta}, \boldsymbol{\xi})\big) - \ln(n_i!) - \mu_i(\boldsymbol{\theta}, \boldsymbol{\xi})\Big) - \sum_{j=1}^{K}\left(\frac{1}{2}\left(\frac{\xi_j - \bar{\xi}_j}{\sigma_{\xi_j}}\right)^2\right) \tag{6.3}$$

with respect to its fit parameters $\boldsymbol{\theta}$ and $\boldsymbol{\xi}$. The physical parameters $\boldsymbol{\theta}$ are free to float within their physical boundaries and correspond to the measurement quantities that are of interest for the analysis. The nuisance parameters $\boldsymbol{\xi}$ are constrained by prior knowledge as modeled in the Gaussian penalty term and correspond to the systematic uncertainties. All model parameters, observables, and systematic uncertainties of the fit will be discussed in Section 6.2.

A specific model is tested through the use of a **likelihood ratio test**. For a chosen set of parameters $\{\boldsymbol{\theta}_t, \boldsymbol{\xi}_t\}$ representing the test hypothesis and the set of parameters $\{\hat{\boldsymbol{\theta}}, \hat{\boldsymbol{\xi}}\}$ which maximizes the likelihood, a *test statistic* is defined by

$$-2\Delta\log\mathcal{L} := -2\ln\left(\frac{\mathcal{L}\big(\boldsymbol{n}|\boldsymbol{\mu}(\boldsymbol{\theta}_t, \boldsymbol{\xi}_t)\big)}{\mathcal{L}\big(\boldsymbol{n}|\boldsymbol{\mu}(\hat{\boldsymbol{\theta}}, \hat{\boldsymbol{\xi}})\big)}\right). \tag{6.4}$$

The factor -2 is added to the definition of the test statistic for convenience, because it allows the determination of a *confidence level* (CL) of a *nested hypothesis* test through the use of **Wilks' theorem** [234]. It states that $-2\Delta\log\mathcal{L}$ approximately follows a χ^2-distribution with $k = \mathrm{dof}(\hat{\boldsymbol{\theta}}, \hat{\boldsymbol{\xi}}) - \mathrm{dof}(\boldsymbol{\theta}_t, \boldsymbol{\xi}_t)$ degrees of freedom, where $\mathrm{dof}(\boldsymbol{\theta}, \boldsymbol{\xi})$ is the number of free parameters in each fit. The test hypothesis is nested if it represents a special case of the free fit with one or more parameters being constrained, thus reducing the degrees of freedom accordingly. Wilks' theorem is powerful for two reasons: First, the calculation of confidence levels for any model test

is extremely fast, because the generation of the exact test statistic distribution from a Monte Carlo simulation is not necessary. Second, the knowledge of the true values of the nuisance parameters is not required as a consequence. However, Wilks theorem is only valid if

1. the sample size is large ($\sum_i n_i \to \infty$) and
2. the model parameters $\{\boldsymbol{\theta}, \boldsymbol{\xi}\}$ are not bounded.

If either condition is not met, the test statistic $-2\Delta\log\mathcal{L}$ may deviate from a χ^2-distribution. In this case, the exact distribution must be obtained from performing a large number of **Monte Carlo pseudo experiments**. A pseudo experiment (or *trial*) is generated by injecting the parameter set $\{\boldsymbol{\theta}_\mathrm{t}, \boldsymbol{\xi}_\mathrm{t}\}$ of the test model as the true simulated value. Each trial is fitted twice (once with the parameters of the test model constrained and once again with all parameters left free in the fit) in order to calculate the test statistic in Equation 6.4. The distribution of $-2\Delta\log\mathcal{L}$ from all trials is then used to construct confidence levels. Note that the required number of trials depends on the desired confidence level and must be large enough that statistical fluctuations of the distribution are at an acceptable level. For example, a chosen confidence level of 90% should be obtained from at least $\sim$1000 pseudo experiments, which would place the uncertainty at $(90 \pm 1\%)$ CL (obtained from the confidence intervals of a binomial distribution).

Confidence regions of model parameters are obtained by evaluating the test statistic defined in Equation 6.4 in a **profile likelihood scan**. For example, the likelihood ratio reads

$$\lambda := -2\Delta\log\mathcal{L} = -2\ln\left(\frac{\mathcal{L}\big(\boldsymbol{n}|\boldsymbol{\mu}(\theta_1 = \theta_\mathrm{t}, \hat{\hat{\boldsymbol{\theta}}}_\mathrm{r}, \hat{\hat{\boldsymbol{\xi}}})\big)}{\mathcal{L}\big(\boldsymbol{n}|\boldsymbol{\mu}(\hat{\boldsymbol{\theta}}, \hat{\boldsymbol{\xi}})\big)}\right), \tag{6.5}$$

for one parameter of interest θ_1 that is fixed to a test value θ_t of the profile likelihood scan, while all other parameters are free. The likelihood in the denominator contains the *global* best-fit values $\{\hat{\boldsymbol{\theta}}, \hat{\boldsymbol{\xi}}\}$ of the unconstrained fit with $\hat{\boldsymbol{\theta}} = \{\hat{\theta}_1, \ldots, \hat{\theta}_M\}$ and $\boldsymbol{\xi} = \{\xi_1, \ldots, \xi_K\}$, and the likelihood in the numerator contains the *conditional* best-fit values $\{\hat{\hat{\boldsymbol{\theta}}}_\mathrm{r}, \hat{\hat{\boldsymbol{\xi}}}\}$ with the reduced set $\hat{\hat{\boldsymbol{\theta}}}_\mathrm{r} = \{\hat{\hat{\theta}}_2, \ldots, \hat{\hat{\theta}}_M\}$. If Wilks' theorem is valid at $\theta_1 = \theta_\mathrm{t}$, the confidence interval (e.g. at 68% CL) can simply be obtained from the cumulative distribution of $\chi^2_{k=1}(\lambda \leq \lambda_\mathrm{c}) = 0.68$. The confidence interval of $\theta_1 \in [\theta_\mathrm{t}^\mathrm{lower}, \theta_\mathrm{t}^\mathrm{upper}]$ is then given by those values $(\theta_\mathrm{t}^\mathrm{lower}, \theta_\mathrm{t}^\mathrm{upper})$ which place the likelihood ratio in Equation 6.5 at the critical test statistic value λ_c. Note that this profile likelihood scan is one-dimensional and the χ^2-distribution is assumed to have $k = 1$ degree of freedom, because one parameter is fixed and all remaining parameters are free in the conditional best-fit compared to the global best-fit where all parameters are free.

As mentioned above, the exact test statistic distribution is obtained from a large number of Monte Carlo pseudo experiments if Wilks' theorem is not valid for $\theta_1 = \theta_\mathrm{t}$. In this case, the **construction of confidence intervals** follows the procedure originally proposed by Gary Feldman and Robert Cousins [235], with the extension of incorporating nuisance parameters [236, 237]. In particular, the following steps are executed in order to obtain the confidence interval of a parameter of interest θ_1 at the desired confidence level $1 - \alpha$ for a given data sample:

1. The likelihood fit is performed and yields the global best-fit values $\{\hat{\boldsymbol{\theta}}, \hat{\boldsymbol{\xi}}\}$.
2. The parameter of interest θ_1 is evaluated at each of the test points $\{\theta_\mathrm{t}\}$, and the conditional best-fit values $\{\hat{\hat{\boldsymbol{\theta}}}_\mathrm{r}(\theta_\mathrm{t}), \hat{\hat{\boldsymbol{\xi}}}(\theta_\mathrm{t})\}$ of the constrained likelihood fit are obtained.
3. The likelihood ratios $\{\lambda_\mathrm{obs}(\theta_\mathrm{t})\}$ as in Equation 6.5 are calculated for all test points $\{\theta_\mathrm{t}\}$.
4. For each of the test points $\{\theta_\mathrm{t}\}$ a large number of pseudo experiments is performed by sampling from the parent distribution $\{\theta_\mathrm{t} \,|\, \hat{\hat{\boldsymbol{\theta}}}_\mathrm{r}(\theta_\mathrm{t}), \hat{\hat{\boldsymbol{\xi}}}(\theta_\mathrm{t})\}$. Note that the values of the injected model parameters correspond to the conditional best-fit values. If a nuisance parameter is constrained by a Gaussian prior, it is sampled from that distribution.

5. The likelihood ratio $\lambda(\theta_t)$ as in Equation 6.5 is calculated for each trial, and the distribution $f\big(\lambda(\theta_t)\big)$ is obtained from the entirety of all trials. Each distribution has the systematic uncertainties incorporated and is only limited by statistical fluctuations.
6. A critical test statistic value $\lambda_c(\theta_t)$, for which the distribution $f\big(\lambda(\theta_t)\big)$ covers the desired confidence level $1-\alpha$, is determined via

$$\left(\int_0^{\lambda_c(\theta_t)} f\big(\lambda(\theta_t)\big)\,\mathrm{d}\lambda\right) \Big/ \left(\int_0^{\infty} f\big(\lambda(\theta_t)\big)\,\mathrm{d}\lambda\right) = 1-\alpha. \tag{6.6}$$

7. The observed likelihood ratios from the given data sample $\{\lambda_{obs}(\theta_t)\}$ are compared to the critical likelihood ratios $\{\lambda_c(\theta_t)\}$ from the Monte Carlo realizations as defined in Equation 6.6. The confidence interval of the parameter of interest θ_1 at the confidence level $1-\alpha$ is the set of all physically allowed test points $\{\theta_t\}$ for which $\lambda_{obs}(\theta_t) < \lambda_c(\theta_t)$.

A confidence region for a simultaneous measurement of two model parameters (θ_1, θ_2) is constructed analogously via a two-dimensional profile likelihood scan. Note that the procedure sketched above is computationally much more demanding in this case, as the total required number of pseudo experiments for all test points is significantly larger. If Wilks' theorem holds, confidence regions can be estimated via a χ^2-distribution with two degrees of freedom instead.

A convenient method for estimating the median value of the test statistic distribution is the use of the **Asimov dataset** [237]. Instead of generating the distribution from Monte Carlo pseudo experiments, the entire dataset is used as a single representation for all possible realizations. The resulting test statistic value for the (conditional and global) best-fit values that maximize the likelihood of the Asimov dataset is equal to the median test statistic value that is obtained from the full distribution of pseudo experiments. The Asimov dataset and Wilks' theorem are used to estimate the median sensitivity of the analysis, as will be discussed in Section 6.3. This approach is particularly useful for a qualitative comparison of the change in sensitivity for different astrophysical flux models, as will be discussed in Section 6.3.4. Note, however, that the main fit parameter of interest is the astrophysical tau-neutrino flux, which is bounded ($\phi_{\nu_\tau} \geq 0$) and constrained by the small double cascade sample ($\sim 1-3$ events). Therefore, the validity of Wilks' theorem is examined where necessary, and the construction method of confidence regions will be explicitly stated in each case throughout the remaining parts of this thesis.

6.2 Components of the Likelihood Fit

The likelihood $\mathcal{L}\big(\boldsymbol{n}|\boldsymbol{\mu}(\boldsymbol{\theta},\boldsymbol{\xi})\big)$ as defined in Equation 6.2 is constructed as follows: First, the physical parameters of interest $\boldsymbol{\theta}$ are identified and modeled. The goal is to measure the astrophysical electron-, muon-, and tau-neutrino fluxes. Background components are the conventional and prompt atmospheric neutrino fluxes and the atmospheric muon flux. Second, a set of observables that is most sensitive to each astrophysical neutrino flux is chosen, and the combined phase space of all observables is binned. Each bin yields an expectation $\boldsymbol{\mu}(\boldsymbol{\theta},\boldsymbol{\xi})$ which is given by the sum of all astrophysical and atmospheric flux components. Third, all nuisance parameters $\boldsymbol{\xi}$ that can alter the prediction $\boldsymbol{\mu}(\boldsymbol{\theta},\boldsymbol{\xi})$ for a given model hypothesis are incorporated into the likelihood. Fourth, the experiment is performed and the number of observed events in all observable bins $\boldsymbol{n}$ is obtained. Last, the likelihood fit is performed by varying all fit parameters until the sum of all flux components describes the observed data best. The best-fit result for the per-flavor astrophysical neutrino fluxes is obtained from the values that maximize the likelihood. Confidence regions are calculated by evaluating a likelihood ratio which compares the best-fit value to a test value in a profile likelihood scan.

6.2.1 Model Parameters

The model parameters of the likelihood fit including priors are summarized in Table 6.1. They are either flux components of astrophysical or atmospheric origin and enter the likelihood as expectation values. Or, they are nuisance parameters which incorporate systematic uncertainties into the expectation values and additionally enter the likelihood via Gaussian priors. The baseline models are described in this section, and the choice of priors will be explained in Section 6.2.3.

The **astrophysical neutrino flux** is modeled as explained in Section 2.3.2. The parameters of interest are the per-flavor astrophysical neutrino fluxes ϕ_{ν_e}, ϕ_{ν_μ}, and ϕ_{ν_τ}. They are modeled as a single power-law of the form $\phi_\nu \sim E_\nu^{-\gamma}$ with a common astrophysical spectral index γ for all flavors. The assumption that each flavor has an identical spectral index is required due to the small size of the six-year high-energy starting event sample (c.f. Section 4.2). An energy-dependent change of the flavor composition could lead to different spectra (c.f. Section 2.3.3). However, the measurement of the flavor composition presented in this thesis is necessarily integrated over energy and does not have the power to constrain individual spectra for each flavor. Each per-flavor astrophysical neutrino flux is modeled with equal amounts of neutrinos and antineutrinos ($\nu : \bar{\nu} = 1$) and by assuming isotropic arrival directions at Earth. The astrophysical model parameters ϕ_{ν_e}, ϕ_{ν_μ}, ϕ_{ν_τ} and γ are free to float in the fit (with the exception of a lower flux boundary at zero) without the addition of a prior. A benchmark per-flavor astrophysical neutrino flux of $\phi_\nu(E_\nu) = 1.5{\cdot}10^{-18}(E_\nu/100\,\text{TeV})^{-2.3}\,\text{GeV}^{-1}\,\text{cm}^{-2}\,\text{sr}^{-1}\,\text{s}^{-1}$ with an assumed flavor composition of $\nu_e : \nu_\mu : \nu_\tau = 1 : 1 : 1$ is used to study the sensitivity. The chosen normalization and spectral index are based on measurements that were available when the analysis presented in this thesis was initially conducted [48–50]. The neutrino flavor composition is chosen based on the theoretical expectation from pion production and decay in a transparent environment and flavor oscillation between sources and Earth (c.f. Section 2.3.3).

The atmospheric flux components are constrained by priors, because they can be measured more accurately with other IceCube data samples. The high-energy starting event selection is very efficient in the reduction of atmospheric muons, due to the veto requirement, and of down-going atmospheric neutrinos from the same cosmic-ray-induced air shower, due to the self-veto effect (c.f. Section 4.2). The shape of the **atmospheric muon flux** is obtained from the pure-proton extragalactic composition of the GaisserH3a cosmic-ray composition model [118] (abbreviated as GaisserH4a), using SYBILL 2.1 as hadronic interaction model [238]. The normalization of the atmospheric muon flux is obtained from experimental data by tagging muon events in the veto layer and calculating the fraction that pass an equivalent inner veto layer [43]. This method is less susceptible to model uncertainties and will be discussed in Section 6.2.3.

Model Parameter		**Prior** $(\bar{\xi} \pm \sigma_\xi)$
ϕ_{ν_e}	astro. ν_e normalization	free
ϕ_{ν_μ}	astro. ν_μ normalization	free
ϕ_{ν_τ}	astro. ν_τ normalization	free
γ	astro. spectral index	free
ϕ_{muon}	atm. muon normalization	$(1.0 \pm 0.3) \times$ (GaisserH4a $\times$ tagged muon data)
ϕ_{conv}	atm. conv. normalization	$(1.0 \pm 0.3) \times$ (HKKMS06 $\times$ CR-knee mod. $\times$ self-veto prob.)
ϕ_{prompt}	atm. prompt normalization	$(0.0 + 0.65) \times$ (ERS $\times$ CR-knee mod. $\times$ self-veto prob.)
ξ_E	energy scale	$(1.0 \pm 0.15) \times$ (SPICELea $\times$ 0.99 RDE)
ξ_A	ice anisotropy scale	$(1.0 \pm 0.3) \times$ SPICELea

Table 6.1: Model parameters of the likelihood fit. See text for a description of the baseline models and Section 6.2.3 for an explanation of the priors.

The **conventional atmospheric neutrino flux** produced by the decay of charged pions and kaons in cosmic-ray-induced air showers is based on the HKKMS06 model [125]. The **prompt atmospheric neutrino flux** from the decay of heavy charmed mesons is estimated using the ERS model [121]. Note, however, that the baseline of the prompt atmospheric neutrino flux is chosen to be zero, because it has not been observed yet [51]. The choice of prior reflects a large uncertainty of the prompt component, as will be discussed in Section 6.2.3. Both conventional and prompt flux models are modified to account for more recent measurements in the "knee"-region of the primary cosmic-ray spectrum, which are parametrized by the GaisserH3a composition model [118, 130]. In addition, they are folded with the generalized self-veto probability as described in [148] to account for the reduced rate of atmospheric neutrinos that accompany vetoed muons from the same cosmic-ray-induced air shower.

Additional nuisance parameters are an **energy scale** ξ_E and an **ice anisotropy scale** ξ_A, which quantify the most relevant systematic uncertainties of the detector. Both are relative scale parameters with respect to different observables. The energy scale modifies the deposited electromagnetic-equivalent energy, because it accounts for an imprecise knowledge of the DOM efficiency as well as the scattering and absorption coefficients of the ice model. The relative DOM efficiency (RDE) is normalized to the 25% baseline quantum efficiency of a standard IceCube DOM (c.f. Section 3.2.2) and the baseline ice model is SPICELea (c.f. Section 3.2.4). The ice anisotropy scale incorporates a potential bias of the double cascade length, which reflects the uncertainty of the magnitude of the ice anisotropy (c.f. Chapter 5). Both nuisance parameters will be discussed in greater detail in Section 6.2.3.

6.2.2 Observables

The **total deposited electromagnetic-equivalent energy** and the **zenith angle** have been used as observables in previous spectral fits of the diffuse astrophysical neutrino flux with multiple years of high-energy starting events [4, 43, 44, 50]. This is motivated by the distinct distributions these observables have for astrophysical neutrinos, atmospheric neutrinos, and atmospheric muons, as explained in Section 2.3.2. Note that a key difference is the efficient suppression of down-going atmospheric neutrinos due to the self-veto effect. In contrast, up-going atmospheric neutrinos are irreducible background that can only be distinguished from astrophysical neutrinos using the deposited energy. The distinction between astrophysical and atmospheric neutrinos is not performed on an individual event basis, but rather statistically on the entire data sample.

The **observable templates** for each flux model are calculated through Monte Carlo simulation. Neutrino events are simulated with `NuGen` and muon events with `MuonGun` (c.f. Section 3.3.2). Each observable template represents a flux component by weighting the underlying events according to the astrophysical or atmospheric flux models described in the previous section. The observable distributions for the total deposited energy and the zenith angle of all high-energy starting events are depicted in Figure 6.2 for all flux models. The distributions of the total deposited energy clearly show distinct slopes, as expected from different primary spectra. The energy region below 60 TeV is excluded from the likelihood fit, as the statistical error of the available `MuonGun` simulation is too large to meaningfully constrain the atmospheric muon flux (see Section 6.3.1). Additionally, the energy region above 10 PeV is excluded, because it cannot be constrained due to the lack of observed events (c.f. Section 4.2). This is chosen in accordance with previous spectral fits using the high-energy starting event selection. The zenith angle distributions illustrate the aforementioned distinct properties of each flux component. Atmospheric muons are exclusively down-going as they cannot penetrate the Earth from below. Both conventional and prompt atmospheric neutrinos are strongly reduced in the down-going region due to the self-veto effect. Astrophysical neutrinos are isotropic in the down-going region and reduced in the up-going region due to Earth absorption at high energies.

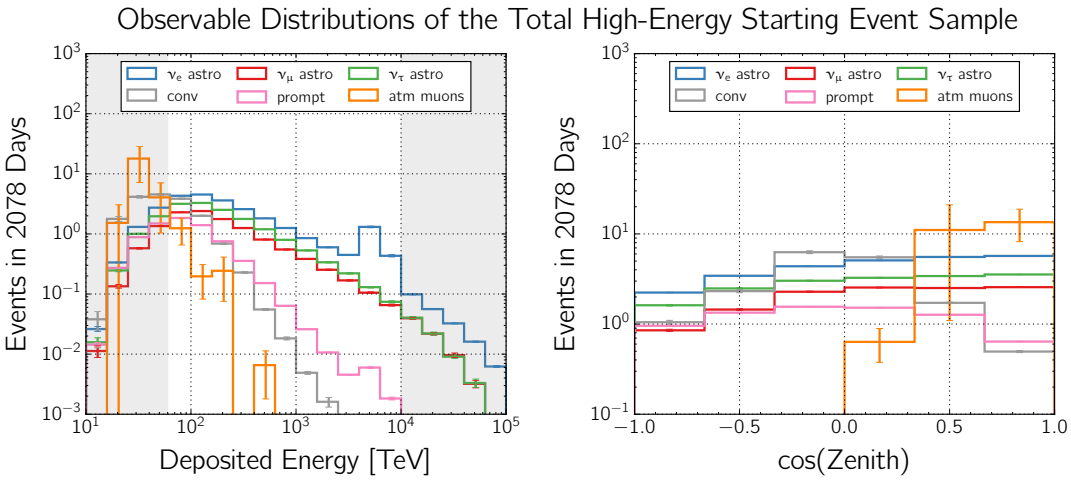

Figure 6.2: Observable distributions for the total high-energy starting event sample. The expected number of events in six years of data is depicted as a function of the deposited energy (left) and zenith angle (right). The energy regions below 60 TeV and above 10 PeV are excluded from the likelihood fit. Vertically up-going events have cos(zenith) $= -1$ and vertically down-going events have cos(zenith) $= +1$. Distributions are shown for each flux component using the baseline models discussed in Section 6.2.1. Indicated errors are statistical only.

Note that each distribution shows the expected number of events in 2078 days, which is approximately equal to 5.7 years. This is slightly less than six years, because data taking runs for calibration purposes or with poor quality are excluded. The depicted binning of both observables is identical to previously published likelihood fits and will be discussed in greater detail with respect to the systematic uncertainties in Section 6.2.3.

The reconstruction quality of each observable depends on the event topology (c.f. Section 4.3.3). A total deposited energy is reconstructed more precisely for a cascade event and can constrain the related neutrino energy much better due to the calorimetric nature of a cascade. A zenith angle is much better constrained for tracks, due to the longer lever arm of the event, and is approximately equal to the initial neutrino direction. Therefore, it makes sense to split each observable distribution into the identifiable event topologies using a

- **binary topology ID**: cascade and track,
- **ternary topology ID**: single cascade, double cascade, and track.

While previous IceCube analyses were based on a binary topology ID, the analysis presented in this thesis is based on the ternary topology ID (c.f. Section 4.3.2). In particular, all prior spectral fits using the high-energy starting event sample were based on a binary topology ID. It was determined from the true neutrino interaction for simulation data and from likelihood scans around the best-fit direction for experimental data. In the context of this thesis, a binary topology ID is defined by reclassifying double cascade events as single cascade events. This is reasonable, because the dominant background in the double cascade sample are single cascade events, and yields a successfully identified fraction of $(90.4 \pm 0.3)\%$ cascade events and $(90.8 \pm 5.8)\%$ track events above a deposited energy of 60 TeV. A consistent comparison between binary and ternary topology ID ultimately allows the assessment of the sensitivity improvements due to the additional double cascade event topology. The ternary topology ID is used to split the total high-energy starting event sample into a single cascade, a double cascade, and a track sample. A different set of observables is used for each topology sample. While the total deposited energy is used for all of them, the zenith angle is only used for the single cascade and track samples. The **length** is employed for the double cascade sample instead, because it is more sensitive to tau-neutrino interactions as a proxy for the tau decay length.

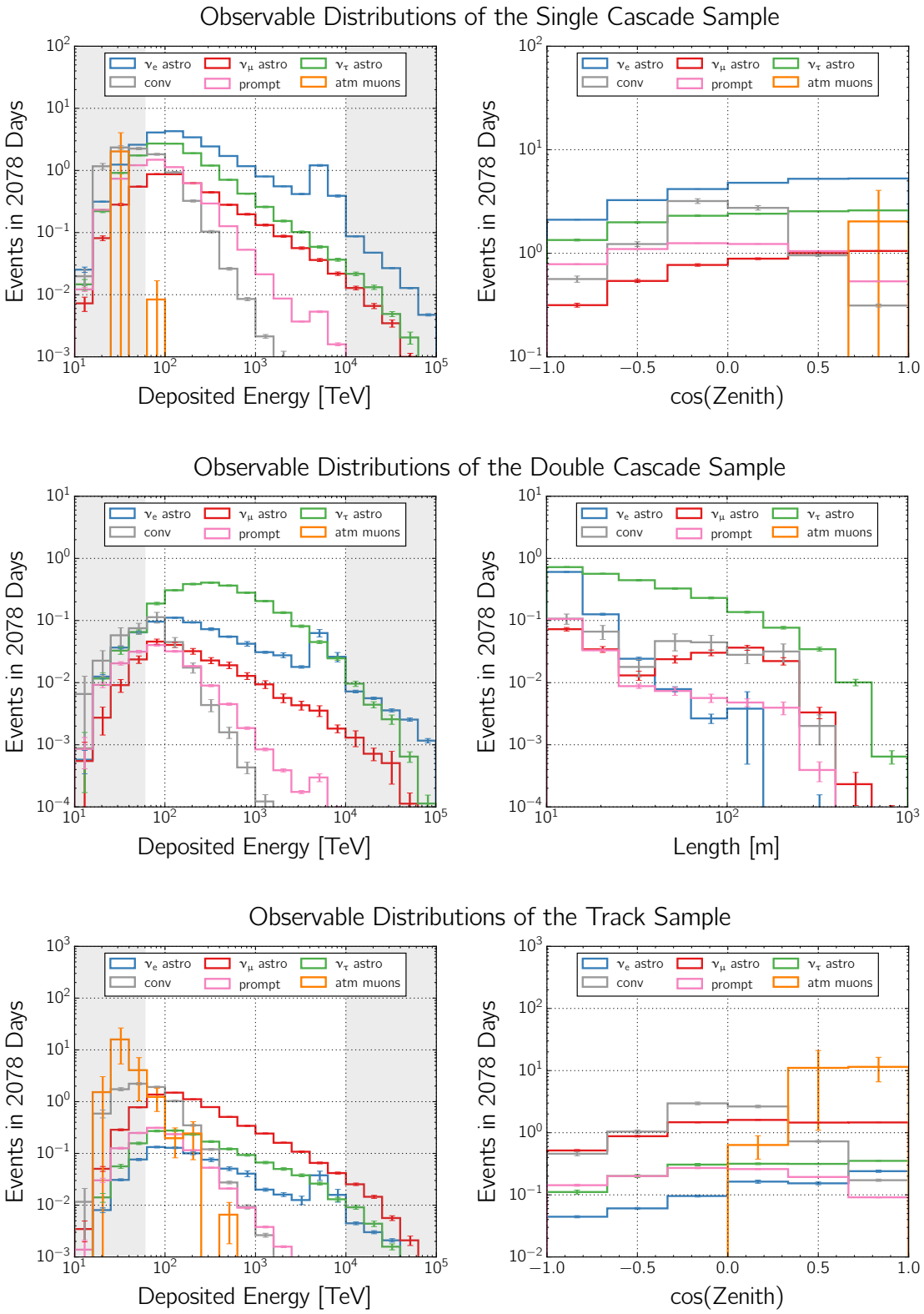

Figure 6.3: Observable distributions for the single cascade, double cascade, and track event samples. The expected number of events in six years of data is depicted as a function of the deposited energy (left) and zenith angle (right) for the single cascade sample (top) and the track sample (bottom) and as a function of the deposited energy (left) and double cascade length (right) for the double cascade sample (center). Distributions are shown for each flux component using the baseline models discussed in Section 6.2.1. The choice of binning in each plot is identical to binning of the likelihood. Only the energy region between 60 TeV and 10 PeV is included in the fit. Indicated errors are statistical only.

The **observable distributions** are shown in Figure 6.3 for each topology sample. It is clearly visible how each flux component is divided differently according to the event topology that contributes most. The single cascade sample is dominated by astrophysical electron-neutrinos. Tau-neutrino interactions inducing a double cascade event topology have a large contribution to the single cascade sample for events with tau decay lengths, which are too short to be resolvable. However, above 10 m decay length, these events make up the largest fraction of events in the double cascade sample. Both astrophysical and atmospheric muon-neutrino interactions as well as atmospheric muons predominantly contribute to the track sample. Note that all distributions are only one-dimensional projections of the two-dimensional templates that are fitted simultaneously (though separately for each topology sample). The correlation between observables is thereby exploited, and double counting of events is avoided. The omission of the zenith angle in the double cascade sample is due to technical reasons, as the available amount of simulation data is not sufficient enough to construct the Monte Carlo templates in three dimensions. The loss of directional information in the double cascade sample is acceptable as the zenith angle is particularly important for distinguishing events of astrophysical and atmospheric origin. However, the dominant contribution in the double cascade sample and background for tau-neutrino interactions are astrophysical neutrinos of different flavors which cannot be distinguished using the zenith angle. The atmospheric background in the double cascade sample is negligible and mostly divided among the single cascade and track samples. The gain in sensitivity to tau-neutrino interactions from the double cascade sample – although small in contribution to the total number of expected events – can clearly be seen in both distributions (Figure 6.3, center row). The length is a powerful additional observable, because the background for true double cascade events is particularly low above 20 m.

6.2.3 Systematic Uncertainties

The treatment of systematic uncertainties in this analysis is based on the most recent spectral fit of the astrophysical neutrino flux using the six-year high-energy starting event sample [4]. It follows the same arguments and is extended where necessary. Systematic uncertainties can be divided into two different types. The first is due to imprecisely known **detector properties**. Depending on the event selection, these uncertainties may alter the threshold and shape of observable distributions and thereby change the event rate expected in the sample from different flux components. The second type of uncertainty is due to the imprecise knowledge of **particle flux and interaction models**. These directly alter the expected event rate and thus the measured neutrino and muon flux components. An overview of systematic uncertainties typically considered in spectral fits of the astrophysical neutrino flux is given in Table 6.2. They are quoted with respect to the energy range of the high-energy starting event sample and relative to the baseline model of each property. This means that the detector property uncertainties do not reflect the variation of the observables they affect. The given flux and interaction model uncertainties, however, directly scale with the quoted lepton flux components. The relevance of each uncertainty for this analysis is discussed in greater detail in the following.

The **DOM efficiency** combines different effects such as the overall quantum efficiency of the PMT and a possible shadowing of the photo-sensitive area by the cable and harness that are attached to the DOM [42]. It is assumed that this cable shadow reduces the relative DOM efficiency by 1%. The combined uncertainty of the DOM efficiency is estimated to be $\pm 10\%$. It affects the reconstructed energy, because a lower DOM efficiency than assumed causes an underestimation of the photon light yield expected from a source. In the relevant energy range, this effect scales linearly, i.e. a variation of $\pm 10\%$ in the overall DOM efficiency translates to a $\pm 10\%$ uncertainty of the reconstructed energy. This effect is relevant in the analysis, as it shifts the energy distribution across bins and the energy thresholds in particular.

Type	Property	Baseline	Uncertainty	Affects	Relevant
Detector	DOM efficiency	$0.99 \times$ RDE	$\pm 10\%$	energy	yes
Detector	hadronic shower energy	visible em. shower energy	$+10 \ldots 20\%$	energy	yes
Detector	light scattering and absorption in ice	SPICELea	$^{+10\%}_{-\ 7\%}$	energy, zenith	yes
Detector	ice anisotropy	SPICELea	$\pm 30\%$	length, zenith, topology ID	yes
Detector	hole ice	H-50cm	$< 15\%$	zenith	no
Flux	cosmic-ray flux and composition	GaisserH3a	$\pm 5 \ldots 30\%$	$\phi_{\text{conv}}, \phi_{\text{prompt}}, \phi_{\text{muon}}$	yes
Flux	π/K ratio	HKKMS06	$< 5\%$	$\phi_{\text{conv}}, \phi_{\text{muon}}$	no
Flux	hadronic interaction model	SYBILL 2.1	$\pm 10 \ldots 25\%$	$\phi_{\text{conv}}, \phi_{\text{prompt}}, \phi_{\text{muon}}$	yes
Flux	neutrino-nucleon cross section	CSMS	$< 5\%$	ϕ_{ν}, $\phi_{\text{conv}}, \phi_{\text{prompt}}$	no

Table 6.2: Systematic uncertainties which are typically considered for a measurement of the diffuse astrophysical neutrino flux. They are grouped into two categories, i.e. uncertainties of detector properties and of flux and interaction models. Each uncertainty is quoted with respect to the baseline model. It is indicated which observables or flux components are affected and how relevant the effect is in this analysis. See text for full explanation.

The light yield of electromagnetic and hadronic showers in ice was parameterized using GEANT4 with negligible uncertainties [202, 219]. An important systematic uncertainty, however, is given by the **hadronic shower energy**. Due to the contribution of neutral and heavy particles to the shower, the visible part is systematically lower than for electromagnetic showers (c.f. Section 3.1.3). Unfortunately, there is currently no way of distinguishing hadronic and electromagnetic showers in IceCube, although a recent proposal of using delayed light from muon decay and neutron capture is currently investigated [239]. Therefore, cascade energies are always reconstructed by assuming an electromagnetic shower as light source. This introduces a systematic bias of $+10 \ldots 20\%$ in the relevant energy range [226] which must be considered in this analysis.

The Antarctic ice is an important detector component and many observables are directly affected by model uncertainties of **light scattering and absorption** [211]. The baseline model is SPICELea, and systematic variations of the scattering and absorption coefficients are grouped into three pairs. Either the scattering or the absorption coefficients are individually increased by $+10\%$ or both are simultaneously decreased by -7%. This is due to the correlated effect that scattering and absorption have on the observable light pattern. An increase of the scattering coefficients extends the effective scattering path of a photon and hence increases the probability that it is absorbed before detection. Systematic variation of the light scattering and absorption in ice certainly affects energy reconstruction and may also introduce a small bias in directional reconstruction. For this analysis, it is predominantly important due to the shift in energy.

Another important component is the **ice anisotropy**, which is a modulation of the nominal scattering coefficient by $^{+4\%}_{-8\%}$ depending on the direction of photon propagation. The baseline model is incorporated in SPICELea [212]. The ice anisotropy affects the double cascade length and thereby the topology ID, in particular, as discussed in Chapter 5. It may also bias zenith angle reconstruction in particular due to the vertical anisotropy axis. An uncertainty of the aforementioned modulation size of the scattering coefficient can conservatively be estimated as $\pm 30\%$. Note that this is not a well-defined $1\,\sigma$-interval, but rather reflects the best knowledge due to different fitting methods of the ice anisotropy.

The optical properties of the **hole ice** into which an IceCube string is deployed are different from the surrounding bulk ice. The holes were drilled with hot water, which remained inside and froze after a string had been deployed. In the process, dissolved gases were pushed to the center and trapped there, forming the "bubble column". Both the ice of the drill hole and the bubble column are assumed to have a much shorter scattering length than the bulk ice. It is estimated to be 50 cm in the baseline model, which is used in this analysis. It is effectively incorporated in simulation and reconstruction by modulating the angular DOM acceptance. Although the optical properties of the hole ice are not well known, the corresponding variation of the angular DOM acceptance is estimated to be smaller than 15% [240]. It affects the reconstructed zenith angle, however, predominantly at energies much lower than the threshold of the high-energy starting event selection. Hole ice is therefore negligible in this analysis.

The most important uncertainty not related to detector properties is due to the limited knowledge of the highest-energy **cosmic-ray flux and composition**. The baseline model is the GaisserH3a cosmic-ray composition model with a modification in the "knee"-region of the cosmic-ray spectrum [118, 130]. The uncertainty is calculated from a global spline fit of the cosmic-ray flux model using measurement data from many different experiments and varies between $\pm 5\% \ldots 30\%$ depending on energy [241]. It affects the predicted atmospheric muon flux and both conventional and prompt atmospheric neutrino fluxes. The cosmic-ray model uncertainty is relevant in this analysis, because it is the largest contribution to the overall uncertainty of the entire atmospheric background.

The **ratio of pions and kaons** (π/K ratio) produced in cosmic-ray-induced air showers determines the individual contribution of ν_e and ν_μ to the conventional atmospheric neutrino flux (c.f. Section 2.2.2). The HKKMS06 model is used as baseline [125]. The π/K ratio is constrained to below 5% precision [49]. It depends on energy, because the decay length of a charged meson depends on its energy, whereas its interaction length is approximately constant in comparison. Due to their longer lifetime, charged pions are more likely to interact before decay than kaons at the same energy. Above the energy threshold of the high-energy starting event selection, the conventional atmospheric neutrino flux (of both ν_e and ν_μ) is predominantly generated in kaon production and decay in cosmic-ray-induced air showers, because pions are more likely to interact instead of decay [120]. Therefore, the π/K ratio is irrelevant for this analysis.

The **hadronic interaction model** is important for calculating predictions for any atmospheric flux component produced in cosmic-ray-induced air showers. The SYBILL 2.1 model is used as a baseline [238]. The uncertainty approximately ranges between $\pm 10\%$ and $\pm 25\%$ depending on the atmospheric lepton flux [242]. It is best constrained for the atmospheric muon flux, less for the atmospheric electron-neutrino, and least for the atmospheric muon-neutrino flux over a wide range of energies. In the relevant energy region, the overall uncertainties of the atmospheric flux predictions are dominated by the cosmic-ray model rather than the hadronic interaction model. However, it is still a relevant uncertainty that is considered in this analysis.

The **neutrino-nucleon cross section** is used to calculate a rate prediction for any neutrino flux (c.f. Section 3.1.1). The CSMS model is used as a baseline with a given uncertainty of less than 5% in the relevant energy region for both NC and CC interactions [243]. A recent measurement of the neutrino-nucleon cross section with the IceCube detector confirmed the theoretical prediction in this energy range [244]. Note that a variation of the neutrino-nucleon cross section equally affects all predicted rates from any astrophysical or atmospheric neutrino flux. It neither affects the ability to distinguish astrophysical from atmospheric neutrino interactions nor distorts the neutrino flavor composition. In addition, the uncertainty of the neutrino-nucleon cross section is small compared to other error sources. Hence, it is mostly negligible in this analysis and only relevant for estimating event rates induced by astrophysical neutrinos (see Section 6.3.1).

Relevant systematic uncertainties do not need to be treated individually. Instead, some are combined into a single nuisance parameter depending on the affected observable. Others are directly incorporated into the uncertainty of atmospheric flux components. In the following all model parameters with a prior as listed in Table 6.1 are discussed with respect to the relevant systematic uncertainties listed in Table 6.2. Nuisance parameters are modeled via a symmetric Gaussian prior into the likelihood as defined in Equation 6.2. Where a systematic error is expected to be asymmetrical, the larger value of the two confidence boundaries is used.

Atmospheric Muon Flux The atmospheric muon flux component is constrained by a prior that is partially derived from experimental data. On the one hand, the spectral shape is determined by the pure-proton extragalactic composition of the GaisserH3a model. The pure-proton composition is chosen because it gives the largest contribution of highly energetic single muons from air showers. On the other hand, the normalization is estimated using the tagging method described in [43]. The requirement of the veto-based event selection (c.f. Section 4.2) is inverted to obtain a set of events that enter the detector from the outside and are tagged in the veto region. Adjacent to the outer veto region, a (smaller) inner veto region is defined with the same properties and requirements as used in the event selection. The passing fraction is estimated by counting events that are tagged in the outer veto region and pass the inner veto region without detection. The atmospheric muon background is estimated by scaling the number of tagged events to the full detector size under the assumption that the passing fraction stays constant for different veto regions. This method yields a total of 25.2 ± 7.3 atmospheric muons in six years of high-energy starting events. Note that the error is statistical and determined by the number of tagged events.[1] However, as the atmospheric muon normalization is obtained directly from experimental data it is not dependent on model assumptions. The prior 1 ± 0.3 of the atmospheric muon flux quoted in Table 6.1 refers to this normalization. The systematic errors of the observable distributions due to the uncertainty of the atmospheric muon flux are shown in Figure 6.4. Note that this also involves the large statistical error of the Monte Carlo simulation. Most atmospheric muons have an energy below the 60 TeV threshold of the analysis.

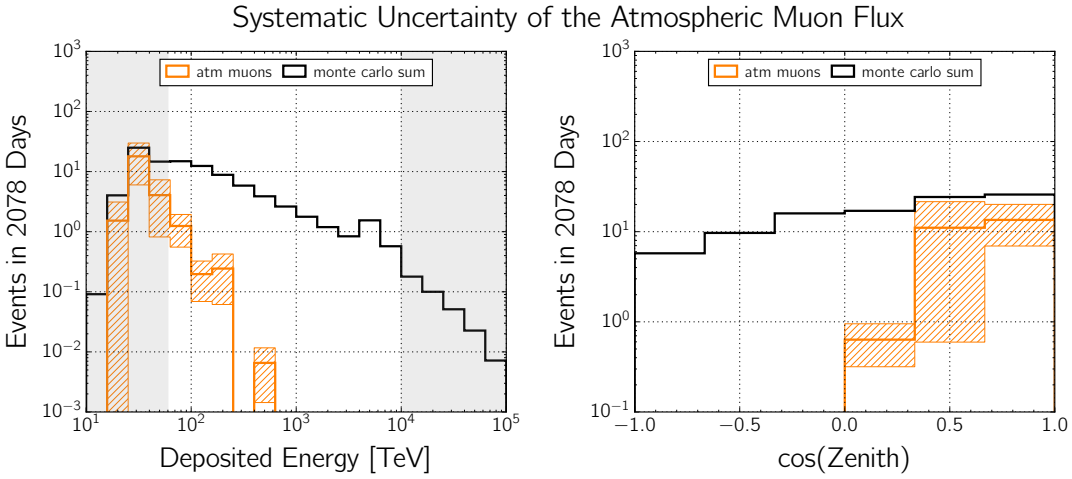

Figure 6.4: Observable distributions including systematic error due to the uncertainty of the atmospheric muon flux. The expected number of events in the six-year high-energy starting event sample is depicted as a function of the total deposited energy (left) and the zenith angle (right). The expectation of the atmospheric muon flux is shown including systematic uncertainties as shaded areas. In addition, the sum of all Monte Carlo templates is shown for comparison. Only the energy region between 60 TeV and 10 PeV is included in the fit.

[1] The quoted error deviates from the naive Poisson expectation of $\sqrt{25.2} \simeq 5$. The actual number of tagged events is exactly 12 and scaled up by a factor of 2.1 as the outer veto region makes up approximately half of the detector volume. The Poisson error must also be scaled up, yielding $\sqrt{12} \cdot 2.1 \simeq 7.3$.

Conventional Atmospheric Neutrino Flux The conventional atmospheric neutrino flux produced by the decay of charged pions and kaons in cosmic-ray-induced air showers is constrained by a prior that combines three different systematic uncertainties. First, the cosmic-ray flux and composition model and, second, the hadronic interaction model are taken into account as they directly alter the expected event rate due to atmospheric neutrino interactions. Third, the uncertainty of the hadronic shower energy is considered for the upper error calculation. As there is currently no way to distinguish electromagnetic and hadronic showers, it makes more sense to incorporate this error into the uncertainty of the conventional atmospheric neutrino flux. This is reasonable, because the flux has a steeper spectrum than the astrophysical or prompt atmospheric neutrino fluxes. Therefore, it generates a larger contribution of events at lower energies where the light yield of hadronic cascades is particularly smaller than of electromagnetic cascades. This may systematically underestimate the conventional atmospheric neutrino flux and corresponds to a lower limit of interactions close to the threshold of the event selection. The combined variation of the conventional atmospheric neutrino flux due to all three aforementioned uncertainties is estimated to be less than 30% as initially discussed in [43]. The prior of 1 ± 0.3 quoted in Table 6.1 is given in units of the HKKMS06 model as a baseline that corresponds to the best-fit value of a recent measurement using six years of through-going muon-neutrino events in IceCube [49]. The systematic errors of the observable distributions due to the uncertainty of the conventional atmospheric neutrino flux are shown in Figure 6.5.

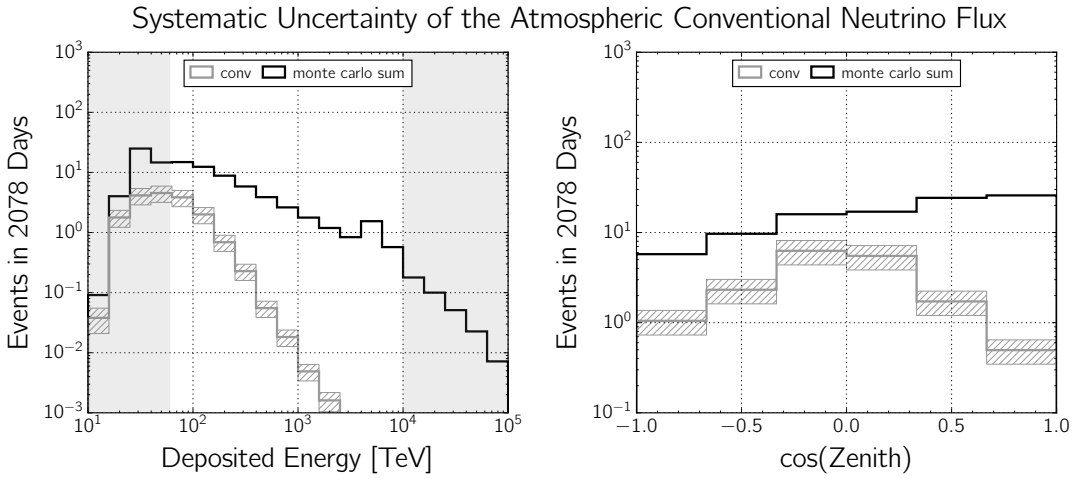

Figure 6.5: Same as Figure 6.4, but for the conventional atmospheric neutrino flux.

Prompt Atmospheric Neutrino Flux The prompt atmospheric neutrino flux generated in the decay of charmed mesons in cosmic-ray-induced air showers is constrained by an upper limit. Because no prompt neutrino flux has been observed so far, the central value of the prior is set to zero. The $1\,\sigma$-uncertainty of the prior is estimated to be $+65\%$ in units of the ERS model, which corresponds to the 90% upper limit of $1.06 \times$ ERS obtained in the six-year through-going muon-neutrino analysis [49]. In Figure 6.6, the upper limit of the prompt atmospheric neutrino flux is shown for the observable distributions. Note that the choice of centering the prior to zero is based on the argument that a lack of observation at the given level is a stronger argument than its theoretical prediction. Most importantly, however, a prompt atmospheric neutrino flux is not a significant background for tau-neutrino interactions. This is due to the increasing efficiency of the self-veto effect with energy and the central sensitivity region to tau-neutrino interactions at high energies between $\sim 100\,\text{TeV} - 10\,\text{PeV}$ (c.f. Section 4.4). The negligible effect of a prompt atmospheric neutrino flux on the tau-neutrino sensitivity will be shown in Section 6.3.2.

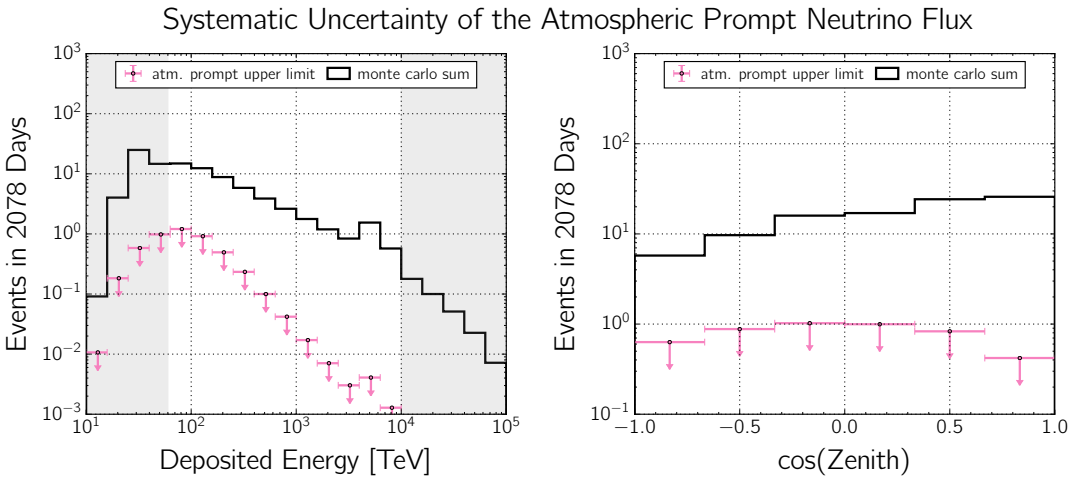

Figure 6.6: Same as Figure 6.4, but for the prompt atmospheric neutrino flux. The distribution is depicted for the upper limit of 0.65 × ERS at 68% confidence level as discussed in the text.

Energy Scale The reconstructed energy is affected by the ±10% uncertainty of the relative DOM efficiency and the $^{+10\%}_{-7\%}$ uncertainty of the scattering and absorption coefficients of the ice model. The energy scale is a nuisance parameter that incorporates both uncertainties. The combined energy uncertainty is approximately ±15% as could be shown during the development of a recent measurement of the astrophysical neutrino flux using cascade events [61]. In the relevant energy region of the high-energy starting event selection, a variation of either the DOM efficiency or the scattering and absorption in the ice scales linearly with the reconstructed energy. Therefore, the prior 1 ± 0.15 of the energy scale as listed in Table 6.1 corresponds to a linear variation of ±15% centered around the nominally reconstructed energy. The systematic errors of the affected observable distributions due to the uncertainty of the energy scale are shown in Figure 6.7. Note that boundary effects play a particular role for the low-energy region of the event selection, in which the dominating atmospheric background may be moved in either direction across the analysis threshold of 60 TeV.

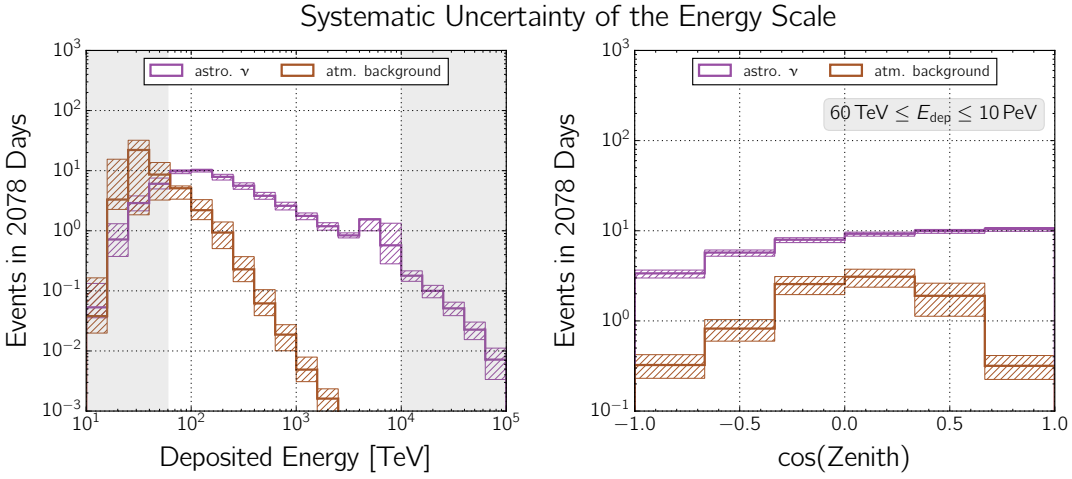

Figure 6.7: Observable distributions including systematic error due to the uncertainty of the energy scale. The expected number of events is depicted as a function of the total deposited energy (left) and the zenith angle (right). The uncertainties are shown separately for the sum of astrophysical neutrinos and for the sum of atmospheric background events. The zenith angle distribution is only shown for the energy region between 60 TeV and 10 PeV as marked for the distribution of the total deposited energy.

Ice Anisotropy Scale A variation of the size of the ice anisotropy introduces a bias of the reconstructed length and hence alters the topology ID by redistributing single cascade-like and double cascade-like events across the threshold of 10 m (c.f. Chapter 5). The uncertainty of the ice anisotropy is parameterized as a directional-dependent length shift (see Appendix A). The ice anisotropy scale is a nuisance parameter with a prior of 1 ± 0.3 as quoted in Table 6.1. It is given in units of the SPICELea ice model in which the ice anisotropy corresponds to a modulation of the nominal light scattering of $+4\%$ and -8% along the horizontal anisotropy axes and $+4\%$ along the vertical anisotropy axis. The length bias vanishes exactly at these ice anisotropy values modeled in SPICELea. The uncertainty is estimated as $\pm 30\%$, which corresponds to a length bias of a few meters depending on the direction of the event. The systematic errors of the affected observable distributions are depicted in Figure 6.8.

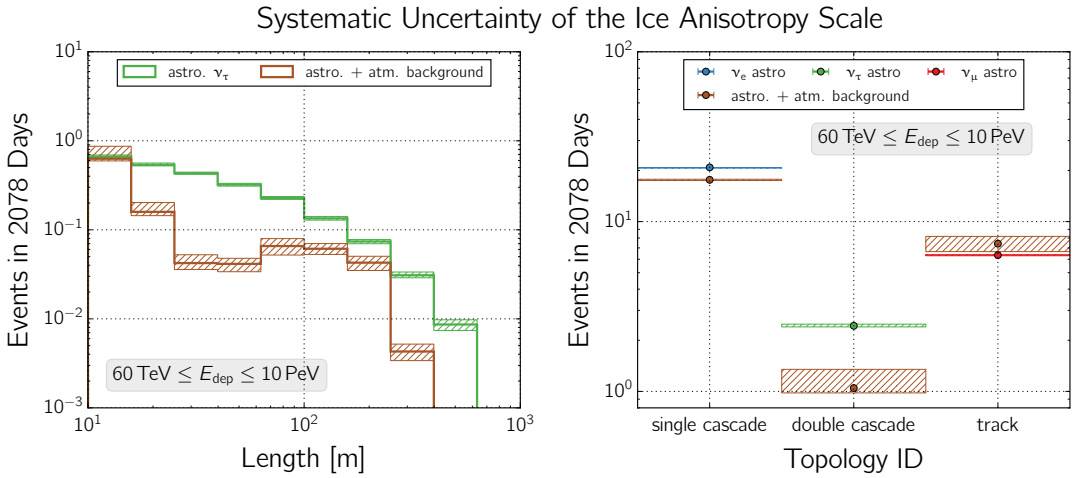

Figure 6.8: Observable distributions including systematic error due to the uncertainty of the ice anisotropy scale. In the left plot, the number of events expected in the double cascade sample is shown as a function of the length. The uncertainties are shown for astrophysical tau-neutrino interactions and for the sum of all other astrophysical and atmospheric events. The number of events expected in each topology sample is depicted in the right plot. For each topology bin, the expectation is divided into the most relevant flux contributions (astrophysical ν_e for single cascade, ν_τ for double cascade, and ν_μ for track events) and into the individually different background contributions (all remaining astrophysical and atmospheric events).

The **binning of each observable** is chosen such that systematic uncertainties that are not modeled into the analysis as nuisance parameters do not have a significant impact on the result. In particular, the binning of the zenith angle is chosen to be very coarse (six bins in total), because relevant ice model uncertainties that affect the zenith angle are not treated otherwise. The zenith angle is particularly important for distinguishing atmospheric from astrophysical neutrinos, but less important for a measurement of the astrophysical neutrino flavor composition, in particular with respect to constraining the tau-neutrino fraction. Therefore, the ice model uncertainties with respect to the zenith angle are not treated differently than in previous publications [4, 43, 44, 50]. The total deposited energy is divided into five bins per decade. This much finer choice of binning is possible as the uncertainty of the energy scale is incorporated into the fit. It is also necessary, because a more precisely modeled spectral shape of the flux components is important for the fit of the astrophysical spectral index. The double cascade length is divided into five bins per decade. This choice of binning is a compromise between optimizing the sensitivity to tau-neutrino interactions and reducing the statistical error of the Monte Carlo simulation. Furthermore, the resulting bin size is much larger the median resolution of ~ 2 m, as discussed in Section 4.3.3. The discussed binning of each observable is used in the likelihood fit and to plot the distributions as shown in Figure 6.3.

It is important to keep the **statistical error of the Monte Carlo simulation** as low as possible for each bin of the likelihood because it is not included in the fit. A method to incorporate the statistical Monte Carlo error into the likelihood as discussed in [245] is not considered in the scope of this thesis. Instead, the statistical error is kept well below 10% in the relevant observable phase space, where a precise background description is important. As mentioned in Section 6.2.2, the atmospheric muon flux is an exception due to lack of muon simulation data. This is the reason for excluding the energy region below 60 TeV from the likelihood fit, where atmospheric muons make up the dominant contribution to the observed number of events. Note that this problem has remained the same since the development of the high-energy starting event selection [43]. However, it is even more relevant to the analysis presented here, because the entire high-energy starting event sample is split into three topology samples, which further increases the statistical error. In the double cascade sample, the event expectation is so low that there is not a single simulated atmospheric muon event left. If this causes the overall Monte Carlo template to contain empty bins, it would be problematic for the likelihood fit in case of an observed event in such a bin. However, the overall background template predominantly contains astrophysical neutrino events for which a sufficient amount of simulation data is available. Empty bins in the template are thereby avoided in the relevant observable phase space. It is nevertheless important to estimate an upper limit of atmospheric muons contributing to the background of the double cascade sample. This can be achieved by calculating the misidentification fraction of track events induced by conventional atmospheric neutrino interactions and converting this to the expected background contamination from atmospheric muon events. The implicit assumption that the track topology caused by atmospheric neutrinos and atmospheric muons is sufficiently similar is reasonable. The usage of conventional atmospheric neutrino events guarantees that the underlying spectrum is similar to the atmospheric muon flux. Above a deposited energy of 60 TeV, conventional atmospheric neutrino interactions contribute a total of 5.3 track events (with a negligible statistical error) in the six-year data sample, of which ~ 0.16 events are expected to be misidentified as double cascade events. This corresponds to a misidentification fraction of $\sim 3.1\%$. Scaling the total atmospheric muon background of 1.7 ± 0.8 events above 60 TeV with this fraction and incorporating the statistical uncertainty yields an upper limit of ~ 0.08 atmospheric muon events in the double cascade sample. This is well below the dominant astrophysical neutrino background, as will be discussed in Section 6.3.1.

Another question is the potential contribution of **atmospheric tau-neutrino interactions** in the event sample. As discussed in Section 2.2.2, only the prompt atmospheric neutrino flux can generate tau-neutrinos is the decay of the D_s and the subsequent decay of the tau. The expected flavor composition is $\nu_e : \nu_\mu : \nu_\tau \simeq 1 : 1 : 0.1$ in the relevant energy range. Note that this is not modeled in the likelihood fit, because it is deemed insignificant. An upper limit of this contribution can be estimated in the following way. First, the energy-integrated identification efficiency of double cascade events induced by astrophysical tau-neutrino interactions is calculated for an $E_\nu^{-2.8}$ spectrum. This is similar to the modeled prompt atmospheric neutrino spectrum and allows for a reasonable estimate. Second, the number of electron-neutrino events expected from a prompt flux at or below the 90% upper limit of $1.06 \times$ ERS as obtained in [49] is calculated for the same energy range. Third, this expectation is scaled down by the aforementioned flavor composition to obtain the upper limit of the tau-neutrino fraction of the prompt flux. Fourth, this value is multiplied by the fraction of tau-neutrinos interacting in the "double bang" channel and last, with the energy-integrated identification efficiency obtained from the astrophysical $E_\nu^{-2.8}$ tau-neutrino flux. This method yields an upper limit of ~ 0.05 identifiable tau-neutrino interactions from a prompt atmospheric neutrino flux in the six-year data sample. Assuming the benchmark $E_\nu^{-2.3}$ spectrum for the astrophysical neutrino flux, the observation of a double cascade event would imply that the inducing tau-neutrino is ~ 50 times more likely to be of astrophysical than of atmospheric origin (see Table 6.3).

6.3 Sensitivity

The goal of the analysis is to measure the astrophysical neutrino flavor composition with the explicit focus of constraining the tau-neutrino fraction. The sensitivity of the analysis is therefore discussed with respect to two different aspects of the same measurement. The Asimov dataset is constructed by using the atmospheric flux components and the benchmark per-flavor astrophysical neutrino flux of $\phi_\nu(E_\nu) = 1.5 \cdot 10^{-18} (E_\nu/100\,\mathrm{TeV})^{-2.3}\,\mathrm{GeV}^{-1}\,\mathrm{cm}^{-2}\,\mathrm{sr}^{-1}\,\mathrm{s}^{-1}$ with a flavor composition of $\nu_e : \nu_\mu : \nu_\tau = 1 : 1 : 1$, as discussed in Section 6.2.1. A profile likelihood fit is performed on this dataset by employing the observables, as discussed in Section 6.2.2, and the systematic uncertainties, as discussed in Section 6.2.3. The astrophysical neutrino flavor composition is constrained by evaluating a likelihood ratio in a profile likelihood scan and estimating confidence regions using Wilks' theorem. The sensitivity to the tau-neutrino fraction is examined in two ways. First, it is defined as the median confidence level for which $\phi_{\nu_\tau} = 0$ can be excluded assuming the benchmark model. Second, it is defined as the median upper limit that can be derived in the absence of a detectable tau-neutrino interaction.

6.3.1 Signal and Background Expectations

In the six-year high-energy starting event sample, a total atmospheric background of 25.2 ± 7.3 atmospheric muons and $17.4^{+8.0}_{-4.4}$ atmospheric neutrinos is expected. Above a deposited energy of 60 TeV these numbers reduce to an atmospheric muon background of 1.7 ± 0.8 and an atmospheric neutrino background of $7.3^{+3.9}_{-1.8}$. The uncertainties include a prompt atmospheric neutrino flux that has not yet been measured but is only constrained by an upper limit. An overview of the expected number of events for the baseline models and statistical and systematic uncertainties as discussed in the previous sections is given in Table 6.3. It is divided into the different astrophysical and atmospheric flux components as well as the individual topology samples. Assuming the aforementioned benchmark astrophysical neutrino flux and composition, it can be seen that the majority of the total ~ 56 events expected between 60 TeV and 10 PeV are induced by astrophysical neutrinos. Most of these are electron-, fewer tau-, and least muon-neutrino events as expected from the flavor-dependent neutrino effective areas of the event selection (c.f. Section 4.2). As discussed in Section 6.2.2, electron-neutrino events are the dominant contribution to the single cascade sample, tau-neutrino events to the double cascade sample, and muon-neutrino events to the track sample. Note that neutrinos of all flavors contribute to the single cascade sample due to neutral-current interactions. The fraction of tau-neutrino events in the single cascade sample is particularly large due to the limited resolution of the double cascade topology. Also note that there is a significant contribution of tau-neutrino interactions in the track sample due to the muonic decay channel of the tau. It can be deduced from the number of events expected from each astrophysical neutrino flux that the ternary topology ID is able to constrain each flavor fraction.

The expected number of **signal and background events** in the double cascade sample is most interesting, as these determine the sensitivity to the tau-neutrino fraction. A total of

$$2.43^{+0.13}_{-0.13} \quad \text{signal events and} \tag{6.7}$$

$$1.05^{+0.29}_{-0.10} \quad \text{background events} \tag{6.8}$$

are expected in the double cascade sample between 60 TeV and 10 PeV deposited energy. These expectation values are calculated by assuming the benchmark astrophysical neutrino flux and composition. In this context, signal is defined as all astrophysical tau-neutrino interactions and background is defined as the sum of all remaining events induced by any astrophysical or atmo-

Flux Component	Expected Events in Each Sample			
	Total	**Single Cascade**	**Double Cascade**	**Track**
ϕ_{ν_e}	$22.14^{+1.39}_{-1.64}$	$20.85^{+1.36}_{-1.64}$	$0.65^{+0.25}_{-0.05}$	$0.64^{+0.05}_{-0.05}$
ϕ_{ν_μ}	$10.24^{+0.50}_{-0.60}$	$3.70^{+0.26}_{-0.32}$	$0.20^{+0.01}_{-0.02}$	$6.34^{+0.42}_{-0.51}$
ϕ_{ν_τ}	$14.31^{+0.81}_{-1.00}$	$10.50^{+0.80}_{-0.99}$	$2.43^{+0.13}_{-0.13}$	$1.38^{+0.09}_{-0.10}$
ϕ_{muon}	$1.70^{+0.81}_{-0.80}$	$0.01^{+0.01}_{-0.01}$	< 0.08	$1.69^{+0.80}_{-0.80}$
ϕ_{conv}	$7.32^{+1.77}_{-1.84}$	$3.42^{+1.23}_{-1.23}$	$0.20^{+0.07}_{-0.08}$	$3.70^{+1.27}_{-1.36}$
ϕ_{prompt}	< 3.46	< 2.81	< 0.09	< 0.56
ϕ_{sum}	$55.71^{+4.31}_{-2.84}$	$38.48^{+3.46}_{-2.30}$	$3.48^{+0.31}_{-0.16}$	$13.75^{+1.67}_{-1.66}$

Table 6.3: Number of events expected from different flux components for the total the six-year high-energy starting event sample and when split into the single cascade, double cascade, and track samples. Only events with a total deposited energy between 60 TeV and 10 PeV are considered. The assumed flux models and 1 σ-uncertainties are given in Table 6.1.

spheric flux component.[2] The quoted errors include all statistical and systematic uncertainties as described in Section 6.2.3. Note that the errors of the signal expectation seem comparably low, because they are not affected by the large uncertainties of the atmospheric background. However, it is important to realize that the expected number of identifiable tau-neutrino interactions strongly depends on the assumed spectral shape (and trivially on the flavor composition) of the astrophysical neutrino flux. Those properties are to be measured and are therefore modeled as free fit parameters ϕ_{ν_e}, ϕ_{ν_μ}, ϕ_{ν_τ}, and γ (c.f. Table 6.1). Consequently, they are not incorporated into the quoted uncertainty of the expected signal rate. However, fixing the flavor composition to $\nu_e : \nu_\mu : \nu_\tau = 1 : 1 : 1$ while changing the spectral shape of the astrophysical neutrino flux drastically increases the variation of the expected number of signal events to $2.43^{+0.34}_{-1.96}$. This will be discussed in greater detail in Section 6.3.4.

In addition to the number of expected events in each topology sample as quoted in Table 6.3, the corresponding **observable distributions** are shown in Figure 6.9. Each distribution is divided into the astrophysical neutrino flux components ($\phi_{\nu_e}, \phi_{\nu_\mu}, \phi_{\nu_\tau}$) and the sum of all atmospheric flux components ($\phi_{\text{muon}} + \phi_{\text{conv}} + \phi_{\text{prompt}}$). Statistical and systematic uncertainties are marked as shaded areas. Note that zenith angle and length are only shown for events with a total deposited electromagnetic-equivalent energy between 60 TeV and 10 PeV, as these are the boundaries of the likelihood fit. A comparison of the energy and zenith angle distributions for the electron- and tau-neutrino flux components in the single cascade sample reveals the degeneracy between both. Apart from the Glashow resonance for $\bar{\nu}_e$ events at ~ 6.3 PeV deposited energy, their shapes are approximately equal. Consequently, a hypothetical observation of the energy and zenith angle distributions as depicted in the single cascade sample would not require the presence of a tau-neutrino flux but could fully be explained with an electron-neutrino flux. It is only the additional information of the double cascade sample that allows constraining the astrophysical tau-neutrino flux. It can be seen that the length distributions, in particular, are very different for signal and background events. Although it is clear that the overall event expectation in the double cascade sample is rather low, the ternary topology ID is still the most sensitive method to tau-neutrino interactions that has been developed so far.

[2] It could be argued that the signal should only be defined by tau-neutrino interactions which induce a double cascade event topology, i.e. by excluding NC interactions and muonic tau decays (c.f. Section 4.1). However, the model parameter of interest is the total tau-neutrino flux and not its fraction of induced double cascade events. Due to the relatively low misidentification fraction of the double cascade event topology, the expected number of signal events for each of the two possible definitions differ by less than 5%.

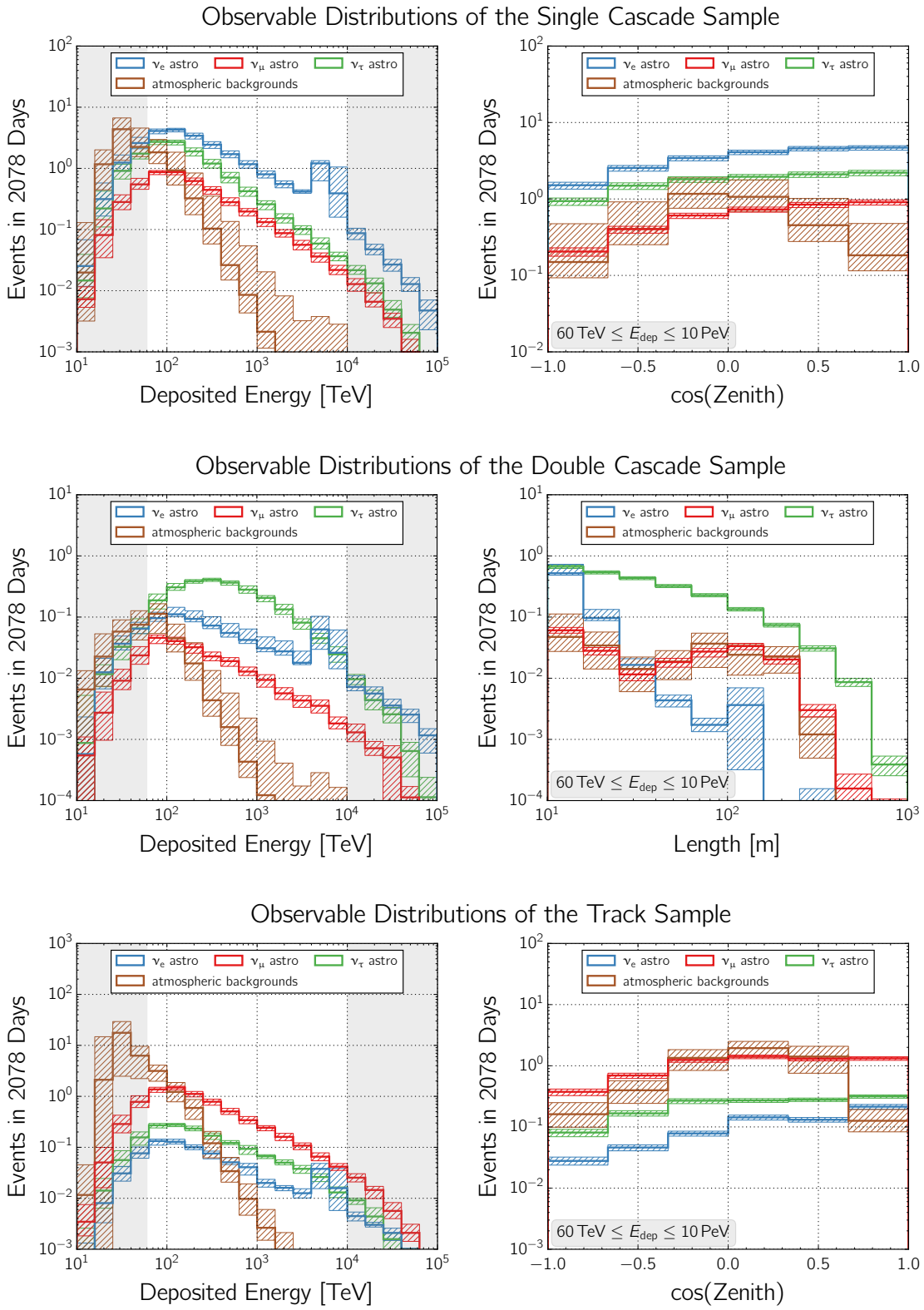

Figure 6.9: Observable distributions for the single cascade, double cascade, and track event samples including systematic uncertainties. The expected number of events in six years of data is depicted as a function of the deposited energy (left) and zenith angle (right) for the single cascade sample (top) and the track sample (bottom) and as a function of the deposited energy (left) and double cascade length (right) for the double cascade sample (center). In all plots, the astrophysical neutrino flux is shown individually for each flavor. In addition, the sum of atmospheric muons and conventional atmospheric neutrinos is shown as atmospheric background. The upper limit on the prompt atmospheric neutrino flux is included in the systematic uncertainties shown as shaded areas.

6.3.2 Astrophysical Tau-Neutrino Flux Sensitivity

The sensitivity to an astrophysical tau-neutrino flux is defined via a nested likelihood ratio test of different hypotheses. The likelihood as introduced in Section 6.1 is constructed using the model parameters, observables, and uncertainties that were discussed in Section 6.2. A realization of the high-energy starting event sample for six years of data collection is fitted in order to constrain the astrophysical tau-neutrino flux ϕ_{ν_τ} as the main parameter of interest. The sensitivity of this method is constructed in two ways:

1. **Detection sensitivity**: median confidence level $\alpha_{\nu_\tau}^{\text{det}}$ at which $\phi_{\nu_\tau} = 0$ can be excluded, assuming the benchmark astrophysical $E_\nu^{-2.3}$ flux and composition $\nu_e : \nu_\mu : \nu_\tau = 1 : 1 : 1$.
2. **Upper limit**: median upper limit flux $\phi_{\nu_\tau}^{\text{u.l.}}$ for which $\phi_{\nu_\tau} > \phi_{\nu_\tau}^{\text{u.l.}}$ can be excluded at 90% confidence level, assuming an $E_\nu^{-2.3}$ flux and a composition of $\nu_e : \nu_\mu : \nu_\tau = 1 : 1 : 0$.

Both are calculated using the Asimov dataset and therefore correspond to the median outcome of a hypothetical set of pseudo experiments. Confidence levels are calculated via likelihood ratio tests using Wilks' theorem (c.f. Section 6.1). Note that this may not be strictly correct, because the astrophysical tau-neutrino flux is bounded ($\phi_{\nu_\tau} \geq 0$), and the constraining sample size is small ($\sim 1 - 3$ double cascade events). The validity of Wilks' theorem is examined by performing Monte Carlo pseudo experiments for both the median detection sensitivity and the median upper limit. Nevertheless, any quoted sensitivity can only to be understood as an estimate on the median expected outcome of the measurement under the assumption that the modeled benchmark astrophysical neutrino flux and composition are realized in nature.

Detection sensitivity The detection sensitivity $\alpha_{\nu_\tau}^{\text{det}}$ is constructed via the likelihood ratio as defined in Equation 6.5 between the hypothesis where the tau-neutrino flux is fixed to $\phi_{\nu_\tau} = 0$ and where it is free to float to its best-fit value $\hat{\phi}_{\nu_\tau}$, i.e.

$$\left(\exists\, \alpha_{\nu_\tau}^{\text{det}}\right)\ \lambda_c = -2 \ln \left(\frac{\mathcal{L}\left(\boldsymbol{n} | \boldsymbol{\mu}(\phi_{\nu_\tau} = 0, \hat{\hat{\boldsymbol{\theta}}}, \hat{\hat{\boldsymbol{\xi}}})\right)}{\mathcal{L}\left(\boldsymbol{n} | \boldsymbol{\mu}(\hat{\phi}_{\nu_\tau}, \hat{\boldsymbol{\theta}}, \hat{\boldsymbol{\xi}})\right)} \right) \implies f(\lambda \leq \lambda_c) = 1 - \alpha_{\nu_\tau}^{\text{det}}. \tag{6.9}$$

The likelihood $\mathcal{L}$ is defined in Equation 6.2 and the "observed" data $\boldsymbol{n}$ is given by the Asimov dataset. Aside from ϕ_{ν_τ} as the parameter of interest, the remaining fit parameters are given by $\boldsymbol{\theta} = (\phi_{\nu_e}, \phi_{\nu_\mu}, \gamma)$ and $\boldsymbol{\xi} = (\phi_{\text{muon}}, \phi_{\text{conv}}, \phi_{\text{prompt}}, \xi_E, \xi_A)$ as defined in Table 6.1. The global best-fit values are denoted by $\{\hat{\boldsymbol{\theta}}, \hat{\boldsymbol{\xi}}\}$ and the conditional best-fit values for the test hypothesis by $\{\hat{\hat{\boldsymbol{\theta}}}, \hat{\hat{\boldsymbol{\xi}}}\}$. The test hypothesis where the tau-neutrino flux is fixed to zero is a nested case of the best-fit hypothesis where all parameters are free. Consequently, the fit of the test hypothesis has one degree of freedom less than the fit of the test hypothesis. Assuming that Wilks' theorem holds, the exact test statistic distribution from Monte Carlo simulation is not required but can be modeled. In the background-only model where the true injected astrophysical tau-neutrino flux is $\phi_{\nu_\tau} = 0$, the distribution of the likelihood ratio in Equation 6.9 can be empirically modeled by a function $f(\lambda) = 0.5\,\delta(\lambda) + 0.5\,\chi^2_{k=1}(\lambda)$, where $\delta(\lambda)$ is the Dirac delta function. The reason is that the test statistic distribution is expected to peak at $\lambda = 0$, because the size of the signal sample is small and, consequently, the best-fit value of the tau-neutrino flux is expected close to its boundary of $\phi_{\nu_\tau} = 0$. Therefore, the $\delta(\lambda)$-function describes the large peak at $\lambda = 0$ and the χ^2-function describes the tail for $\lambda > 0$. The factor 0.5 is based on the assumption that the underlying parameter distribution is symmetrical and that the bound at $\phi_{\nu_\tau} = 0$ prohibits the best-fit values from being negative for half of all realizations. The detection sensitivity $\alpha_{\nu_\tau}^{\text{det}}$ corresponds to the p-value of the cumulative distribution function $f(\lambda \leq \lambda_c)$ where a test statistic value larger than λ_c as defined in Equation 6.9 is only caused by a fraction $\alpha_{\nu_\tau}^{\text{det}}$ of all modeled realizations of the experiment. The detection sensitivity $\alpha_{\nu_\tau}^{\text{det}}$ is either quoted as a p-value or as an equivalent significance in units of a one-tailed Gaussian standard deviation.

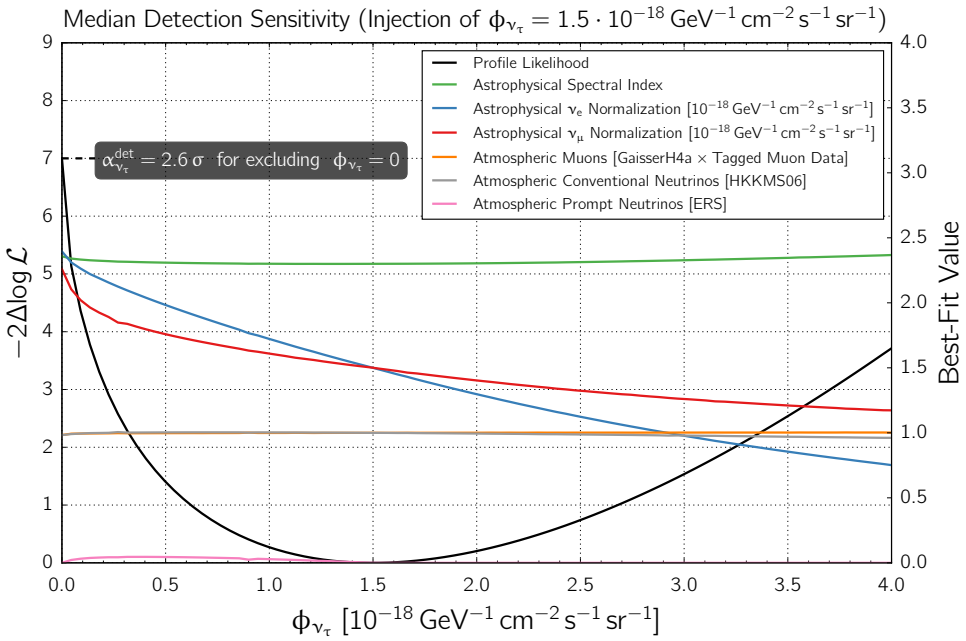

Figure 6.10: Median detection sensitivity. A profile likelihood scan of the ϕ_{ν_τ} flux normalization is depicted for the Asimov dataset. The black line corresponds to the test statistic (left axis) which is defined as the likelihood ratio $-2\Delta\log\mathcal{L}$ at a fixed value of ϕ_{ν_τ} in comparison to the best-fit value. The true injected flux normalization of $\phi_{\nu_\tau} = 1.5{\cdot}10^{-18}\,\mathrm{GeV}^{-1}\,\mathrm{cm}^{-2}\,\mathrm{sr}^{-1}\,\mathrm{s}^{-1}$ at 100 TeV assuming an $E_\nu^{-2.3}$ spectrum and the composition of $\nu_e : \nu_\mu : \nu_\tau = 1 : 1 : 1$ are recovered. The colored lines correspond to the conditional best-fit values of the remaining parameters (right axis). The median detection sensitivity $\alpha^{\mathrm{det}}_{\nu_\tau}$ defined in Equation 6.9 is obtained from the "observed" test statistic $\lambda_{\mathrm{obs}}(\phi_{\nu_\tau} = 0) \simeq 7$.

In Figure 6.10, a profile likelihood scan of the astrophysical tau-neutrino flux is depicted around its best-fit value. It is obtained by constructing the Asimov dataset with a modeled astrophysical neutrino flux of $\phi_\nu(E_\nu) = 1.5 \cdot 10^{-18}(E_\nu/100\,\mathrm{TeV})^{-2.3}\,\mathrm{GeV}^{-1}\,\mathrm{cm}^{-2}\,\mathrm{sr}^{-1}\,\mathrm{s}^{-1}$ per flavor and a composition of $\nu_e : \nu_\mu : \nu_\tau = 1 : 1 : 1$. The best-fit result is identical to the true injected flux which is the expected outcome for the Asimov dataset. The profile likelihood scan is performed by setting $\phi_{\nu_\tau} = \phi^{\mathrm{s.p.}}_{\nu_\tau}$ to the value of every scan point and varying all other parameters such that the likelihood is maximal. The test statistic of the profile likelihood scan is calculated by $-2\Delta\log\mathcal{L} = -2\big(\ln\mathcal{L}\big(\boldsymbol{n}|\boldsymbol{\mu}(\phi_{\nu_\tau} = \phi^{\mathrm{s.p.}}_{\nu_\tau}, \hat{\hat{\boldsymbol{\theta}}}, \hat{\hat{\boldsymbol{\xi}}}\big) - \ln\mathcal{L}\big(\boldsymbol{n}|\boldsymbol{\mu}(\hat{\phi}_{\nu_\tau}, \hat{\boldsymbol{\theta}}, \hat{\boldsymbol{\xi}})\big)$. The "observed" test statistic value $\lambda_{\mathrm{obs}}(\phi_{\nu_\tau} = 0) \simeq 7$ for excluding a vanishing astrophysical tau-neutrino flux can be read off the left-hand intercept of Figure 6.10. It translates to a median detection sensitivity of $\alpha^{\mathrm{det}}_{\nu_\tau} \simeq 2.6\,\sigma$ ($p \simeq 0.5\%$) which is obtained by modeling the background distribution of a true injected flux of $\phi_{\nu_\tau} = 0$ with $f(\lambda)$, as described above. Consequently, $\phi_{\nu_\tau} = 0$ can be excluded at a significance of $\sim 2.6\,\sigma$ for the median realization of the experiment and the assumed astrophysical neutrino spectrum and composition. Note that this estimate is compatible with the result of $\alpha^{\mathrm{det}}_{\nu_\tau} \simeq 2.3\,\sigma$ ($p \simeq 1.0\%$) obtained by generating the exact test statistic distributions from Monte Carlo pseudo experiments (see Appendix C.1).

In addition to the profile likelihood, the conditional best-fit values of the other parameters can be read off the right axis in Figure 6.10. All atmospheric flux components stay approximately constant throughout the entire phase space of the conditional fit. In particular, the atmospheric prompt neutrino flux cannot account for variations of the astrophysical tau-neutrino flux which is almost entirely compensated by the astrophysical electron- and muon-neutrino flux components. In fact, it can be seen that ϕ_{ν_τ} has a stronger correlation to ϕ_{ν_e} than to ϕ_{ν_μ}. Both observations are in agreement with the explanation given in Section 6.3.1 that the background for tau-neutrino

interactions in the constraining double cascade sample has a negligible atmospheric contribution. Instead, it is mostly dominated by astrophysical electron-neutrino interactions close to the length threshold of 10 m. Consequently, an increase in the astrophysical tau-neutrino flux is mostly compensated by a decrease of the astrophysical electron-neutrino flux and vice versa. Note that the injected flavor composition of $\nu_e : \nu_\mu : \nu_\tau = 1 : 1 : 1$ is recovered as can be seen at the intersection where $\phi_{\nu_e} = \phi_{\nu_\mu} = \phi_{\nu_\tau} = 1.5 \cdot 10^{-18}\,\mathrm{GeV}^{-1}\,\mathrm{cm}^{-2}\,\mathrm{sr}^{-1}\,\mathrm{s}^{-1}$. It can also be seen that the best-fit value of the spectral index does not significantly change with a variation of the astrophysical tau-neutrino flux. It becomes slightly softer with increasing ϕ_{ν_τ} to compensate for the lack of identifiable double cascade events that such a large flux would need to produce. The spectral index is best constrained by the single cascade sample. It contains the largest fraction of all observed events and is therefore statistically dominant (c.f. Table 6.3).

Upper limit The upper limit $\phi^{\text{u.l.}}_{\nu_\tau}$ is constructed via the likelihood ratio test

$$\left(\exists\, \phi^{\text{u.l.}}_{\nu_\tau}\right)\ \lambda_c = -2\ln\left(\frac{\mathcal{L}\left(\boldsymbol{n}|\boldsymbol{\mu}(\phi_{\nu_\tau} = \phi^{\text{u.l.}}_{\nu_\tau}, \hat{\hat{\boldsymbol{\theta}}}, \hat{\hat{\boldsymbol{\xi}}})\right)}{\mathcal{L}\left(\boldsymbol{n}|\boldsymbol{\mu}(\hat{\phi}_{\nu_\tau}, \hat{\boldsymbol{\theta}}, \hat{\boldsymbol{\xi}})\right)}\right) \implies \chi^2_{k=1}(\lambda \leq \lambda_c) = 90\% \tag{6.10}$$

by requiring that a true astrophysical tau-neutrino flux larger than $\phi^{\text{u.l.}}_{\nu_\tau}$ is excluded at 90% confidence level for the median realization in which $\phi_{\nu_\tau} = 0$. The median upper limit is obtained through the use of the Asimov dataset with a flavor composition of $\nu_e : \nu_\mu : \nu_\tau = 1 : 1 : 0$ and a rescaled per-flavor flux of $\phi_\nu(E_\nu) = 2.25 \cdot 10^{-18} (E_\nu/100\,\mathrm{TeV})^{-2.3}\,\mathrm{GeV}^{-1}\,\mathrm{cm}^{-2}\,\mathrm{sr}^{-1}\,\mathrm{s}^{-1}$. The total astrophysical neutrino flux thus stays constant and is not underestimated compared to the benchmark flavor composition $\nu_e : \nu_\mu : \nu_\tau = 1 : 1 : 1$. Wilks' theorem is used to calculate the confidence level from the cumulative distribution function $\chi^2_{k=1}(\lambda \leq \lambda_c)$ with $k = 1$ degree of freedom. Note that a χ^2-distribution is used (instead of $f(\lambda) = 0.5\,\delta(\lambda) + 0.5\,\chi^2_{k=1}(\lambda)$ used for the detection sensitivity), because the upper limit flux $\phi^{\text{u.l.}}_{\nu_\tau}$ is expected to be sufficiently far from the phase space boundary at $\phi_{\nu_\tau} = 0$. The median upper limit is obtained for the flux $\phi_{\nu_\tau} = \phi^{\text{u.l.}}_{\nu_\tau}$ for which the "observed" test statistic is $\lambda_{\text{obs}}(\phi_{\nu_\tau} = \phi^{\text{u.l.}}_{\nu_\tau}) = \lambda_c$, as defined above.

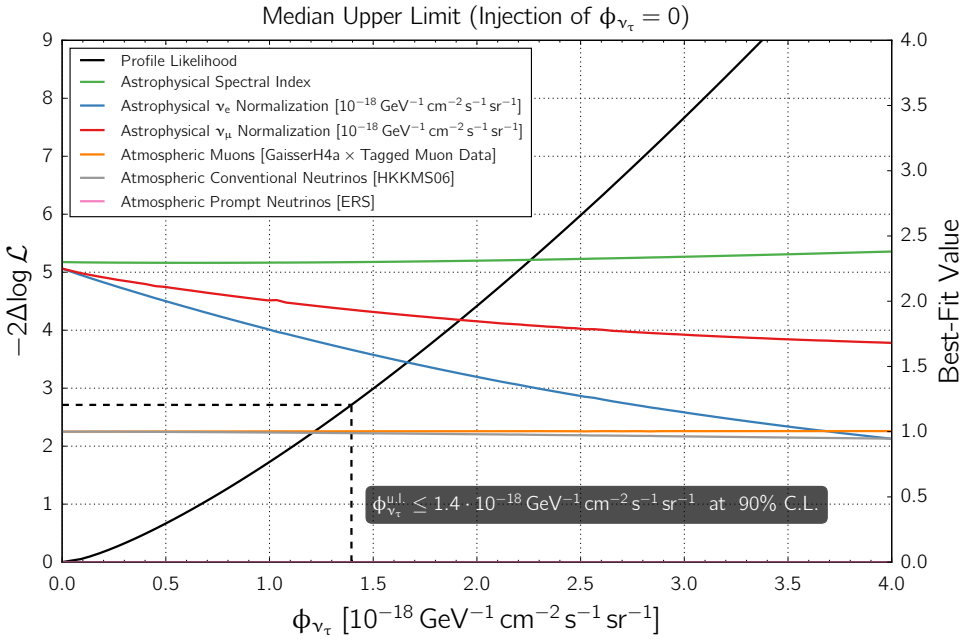

Figure 6.11: Median upper limit. Same as in Figure 6.10, but for a true injected flux of $\phi_{\nu_\tau} = 0$ assuming a flavor ratio of $\nu_e : \nu_\mu = 1 : 1$ and a rescaled $E_\nu^{-2.3}$ flux as explained in the text. The median upper limit $\phi^{\text{u.l.}}_{\nu_\tau}$ defined in Equation 6.10 is obtained from the "observed" test statistic $\lambda_{\text{obs}}(\phi_{\nu_\tau} = \phi^{\text{u.l.}}_{\nu_\tau}) \simeq 2.7$ corresponding to $\chi^2_{k=1}(\lambda \leq \lambda_{\text{obs}}) = 90\%$.

In Figure 6.11, a profile likelihood scan of the astrophysical tau-neutrino flux is depicted above its best-fit value of $\phi_{\nu_\tau} = 0$. As expected for the Asimov dataset, the injected flavor composition $\nu_e : \nu_\mu : \nu_\tau = 1 : 1 : 0$ is recovered. The median upper limit at 90% confidence level is $\phi^{\text{u.l.}}_{\nu_\tau}(E_{\nu_\tau}) \leq 1.4 \cdot 10^{-18} (E_{\nu_\tau}/100\,\text{TeV})^{-2.3}\,\text{GeV}^{-1}\,\text{cm}^{-2}\,\text{sr}^{-1}\,\text{s}^{-1}$. It is obtained from the "observed" test statistic value $\lambda_{\text{obs}}(\phi_{\nu_\tau} = \phi^{\text{u.l.}}_{\nu_\tau}) \simeq 2.7$ which corresponds to 90% CL, assuming that the test statistic distribution for the likelihood ratio as defined in Equation 6.10 follows a χ^2-distribution for a true injected flux of $\phi_{\nu_\tau} = \phi^{\text{u.l.}}_{\nu_\tau}$. Keep in mind that the likelihood fit allows all three flavor components to float independently and that the upper limit is therefore obtained without any restrictions on the $\nu_e : \nu_\mu$ ratio. Furthermore, the upper limit is compatible with the exact test statistic distribution obtained from performing pseudo experiments, which is described well by a χ^2-distribution (see Appendix C.1). In fact, the coverage of the cumulative test statistic distribution for values smaller than the "observed" $\lambda_{\text{obs}} \simeq 2.7$ is $(89 \pm 1)\%$, which agrees well with the desired confidence level of 90%.

In Figure 6.12, the sensitivity to the astrophysical tau-neutrino flux is compared for using the binary topology ID and the ternary topology ID, as described in Section 6.2.2. Evidently, the constraints are much weaker using the binary topology ID. This is expected because only an identification of the double cascade topology is unambiguously sensitive to tau-neutrino interactions. Note that it is nevertheless possible to constrain an upper limit flux to some extent in this case. This is due to the increase of the cascade-to-track ratio from $\sim 75\% : 25\%$ for $\nu_e : \nu_\mu : \nu_\tau = 1 : 1 : 0$ to $\sim 79\% : 21\%$ for $\nu_e : \nu_\mu : \nu_\tau = 1 : 1 : 1$ caused by the different tau decay channels. The median detection sensitivity $\alpha^{\text{det}}_{\nu_\tau} = 0.4\,\sigma$ ($p = 35\%$) and the median upper limit $\phi^{\text{u.l.}}_{\nu_\tau}(E_{\nu_\tau}) \leq 3.6 \cdot 10^{-18} (E_{\nu_\tau}/100\,\text{TeV})^{-2.3}\,\text{GeV}^{-1}\,\text{cm}^{-2}\,\text{sr}^{-1}\,\text{s}^{-1}$ are obtained equivalently by using the binary topology ID. Consequently, the constraints that are obtained using the ternary topology ID are considerably stronger.

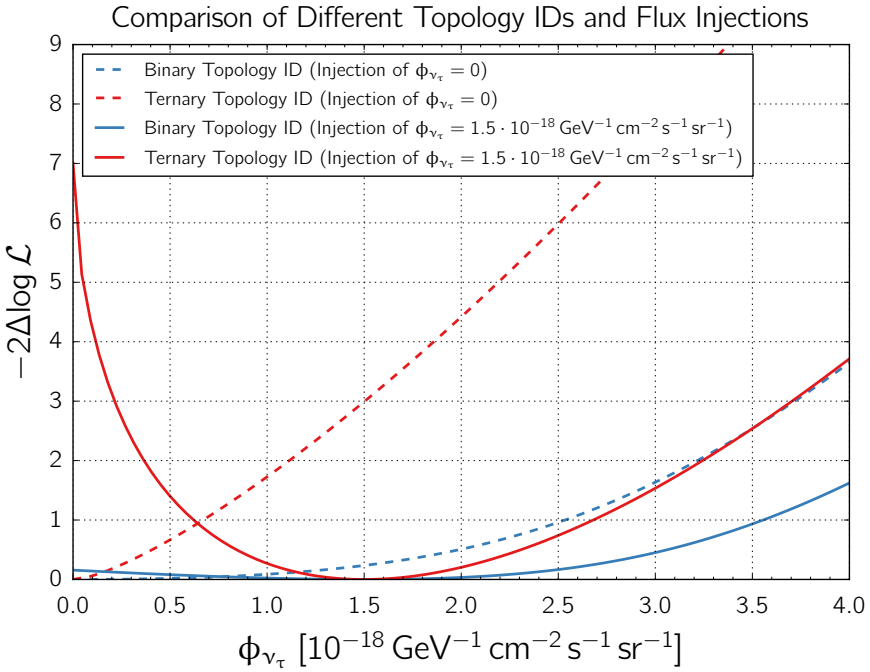

Figure 6.12: Comparison of the median profile likelihood scan of the ϕ_{ν_τ} flux normalization for fits using a binary or ternary topology ID and for different flux injections. The likelihood ratio $-2\Delta\log\mathcal{L}$ is obtained by comparing a fixed value of ϕ_{ν_τ} to the best-fit. The blue lines correspond to the binary and the red lines to the ternary topology ID (c.f. Section 6.2.2). The solid lines correspond to an injected flux normalization of $\phi_{\nu_\tau} = 1.5 \cdot 10^{-18}\,\text{GeV}^{-1}\,\text{cm}^{-2}\,\text{sr}^{-1}\,\text{s}^{-1}$ at 100 TeV for an $E_\nu^{-2.3}$ spectrum and a composition of $1 : 1 : 1$. The dashed lines correspond to an injected flux of $\phi_{\nu_\tau} = 0$ for a composition of $1 : 1 : 0$ assuming the same spectrum.

6.3.3 Astrophysical Neutrino Flavor Composition Sensitivity

The sensitivity of this analysis to an astrophysical tau-neutrino flux is certainly its most important feature. It is implemented such that the per-flavor astrophysical neutrino flux components are fitted individually. It was discussed in the previous section that a simultaneous measurement of all flavor fractions is strongly correlated due to the overlap of event topologies induced by neutrinos of different flavors. This correlation was illustrated in Figure 6.10, but only the constraints on the astrophysical tau-neutrino flux were depicted and not on the other flavor components. In this section, the sensitivity to the astrophysical neutrino flavor composition is presented by analyzing the possible constraints on all flavor fractions simultaneously.

The fit parametrization listed in Table 6.1 is adapted to scan each flavor fraction around the best-fit composition. Instead of the flux normalizations $(\phi_{\nu_e}, \phi_{\nu_\mu}, \phi_{\nu_\tau})$, the flavor fractions

$$f_{\nu_e} = \frac{\phi_{\nu_e}}{\phi_{\nu_{tot}}}, \; f_{\nu_\mu} = \frac{\phi_{\nu_\mu}}{\phi_{\nu_{tot}}}, \; f_{\nu_\tau} = \frac{\phi_{\nu_\tau}}{\phi_{\nu_{tot}}} \quad \text{with} \quad \phi_{\nu_{tot}} = \phi_{\nu_e} + \phi_{\nu_\mu} + \phi_{\nu_\tau} \tag{6.11}$$

are used to reparametrize the fit parameters as $(f_{\nu_e}, f_{\nu_\mu}, \phi_{\nu_{tot}})$. Note that the number of degrees of freedom stays constant because the third flavor fraction is fixed to $f_{\nu_\tau} = 1 - f_{\nu_e} - f_{\nu_\mu}$. A profile likelihood scan of the flavor composition is obtained evaluating a likelihood ratio comparing the best-fit parameters $(\hat{f}_{\nu_e}, \hat{f}_{\nu_\mu})$ to each scan point $(f_{\nu_e}^{\text{s.p.}}, f_{\nu_\mu}^{\text{s.p.}})$, i.e.

$$\lambda := -2\Delta\log\mathcal{L} = -2\ln\left(\frac{\mathcal{L}\left(\boldsymbol{n}|\boldsymbol{\mu}(f_{\nu_e} = f_{\nu_e}^{\text{s.p.}}, f_{\nu_\mu} = f_{\nu_\mu}^{\text{s.p.}}, \hat{\hat{\boldsymbol{\theta}}}, \hat{\hat{\boldsymbol{\xi}}})\right)}{\mathcal{L}\left(\boldsymbol{n}|\boldsymbol{\mu}(\hat{f}_{\nu_e}, \hat{f}_{\nu_\mu}, \hat{\boldsymbol{\theta}}, \hat{\boldsymbol{\xi}})\right)}\right). \tag{6.12}$$

The remaining fit parameters $\boldsymbol{\theta} = (\phi_{\nu_{tot}}, \gamma)$ and $\boldsymbol{\xi} = (\phi_{\text{muon}}, \phi_{\text{conv}}, \phi_{\text{prompt}}, \xi_E, \xi_A)$ are varied for each hypothesis until the likelihood is maximal. This is a nested hypothesis with two degrees of freedom fewer than the fit for which all flavor components are free to float. Assuming Wilks' theorem is valid, the test statistic distribution can be modeled with $\chi^2_{k=2}(\lambda)$ for $k = 2$ degrees of freedom. As in the previous section, the Asimov dataset is constructed by injecting the benchmark astrophysical neutrino flux of $\phi_\nu(E_\nu) = 1.5 \cdot 10^{-18} (E_\nu/100\,\text{TeV})^{-2.3}\,\text{GeV}^{-1}\,\text{cm}^{-2}\,\text{sr}^{-1}\,\text{s}^{-1}$ and a flavor composition of $\nu_e : \nu_\mu : \nu_\tau = 1 : 1 : 1$.

In Figure 6.13, the sensitivity to the astrophysical neutrino flavor composition is depicted. As expected, the injected flavor fractions $f_{\nu_e} = f_{\nu_\mu} = f_{\nu_\tau} = 1/3$ are recovered by the likelihood fit when using the Asimov dataset. In comparison to Figure 6.1, the contours are much broader than for the previously published measurement of the flavor composition using multiple IceCube data samples in a global fit [46]. This is particularly prominent for f_{ν_μ}, because these data samples contain a much larger track sample of through-going muons from the Northern Hemisphere.[3] Therefore, the constraints on f_{ν_μ} are much better for the global fit than the median sensitivity estimated for this analysis. There is a degeneracy between f_{ν_e} and f_{ν_τ} observed in both the global fit and the profile likelihood scan using the binary topology ID. The binary topology ID is only able to constrain f_{ν_μ} via the track topology and leaves a large degeneracy between f_{ν_e} and f_{ν_τ} via the cascade topology, as expected. The additional double cascade topology of the ternary topology ID significantly reduces this degeneracy. The stronger constraints on the full flavor composition are clearly visible along the direction of the f_{ν_τ}-axis. In the median realization, the flavor fractions are constrained to $f_{\nu_e} = 0.33^{+0.17}_{-0.16}$, $f_{\nu_\mu} = 0.33^{+0.16}_{-0.17}$, and $f_{\nu_\tau} = 0.33^{+0.24}_{-0.19}$ in the respective projections of the contours. The constraints on f_{ν_τ} are compatible with the median detection sensitivity estimated in the previous section. Note, however, that the validity of Wilks' theorem is not examined in this case, as it is computationally too expensive, considering that the confidence region of the flavor composition is depicted mostly for illustrative purposes.

[3] Among others, the data samples also contain the four-year high-energy starting event sample. Note that the global fit and the analysis presented in this thesis are therefore not statistically independent.

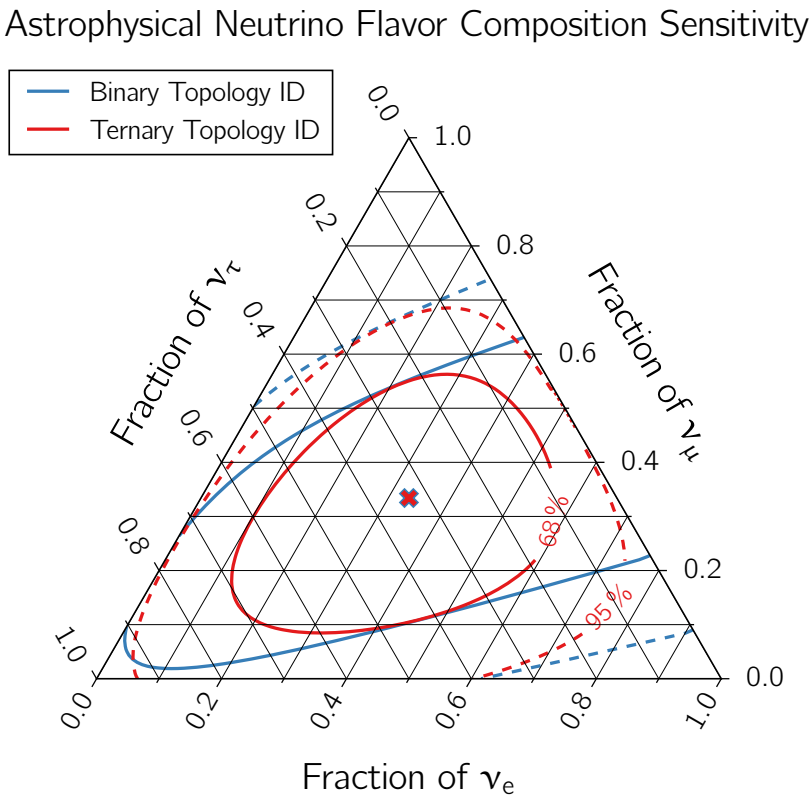

Figure 6.13: Median sensitivity to the astrophysical neutrino flavor composition using a binary and ternary topology ID. The 68% (solid lines) and 95% (dashed lines) confidence regions are depicted around the best-fit flavor composition of 1/3 : 1/3 : 1/3 marked with '×'. The best-fit flavor composition is identical to the true injected flavor composition of the Asimov dataset. The differently colored contours are obtained from profile likelihood scans using the binary topology ID (blue) and the ternary topology ID (red), respectively.

6.3.4 Dependence on the Spectral Shape of the Astrophysical Neutrino Flux

There are a few spectral fits of the astrophysical neutrino flux that are based on different event selections in the IceCube detector. An overview of these fits in which the spectrum is modeled as a single power-law $\mathrm{d}\phi_\nu/\mathrm{d}E_\nu \sim E_\nu^{-\gamma}$ is given in Table 6.4. It illustrates the **large uncertainties of the spectral shape**, as the spectral index γ varies from 2.1 to 2.9. Not all listed analyses are statistically independent, and some are sensitive to different energy ranges.[4] A softer spectrum is fitted by analyses with a low energy threshold around $\sim$20 TeV and a harder one above $\sim$200 TeV. For different years of the high-energy starting event selection, the spectral index is fitted increasingly soft over time, although the uncertainties are large and measurement results consistent. A spectral cutoff was studied in the global fit, where multiple data samples were combined. It was found that there was a slight (but insignificant) preference to a single power-law flux with cutoff [48]. A dedicated search for a spectral cutoff is under development [246]. More complex spectral shapes such as a dual power-law have been recently investigated without a clear indication of whether the observed data is better explained than by a single power-law flux model [4]. With the currently available data, the shape of the astrophysical neutrino spectrum is not well known. Although there are hints that a single power-law flux model might not be the final answer, it is still the model with the fewest assumptions that is able to consistently explain the observed data within uncertainties.

[4] They are also sensitive to different declination bands, e.g. the through-going track analysis is only sensitive to the Northern Hemisphere. This will become important if a Galactic neutrino component is detected.

Diffuse Astrophysical ν Analysis		E_ν^{thr} [TeV]	γ	ϕ_ν [$\text{GeV}^{-1}\,\text{cm}^{-2}\,\text{sr}^{-1}\,\text{s}^{-1}$]	E_c [PeV]
2-year HESE	[43]	~ 60	2.2 ± 0.4	1.2 ± 0.4	–
3-year HESE	[44]	~ 60	2.3 ± 0.3	1.5 ± 0.5	–
4-year HESE	[50]	~ 60	2.6 ± 0.3	2.2 ± 0.7	–
6-year HESE	[4]	~ 60	2.9 ± 0.3	2.5 ± 0.8	–
2-year starting events	[45]	~ 25	2.5 ± 0.1	2.1 ± 0.4	–
4-year cascade	[61]	~ 20	2.5 ± 0.1	1.6 ± 0.2	–
6-year through-going tracks	[49]	~ 200	2.1 ± 0.1	0.9 ± 0.3	–
Global fit without cutoff	[48]	~ 20	2.5 ± 0.1	2.3 ± 0.3	–
Global fit with cutoff	[48]	~ 20	2.3 ± 0.1	2.7 ± 0.4	$2.7^{+7.7}_{-1.4}$

Table 6.4: Overview of different spectral fits of the diffuse astrophysical neutrino flux with the IceCube detector. The tabulated values are the lower threshold neutrino energy E_ν^{thr} of the analysis, the spectral index γ, the per-flavor normalization ϕ_ν at $E_\nu = 100\,\text{TeV}$, and the spectral cutoff energy E_c of the astrophysical neutrino flux.

The sensitivity of this analysis to the astrophysical tau-neutrino flux is strongly dependent on the assumed spectral shape of the neutrino flux.[5], which is due to the **energy-dependent identification efficiency**. Tau-neutrino interactions at higher energies transfer more energy to the secondary tau, which increases its average propagation distance before it decays. Double cascade events with a longer decay length can be more efficiently identified. A softer spectrum induces more tau-neutrino interactions at lower energies for which they cannot be identified. A spectral cutoff causes a similar effect by reducing the number of identifiable tau-neutrino interactions at high energies. This number can also be significantly lower for a dual power-law flux model if the spectral break (see below) happens to be within the energy range where the sensitivity is maximal (c.f. Section 4.4). In summary, the ability to constrain the astrophysical tau-neutrino flux increases with any spectrum that has a large contribution at high energies.

In the previous sections, the number of identifiable tau-neutrino interactions and the corresponding flux sensitivity of the likelihood fit were quoted for a benchmark astrophysical neutrino flux that is modeled as a single power-law spectrum. Systematic uncertainties were considered and incorporated, as discussed in Section 6.2.3. It became apparent that the uncertainties of the expected tau-neutrino signal, unlike the background expectation, are not dominated by an imprecise knowledge of the detector properties. Instead, the **model uncertainties of the astrophysical neutrino spectrum** are much more significant to the estimated tau-neutrino sensitivity. As the spectrum is a quantity to be measured, it is not treated as a systematic uncertainty. However, it is important to be aware of this dependence.

In the following, three different astrophysical neutrino flux models are considered in order to estimate their effect on the tau-neutrino sensitivity. These models are motivated by similar properties observed in the cosmic-ray flux (c.f. Chapter 2).

1. a **single power-law spectrum** is defined by

$$\frac{\mathrm{d}\phi_\nu}{\mathrm{d}E_\nu} = \phi_\nu \cdot \left(\frac{E_\nu}{100\,\text{TeV}}\right)^{-\gamma}, \tag{6.13}$$

with a spectral index γ and a flux normalization ϕ_ν at $E_\nu = 100\,\text{TeV}$. It is the standard astrophysical neutrino flux model with minimal assumptions and based on the correlation to the cosmic-ray flux. However, an E_ν^{-2} spectrum that had been used as a benchmark model for many years was excluded at a significance of $4.6\,\sigma$ [48].

[5] The sensitivity also depends on the assumed astrophysical flavor composition. However, a variation is simply an energy-independent scaling of the number of identifiable tau-neutrino interactions.

2. a **single power-law spectrum with a spectral cutoff** is defined by

$$\frac{\mathrm{d}\phi_\nu}{\mathrm{d}E_\nu} = \phi_\nu \cdot \left(\frac{E_\nu}{100\,\mathrm{TeV}}\right)^{-\gamma} \cdot \exp\left(-\frac{E_\nu}{E_\mathrm{c}}\right), \tag{6.14}$$

with an additional cutoff energy E_c that is modeled with a *soft* exponential suppression at high energies. Note that this model is in contrast to a *hard* cutoff, for which exactly zero events would be expected above E_c. A spectral cutoff could be caused by a lack of sources that are capable of producing neutrinos at high energies.

3. a **dual power-law spectrum with a spectral break** is defined by

$$\frac{\mathrm{d}\phi_\nu}{\mathrm{d}E_\nu} = \frac{\mathrm{d}\phi_{\nu_1}}{\mathrm{d}E_\nu} + \frac{\mathrm{d}\phi_{\nu_2}}{\mathrm{d}E_\nu} = \left[\phi_{\nu_1} \cdot \left(\frac{E_\nu}{100\,\mathrm{TeV}}\right)^{-\gamma_1}\right] + \left[\phi_{\nu_2} \cdot \left(\frac{E_\nu}{100\,\mathrm{TeV}}\right)^{-\gamma_2}\right], \tag{6.15}$$

which is a simple superposition of two independent single power-law spectra with spectral indices γ_1 and γ_2 and flux normalizations ϕ_{ν_1} and ϕ_{ν_2} at $E_\nu = 100\,\mathrm{TeV}$, respectively. The experimentally relevant case in the context of this thesis is a soft component that is dominant in the low-energy region and a hard component that is dominant in the high-energy region. For this case, it follows that $\phi_{\nu_1} > \phi_{\nu_2}$ and $\gamma_1 > \gamma_2$. A more convenient way of parametrizing the dual power-law spectrum under these conditions is to replace the second normalization by a spectral break energy E_b. It is defined by

$$\frac{\mathrm{d}\phi_{\nu_1}}{\mathrm{d}E_\nu}(E_\mathrm{b}) = \frac{\mathrm{d}\phi_{\nu_2}}{\mathrm{d}E_\nu}(E_\mathrm{b}) \quad \Longrightarrow \quad \log\left(\frac{E_\mathrm{b}}{100\,\mathrm{TeV}}\right) = \frac{\log\phi_{\nu_1} - \log\phi_{\nu_2}}{\gamma_1 - \gamma_2}, \tag{6.16}$$

and denotes the neutrino energy above which the harder spectral component $\mathrm{d}\phi_{\nu_2}/\mathrm{d}E_\nu$ becomes dominant over the softer $\mathrm{d}\phi_{\nu_1}/\mathrm{d}E_\nu$. A dual power-law spectrum could be indicative for different neutrino source populations such as a diffuse neutrino emission from galactic and extra-galactic sources.

Naturally, there are many other possible flux models. However, the focus is on testing the dependence of the tau-neutrino sensitivity on the shape of some representative astrophysical flux models and not on testing the models themselves.

Only one parameter of interest is varied for each model while all other parameters are fixed to a chosen value. For the single power-law model, the parameter of interest is γ, for the cutoff model it is E_c with fixed γ, and for the dual-power law, the parameter of interest is E_b with fixed γ_1 and γ_2. Note that for every model, the respective flux normalization ϕ_ν is rescaled to exactly predict the number of observed events that are expected from the benchmark flux model of $\phi_\nu(E_\nu) = 1.5 \cdot 10^{-18}(E_\nu/100\,\mathrm{TeV})^{-2.3}\,\mathrm{GeV}^{-1}\,\mathrm{cm}^{-2}\,\mathrm{sr}^{-1}\,\mathrm{s}^{-1}$. The change in sensitivity is thus only due to a different spectral shape and not due to a statistical variation of the total expected number of events. For the single power-law model, the spectral index is scanned in $\gamma = 2 \ldots 3$ to cover a wide range of measured values (c.f. Table 6.4). The cutoff model is scanned in $E_\mathrm{c} = 500\,\mathrm{TeV} \ldots 10\,\mathrm{PeV}$ while the spectral index is fixed to the benchmark value of $\gamma = 2.3$. The lower limit of the chosen cutoff energies is purely for illustrative purposes, as there is no indication for a sub-PeV cutoff [48]. For the dual power-law model the spectral break energy is scanned in $E_\mathrm{b} = 200\,\mathrm{TeV} \ldots 5\,\mathrm{PeV}$ while the spectral indices are fixed to $\gamma_1 = 2.9$ and $\gamma_2 = 2.1$. These choices are representative for a lower and upper bound of the measured spectral index as listed in Table 6.4. The value region of the spectral break energy covers a wide range, which is indicative for the lack of knowledge regarding if and where a break in the spectrum could be located. In a recently updated measurement which combines the result of the high-energy starting event sample with the result of a through-going track analysis, there are hints (albeit insignificant) that a spectral break energy could be of the order of a few hundred TeV [4].

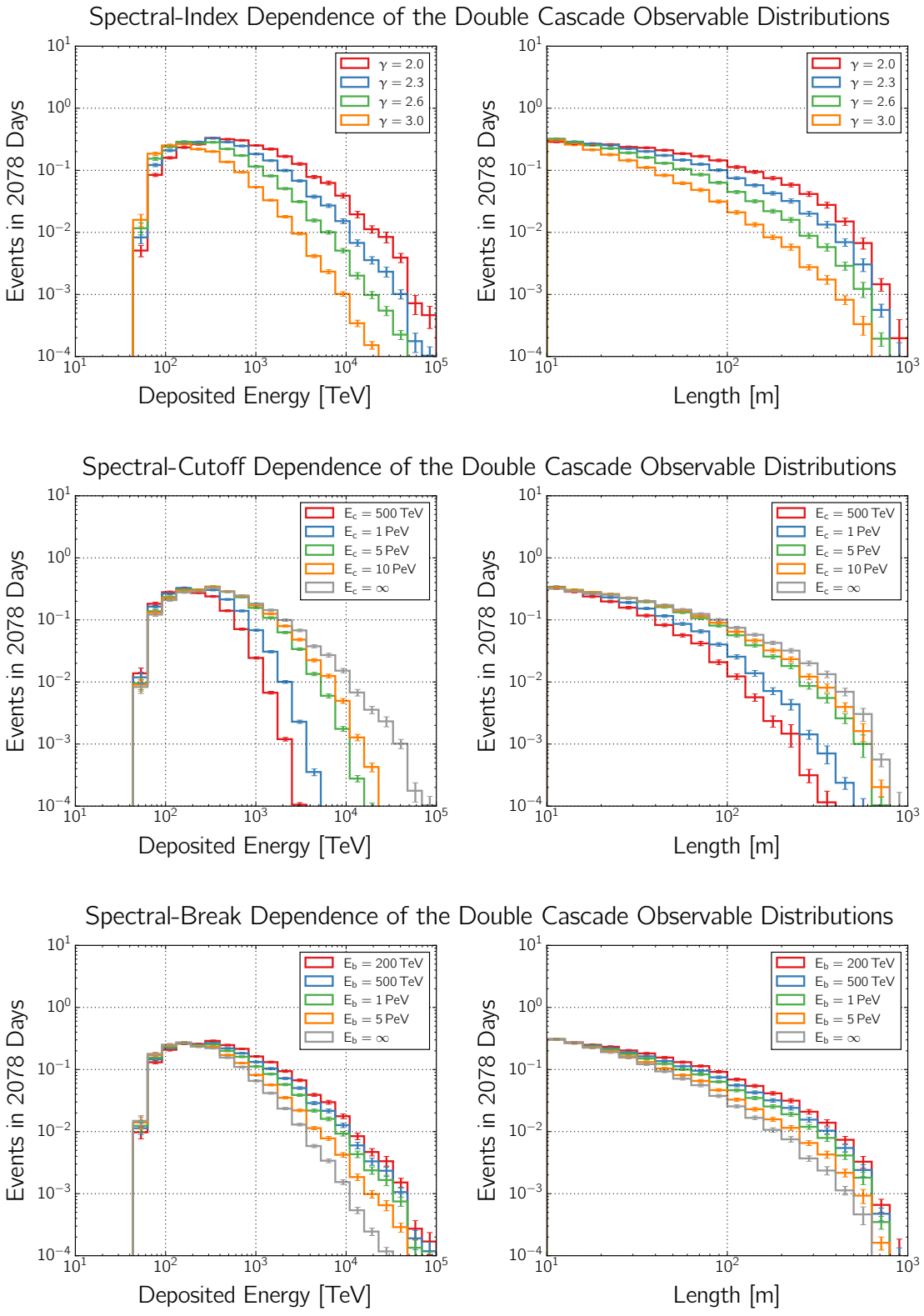

Figure 6.14: Observable distributions of the double cascade sample for different spectral shapes of the astrophysical tau-neutrino flux. The expected number of signal events in the double cascade sample of six years is depicted as a function of the total deposited energy (left) and the double cascade length (right). The distributions are shown for different realizations of a spectral index γ (top), spectral cutoff energy E_c (center), and spectral break energy E_b (bottom). See text for a full description of each flux model.

In Figure 6.14, the **double cascade observable distributions** of astrophysical tau-neutrino interactions in the respective topology sample are shown for the aforementioned astrophysical neutrino flux models. Note that these are the distributions of identifiable tau-neutrino interactions, i.e. only a fraction of all tau-neutrino interactions. It can clearly be seen how it decreases with a softer spectrum. A harder spectral index shifts the maximum of the energy distribution towards higher energies, and the slope becomes more gradual. More importantly, the length distribution strongly depends on the spectral index due to the correlation $E_{\nu_\tau} \sim E_\tau \sim \lambda_\tau$. Consequently, a soft spectrum suppresses the number of efficiently identifiable tau-neutrino interactions for which the tau has a long decay length. For example, a soft $\sim E_\nu^{-3}$ spectrum decreases the number of identifiable double cascade events at $L \simeq 100\,\mathrm{m}$ by a factor ~ 5 compared to a hard $\sim E_\nu^{-2}$ spectrum. A similar effect is caused by a spectral cutoff: the lower in energy the spectral cutoff, the lower the number of high-energy neutrino interactions. Note that the change for a cutoff at $E_c = 500\,\mathrm{TeV}$ is both drastic and unlikely because it is incompatible with the observed PeV neutrinos [4]. A more realistic cutoff of a few PeV still has a significant impact on the number of identifiable tau-neutrino interactions. However, the relative change weakens with larger cutoff energies due to the decreasing identification efficiency at energies above a few PeV (c.f. Section 4.4). The impact of a break in the astrophysical tau-neutrino spectrum is smaller compared to the variations of the other flux models. In effect, the representation of a varying spectral break energy is equivalent to changing the spectral index. For a very low break energy at $E_b = 200\,\mathrm{TeV}$, the flux is mostly dominated by the hard $\sim E_\nu^{-2}$ component, and for a very high break energy $E_b = 5\,\mathrm{PeV}$ it is mostly dominated by the soft $\sim E_\nu^{-3}$ component. This parametrization, however, is helpful for studying a potentially more realistic case where the flux is neither described well by a soft spectrum nor by a hard spectrum. It can be seen that the mixture of both, as defined by the spectral break energy, has a significant impact of the number of identifiable tau-neutrino interactions.

In the following, the different astrophysical neutrino flux models defined in Equations 6.13 to 6.15 are incorporated by an **extension of the likelihood fit**. Only one additional flux parameter is allowed to be free in the fit, while the others are fixed. The single power-law model corresponds to the default hypothesis as described in Section 6.2.1 and has γ as a free fit parameter. For a fit of the single power-law model with cutoff, γ is fixed to its true value and E_c is a free parameter in the likelihood. The dual power-law hypothesis is fitted by fixing γ_1 and γ_2 to their true values and adding E_b as a free parameter.[6] Two-dimensional likelihood scans are performed which depict the dependence of the astrophysical tau-neutrino fraction on the spectral index, the spectral cutoff energy, and the spectral break energy. Confidence intervals are obtained using Wilks' theorem for a likelihood ratio test with two degrees of freedom.

In Figure 6.15, the likelihood scan of the **tau-neutrino fraction** and **spectral index** is shown for four different injected values. As expected, the contours are broader for a soft spectrum. Note that the constraints on both the tau-neutrino fraction and the spectral index are stronger for a hard spectrum. In this case, the fit is more sensitive to the tau-neutrino fraction due to an increase of identifiable tau-neutrino interactions, as explained above. The spectral index itself can be better constrained for a harder spectrum due to the increase of high-energy events that make a distinction between astrophysical and atmospheric neutrino flux easier. Note that the two-dimensional contours are approximately parallel to the axis of the tau-neutrino fraction, which means that they can be measured independently by the likelihood fit. As discussed in Section 6.3.2, the spectral index is mostly constrained by the single cascade and track samples due to the larger number of events, whereas the tau-neutrino fraction is almost exclusively constrained by the much smaller double cascade sample.

[6] Note that the likelihood fit is only changed to study the dependence of the sensitivity on the spectral shape of the astrophysical tau-neutrino flux. These models are not tested in this analysis, because the high-energy starting event sample is not well suited for such a fit due to the low statistical power of the data sample.

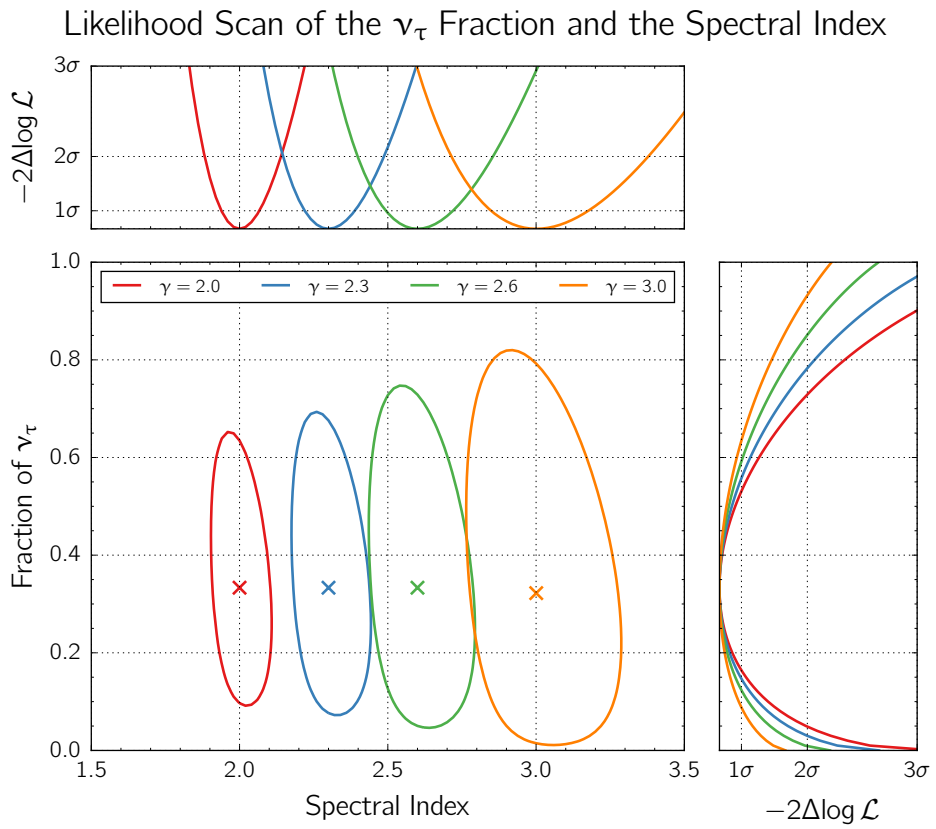

Figure 6.15: Likelihood scan of the astrophysical tau-neutrino fraction and the spectral index. In the central panel, the 68% contours are depicted for different injections of γ around their best-fit values marked with '$\times$'. The one-dimensional likelihood scans are shown in the top panel for γ and in the right panel for f_{ν_τ}. The test statistic $-2\Delta\log\mathcal{L}$ is given in units of Gaussian standard deviations using Wilks' theorem.

In Figure 6.16, the likelihood scan of the **tau-neutrino fraction** and **spectral cutoff energy** is shown for four different injected values. As expected, the constraints on the tau-neutrino fraction are increasingly stronger for a higher spectral cutoff energy. This is due to the weaker suppression of identifiable tau-neutrino interactions at higher energies. Note that the constraints on the cutoff energy itself become weaker with increasing values. It can be seen that the contours do not close in the depicted energy range for a 10 PeV cutoff. At these energies, the flux is so low that the statistical power of the six-year high-energy starting event sample are too weak to be sensitive to a spectral cutoff. The contours show no correlation between the tau-neutrino fraction and the cutoff energy for the same reason as discussed above for the likelihood scan of the spectral index.

In Figure 6.17, the likelihood scan of the **tau-neutrino fraction** and **spectral break energy** is shown for four different injected values. As expected, the contours increase with a higher spectral break energy. The constraints on the tau-neutrino fraction are increasingly weaker due to the stronger contribution of the soft spectral component. As discussed above, a soft spectrum reduces the number of identifiable tau-neutrino interactions significantly. Similar to the spectral cutoff energy, the constraints on the spectral break energy itself become weaker with increasing values. The explanation is the same as above, because the neutrino flux at a few PeV and thereby the number of expected events are too small to be sensitive to a spectral break in this energy range. The contours show no strong correlation between the tau-neutrino fraction and the spectral break energy, as observed for the other flux models.

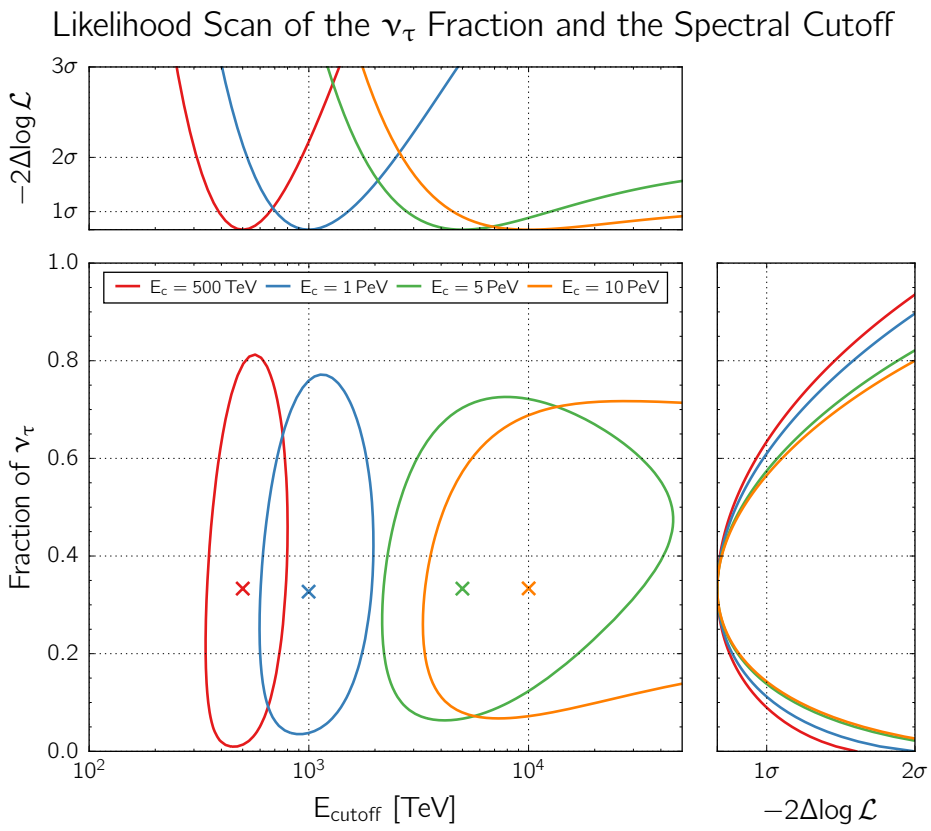

Figure 6.16: Same as in Figure 6.15, but for the spectral cutoff energy.

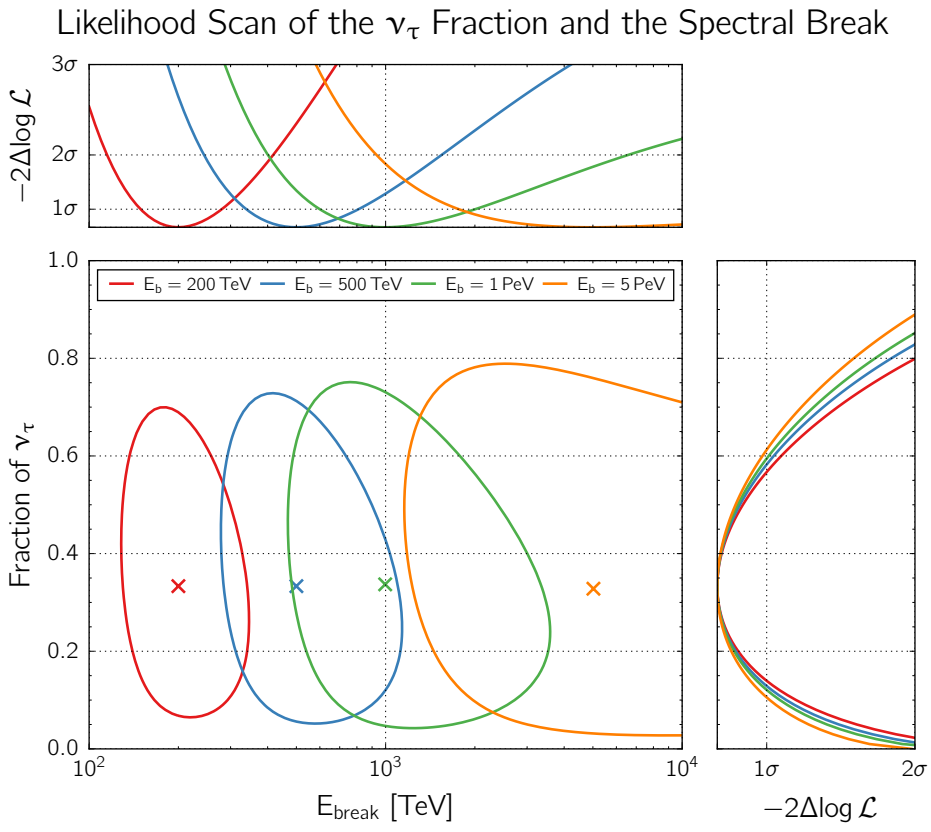

Figure 6.17: Same as in Figure 6.15, but for the spectral break energy.

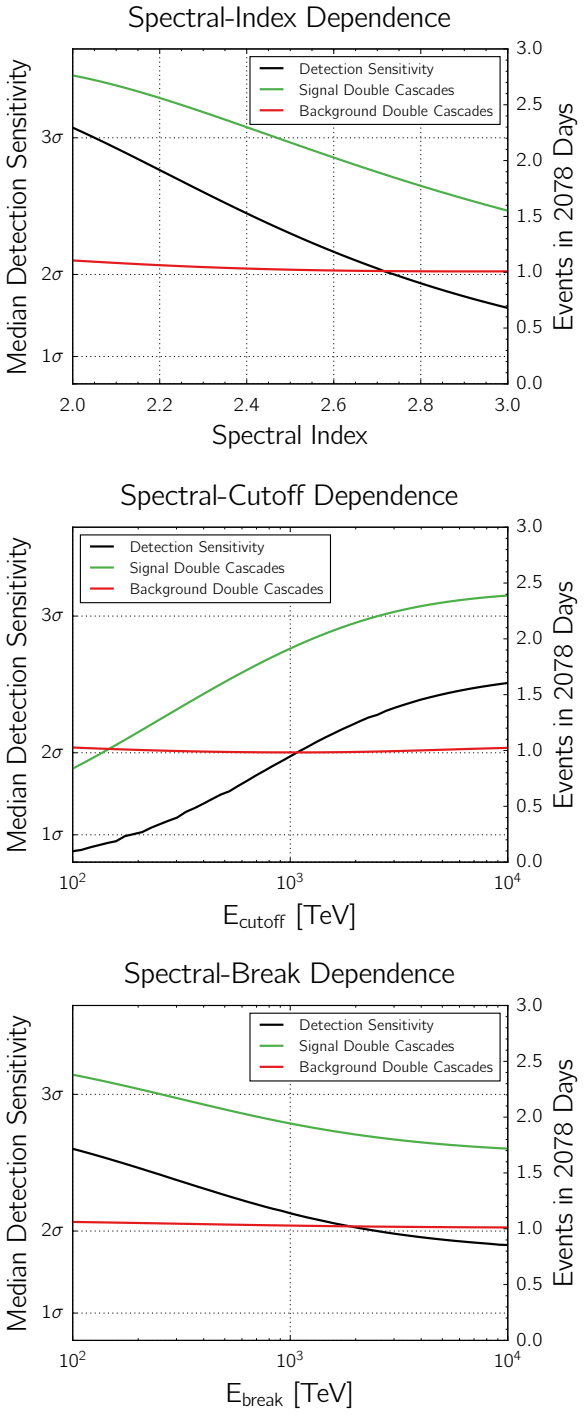

Figure 6.18: Median detection sensitivity and expected number of signal and background events as a function of the spectral index (top), cutoff energy (center) and break energy (bottom). The black line corresponds to the detection sensitivity as defined in Equation 6.9 (left axis). The colored lines correspond to the number of signal and background events in the double cascade sample as presented in Section 6.3.1 (right axis).

It can already be deduced from the two-dimensional likelihood scans that the ability to constrain the tau-neutrino fraction strongly varies with the spectral shape of the assumed astrophysical neutrino flux. In Figure 6.18, this is quantified more precisely in terms of the **median detection sensitivity** as defined in Equation 6.9 and the expected number of **signal and background events** as presented in Section 6.3.1. A strong correlation between the median detection sensitivity and the spectral shape is visible for all three flux models. A hard spectrum with $\sim E_\nu^{-2.1}$ as observed using the six-year through-going track sample (c.f. Table 6.4) would correspond to a detection sensitivity of $\sim 2.9\,\sigma$. However, for the much softer spectrum $\sim E_\nu^{-2.9}$ as observed using the six-year high-energy starting event sample, the detection sensitivity would drastically decrease to $\sim 1.8\,\sigma$. While the number of background events remains approximately constant, the number of identifiable tau-neutrino interactions is reduced by $\sim 40\%$ in comparison. In the intermediate range for an $\sim E_\nu^{-2.3}$ spectrum, the median detection sensitivity $\sim 2.6\,\sigma$ of the benchmark model is recovered (c.f. Section 6.3.2). A similar variation of the sensitivity can be seen for a spectral cutoff. An unrealistic cutoff energy of $E_c = 100\,\text{TeV}$ would imply that the tau-neutrino fraction cannot be constrained. A more realistic scenario of $E_c = 2.7\,\text{PeV}$, as obtained in the global fit, would correspond to a detection sensitivity of $\sim 2.4\,\sigma$. This does not deviate much from the sensitivity for the assumed benchmark flux model. As discussed above, the variation due to the spectral break energy is slightly smaller. A break energy at a few PeV only corresponds to a superposed flux that is increasingly dominated by the soft spectral component but does not reduce the number of high-energy neutrino interactions as abruptly as a spectral cutoff. As expected, the detection sensitivity decreases with an increasing break energy. In the potentially interesting region of a few hundred TeV, the detection sensitivity varies between $\sim 2.4\,\sigma$ to $\sim 2.6\,\sigma$. Also, the occurrence of a potential spectral break does not cause a large deviation from the sensitivity expected for the benchmark flux model. Note that the number of

expected background events in the double cascade sample is approximately constant for all spectral shapes. This is due to the unique features of the double cascade topology, for which the misidentification rate of background events is independent of the energy but the identification efficiency of tau-neutrino interactions increases with energy. Consequently, the variation of the detection sensitivity due to different spectral shapes is entirely caused by a variation of the expected number of identifiable signal events.

In summary, the diffuse astrophysical neutrino flux has been continuously measured with different event samples of the IceCube detector. The uncertainties of its spectral shape are large, and various possible features, such as a spectral cutoff or a spectral break, remain unknown. The flux model with the least assumptions is a continuous single power-law spectrum, which is also used in this analysis. The median detection sensitivity of excluding a tau-neutrino flux of zero particularly depends on the spectral index of the power-law model and varies from $\sim 1.8 - 2.9\,\sigma$. Consequently, the expected outcome of the measurement of the tau-neutrino flux has large variations. Although its estimation yields a good chance of observing $\sim 1 - 3$ double cascade events, it cannot be ruled out that none are found at all. In this case, the astrophysical tau-neutrino flux is constrained by an upper limit.

7 Results

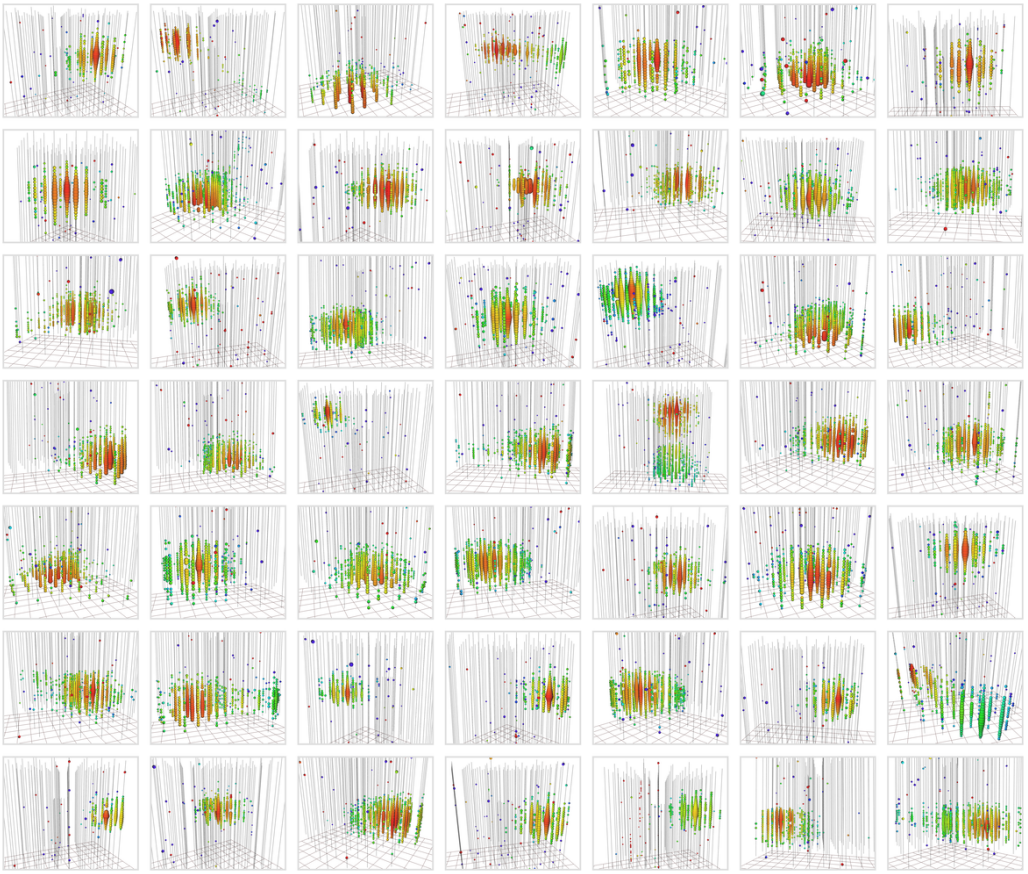

Figure 7.1: Event displays of all 49 high-energy starting events observed in six years with a deposited energy above 60 TeV. A complete list of the event properties can be found in the respective publications for two, three, four, and six years of detector data [4, 43, 44, 50].

The high-energy starting event selection yields 82 events in six years, of which 49 have a deposited energy above 60 TeV (see Figure 7.1). Using the ternary topology ID presented in this thesis, 35 events are identified as single cascades, none as double cascades, and 14 as tracks. The lack of double cascade events implies that the measured astrophysical tau-neutrino fraction is zero and the corresponding flux can only be constrained by an upper limit.

In Section 7.1, the fit results are summarized and compared to previously published measurements of the diffuse astrophysical neutrino flux using the high-energy starting event sample. The agreement between experimental data and simulation data is discussed. In Section 7.2 and Section 7.3, the upper limit on the astrophysical tau-neutrino flux and the measurement of the astrophysical neutrino flavor composition, respectively, are presented in comparison to previous measurements as well as the estimated sensitivity. In Section 7.4, the results are discussed and implications for possible neutrino production scenarios at the cosmic sources are examined.

7.1 Fit Results and Data-Monte-Carlo Agreement

The **best-fit parameter values** for the 49 events of the six-year high-energy starting event sample are summarized in Table 7.1. The nuisance parameters are mostly fitted to their priors with negligible deviations with respect to the modeled uncertainties. The lack of observed double cascade events causes the best-fit value of the astrophysical tau-neutrino flux to be zero. This will be discussed in greater detail in Section 7.2. The best-fit values of the astrophysical electron- and muon-neutrino fluxes are approximately equal, which places the measured flavor composition at $\nu_e : \nu_\mu : \nu_\tau \simeq 1 : 1 : 0$. This will be discussed in greater detail in Section 7.3.

The best-fit value of the spectral index $\gamma = 2.93 \pm 0.21$ is softer than the modeled $E_\nu^{-2.3}$ benchmark spectrum used to estimate the sensitivity of this analysis (c.f. Section 6.2.1). Note that the spectral fit using the three-year high-energy starting event sample was chosen as benchmark model [44]. An accumulation of events at lower energies and a lack of events at higher energies in the succeeding three years of detector data cause the spectral index to be softer than previously observed (although the spectral fit results are still compatible within uncertainties). In addition, an error in the neutrino cross section calculation caused an overestimation of the astrophysical neutrino flux in previous measurements [43, 44, 50]. This was corrected in the most recent iteration, which causes the flux normalization to be $\sim$20% lower [4]. The corrected neutrino cross section model is also used in this analysis. Both the softer spectral index and the lower flux normalization reduce the estimated astrophysical tau-neutrino sensitivity of this analysis (c.f. Section 6.3.4). The best-fit values of the astrophysical neutrino flux normalizations are in agreement with the published results using the same data sample, in which the flux was fitted as a sum of all flavors with a fixed composition of $\nu_e : \nu_\mu : \nu_\tau = 1 : 1 : 1$ [4]. The resulting best-fit spectrum was $\phi_\nu(E_\nu) = (2.46 \pm 0.8) \cdot 10^{-18} (E_\nu/100\,\mathrm{TeV})^{-2.92^{+0.33}_{-0.29}}\,\mathrm{GeV}^{-1}\,\mathrm{cm}^{-2}\,\mathrm{sr}^{-1}\,\mathrm{s}^{-1}$ per flavor. The best-fit value of the spectral index is the same in both analyses. The flux sum $\phi_{\nu_{tot}} = \phi_{\nu_e} + \phi_{\nu_\mu} + \phi_{\nu_\tau}$ is slightly different, i.e. $\phi_{\nu_{tot}} = (6.41^{+2.72}_{-1.97}) \cdot 10^{-18}\,\mathrm{GeV}^{-1}\,\mathrm{cm}^{-2}\,\mathrm{sr}^{-1}\,\mathrm{s}^{-1}$ at 100 TeV for this analysis and $\phi_{\nu_{tot}} = (7.38 \pm 2.4) \cdot 10^{-18}\,\mathrm{GeV}^{-1}\,\mathrm{cm}^{-2}\,\mathrm{sr}^{-1}\,\mathrm{s}^{-1}$ at 100 TeV for the previously published result. This difference is reasonable due to the different neutrino effective areas for each flavor and is expected when each flavor component is allowed to be free in the fit rather than being constrained to $\nu_e : \nu_\mu : \nu_\tau = 1 : 1 : 1$.

Model Parameter		Best-Fit	Unit
ϕ_{ν_e}	astro. ν_e normalization	$3.27^{+1.02}_{-1.08}$	$10^{-18}\,\mathrm{GeV}^{-1}\,\mathrm{cm}^{-2}\,\mathrm{sr}^{-1}\,\mathrm{s}^{-1}$
ϕ_{ν_μ}	astro. ν_μ normalization	$3.14^{+2.30}_{-1.65}$	$10^{-18}\,\mathrm{GeV}^{-1}\,\mathrm{cm}^{-2}\,\mathrm{sr}^{-1}\,\mathrm{s}^{-1}$
ϕ_{ν_τ}	astro. ν_τ normalization	$0.00^{+1.03}_{-0.00}$	$10^{-18}\,\mathrm{GeV}^{-1}\,\mathrm{cm}^{-2}\,\mathrm{sr}^{-1}\,\mathrm{s}^{-1}$
γ	astro. spectral index	$2.93^{+0.21}_{-0.21}$	–
ϕ_{muon}	atm. muon normalization	$1.01^{+0.27}_{-0.27}$	GaisserH4a × tagged muon data
ϕ_{conv}	atm. conv. normalization	$1.04^{+0.28}_{-0.28}$	HKKMS06 × CR-knee mod. × self-veto prob.
ϕ_{prompt}	atm. prompt normalization	$0.00^{+0.53}_{-0.00}$	ERS × CR-knee mod. × self-veto prob.
ξ_E	energy scale	$1.00^{+0.10}_{-0.16}$	SPICELea × 0.99 DOM efficiency
ξ_A	ice anisotropy scale	$1.00^{+0.24}_{-0.30}$	SPICELea

Table 7.1: Best-fit parameter values using the six-year high-energy starting event sample above 60 TeV deposited energy. The astrophysical flux normalizations are given for a single power-law model at 100 TeV neutrino energy and correspond to the sum of neutrinos and antineutrinos. The uncertainties are at 68% confidence level obtained from a profile likelihood scan and by using Wilks' theorem. Note that Wilks' theorem is only employed for estimating the uncertainties in the context of this overview. Proper constraints on ϕ_{ν_e}, ϕ_{ν_μ} and ϕ_{ν_τ} are derived from pseudo experiments through Monte Carlo simulation (see Section 7.2 and Section 7.3).

As described in Section 5.3, the double cascade event topology and related observables could only be tested on Monte Carlo simulation data and on experimental flasher LED data. Therefore, it is vital to test the **agreement between simulation and experimental data** using the 49 high-energy starting events. For this purpose, the best-fit parameter values listed in Table 7.1 are used to calculate the Monte Carlo sum of all flux components. Observables that are fitted directly (deposited energy and zenith angle) necessarily reflect the best possible agreement between simulated and experimental data. However, observables that are indirectly used to calculate the topology ID (energy confinement, energy asymmetry, and double cascade length) are more important with respect to testing the agreement between experimental and simulated data.

In Figure 7.2, the best-fit Monte Carlo sum is shown in comparison to the experimental data for the **deposited energy** and **zenith angle**. The depicted distributions are combined for all topology samples. Statistical and systematic uncertainties of the Monte Carlo sum are shown as shaded areas. Statistical errors of experimental data are calculated using the Feldman-Cousins approach [235]. It can be seen that simulated and experimental data agree well within errors. An interesting feature of the deposited energy distribution is visible at high energies. The under-fluctuation of events at a few hundred TeV and the over-fluctuation at a few PeV might indicate that the astrophysical neutrino spectrum could be more complex than the assumed single power-law hypothesis. The statistical power of the currently available data, however, is too limited to constrain different flux models. The impact of the flux model in the context of the neutrino flavor composition will be discussed in Section 7.4. Note that a slight mismatch in the zenith angle distribution might be possible. Though not significant with respect to the depicted uncertainties, it seems that the contribution of up-going events in the detector is overestimated and the contribution of down-going events is underestimated. This effect might be linked to the uncertainty of the optical properties of the hole ice (c.f. Section 6.2.3) and is currently under investigation in complementary analyses [61, 247].

In Figure 7.3, the agreement between simulated data and experimental data is shown for the **energy asymmetry** and **energy confinement**. These observables are related to tau-neutrino identification and are used to define the ternary topology ID (c.f. Section 4.3.2). The distributions are shown for events which pass the selection criteria of the first level of the double cascade classification as depicted in Figure 4.9. It can be seen that simulated and experimental data agree well within errors. This is particularly important, because these observables are used to calculate the ternary topology ID which is part of the likelihood fit.

In Figure 7.4, the **length separation** and **ternary topology ID** are shown. The length separation is an additional selection criteria and corresponds to the second level of the double cascade classification, as depicted Figure 4.9. Events with a length $L < 10\,\mathrm{m}$ contribute to the single cascade topology sample and events with $L \geq 10\,\mathrm{m}$ contribute to the double cascade topology sample. The ternary topology ID is calculated with the additional selection criteria using the energy asymmetry and energy confinement (third and fourth level of the double cascade classification in Figure 4.9). As initially mentioned, 35 events out of all 49 events observed above 60 TeV are classified as single cascades, none as double cascades, and 14 as tracks. It can be seen that the topology ID of simulated data and experimental data agree well. Note that the expectation of the double cascade topology sample is substantially determined by the astrophysical tau-neutrino fraction. Because the distribution is shown for the Monte Carlo sum of the best-fit parameter values and the best-fit flavor composition is $\nu_e : \nu_\mu : \nu_\tau \simeq 1 : 1 : 0$, the depicted expectation in the double cascade topology bin is a pure background description for the astrophysical tau-neutrino fraction. As can be seen, an observation of zero events in the double cascade sample agrees well with the background-only expectation. However, a potential disagreement with flavor compositions that have a tau-neutrino fraction larger than zero expected at Earth, such as $\nu_e : \nu_\mu : \nu_\tau \simeq 1 : 1 : 1$ due to the production and decay of charged pions at the cosmic sources, will be discussed in Section 7.3.

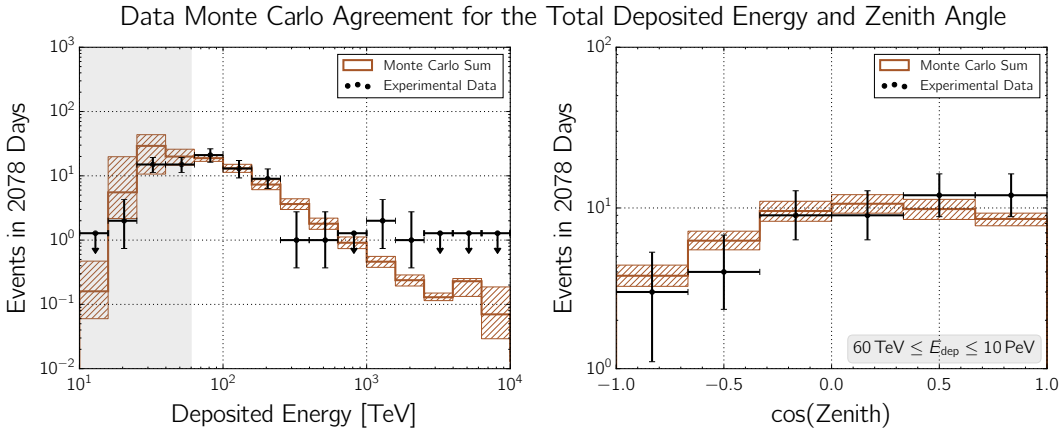

Figure 7.2: Observable distributions of the total deposited energy (left) and the zenith angle (right) for experimental data and the sum of all Monte Carlo best-fit flux templates listed in Table 7.1. Statistical and systematic uncertainties of the Monte Carlo sum are depicted as shaded areas. Events with a deposited energy between 60 TeV and 10 PeV are included in the likelihood fit. The zenith angle distribution is only shown for these events.

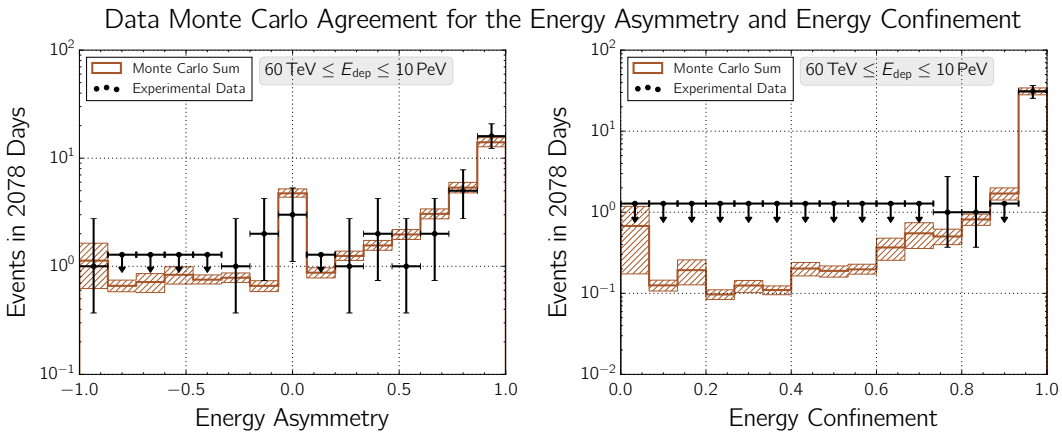

Figure 7.3: Observable distributions of the energy asymmetry (left) and the energy confinement (right) for experimental data and the sum of all Monte Carlo best-fit flux templates. The distributions include events with a deposited energy between 60 TeV and 10 PeV and which pass the first level of the double cascade classification as depicted in Figure 4.9.

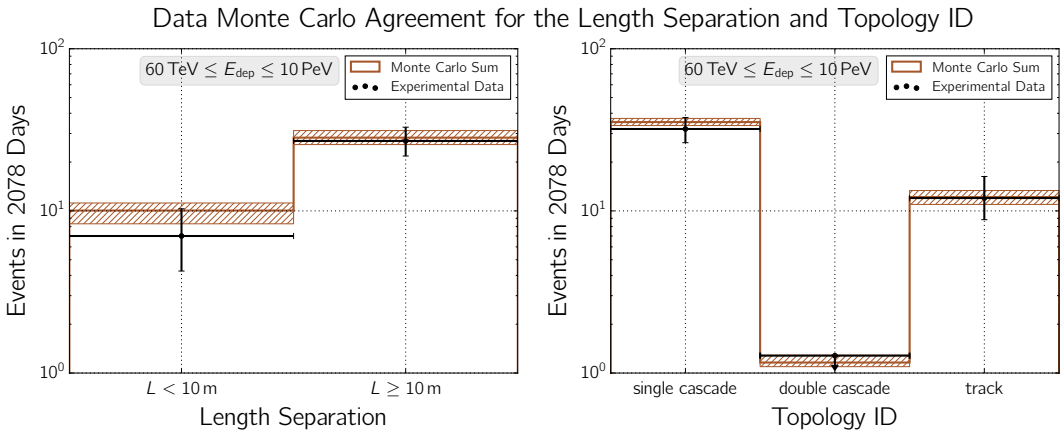

Figure 7.4: Observable distributions of the length separation (left) and the topology ID (right) for experimental data and the sum of all Monte Carlo best-fit flux templates. The distributions include events with a deposited energy between 60 TeV and 10 PeV and which pass the second (left) and the final (right) levels of the double cascade classification as depicted in Figure 4.9.

7.2 Upper Limit on the Astrophysical Tau-Neutrino Flux

The lack of observed double cascade events causes the measured astrophysical tau-neutrino flux to be zero. However, the non-observation is information that can still be used to derive an upper limit on the flux. As described in Section 6.3.2, the developed ternary topology ID is a significant improvement towards tau-neutrino identification compared to the preceding binary topology ID. Consequently, this allows for much stronger constraints on the astrophysical tau-neutrino flux than was previously possible using the high-energy starting event sample.

In Figure 7.5, a profile likelihood scan of the astrophysical tau-neutrino flux is depicted. The test statistic $-2\Delta\log\mathcal{L}$ is a likelihood ratio comparing the best-fit result $\phi_{\nu_\tau} = 0$ to a fixed value $\phi_{\nu_\tau} \geq 0$. For each scan point, all remaining fit parameters are free to float to their conditional best-fit values. Assuming Wilks' theorem is valid, the estimated 90% CL upper limit flux is $\phi^{\text{u.l.}}_{\nu_\tau} \leq 2.68 \cdot 10^{-18} \, (E_{\nu_\tau}/100\,\text{TeV})^{-2.97} \,\text{GeV}^{-1}\,\text{cm}^{-2}\,\text{sr}^{-1}\,\text{s}^{-1}$. It is derived from the critical test statistic value $\lambda_c = \lambda_{\text{obs}} \simeq 2.7$ for which the modeled test statistic distribution yields $\chi^2_{k=1}(\lambda \leq \lambda_c) = 90\%$. The validity of this result is assessed by generating 1 000 pseudo experiments from Monte Carlo simulation, for which a true flux of $\phi_{\nu_\tau} = \phi^{\text{u.l.}}_{\nu_\tau}$ and the conditional best-fit values of all remaining model parameters at $\phi_{\nu_\tau} = \phi^{\text{u.l.}}_{\nu_\tau}$ are injected (see Appendix C.2). The coverage of the cumulative test statistic distribution for test statistic values smaller than the observed value $\lambda_{\text{obs}} \simeq 2.7$ is $(90 \pm 1)\%$, which means that the estimated upper limit flux derived from Wilks' theorem and the more precise upper limit flux derived from performing Monte Carlo pseudo experiments are in fact equal within uncertainties.

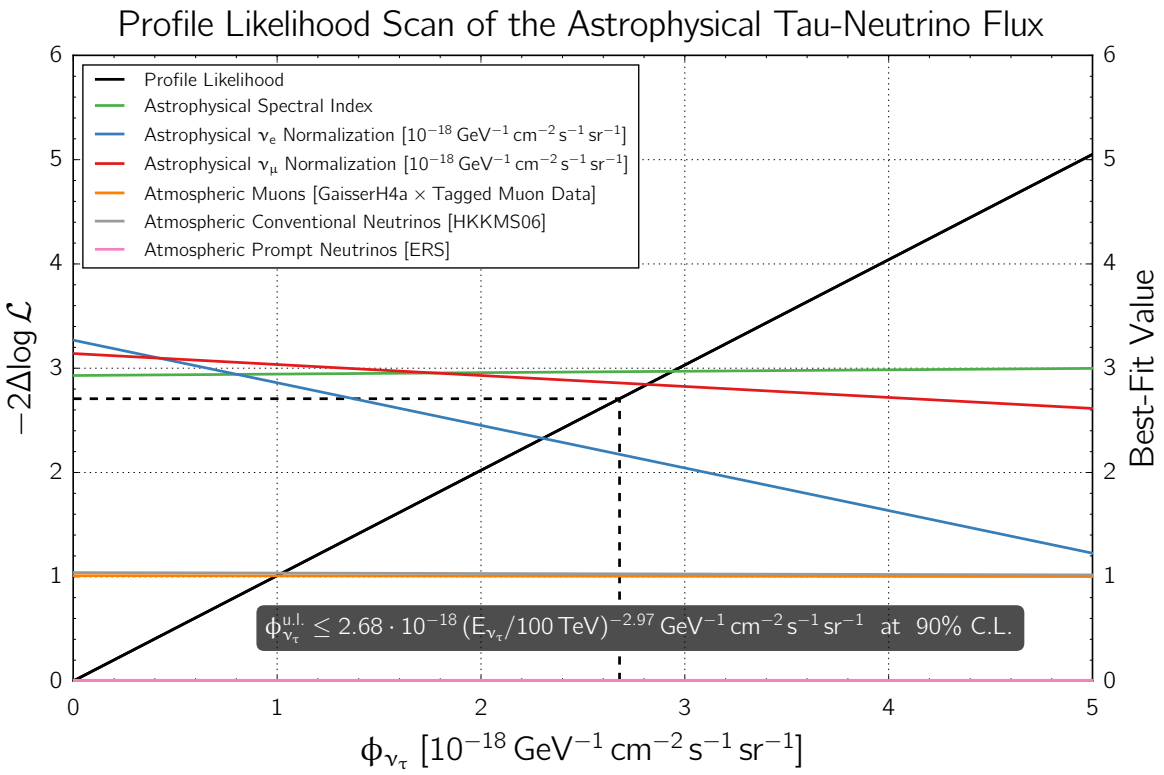

Figure 7.5: Profile likelihood scan of the astrophysical tau-neutrino flux. The flux normalization ϕ_{ν_τ} is quoted at 100 TeV neutrino energy. The black line corresponds to the profile likelihood (left axis) which is defined by the likelihood ratio $-2\Delta\log\mathcal{L}$ comparing a fixed value $\phi_{\nu_\tau} \geq 0$ to the best-fit value $\phi_{\nu_\tau} = 0$. The colored lines correspond to the conditional best-fit values of the remaining fit parameters (right axis). The 90% CL upper limit is indicated by the dashed line. The confidence interval is derived from Monte Carlo pseudo experiments (see Appendix C.2).

Note that this upper limit is not restricted by additional assumptions on the shape and composition of the astrophysical neutrino flux, i.e. the electron- and muon-neutrino flux normalizations and the spectral index are free to float in the constrained likelihood fit. The resulting neutrino flavor composition at the obtained upper limit of the astrophysical tau-neutrino flux is $\nu_e : \nu_\mu : \nu_\tau = 0.33 : 0.40 : 0.26$ and the spectral index $\gamma = 2.97$ is slightly softer than the global best-fit value $\gamma = 2.93$. In contrast, this result is different from a previously published upper limit of $\phi^{\text{u.l.}}_{\nu_\tau} \leq 5.1 \cdot 10^{-18} \, (E_{\nu_\tau}/100\,\text{TeV})^{-2} \, \text{GeV}^{-1} \, \text{cm}^{-2} \, \text{sr}^{-1} \, \text{s}^{-1}$ based on the double pulse method [68]. In that case, the upper limit was derived assuming a fixed flavor composition of $\nu_e : \nu_\mu : \nu_\tau = 1 : 1 : 1$ and a fixed spectrum of E_ν^{-2}. Consequently, the analysis presented in this thesis does not simply improve the upper limit by a factor ~ 2, but rather places a significantly stronger constraint on the astrophysical tau-neutrino flux at a much steeper spectrum.[1]

The stronger constraints on the astrophysical tau-neutrino flux also entail a potential disagreement between the measured flavor composition $\nu_e : \nu_\mu : \nu_\tau \simeq 1 : 1 : 0$ and the benchmark flavor composition $\nu_e : \nu_\mu : \nu_\tau \simeq 1 : 1 : 1$. A first test is realized by constraining the likelihood fit to only two independent components $\phi_{\nu_e+\nu_\mu}$ and ϕ_{ν_τ} with a fixed ratio $\nu_e : \nu_\mu = 1 : 1$. Thereby, the flavor composition $\nu_e : \nu_\mu : \nu_\tau = 1 : 1 : 1$ can be assessed by a one-dimensional profile likelihood scan of ϕ_{ν_τ}. In this case, the observed and the benchmark flavor compositions agree with a p-value of $\sim 13.4\%$. The measurement of the neutrino flavor composition in which all flavor fractions are examined simultaneously will be presented in the following section.

7.3 Measurement of the Astrophysical Neutrino Flavor Composition

The measurement of the astrophysical neutrino flavor composition is shown in Figure 7.6. The best-fit flavor composition is $\nu_e : \nu_\mu : \nu_\tau = 0.51 : 0.49 : 0$. Confidence regions are obtained by evaluating a likelihood ratio in a profile likelihood scan. The test statistic $-2\Delta\log\mathcal{L}$ compares the global best-fit values of the unconstrained fit to the conditional best-fit values of all remaining model parameters at a fixed scan point $(f_{\nu_e}, f_{\nu_\mu}, f_{\nu_\tau} = 1 - f_{\nu_e} - f_{\nu_\mu})$. It may be modeled by a χ^2-distribution with two degrees of freedom if Wilks' theorem holds. The confidence regions depicted in Figure 7.6 are calculated using Wilks' theorem, because a full Feldman-Cousins-construction of the entire flavor composition phase space is computationally extremely demanding. Instead, the validity of Wilks' theorem is only assessed for a few select flavor compositions by comparing the coverage of the test statistic distribution from Monte Carlo pseudo experiments to the coverage of a χ^2-distribution (see Appendix C.2). It can be concluded that a large fraction of the flavor composition phase space is slightly over-covered, i.e. Wilks' theorem yields a conservative confidence region. Although the central part of the 68% confidence region seems to suffer from a slight under-coverage, the χ^2-approximation is deemed sufficient for the presentation of the measurement result in Figure 7.6. In contrast, the confidence levels of the source scenario tests are derived from the exact test statistic distribution of Monte Carlo pseudo experiments in order to be more precise (see below).

The best-fit flavor composition $\nu_e : \nu_\mu : \nu_\tau = 0.51 : 0.49 : 0$ agrees well with the previously published measurement of $\nu_e : \nu_\mu : \nu_\tau = 0.49 : 0.51 : 0$ using a combination of multiple IceCube data samples in a global fit [46]. In comparison, the respective confidence regions depicted in Figure 7.6 illustrate that f_{ν_τ} is constrained rather tightly by employing the ternary topology ID. This is due to the additional double cascade event topology and is in agreement with the result presented in the previous section. In contrast, the global fit yields a large degeneracy between f_{ν_e} and f_{ν_τ} because it is based on a binary topology ID which only distinguishes between cascade-

[1] As explained in Section 4.3.2, the method of the previously published double pulse analysis has been based on a pure counting experiment which did not include a fit of the energy spectrum. Note, however, that the previous upper limit has been derived using only three years of detector data.

like and track-like events. However, the constraints on f_{ν_μ} are much stronger for the global fit, which can be explained by the different underlying data samples. The global fit is based on a few thousand track events compared to only 14 track events in the high-energy starting event sample. As tracks are predominantly induced by muon-neutrino interactions, f_{ν_μ} is constrained much better by the global fit. Note that the tilt of the contours obtained in this analysis compared to the contours from the global fit can also be explained by the composition of the respective data samples. Although no double cascade event is observed, the combination of 35 single cascade and 14 track events cannot be explained by an independently scaling f_{ν_τ}. Because electron-neutrino interactions do not induce track events (aside from the Glashow resonance), the few observed track events can only be compensated by an increasing f_{ν_τ}, due to the muonic tau decay, if f_{ν_μ} is simultaneously decreased. This effect is significantly less pronounced for the global fit because the numerous track events cause a decoupling of f_{ν_τ} from f_{ν_μ}. Evidently, the incorporation of the ternary topology ID into the global fit would significantly increase the overall constraints on the astrophysical neutrino flavor composition. However, this effort is outside the scope of this thesis, but is currently investigated by the IceCube collaboration (see Chapter 8).

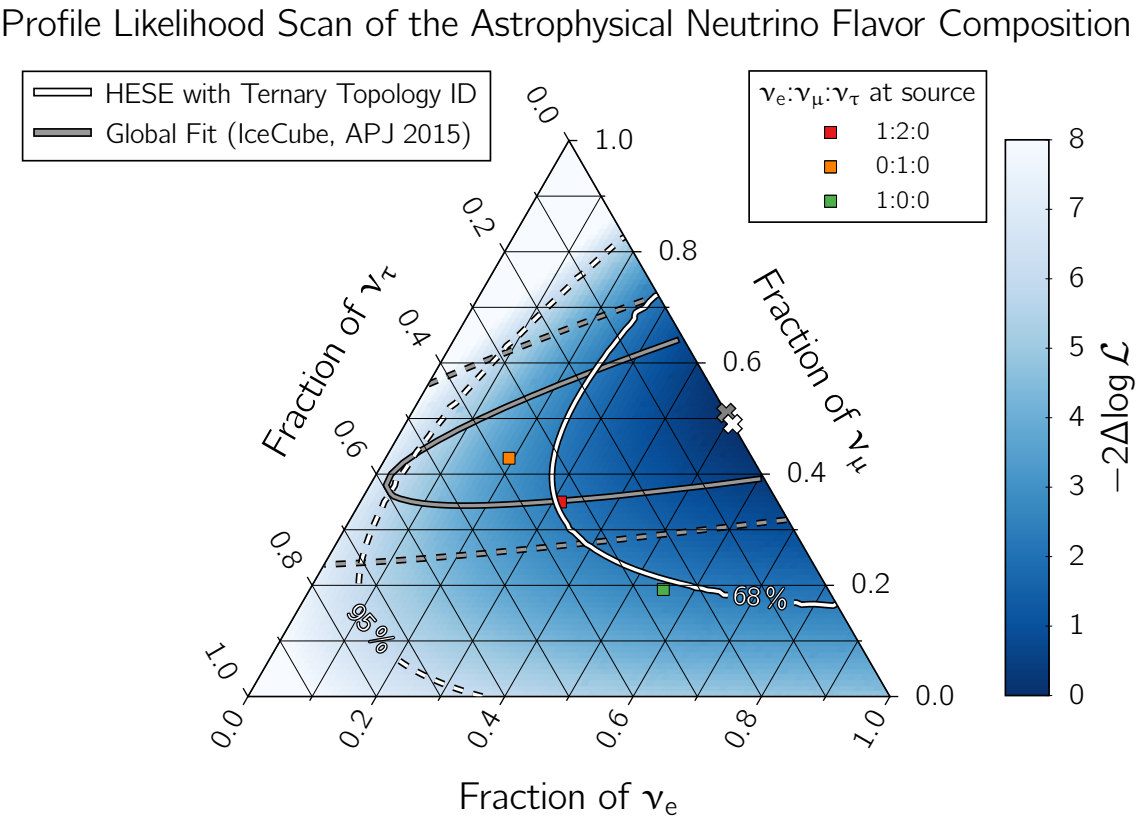

Figure 7.6: Profile likelihood scan of the astrophysical neutrino flavor composition at Earth. Each point in the triangle plot corresponds to a flavor composition $\nu_e : \nu_\mu : \nu_\tau$ which is read off the corresponding axes along the direction of the ticks. The result of this analysis is based on the six-year high-energy starting event sample using the ternary topology ID. The best-fit flavor composition of 0.51 : 0.49 : 0 is marked with a white '×'. The white solid and dashed lines represent the 68% and 95% confidence regions, respectively, obtained from the χ^2-approximation. Three flavor compositions expected at Earth from different source scenarios are marked with differently colored '□' (c.f. Section 2.3.3). The best-fit flavor composition of a previous measurement is marked with a gray '×', and the 68% and 95% confidence regions are represented by the gray solid and dashed lines, respectively [46].

The marked flavor compositions expected at Earth represent different production scenarios at the neutrino sources (c.f. Section 2.3.3): the pion-production scenario with a flavor composition of $1:2:0$, the neutron-beam scenario with $1:0:0$, and the muon-damped scenario with $0:1:0$. The flavor compositions expected at Earth are altered to $0.31:0.35:0.34$, $0.55:0.19:0.26$, and $0.19:0.43:0.38$, respectively, by using the oscillation parameters for an inverted neutrino mass hierarchy listed in Table 2.1. The compatibility of each source scenario with the observed flavor composition is assessed by a likelihood ratio test using the test statistic distribution from Monte Carlo pseudo experiments (see Appendix C.2). This procedure yields $p = 37.5\%$ for the pion-production scenario, $p = 23.6\%$ for the muon-damped scenario, and $p = 26.1\%$ for the neutron-beam scenario. Consequently, all tested source scenarios are compatible with the measured neutrino flavor composition.

7.4 Discussion

It was estimated that $\sim 1-3$ tau-neutrino interactions could have been identified via the double cascade event topology (c.f. Section 6.3.1). However, the sensitivity strongly depends on the spectral shape of the assumed flux model (c.f. Section 6.3.4). In fact, the median detection sensitivity varied between $\sim 1.8-2.9\,\sigma$ ($p = 0.2\%-3.6\%$), depending on the spectral index. The accumulation of events at lower energies, and the lack of events at higher energies over recent years, reduce the expected number of identifiable tau-neutrino interactions significantly. In Figure 7.7, the energy distributions for signal and background double cascade events are depicted for the assumed $\sim E_\nu^{-2.3}$ benchmark spectrum alongside the $\sim E_\nu^{-2.9}$ best-fit spectrum. The distribution for the benchmark flux model illustrates that the largest tau-neutrino contribution expected in the double cascade sample is in an energy region with an observed deficit of events. This is due to the steeply increasing tau-neutrino identification efficiency from $\sim 200\,\mathrm{TeV}$ to $\sim 2\,\mathrm{PeV}$ (c.f. Section 4.4). Consequently, the lack of observed events in the few hundred TeV to PeV range, and the resulting soft fit of the spectrum, significantly reduce the expected number of identifiable tau-neutrino events. Note that neither of the spectral slopes appear to be a precise description of the observed distribution in this energy range. Even the $\sim E_\nu^{-2.9}$ best-fit spectrum overestimates the contribution below $\sim 1\,\mathrm{PeV}$ and underestimates it above.

If the softer spectrum of the observed astrophysical neutrino flux is taken into account, the expected number of identifiable tau-neutrino interactions reduces to $1.48^{+0.08}_{-0.08}$, while the expected number of background events remains at $0.93^{+0.26}_{-0.09}$. The median detection sensitivity becomes $\alpha^{\mathrm{det}}_{\nu_\tau} \simeq 1.7\,\sigma$ ($p \simeq 4.5\%$). These estimates are derived by assuming the best-fit per-flavor flux of $\phi_\nu(E_\nu) = 2.46 \cdot 10^{-18} (E_\nu/100\,\mathrm{TeV})^{-2.92}\,\mathrm{GeV}^{-1}\,\mathrm{cm}^{-2}\,\mathrm{sr}^{-1}\,\mathrm{s}^{-1}$ which is obtained under the assumption of equal flavor fractions. This is compatible with the p-value of $\sim 13.4\%$ when comparing the benchmark flavor composition $\nu_e : \nu_\mu : \nu_\tau = 1:1:1$ to the observed flavor composition $\nu_e : \nu_\mu : \nu_\tau = 1:1:0$ in a one-dimensional likelihood ratio test (c.f. Section 7.2).

Another method of describing the astrophysical neutrino flux which is less dependent on the spectral modeling is a *differential unfolding* of the energy spectrum [44]. The idea is to parametrize the flux as a piecewise function of constant $\sim E_\nu^{-2}$ spectra for which independent flux normalizations are fitted in each neutrino energy bin instead of fitting a continuous single power-law spectrum over the entire energy range. The result is shown in Figure 7.8 for the six-year high-energy starting event sample in comparison to the best-fit result of the single power-law flux model. It can be seen that both the differential unfolding and the power-law model agree within uncertainties. Although this ansatz reduces the assumption of the spectral shape, it is still necessary to assume a flavor composition for the flux.[2]

[2] The remaining model assumptions which require the astrophysical neutrino flux to contain equal amounts of neutrinos and antineutrinos and to arrive isotropically at Earth are also retained.

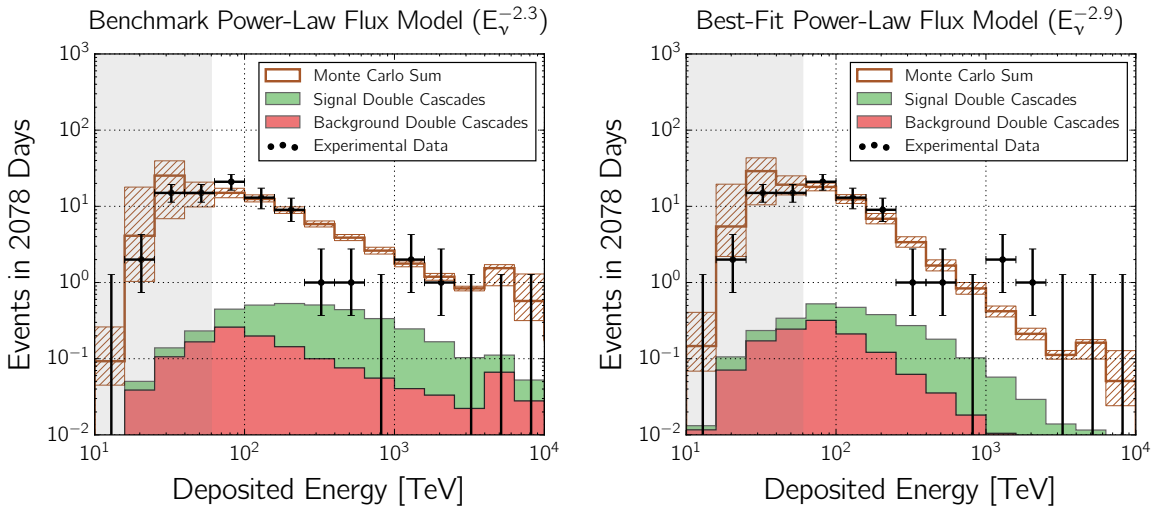

Figure 7.7: Deposited energy distributions expected for the benchmark $\sim E_\nu^{-2.3}$ (left) and the observed $\sim E_\nu^{-2.9}$ (right) energy spectra of the astrophysical neutrino flux. The number of events in the six-year high-energy starting event sample is depicted for experimental data and the sum of all Monte Carlo best-fit flux templates. Statistical and systematic uncertainties are shown as shaded areas. Expected astrophysical tau-neutrino signal and background distributions of the double cascade sample are depicted for both flux models assuming $\nu_e : \nu_\mu : \nu_\tau = 1 : 1 : 1$.

Naturally, it would be desirable to perform the differential unfolding separately for each flavor. This would eliminate the assumption that each flavor has the same spectral shape (c.f. Section 6.2.1). In addition, it would certainly be of interest to measure the flavor composition as a function of the energy, because many neutrino flavor production processes are energy-dependent (c.f. Section 2.3.3). However, the statistical power of the data sample is too weak to obtain a meaningful result. Instead, the differential unfolding of the energy spectrum is performed by assuming the benchmark flavor composition of $\nu_e : \nu_\mu : \nu_\tau = 1 : 1 : 1$.[3] The obtained neutrino spectrum is then used to refit the data for the per-flavor astrophysical neutrino fluxes without the need to include the

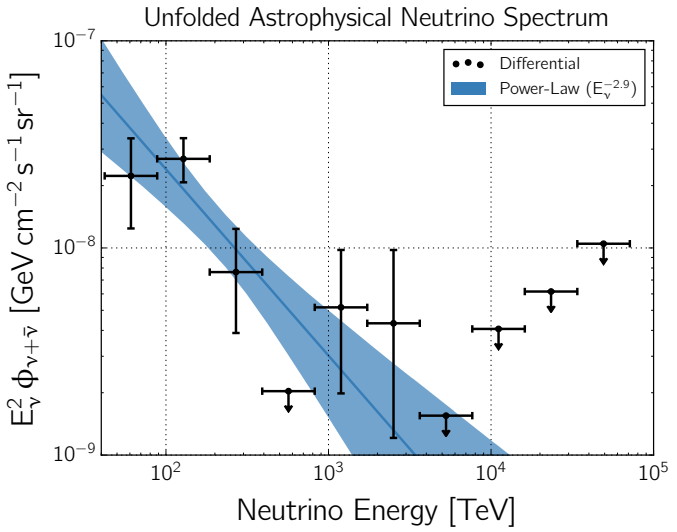

Figure 7.8: Measured astrophysical neutrino spectrum for the differential unfolding and the single power-law model including the 68% uncertainties depicted as colored band. The flux normalization is given per flavor for an assumed flavor composition of $\nu_e : \nu_\mu : \nu_\tau = 1 : 1 : 1$ and for the sum of $\nu + \bar{\nu}$. Figure adapted from [4].

[3] Note that the result of the differential unfolding does not significantly change if the best-fit flavor composition $\nu_e : \nu_\mu : \nu_\tau \simeq 1 : 1 : 0$ is assumed, which can be explained for two reasons. First, the neutrino effective areas of the high-energy starting event selection are similar for electron- and tau-neutrino interactions (c.f. Section 4.2). Hence, the corresponding expected event rate due to each flavor is approximately the same. Second, electron- and tau-neutrinos predominantly induce single and double cascade events, respectively, for which the relation between the total deposited energy and the neutrino energy is similar (c.f. Section 4.3.1). Hence, the contribution of both event topologies to each unfolded neutrino energy bin is about the same.

spectral index. Although the best-fit astrophysical tau-neutrino flux remains zero, the upper constraint is marginally stronger. This is due to the increased contribution of events in the neutrino energy region of a few PeV relative to the decreased contribution in the few hundred TeV region of the differential energy spectrum. Because the tau-neutrino identification efficiency is maximal near $\sim 1\,\mathrm{PeV}$ neutrino energy (c.f. Section 4.4), the folding of the differential energy spectrum with the energy-dependent tau-neutrino identification efficiency happens to approximately retain the expected number of identifiable tau-neutrino interactions at $1.45^{+0.08}_{-0.08}$ while the expected number of background events reduces to $0.73^{+0.20}_{-0.07}$. The best-fit result of the flavor composition for the differential energy spectrum is $\nu_e : \nu_\mu : \nu_\tau = 0.53 : 0.47 : 0$ and agrees with the best-fit flavor composition $\nu_e : \nu_\mu : \nu_\tau \simeq 0.51 : 0.49 : 0$ based on the power-law flux model (c.f. Section 7.3). Because the spectral index is removed from the likelihood, the conditional fits at fixed neutrino flavor fractions are slightly more constrained than they are when using a power-law flux model. In comparison, the compatibility of the measured flavor composition with the tested source scenarios changes only slightly. The assumption of a differential energy spectrum yields $p = 41.0\%$ for the pion-production scenario, $p = 21.1\%$ for the muon-damped scenario, and $p = 31.5\%$ for the neutron-beam scenario. Hence, all tested source scenarios remain compatible with the measured flavor composition.

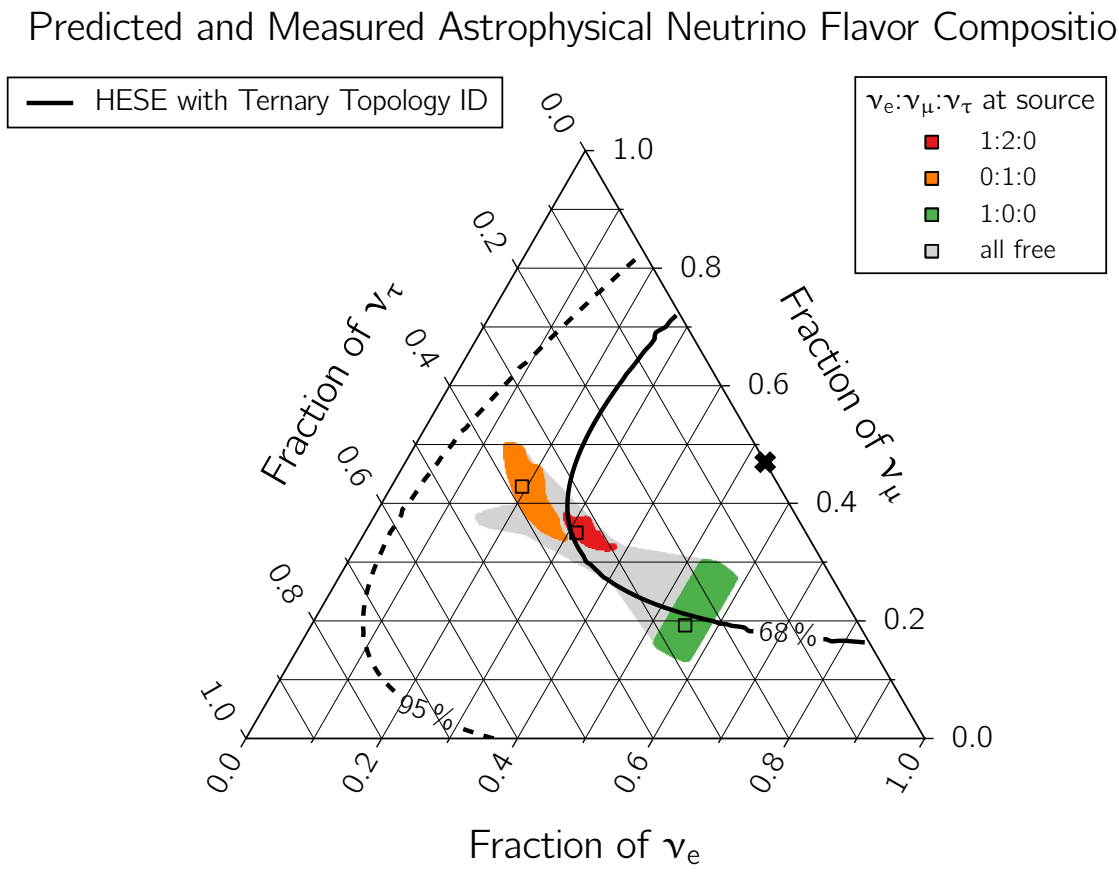

Figure 7.9: Comparison of the measured and theoretical astrophysical neutrino flavor compositions at Earth. The measurement result and the source scenarios are the same as in Figure 7.6. The best-fit flavor composition 0.51 : 0.49 : 0 is marked with '×'. The solid and dashed lines mark the 68% and 95% confidence regions, respectively. Three flavor compositions expected at Earth from different production scenarios at the source are marked with '□'. The colored regions correspond to the uncertainty of each composition due to a variation of the mixing parameters within the $3\,\sigma$ range listed in Table 2.1. The gray area represents the composition expected at Earth for any possible production scenario ($x : y : 1 - x - y$) including the aforementioned uncertainties of the oscillation parameters.

As discussed above, a measured tau-neutrino fraction of zero is not unexpected. However, it is worth noting that no production scenario for astrophysical neutrinos is expected to produce a vanishing tau-neutrino fraction at Earth. Hence, the model uncertainties of the predicted astrophysical neutrino fractions observable at Earth are of particular interest in this context. In Figure 7.9, the best-fit flavor composition derived by assuming the power-law flux model is compared to generalized source scenarios which are possible theoretically if standard three-flavor neutrino oscillations are assumed. The different regions represent flavor compositions expected at Earth due to a variation of the neutrino mixing parameters within $3\,\sigma$ uncertainties (c.f. Section 2.3.3). The corresponding possible phase space of the tau-neutrino fraction is small compared to the electron- and muon-neutrino fractions. This is illustrated by the shape of the gray region in Figure 7.9, which happens to be tilted such that it is nearly parallel to the axis of the tau-neutrino fraction. The resulting variation expected at Earth is $f_{\nu_\tau} = 0.33^{+0.01}_{-0.03}$ for the pion-production scenario ($\nu_e : \nu_\mu : \nu_\tau = 1 : 2 : 0$), $f_{\nu_\tau} = 0.38^{+0.02}_{-0.04}$ for the muon-damped scenario ($\nu_e : \nu_\mu : \nu_\tau = 0 : 1 : 0$) and $f_{\nu_\tau} = 0.23^{+0.08}_{-0.08}$ for the neutron-beam scenario ($\nu_e : \nu_\mu : \nu_\tau = 1 : 0 : 0$). The overall variation of the tau-neutrino fraction for any possible production scenario is $f_{\nu_\tau} = 0.31^{+0.16}_{-0.16}$. The quoted central values correspond to the mean of the projected distributions, and the range represents the aforementioned uncertainties at $3\,\sigma$ confidence level. Therefore, the predicted tau-neutrino fraction at Earth is not expected to vary by more than $\sim 50\%$ in either direction compared to the benchmark of $f_{\nu_\tau} = 1/3$, which is used to estimate the sensitivity of the analysis. In particular, $f_{\nu_\tau} = 0$ is excluded for standard model particle physics and neutrino oscillations.

Hypothetically, a tau-neutrino fraction of zero could be explained by extreme variations of certain beyond-standard-model theories (c.f. Section 2.3.4). This, however, is theoretically less motivated and not supported experimentally by the presently available data. A tau-neutrino fraction of zero could also be explained within the context of standard model physics, if all observed 49 high-energy starting events above 60 TeV were of atmospheric origin. This is due to the large suppression of tau-neutrino production in the atmosphere (c.f. Section 2.2.2). However, the atmospheric-only hypothesis is excluded at a significance of $\sim 8\,\sigma$ with the six-year high-energy starting event sample alone. In addition, multiple other IceCube analyses as listed in Table 6.4 have detected a diffuse astrophysical neutrino flux at high significance.

It can therefore be concluded that the most plausible explanation for the lack of observed tau-neutrino interactions is a statistical under-fluctuation of high-energy events, which may occur in combination with a more complex spectral shape than the single power-law flux model. The constraints on the astrophysical neutrino flavor composition are only marginally different for the power-law and the differential flux model. There is no significant disagreement between the observed flavor composition and any possible composition expected from different source scenarios. Considering the currently available amount of data and the improved but limited efficiency of the tau-neutrino identification method presented in this thesis, even a persisting lack of double cascade events will not introduce a significant tension between observed and expected flavor compositions for some time yet. Nevertheless, it is expected that the number of identified tau-neutrino interactions will not remain zero by adding more detector data in the next few years. Future experiments in particular, as well as supplementary improvements to the IceCube detection methods, may further increase the sensitivity to the astrophysical neutrino flavor composition. These efforts will be briefly discussed in the following chapter.

8 Summary and Outlook

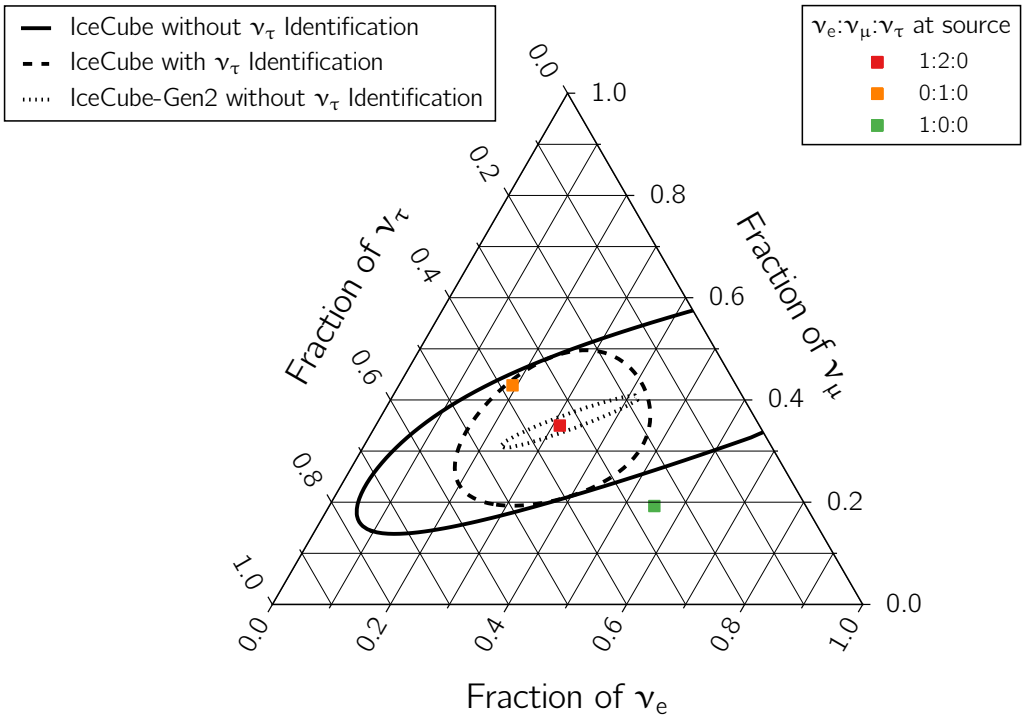

Figure 8.1: Projected sensitivity to the astrophysical neutrino flavor composition over 15 years of detector operation time. Each point in the triangle plot corresponds to a flavor composition $\nu_e : \nu_\mu : \nu_\tau$ which is read off the corresponding axes along the direction of the ticks. Contours represent the 68% confidence regions. IceCube constraints are based on the high-energy starting event sample without and with ν_τ identification using the binary topology ID (cascade, track) and the ternary topology ID (single cascade, double cascade, track), respectively. The IceCube-Gen2 contour is based on the combined operation of IceCube and the IceCube-Gen2 extension for which only the cascade and track event topologies are used [248]. Three flavor compositions expected at Earth from different production scenarios at the source are marked with '□'. The injected astrophysical neutrino flux is $\phi_\nu(E_\nu) = 1.5 \cdot 10^{-18} (E_\nu/100\,\mathrm{TeV})^{-2.3}\,\mathrm{GeV}^{-1}\,\mathrm{cm}^{-2}\,\mathrm{sr}^{-1}\,\mathrm{s}^{-1}$ per flavor. The injected flavor composition corresponds to the pion-production scenario $(1 : 2 : 0)$ at the source.

An unambiguously identified tau-neutrino interaction in the IceCube detector remains undiscovered. The observation of a high-energy tau-neutrino would have been the first of its kind and a smoking-gun signature of astrophysical neutrinos. As their origin is yet to be revealed, the energy spectrum and flavor composition of the measured diffuse neutrino flux contain valuable information about the production mechanisms at their sources. Any knowledge that can be gained from studying astrophysical neutrinos naturally supports the pursuit of answering the century-old question of the origin of the highest-energy cosmic rays.

The goal of the analysis presented in this thesis has been the identification of tau-neutrino interactions in the IceCube detector and the measurement of the astrophysical neutrino flavor composition with hitherto unprecedented constraints on the tau-neutrino fraction. The method is based on the double cascade event topology that is unique to the tau-flavor. It is characterized by a highly energetic charged-current tau-neutrino interaction with a nucleus in the ice, which produces a hadronic cascade and a tau lepton. After an energy-dependent propagation length, the tau decays and produces another hadronic or an electromagnetic cascade, thereby linking two subsequent cascades. An identification method for tau-neutrino interactions has been developed by reconstructing the double cascade event topology. A ternary topology ID of single cascade, double cascade, and track events has been constructed, thereby allowing a neutrino flavor discrimination that is sensitive to all flavors. An anisotropy of the light scattering in the Antarctic ice was determined to be a major source of error for tau-neutrino identification. For the first time, it has been incorporated into existing reconstruction algorithms and tested using experimental flasher LED data. The astrophysical neutrino flavor composition has been measured via a binned maximum likelihood fit using the high-energy starting event sample collected between 2010 and 2016. Depending on the assumed spectral shape of the astrophysical neutrino flux, $\sim 1-3$ identifiable tau-neutrino interactions are expected, and the median detection sensitivity of excluding $\phi_{\nu_\tau} = 0$ is estimated to $\sim 1.8-2.9\,\sigma$ ($p = 0.2\% - 3.6\%$).

No double cascade candidate event has been observed in the six-year high-energy starting event sample. Consequently, the astrophysical tau-neutrino flux is constrained by a 90% CL upper limit of $\phi^{\text{u.l.}}_{\nu_\tau} \leq 2.68 \cdot 10^{-18}\,(E_{\nu_\tau}/100\,\text{TeV})^{-2.97}\,\text{GeV}^{-1}\,\text{cm}^{-2}\,\text{sr}^{-1}\,\text{s}^{-1}$. This is a significant improvement compared to a previous result based on the double pulse method, which produced a considerably weaker upper limit flux at a much harder $\sim E_\nu^{-2}$ spectrum [68]. The measured astrophysical neutrino flavor composition $\nu_e : \nu_\mu : \nu_\tau \simeq 0.51 : 0.49 : 0$ agrees well with a previous result obtained by using multiple IceCube data samples in a global fit [46]. All tested neutrino source scenarios, such as the production and decay of charged pions with a flavor composition of $\nu_e : \nu_\mu : \nu_\tau = 1 : 2 : 0$ at the source, the neutron-beam scenario with $\nu_e : \nu_\mu : \nu_\tau = 1 : 0 : 0$, or the muon-damped scenario with $\nu_e : \nu_\mu : \nu_\tau = 0 : 1 : 0$, are compatible with the observed flavor composition ($p \simeq 20\% - 40\%$). The differences between the power-law and the differential flux model are marginal. It has been concluded that the lack of observed tau-neutrino interactions is not significant and most plausibly explained by a statistical under-fluctuation of high-energy events in recent years. The lack thereof may be connected to a more complex spectral shape than the assumed power-law flux model.

Although no double cascade candidate event has been observed in experimental data, great improvements have been achieved in the context of this thesis. The reconstruction of double cascade events has been established and the formerly assumed resolution limit of the tau decay length has been decreased from a few hundred meters to $\sim 10-20\,\text{m}$. Previous measurements of the flavor composition were only based on a binary topology ID, which is able to distinguish cascade- from track-like events. As both electron- and tau-neutrino interactions predominantly produce cascade-like events, a degeneracy between both flavors left the tau-neutrino fraction largely unconstrained. The development of a ternary topology ID based on the double cascade event topology has broken this degeneracy and has significantly improved the constraints on the tau-neutrino fraction. The ice anisotropy, which had previously not been modeled as a major systematic error, has been incorporated into reconstruction algorithms. It has been shown that a correct treatment of the ice anisotropy is necessary to avoid a reconstruction bias of the tau decay length. The extension of the reconstruction algorithms is not only relevant for the analysis presented in this thesis, but is also applicable to any cascade-like event search in IceCube. For the first time, the in-situ LED calibration system of IceCube has been used to construct experimental double flasher events for testing the novel methods. The search for high-energy tau-neutrinos will certainly continue and benefit from the work presented in this thesis.

In the future, a longer detector operation time will naturally increase the expected number of identifiable tau-neutrino interactions in IceCube. The projected sensitivity over 15 years of detector operation time is shown in Figure 8.1. Evidently, the constraints improve due to the stronger statistical power relative to the six-year data sample. Even with more data, the tau-neutrino fraction remains strikingly unconstrained, unless the ternary topology ID is employed. While the IceCube detector continues to collect data, multiple efforts are investigated for improving the constraints on the flavor composition and the tau-neutrino fraction, in particular. A combination of different event selections, similar to the global fit with the extension of the tau-neutrino identification presented in this thesis, provides a sensible basis for continued investigation [247]. This will improve the constraints on the muon-neutrino fraction due to the inclusion of a larger track-like event sample. However, it will not add more high-energy events and will therefore not change the lack of observed tau-neutrino interactions. Consequently, another approach is to extend the search for tau-neutrinos to other high-energy event selections that are not based on a veto technique [249]. Without discarding events in the outer regions of the detector, the fiducial volume is approximately twice as large. However, this extension is not trivial because the reconstruction of double cascade events in the outer parts of the detector is less precise due to the reduced amount of detected light. Studies based on Monte Carlo simulation show that this approach increases the expected number of identifiable tau-neutrino interactions by $\sim 20 - 45\%$ compared to the sensitivity presented in this thesis. Another approach is an improvement of the double pulse method with a targeted extension to lower energies [250].

An even larger neutrino observatory, *IceCube-Gen2*, is envisioned for the future [251]. The plan is to construct it around the IceCube detector using enhanced drilling and detector technologies. A possible scenario is the deployment of ~ 120 new strings with an average spacing of $\sim 240\,\mathrm{m}$ corresponding to ~ 10 times the volume of IceCube. Studies based on Monte Carlo simulation suggest that identifiable tau-neutrino interactions above 1 PeV neutrino energy increase by a factor of $\sim 5 - 10$ compared to IceCube, depending on energy [251]. The projected constraints on the flavor composition for IceCube-Gen2 are also depicted in Figure 8.1. Note that they are obtained by assuming a binary topology ID for the high-energy starting event selection. Hence, the constraints should be compared to the IceCube contours without tau-neutrino identification. It can be seen how the shape of the contours remains the same but the area is much smaller due to the larger detector volume. The incorporation of tau-neutrino identification into IceCube-Gen2 sensitivity studies is part of future work. Figure 8.1 still illustrates the large potential of a next-generation experiment combined with improved methods for neutrino flavor discrimination.

A different detection technique is based on radio emission from electromagnetic showers that are induced by extremely energetic neutrino interactions in the Antarctic ice. It is employed by the *Askaryan Radio Array* (ARA) [252], which will be built around the IceCube detector. The goal is to be sensitive to an energy region above a few hundred PeV, thereby filling the gap between measurements of the diffuse astrophysical neutrino flux and the extra-galactic cosmic-ray flux (c.f. Figure 1.1). A new radio detection experiment in Antarctica specifically designed to search for tau-neutrinos is proposed in [253]. Its aim is to search for highly energetic tau-neutrinos interacting in a nearby mountain by detecting radio emission from the air shower of the tau decay. A similar experimental setup to search for Earth-skimming tau-neutrinos by employing Cherenkov light instead of radio emission has been examined with the MAGIC telescope [254]. Although experimentally challenging, it may be a promising endeavor for the planned *Cherenkov Telescope Array* (CTA) with larger effective areas than current IACTs [255]. The *Cubic Kilometer Neutrino Telescope* (KM3NeT), currently under construction in the Mediterranean Sea, may further contribute to the characterization of the astrophysical neutrino flux [256] and potentially detect tau-neutrinos [257]. The first identification of a high-energy tau-neutrino interaction in IceCube is likely to occur within the next few years. Other current and future experiments, many of which have not been mentioned, may significantly contribute to this pursuit.

The detection of a high-energy tau-neutrino would only be a small advancement in the search for the sources of the highest-energy neutrinos and cosmic rays. After decades of research as well as the design, construction, operation, and enhancement of many experiments, two new windows to the universe were opened just within the last few years. In 2013, the IceCube Neutrino Observatory laid the foundation for the discovery of astrophysical neutrinos [43]. This result was promptly honored with the *Breakthrough of the Year 2013* award by the British magazine *Physics World*. On September 14, 2015, gravitational waves from a black hole merger event were discovered by the *Laser Interferometer Gravitational-Wave Observatory* (LIGO) [258]. For this ground-breaking observation Kip Thorne, Rainer Weiss, and Barry Barish were awarded the Nobel Prize in Physics in 2017. In combination, both discoveries truly herald the dawn of multi-messenger astronomy. Today, the highest-energy processes in the universe can be readily observed via photons, cosmic rays, neutrinos, and gravitational waves with specific types of observatories. Efforts are increasingly focused on creating a global network of telescopes, with the aim of exchanging rapid notifications about transient phenomena and increasing the availability of simultaneously recorded multi-messenger observations. The first gravitational-wave event in 2015 was followed up by the IceCube and ANTARES experiments and found no correlated neutrinos [259]. On August 17, 2017, another gravitational-wave event from a binary neutron star merger was discovered to coincide with a gamma-ray burst observed by Fermi GBM and INTEGRAL [112]. The first significant detection of a high-energy neutrino to coincide with a gamma-ray burst is probably only a matter of time [260–262]. Very exciting times are ahead, and the revelation of the sources of the highest-energy cosmic rays is closer than ever before.

A Parametrization of the Ice Anisotropy as a Nuisance Parameter

In Chapter 5, the effect of the ice anisotropy in double cascade event reconstruction was illustrated and the solution was described. In summary, it is known that there is an anisotropy of the scattering coefficient in the Antarctic ice, and it has not been incorporated in the event reconstruction in the past. This is acceptable for most analyses, but it was shown that a search for tau-neutrinos via the double cascade event topology is sensitive to this effect. The solution was to incorporate the ice anisotropy by parametrizing an effective distance, which is used in combination with standard photo spline tables describing an isotropic and homogenous ice. The ice anisotropy is thus in fact obeyed during reconstruction, and the misidentified single cascade background significantly reduced (c.f. Figure 5.19).

Because the ice anisotropy has such a large effect on the analysis presented in this thesis, it is equally important to quantize the systematic error of the ice anisotropy itself. The newly developed methods and results presented are based on the assumption that the ice anisotropy is exactly the same in both simulation and reconstruction. More specifically, it is expected to be along three axes, horizontally along an azimuthal angle of 126° and 36° and vertically along the z-axis pointing upward with a -8%, $+4\%$ and $+4\%$ modulation of the nominal scattering coefficient, respectively. An important question is, what the effect on this analysis is if the anisotropy in the Antarctic ice differs from this model. The direction of the anisotropy axes may be slightly different. However, this error can be neglected, because it only shifts the entire bias distribution and does not give a net change (phase shift). More interesting is the question of the magnitude of the ice anisotropy (amplitude shift). In fact, simply by looking at the azimuthal dependence in Figure 5.18 and Figure 5.19, it is already clear that the length bias scales with the magnitude of the anisotropy, because it is clearly visible that the absolute value of the length bias along the minor axis is ~ 2 times smaller than along the major axis. In this chapter, the parametrization of the length bias with respect to the magnitude of the assumed ice anisotropy is described as a systematic uncertainty of the analysis.

Step 0: Prerequisites

There are two assumptions in the following approach:

1. The length bias introduced by a mismatch of the magnitude of the ice anisotropy in simulation and reconstruction is reversible, i.e. it is equivalent if an ice model with anisotropy is assumed in simulation and an ice model without ice anisotropy is assumed in reconstruction or vice versa. In both cases, the direction-dependent absolute values of the introduced length bias are the same. Using the same notation as in Section 5.2.4, this means that the ice model cases **SPICEMie-SPICELea** and **SPICELea-SPICEMie** give the same absolute value of the length bias. This assumption is reasonable as long as the nominal values of the scattering and absorption coefficients are not changed (which they are not). Evidently, it would be ideal to simply have an arbitrary ice model with different scales of the ice anisotropy ready in simulation, reconstruct them using the baseline ice model **SPICELea**, then parametrize the length bias as a function of the ice anisotropy scale. Due to limited computational resources, this could not be realized. The next best alternative would have been to have **SPICEMie** and **SPICELea** simulation data samples

and then check the difference in reconstruction with **SPICELea**. However, **SPICEMie** simulation data samples produced under the same conditions as the data samples used in this analysis are not available. Consequently, based on the aforementioned argument, the third solution is to reasonably assume that the length bias can be parametrized by comparing the ice model cases **SPICELea-SPICEMie** as the maximum mismatch and **SPICELea-SPICELea** as the error-free baseline. Hence, the method is to compare one simulation data sample with different reconstruction outcomes (see Figure A.1).

2. The length bias and the ice anisotropy scale linearly with respect to one another, i.e. the amplitude of the sinusoidal distribution of the length bias in Figure 5.18 would be twice as large if the modulation of the scattering coefficients along the horizontal ice anisotropy axes were -16% and $+8\%$. This assumption is not as straight-forward but can at least be tested for three points where the length bias is compared to the major axis of anisotropy (-8%), to the minor axis of anisotropy ($+4\%$), and to the nominal value ($\pm 0\%$). This is tested in step 3.

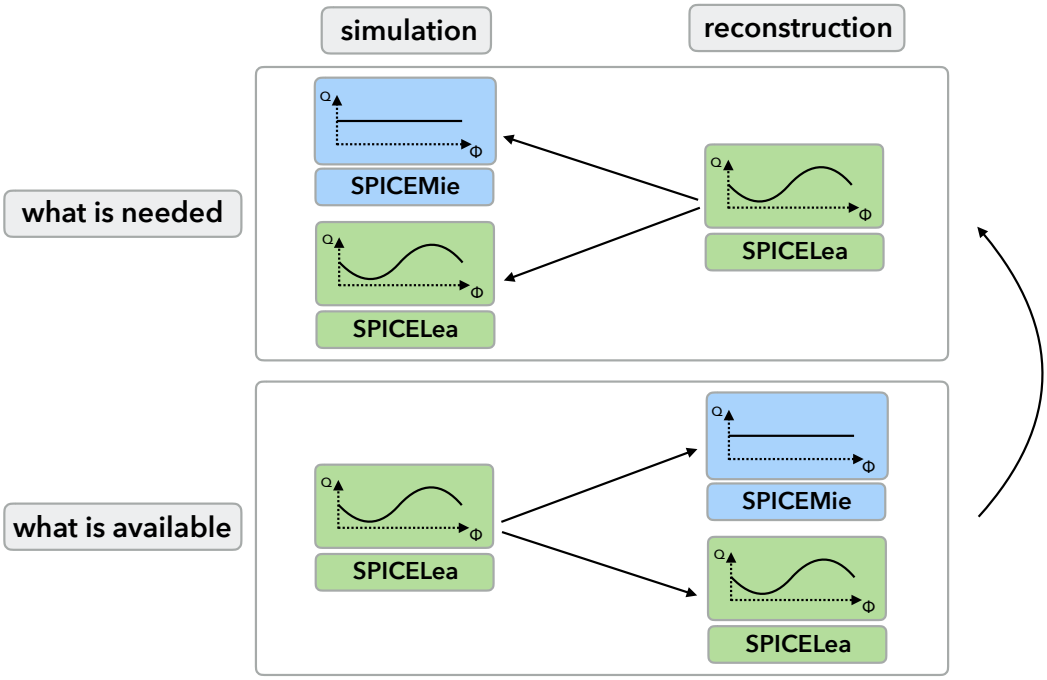

Figure A.1: Sketch of the starting point for the parametrization. Ideally, there would be two simulation data samples assuming the **SPICEMie** and **SPICELea** ice models in order to obtain the parametrization between the ice anisotropy and the length bias. However, only one ice model is available in simulation, whereas two are available in reconstruction. The idea is that this problem is reversible and the parametrization can be obtained by the available data samples.

Step 1: Defining the Length Bias

The goal of the parametrization is to translate a change of the magnitude of the ice anisotropy into a length bias that is applied to the respective observable PDFs. The length bias is parametrized as a function of the zenith and azimuth angles, as it mostly depends on direction. Other possible dependencies such as the depth of the event, the deposited energy, or the length itself can be excluded on average. Consequently, the parametrization is only two-dimensional. Note that it would also be possible to quantify an average length bias which is applied to the readily binned observable PDF. However, it makes more sense to include the main dependencies on the direction on an event-by-event basis in case an ambiguous tau-neutrino candidate along one of the ice anisotropy axes might be observed.

The length bias is defined by comparing the reconstructed length of an event obtained by assuming **SPICEMie** and **SPICELea** during reconstruction:

$$\Delta L = L_{\text{mie}} - L_{\text{lea}}. \tag{A.1}$$

In Figure A.2, the corresponding length bias $L_{\text{reco}} - L_{\text{true}}$ is shown for each ice model and for true single cascades, true double cascades, and true tracks as a cumulative distribution and as a function of the azimuth angle. A piecewise comparison between the distributions of each ice model yields the length bias ΔL as defined in Equation A.1. As discussed in Section 5.2.4, it is clear that the length bias is caused by the ice anisotropy, as it follows the same azimuthal variation of the scattering coefficient. It can be seen that the effect is different for each event topology. Note that the length bias of single cascade events is by definition always positive, because $L_{\text{true}} = 0$ for these events. Hence, the length bias is biggest for single cascades. It is slightly smaller for double cascades. Note that tracks are a special case because

1. they do not have a well-defined "true" length,
2. the differences between ice models are insignificant,
3. the reconstructed average length is larger than 200 m and a bias of $\sim 5 - 10$ m is absorbed by the bin size of the observable PDFs in logarithmic binning.

Therefore, tracks are exempt from this parametrization, because the effect is both ill-defined and negligible in the important region of $\sim 10 - 30$ m decay length.

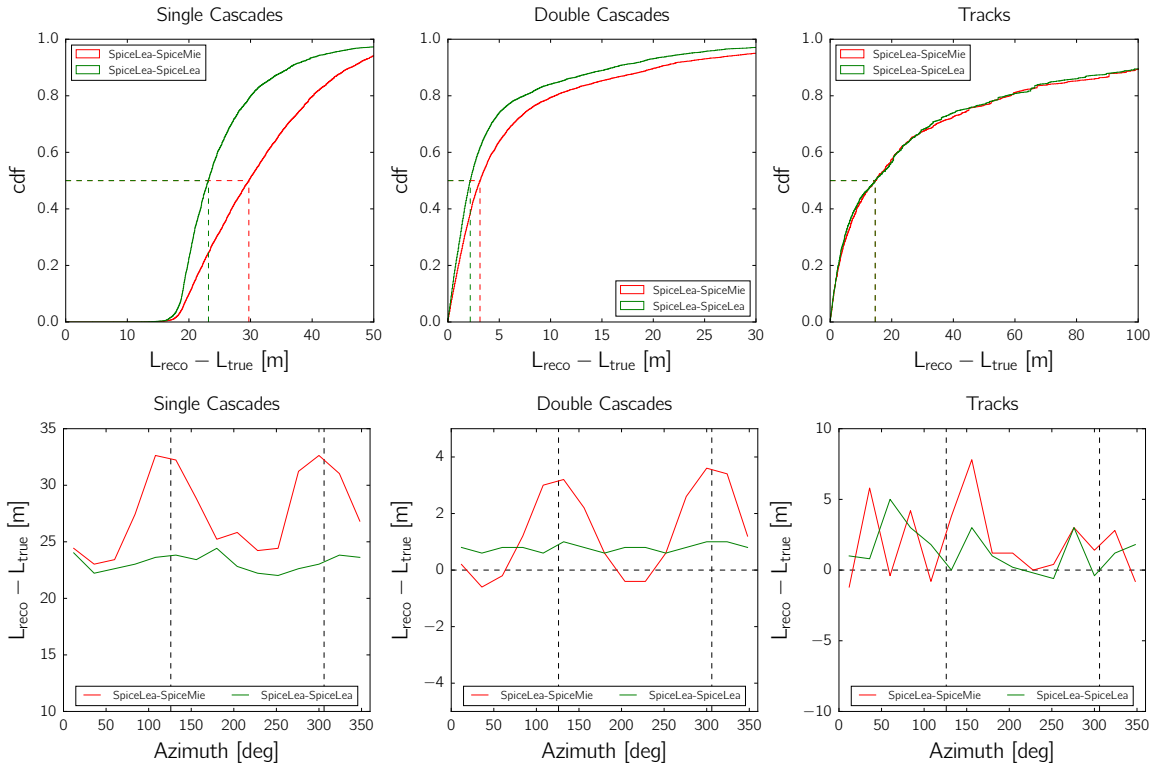

Figure A.2: The length bias $L_{\text{reco}} - L_{\text{true}}$ is depicted using the cumulative distribution (top) and the median as a function of the azimuth angle (bottom) for single cascades (left), double cascades (center), and tracks (right). Each plot contains the two ice model cases **SPICELea-SPICEMie** and **SPICELea-SPICELea**. The dashed lines represent the median of the distributions in the top row and the azimuthal angle of the major anisotropy axis in the bottom row.

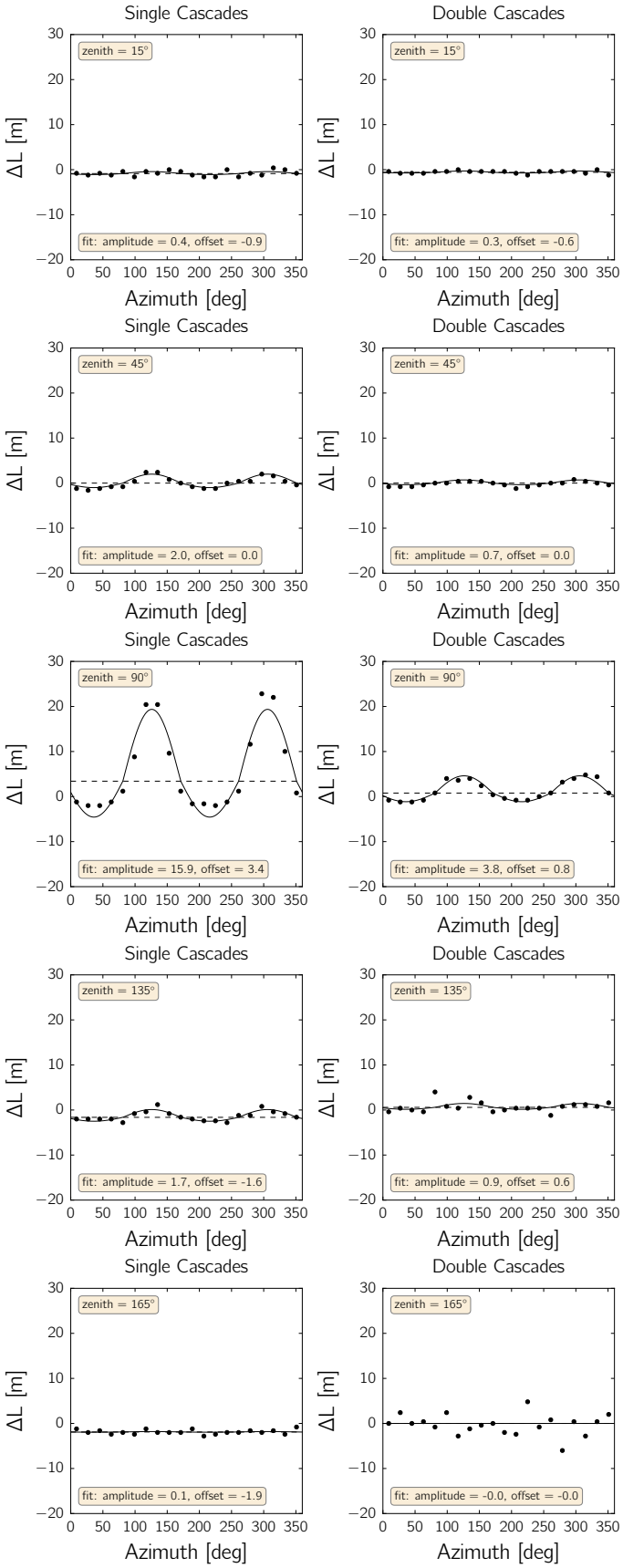

Figure A.3: Distribution and sinusoidal fit of the length bias as a function of the azimuth angle for single cascades (left) and double cascades (right) for different zenith bins centered around 15°, 45°, 90°, 135°, and 165° (from top to bottom).

Step 2: Fitting the Parametrization of the Length Bias

The median length bias $\Delta L = L_{\text{mie}} - L_{\text{lea}}$ is calculated by comparing the reconstructed length using the **SPICEMie** and **SPICELea** ice models. It is depicted as a function of the azimuth angle in Figure A.3 and fitted by an asymmetric sinusoid:

$$\Delta L(\text{azi}, \text{zen}) = \begin{cases} -0.5a(\text{zen}) \sin\left(2(\text{azi} - 9°)\right) + b(\text{zen}) & \text{for azi} \in \{[0°, 90°] \cup [180°, 270°]\}\,, \\ \quad a(\text{zen}) \sin\left(2(\text{azi} - 9°)\right) + b(\text{zen}) & \text{for azi} \in \{[90°, 180°] \cup [270°, 360°]\}\,. \end{cases} \tag{A.2}$$

Note that it has only two free fit parameters, the amplitude a and the offset b, however, both dependent on the zenith angle. The phase of the sinusoid is fixed to the major axis of ice anisotropy (i.e. the domain of definition is shifted by 9°), and the two different amplitudes (corresponding to the -4% and $+8\%$ modulation of the scattering coefficients) are correlated by a fixed ratio of $-0.5 : 1$ [212]. The amplitude a corresponds to the modulation along the major anisotropy axis, thus effectively reducing the two amplitudes to one free fit parameter. The fit is performed for five different zenith bins centered around 15°, 45°, 90°, 135°, and 165°. The resulting best-fit function and values are also depicted in Figure A.3. The best-fit values of the amplitude and offset for each zenith bin and event topology are depicted in Figure A.4 as a function of the zenith angle. In order to obtain a continuous parametrization, the zenith phase space is also fitted by an empirically chosen cosinusoidal function:

$$\begin{aligned} a(\text{zen}) &= c \cos^4\left(\text{zen} - 90°\right) + d, \\ b(\text{zen}) &= e \cos^4\left(\text{zen} - 90°\right) + f\,. \end{aligned} \tag{A.3}$$

In this case, the domain of definition is shifted by 90°, because the effect of the ice anisotropy is maximal in the horizontal plane. Note that the functional form is only motivated empirically and that it is not the best possible description, but good enough for this purpose. This concludes the parametrization of the length bias as a function of the zenith and the azimuth angle. The next step is to introduce a scaling parameter which enables the modeling of arbitrary realizations of the magnitude of the ice anisotropy using this parametrization.

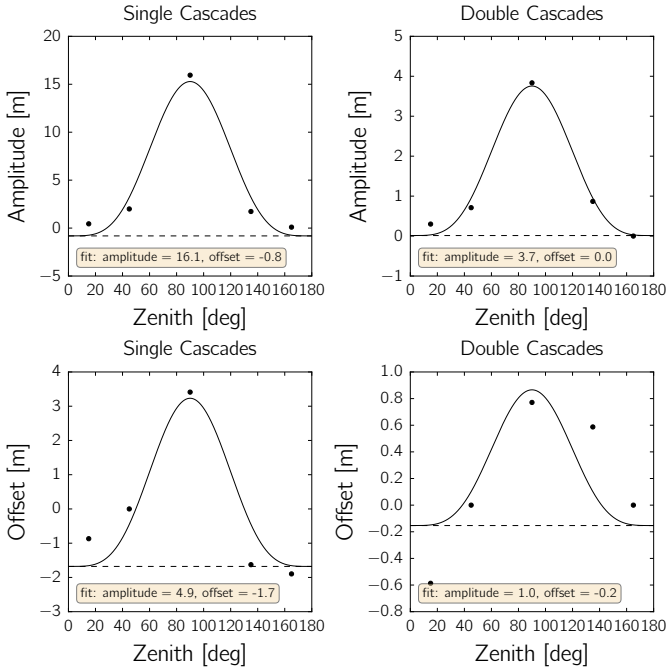

Figure A.4: Distribution and fit of the amplitude (top) and offset (bottom) as defined in Equation A.2 as a function of the zenith angle for single cascades (left) and double cascades (right).

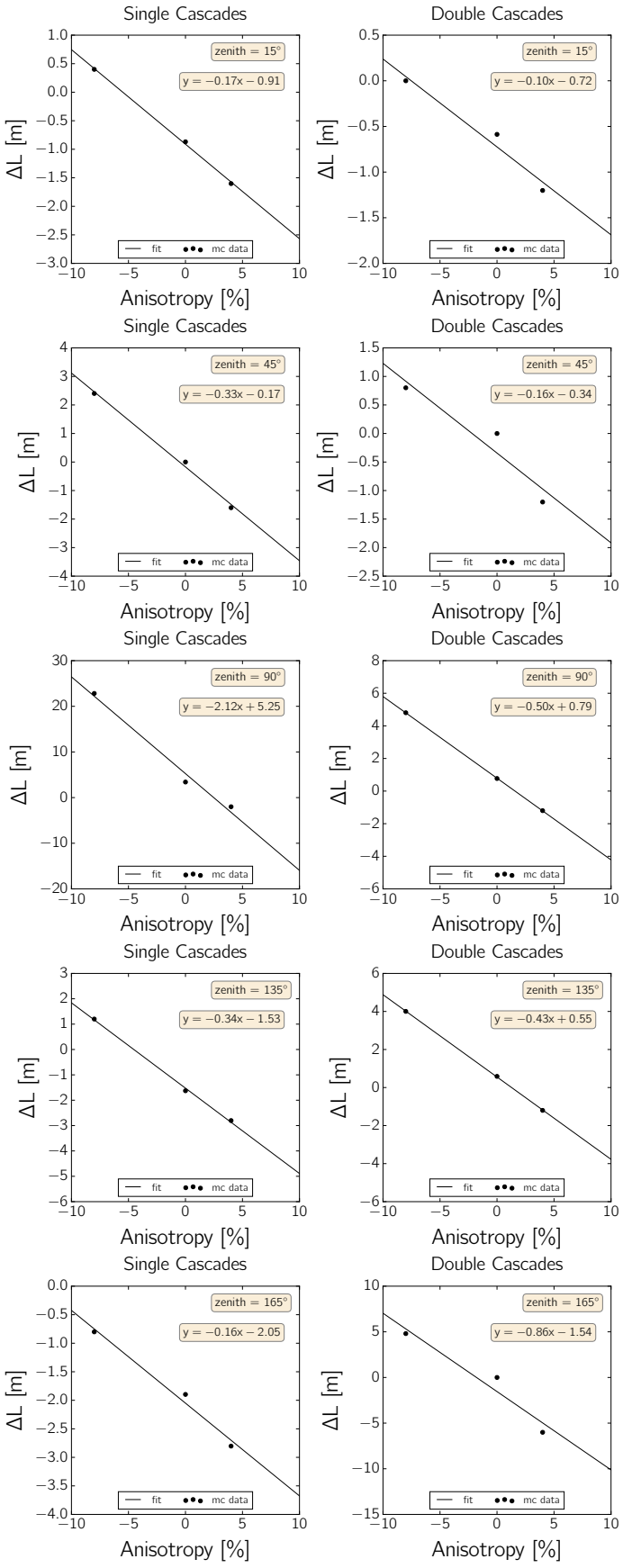

Figure A.5: Distribution and linear fit of the length bias as a function of the magnitude of the ice anisotropy for single cascades (left) and double cascades (right) for different zenith bins centered around 15°, 45°, 90°, 135°, and 165° (from top to bottom).

Step 3: Introducing the Ice Anisotropy Scale

The next step is to characterize the relationship between the length bias and the magnitude of the ice anisotropy. In the second step, a parametrization of the length bias with respect to that very particular realization of the ice anisotropy in **SPICELea** was found. The question is: How does a change of the magnitude of the ice anisotropy translate into the length bias? Because there is only this one realization available as a simulation data sample, an educated guess is that they scale linearly. This can be tested with this one available realization, because it gives three major points in the horizontal plane: -8% and $+4\%$ of anisotropy using the **SPICELea-SPICEMie** case and the nominal value of 0% change of the scattering coefficient by taking the average of the **SPICELea-SPICELea** case. Because the anisotropy axes are along the symmetry axes of the detector and the phase is fixed, these three points are sufficient for a linearity test.

In Figure A.5, the length bias is depicted as a function of these three points of scattering modulation, again for single cascade and double cascade events in different zenith bins. It can be seen that the length bias does in fact scale linearly with the magnitude of the ice anisotropy in good approximation. The extrapolation to smaller and larger values than shown here is acceptable as long as the variation is close enough to the fitted data. This is in fact the case for any realistic modulation of the ice anisotropy, because it is known to some constraint. Different fit methods of the ice anisotropy yielded results that were in agreement within $\sim 20\%$ [212]. Although this is not a well-defined uncertainty, it must suffice as an estimate. The chosen uncertainty is 30% as a more conservative approach and to incorporate additional uncertainties of the parametrization presented in the previous step.

Because the linear correlation holds, it is easy to introduce an anisotropy scale

$$f_{\text{ani}} = \frac{(\text{anisotropy coefficient})_{\text{test}}}{(\text{anisotropy coefficient})_{\text{reco}}} \tag{A.4}$$

in order to model different realization of the ice anisotropy. The denominator stays constant as the **SPICELea** ice model in reconstruction is fixed. The enumerator can be changed to model deviations from the **SPICELea** ice model in simulation. The extreme cases are $f_{\text{ani}} = 0$ for the case where there is no ice anisotropy, $f_{\text{ani}} = 1$ where the ice anisotropy is exactly as big as it is assumed during reconstruction, and $f_{\text{ani}} = 2$ where it is twice as large as in reconstruction (i.e. a modulation of -16% and $+8\%$ of the horizontal minor and major axes, respectively). In the next step, the anisotropy scale f_{ani} is used to model different ice anisotropy realizations.

Step 4: Modeling Different Ice Anisotropy Realizations

The anisotropy scale f_{ani} can be incorporated into the parametrization of the length bias, effectively giving it a dependence on three parameters: f_{ani}, zenith angle, and azimuth angle. Different realizations of the ice anisotropy with respect to the length bias can be effectively modeled by keeping the assumed ice model **SPICELea** in reconstruction fixed. This is sketched in Figure A.6. The parametrized length bias is shown for different anisotropy scales in Figure A.7. Note how the case $f_{\text{ani}} = 1$ yields the baseline case of **SPICELea-SPICELea** by leaving the reconstructed length invariant. The case $f_{\text{ani}} = 2$ can effectively be compared to the case where the baseline magnitude of the ice anisotropy is assumed in simulation but not in reconstruction. This would correspond to the status of the analysis if the incorporation of the ice anisotropy into the reconstruction algorithm as described in Section 5.2 had not been implemented. The cases $f_{\text{ani}} = 0.7$ and $f_{\text{ani}} = 1.3$ represent more realistic variations, because they reflect the estimated $\sim 30\%$ uncertainty of the ice anisotropy (c.f. Section 5.3.3). In the next step, the effect of different ice anisotropy realizations on the observable PDFs is examined.

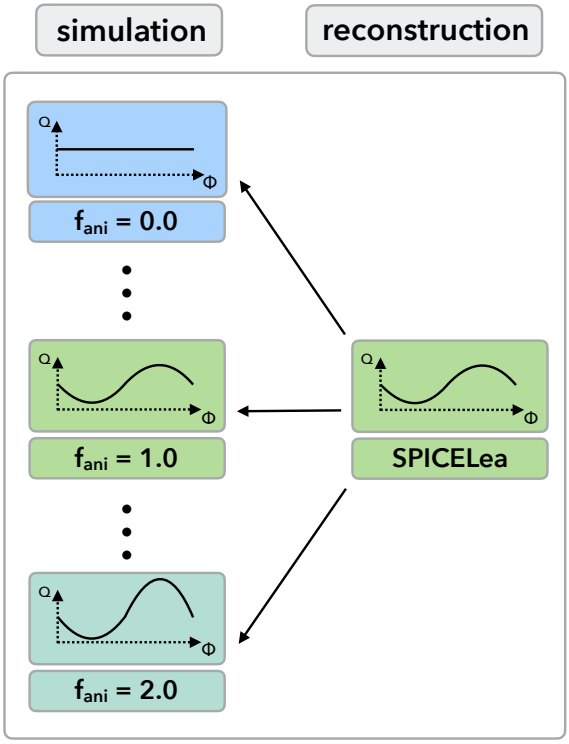

Figure A.6: Sketch of the finish point for the parametrization. The baseline ice model **SPICELea** is fixed during reconstruction, but many ice models with different scales of the ice anisotropy can be parametrized in simulation, however, **only with respect to the length bias**.

Step 5: Applying the Ice Anisotropy Scale to the Observable PDFs

The last step is the application of the length bias to the observable PDFs. Each variation of the anisotropy scale f_{ani} allows the calculation of a length bias from the parametrization. It is applied to each event individually depending on its direction given by the zenith and azimuth angles and on its event topology. After the application of the length bias to all events, the observable PDFs are recalculated. This is shown in Figure A.8 for the reconstructed lengths of all events that are classified as double cascades. The distribution is shown separately for true single cascade events and true double cascades and for different ice anisotropy realizations. The relative change of the integrated signal and background rates in the sample are summarized in Table A.1. Note that a variation of the ice anisotropy does not only cause the integrated event rate in the sample to change, but also shifts the shape of the length distribution.

In conclusion, a variation of the magnitude of the ice anisotropy causes a bias in the length observable that, if not treated correctly, can have a significant effect on the rate of misidentified single cascade events in the double cascade sample. A parametrization was introduced which translates the uncertainty of the ice anisotropy into a length bias on an event-by-event basis depending on the direction and topology of the event. A conservative error of $\sim 30\%$ on the ice anisotropy scale was estimated. Consequently, it is included as a nuisance parameter in the likelihood fit with a prior of $f_{\text{ani}} = 1 \pm 0.3$ as discussed in Section 6.2.1.

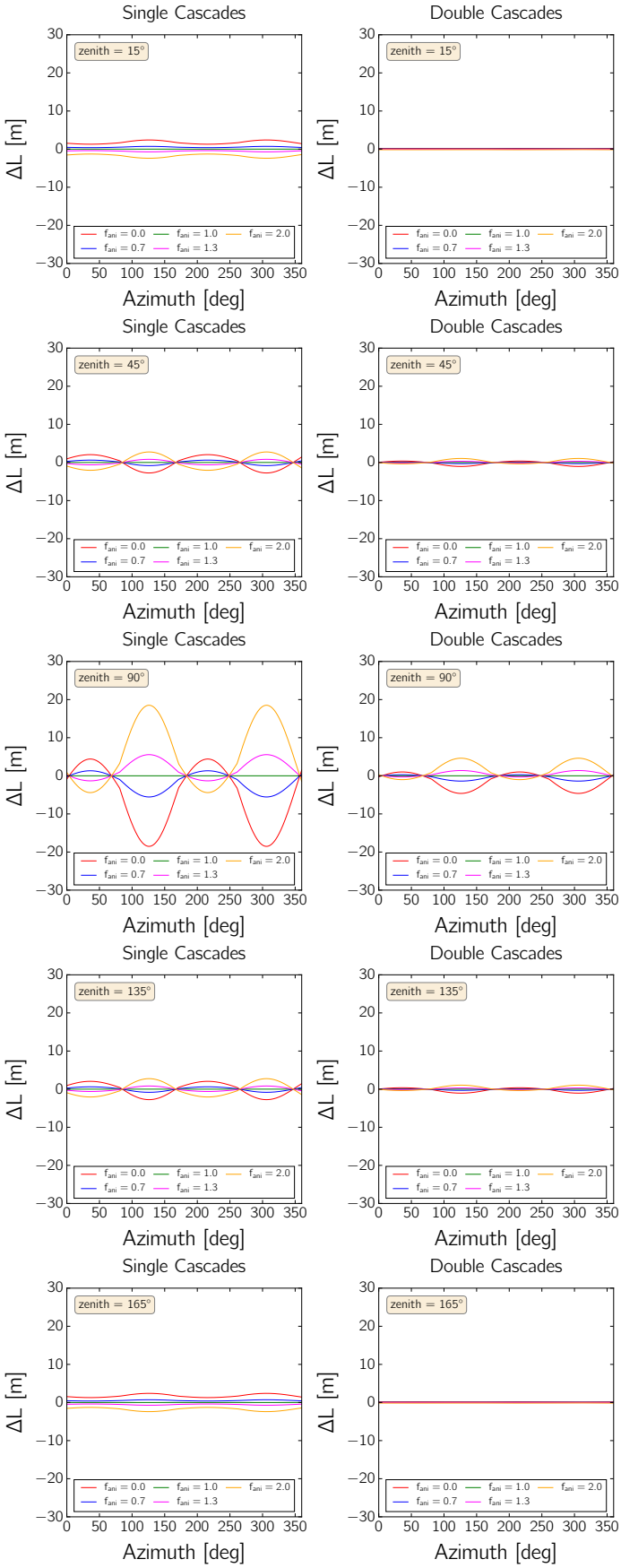

Figure A.7: Length bias as a function of the azimuth angle for different ice anisotropy realizations, shown for single cascades (left) and double cascades (right) for different zenith bins centered around 15°, 45°, 90°, 135°, and 165° (from top to bottom)

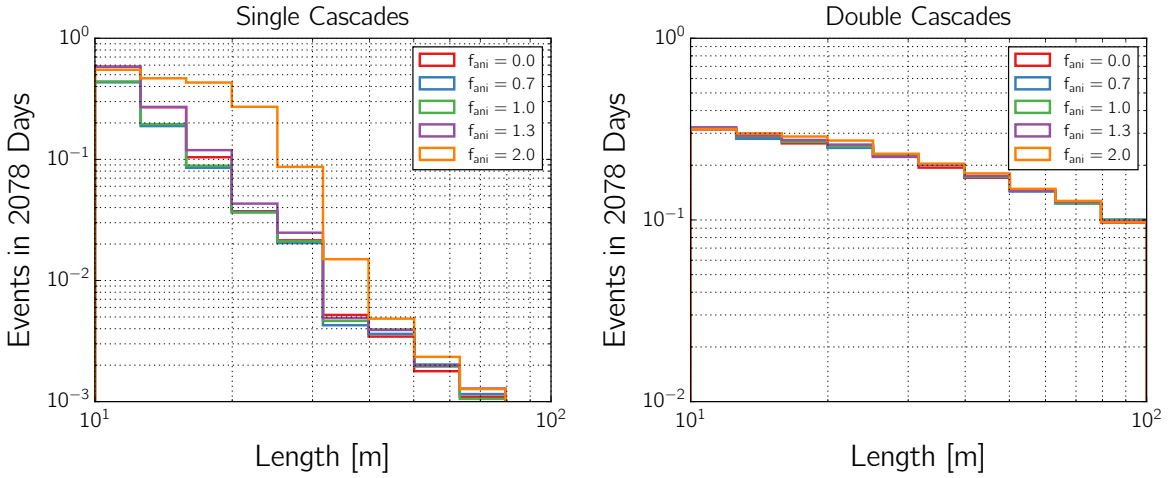

Figure A.8: Reconstructed length of true single cascade events (left) and true double cascade events (right) in the reconstructed double cascade sample. The length bias is applied as a function of the ice anisotropy realization characterized by f_{ani}.

Anisotropy Scale	**Background Deviation**	**Signal Deviation**
0.0	+29.2%	−0.9%
0.7	−2.4%	−0.4%
1.0	±0%	±0%
1.3	+32.7%	+1.0%
2.0	+130%	+3.2%

Table A.1: Deviation of the integrated event rate from the baseline $f_{\text{ani}} = 1$ for misidentified true single cascade events (background) and successfully identified true double cascade events (signal) in the reconstructed double cascade sample as a function of the ice anisotropy realization.

B Selected Single LED Flasher DOMs

String	OM	Angle [deg]	Error [deg]	String	OM	Angle [deg]	Error [deg]
19	12	30.0	2.6	62	12	173.0	1.9
19	13	277.0	2.7	62	14	54.5	2.6
19	20	287.0	2.1	62	15	67.5	2.5
19	23	50.5	2.0	62	16	15.0	2.1
19	25	182.0	1.8	62	24	229.5	2.3
19	26	191.5	2.6	62	25	8.0	2.8
19	27	245.5	1.2	62	29	339.0	1.1
19	29	263.0	1.6	62	39	164.5	2.5
19	30	177.0	2.8	62	40	64.0	2.9
19	39	32.0	3.0	62	41	88.5	1.4
19	42	212.5	2.6	62	42	336.5	2.2
19	43	162.5	1.4	62	43	194.5	1.6
19	45	184.0	1.6	62	45	316.5	2.6
19	47	274.5	2.7	62	46	171.5	2.6
19	54	87.0	2.4	62	48	251.0	2.7
24	13	264.5	2.3	62	49	340.0	2.3
24	15	193.0	2.6	62	50	219.0	1.2
24	26	331.0	1.7	80	5	13.5	2.2
24	45	69.5	2.3	80	19	106.5	1.1
24	46	48.5	2.9	80	31	345.0	2.0
24	47	34.5	1.3	80	44	341.5	2.8
57	14	234.0	2.2	80	46	111.0	2.4
57	16	96.0	1.7	80	47	32.5	1.9
57	18	7.0	2.9	81	7	120.5	2.5
57	19	341.0	2.8	81	9	67.5	2.3
57	21	241.5	2.2	81	15	284.5	1.1
57	22	85.5	0.8	81	19	175.0	2.5
57	23	255.5	1.6	81	20	176.5	2.0
57	24	330.0	2.9	81	21	44.0	2.4
57	27	36.5	1.9	81	22	72.0	1.4
57	28	52.0	2.9	81	28	297.5	2.3
57	30	265.0	1.1	81	31	235.5	2.0
57	45	273.5	2.1	81	37	344.0	2.7
57	46	239.5	1.9	81	46	73.5	1.1
57	47	114.5	0.8	81	48	1.0	2.3
57	50	14.5	1.2	81	50	1.5	2.5
57	51	351.0	1.9	–	–	–	–

Table B.1: Selected DOMs of the single flasher LED anisotropy data sample collected in January, 2015. For each flashing DOM, the azimuth angle of LED 7 is given. It was determined by fitting the leading edge at surrounding DOMs for individually flashing LEDs 7-12. The error of this fit method corresponds to the uncertainty of the obtained DOM rotation.

C Construction of Confidence Regions via Monte Carlo Pseudo Experiments

For many cases in Chapter 6 and Chapter 7, confidence regions are calculated by using Wilks' theorem [234]. As described in Section 6.1, the likelihood ratio compares a conditional best-fit for a test hypothesis $\phi = \phi_t$ to the global best-fit hypothesis $\phi = \hat{\phi}$, i.e.

$$\lambda := -2\Delta\log\mathcal{L} = -2\ln\left(\frac{\mathcal{L}\big(\boldsymbol{n}|\boldsymbol{\mu}(\phi=\phi_t,\hat{\hat{\boldsymbol{\theta}}}_r,\hat{\hat{\boldsymbol{\xi}}})}{\mathcal{L}\big(\boldsymbol{n}|\boldsymbol{\mu}(\hat{\phi},\hat{\boldsymbol{\theta}},\hat{\boldsymbol{\xi}})\big)}\right), \tag{C.1}$$

where $\mathcal{L}$ is the likelihood defined in Equation 6.2, $\boldsymbol{n}$ is the observed data, $\boldsymbol{\mu}$ is the expectation value for a given hypothesis, $\{\hat{\hat{\boldsymbol{\theta}}},\hat{\hat{\boldsymbol{\xi}}}\}$ are the conditional best-fit values of the constrained fit at $\phi = \phi_t$, and $\{\hat{\phi},\hat{\boldsymbol{\theta}},\hat{\boldsymbol{\xi}}\}$ are the global best-fit values of the unconstrained fit. Wilks' theorem states that the test statistic λ can be approximately modeled by $\chi_{k=1}(\lambda)^2$ (or empirically by $f(\lambda) = 0.5\,\delta(\lambda) + 0.5\,\chi^2_{k=1}(\lambda)$ in some cases) for hypotheses that are nested. The χ^2-distribution has $k = 1$ degree of freedom, as the profile likelihood scan is one-dimensional for the aforementioned case. Deviations from a χ^2-distribution are expected, because the sample size is comparably small and the flux parameters are bounded ($\phi_{\nu_e}, \phi_{\nu_\mu}, \phi_{\nu_\tau} \geq 0$). Therefore, the exact distribution of λ is determined for some results by performing a large number of Monte Carlo pseudo experiments. The generated test statistic distribution is used for calculating the correct confidence regions of the parameter(s) of interest and for testing the validity of Wilks' theorem in the process. The procedure for generating pseudo experiments using the conditional best-fit parameters of the profile likelihood scan is described in Section 6.1.

In Section C.1, the technical details of the estimated sensitivity to the astrophysical tau-neutrino flux as presented in Chapter 6 is discussed. The median detection sensitivity $\alpha^{\text{det}}_{\nu_\tau}$ and median upper limit $\phi^{\text{u.l.}}_{\nu_\tau}$ estimated using the Asimov dataset and Wilks theorem are validated by generating the full test statistic distribution from pseudo experiments. In Section C.2, the technical details of the measurement results as presented in Chapter 7 are discussed. The construction of the upper limit on the astrophysical tau-neutrino flux and the confidence levels of the astrophysical neutrino flavor composition for different source scenarios are presented. Furthermore, the confidence region of the measured astrophysical flavor composition obtained using Wilks theorem is assessed by calculating the coverage for several points in the phase space.

C.1 Sensitivity Estimation

The test statistic distributions for calculating the median detection sensitivity and median upper limit are shown in Figure C.1. The respective distributions are obtained by performing 10 000 (1 000) Monte Carlo pseudo experiments for a targeted confidence level of ∼99% (∼90%). Each pseudo experiment is generated by injecting the conditional best-fit parameters of the median profile likelihood scan at the test value of the astrophysical tau-neutrino flux using the Asimov dataset for the astrophysical and atmospheric benchmark models (c.f. Figure 6.10 and Figure 6.11). Note that the likelihood ratio used for the detection sensitivity (c.f. Equation 6.9) is different from the one used for the upper limit (c.f. Equation 6.10).

Detection sensitivity The test statistic distribution for the detection sensitivity (Figure C.1, left plot) is shown as the survival function. The background-only hypothesis is obtained by injecting $\phi_{\nu_\tau} = 0$ and the signal-injection hypothesis corresponds to the astrophysical benchmark model where $\phi_{\nu_\tau}(E_{\nu_\tau}) = 1.5 \cdot 10^{-18} (E_{\nu_\tau}/100\,\mathrm{TeV})^{-2.3}\,\mathrm{GeV}^{-1}\,\mathrm{cm}^{-2}\,\mathrm{sr}^{-1}\,\mathrm{s}^{-1}$. Note that the test statistic distribution of the background-only hypothesis can be modeled empirically with $f(\lambda) = 0.5\,\delta(\lambda) + 0.5\,\chi^2_{k=1}(\lambda)$, as described in Section 6.3.2. The corresponding graph is depicted by integrating the $\delta(\lambda)$-function over the first bin and scaling the survival function of $\chi^2_{k=1}(\lambda)$ by 0.5. It can be seen that the distribution is described well by $f(\lambda)$ for $\lambda \gtrsim 2$. A mismatch below this value is expected to some extent due to the boundary of the flux parameter and the small signal sample size. The test statistic distribution of the signal injection has an entirely different shape because the test hypothesis used in the likelihood ratio is $\phi_{\nu_\tau} = 0$.

From the definition of the confidence level in Equation 6.6 by integrating over the phase space to the critical test statistic value λ_c, it follows that $\chi^2_{k=1}(\lambda \leq \lambda_c) = 1 - \alpha$ is equivalent to $f(\lambda \leq \lambda_c) = 1 - 2\alpha$. That means that the detection sensitivity can be conveniently calculated by $\alpha^{\mathrm{det}}_{\nu_\tau} = \left(1 - \chi^2_{k=1}(\lambda \leq \lambda_c)\right)/2$ in the present case. From the distribution of the signal injection, the median value is extracted at $\lambda_{\mathrm{obs}} \simeq 5.4$, and hence the median detection sensitivity is $\alpha^{\mathrm{det}}_{\nu_\tau} \simeq 2.3\,\sigma$ (p=1%), as can be read off the distribution. Note that the median value $\lambda_{\mathrm{obs}} \simeq 5.4$ obtained from the distribution is slightly lower than the value $\lambda_{\mathrm{obs}} \simeq 7$ obtained from the Asimov dataset (c.f. Figure 6.10). This can be explained by a small over-fluctuation at $\lambda = 0$ for a few trials, in which the "observed" number of signal events has been too low to constrain $\phi_{\nu_\tau} > 0$. Consequently, the detection sensitivity obtained from performing pseudo experiments is slightly slower than estimated in Section 6.3.2.

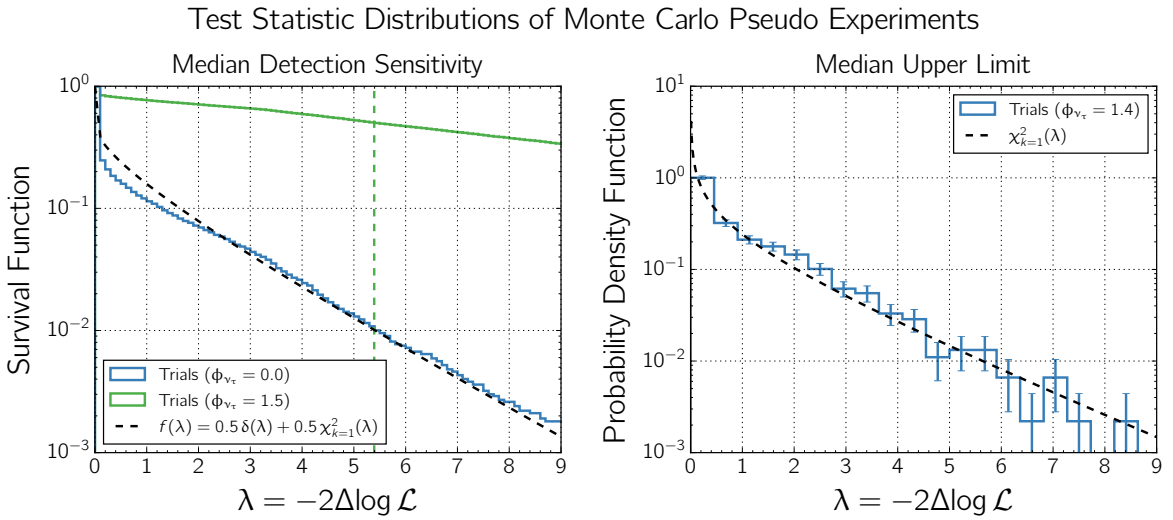

Figure C.1: Test statistic distribution for estimating the sensitivity to the astrophysical tau-neutrino flux. In the left plot, the test statistic distribution is depicted for the likelihood ratio used to define the detection sensitivity $\alpha^{\mathrm{det}}_{\nu_\tau}$ (c.f. Equation 6.9). The background hypothesis is a true injected flux of $\phi_{\nu_\tau} = 0$ (blue), for which the test statistic distribution is expected to follow $f(\lambda) = 0.5\,\delta(\lambda) + 0.5\,\chi^2_{k=1}(\lambda)$. The signal hypothesis is a true injected flux of $\phi_{\nu_\tau}(E_{\nu_\tau}) = 1.5 \cdot 10^{-18} (E_{\nu_\tau}/100\,\mathrm{TeV})^{-2.3}\,\mathrm{GeV}^{-1}\,\mathrm{cm}^{-2}\,\mathrm{sr}^{-1}\,\mathrm{s}^{-1}$ (green), for which the median value is indicated by a vertical dashed line. In the right plot, the test statistic distribution is depicted for the likelihood ratio used to define the upper limit $\phi^{\mathrm{u.l.}}_{\nu_\tau}$ (c.f. Equation 6.10). The true injected flux of $\phi_{\nu_\tau}(E_{\nu_\tau}) = 1.4 \cdot 10^{-18} (E_{\nu_\tau}/100\,\mathrm{TeV})^{-2.3}\,\mathrm{GeV}^{-1}\,\mathrm{cm}^{-2}\,\mathrm{sr}^{-1}\,\mathrm{s}^{-1}$ is taken from the median profile likelihood scan in Figure 6.11, for which the test statistic distribution is expected to follow a χ^2-distribution with $k = 1$ degree of freedom.

Upper Limit The test statistic distribution for the upper limit (Figure C.1, right plot) is shown as the probability density function. The distribution is obtained by injecting the 90% CL upper limit flux $\phi^{\text{u.l.}}_{\nu_\tau}(E_{\nu_\tau}) = 1.4 \cdot 10^{-18} (E_{\nu_\tau}/100\,\text{TeV})^{-2.3}\,\text{GeV}^{-1}\,\text{cm}^{-2}\,\text{sr}^{-1}\,\text{s}^{-1}$ and the conditional best-fit values of all remaining model parameters. The upper limit flux is derived from a profile likelihood scan of the astrophysical tau-neutrino flux using the Asimov dataset for $\phi_{\nu_\tau} = 0$ (with rescaled ϕ_{ν_e} and ϕ_{ν_μ}) and Wilks' theorem (c.f. Figure 6.11). It can be seen that the test statistic distribution is described fairly well by a χ^2-distribution with one degree of freedom. In fact, the coverage of the test statistic distribution for $\lambda \leq \lambda_c$ with $\lambda_c = \lambda_{\text{obs}} \simeq 2.7$ is $(89 \pm 1)\%$. Because λ_c is chosen such that $\chi^2_{k=1}(\lambda \leq \lambda_c) = 90\%$, the coverage compares favorably with the desired 90% CL. It can be concluded that the estimated median upper limit is compatible with the limit obtained from performing pseudo experiments.

C.2 Measurement Results

The test statistic distributions for calculating the upper limit of the astrophysical tau-neutrino flux and the p-values of the astrophysical neutrino flavor composition for different source scenarios are shown in Figure C.2. The distribution for the upper limit is obtained by performing 1 000 Monte Carlo pseudo experiments, and the distributions for the source scenarios are obtained from 2 000 Monte Carlo pseudo experiments for each source scenario. Pseudo experiments are generated by injecting the conditional best-fit parameters of the profile likelihood scans at the test value of the astrophysical tau-neutrino flux or the astrophysical neutrino flavor composition, respectively (c.f. Figure 7.5 and Figure 7.6).

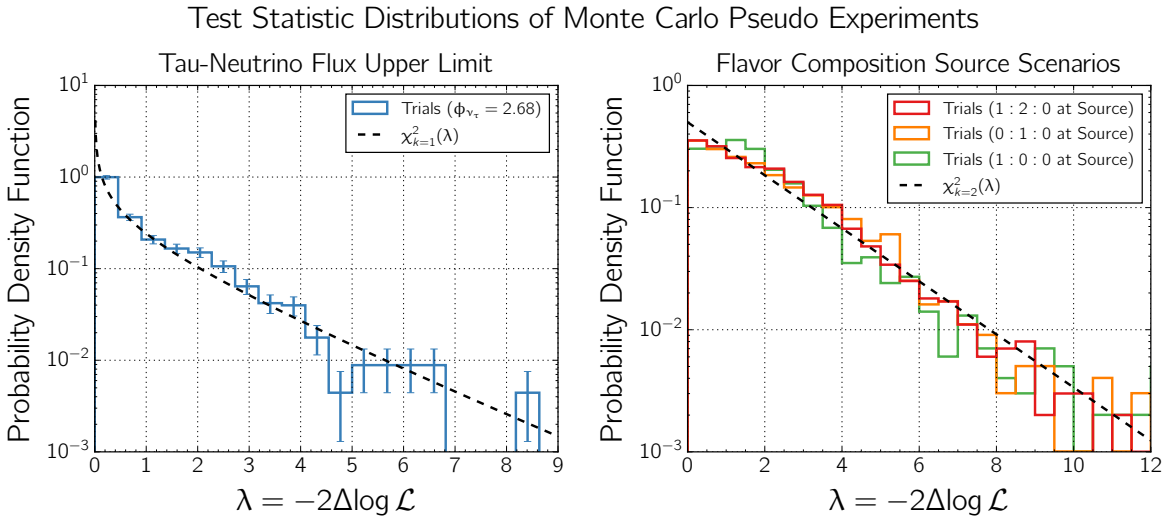

Figure C.2: Test statistic distributions for calculating the upper limit of the astrophysical tau-neutrino flux (left) and the p-values of the astrophysical neutrino flavor composition for different source scenarios (right). The depicted likelihood ratios are defined in Equation C.2 and Equation C.3, respectively. The test statistic distribution in the left plot is generated by injecting $\phi_{\nu_\tau} = \phi^{\text{u.l.}}_{\nu_\tau}(E_{\nu_\tau}) = 2.68 \cdot 10^{-18} (E_{\nu_\tau}/100\,\text{TeV})^{-2.97}\,\text{GeV}^{-1}\,\text{cm}^{-2}\,\text{sr}^{-1}\,\text{s}^{-1}$ into the Monte Carlo simulation. The distributions in the right plot are generated by injecting different flavor compositions as described in the text. The depiction of statistical uncertainties is omitted here in order to enhance the visibility of each distribution. A χ^2-distribution with one and two degrees of freedom, respectively, is shown in comparison for each plot.

Upper limit The likelihood ratio used in the one-dimensional profile likelihood scan of the astrophysical tau-neutrino flux for calculating an upper limit is defined by

$$\lambda := -2\Delta\log\mathcal{L} = -2\ln\left(\frac{\mathcal{L}\big(\boldsymbol{n}|\boldsymbol{\mu}(\phi_{\nu_\tau} = \phi_{\nu_\tau}^{\text{s.p.}}, \hat{\hat{\boldsymbol{\theta}}}, \hat{\hat{\boldsymbol{\xi}}})\big)}{\mathcal{L}\big(\boldsymbol{n}|\boldsymbol{\mu}(\hat{\phi}_{\nu_\tau}, \hat{\boldsymbol{\theta}}, \hat{\boldsymbol{\xi}})\big)}\right). \tag{C.2}$$

The test statistic is evaluated at each scan point $\phi_{\nu_\tau} = \phi_{\nu_\tau}^{\text{s.p.}}$ for which the remaining model parameters $\boldsymbol{\theta} = (\phi_{\nu_e}, \phi_{\nu_\mu}, \gamma)$ and $\boldsymbol{\xi} = (\phi_{\text{muon}}, \phi_{\text{conv}}, \phi_{\text{prompt}}, \xi_E, \xi_A)$ assume their conditional best-fit values $\{\hat{\hat{\boldsymbol{\theta}}}, \hat{\hat{\boldsymbol{\xi}}}\}$, or the global best-fit values $\{\hat{\phi}_{\nu_\tau}, \hat{\boldsymbol{\theta}}, \hat{\boldsymbol{\xi}}\}$ in the unconstrained fit. The test statistic distribution for the upper limit (Figure C.2, left plot) is obtained by injecting the estimated 90% CL upper limit flux $\phi_{\nu_\tau}^{\text{u.l.}}(E_{\nu_\tau}) = 2.68 \cdot 10^{-18}(E_{\nu_\tau}/100\,\text{TeV})^{-2.97}\,\text{GeV}^{-1}\,\text{cm}^{-2}\,\text{sr}^{-1}\,\text{s}^{-1}$ and the conditional best-fit values of all remaining model parameters into the Monte Carlo simulation. The quoted upper limit flux is estimated from a profile likelihood scan of the astrophysical tau-neutrino flux using the 49 observed events above 60 TeV deposited energy and Wilks' theorem (c.f. Figure 7.5). It can be seen that the test statistic distribution is described fairly well by a χ^2-distribution with one degree of freedom. In fact, the coverage of the test statistic distribution for $\lambda \leq \lambda_c$ with $\lambda_c = \lambda_{\text{obs}} \simeq 2.7$ is $(90 \pm 1)\%$, which means that the estimated upper limit flux derived from Wilks' theorem and the more precise upper limit flux derived from performing Monte Carlo pseudo experiments are equal within uncertainties.

Source scenarios The likelihood ratio used in the two-dimensional profile likelihood scan of the astrophysical neutrino flavor composition for calculating confidence regions is defined by

$$\lambda := -2\Delta\log\mathcal{L} = -2\ln\left(\frac{\mathcal{L}\big(\boldsymbol{n}|\boldsymbol{\mu}(f_{\nu_e} = f_{\nu_e}^{\text{s.p.}}, f_{\nu_\mu} = f_{\nu_\mu}^{\text{s.p.}}, \hat{\hat{\boldsymbol{\theta}}}, \hat{\hat{\boldsymbol{\xi}}})\big)}{\mathcal{L}\big(\boldsymbol{n}|\boldsymbol{\mu}(\hat{f}_{\nu_e}, \hat{f}_{\nu_\mu}, \hat{\boldsymbol{\theta}}, \hat{\boldsymbol{\xi}})\big)}\right). \tag{C.3}$$

The flavor fractions are $f_{\nu_e} = \phi_{\nu_e}/\phi_{\nu_{\text{tot}}}$, $f_{\nu_\mu} = \phi_{\nu_\mu}/\phi_{\nu_{\text{tot}}}$, and $f_{\nu_\tau} = \phi_{\nu_\tau}/\phi_{\nu_{\text{tot}}}$ with the total astrophysical neutrino flux $\phi_{\nu_{\text{tot}}} = \phi_{\nu_e} + \phi_{\nu_\mu} + \phi_{\nu_\tau}$. The test statistic is evaluated at each scan point $(f_{\nu_e} = f_{\nu_e}^{\text{s.p.}}, f_{\nu_\mu} = f_{\nu_\mu}^{\text{s.p.}})$ for which the remaining model parameters $\boldsymbol{\theta} = (\phi_{\nu_{\text{tot}}}, \gamma)$ and $\boldsymbol{\xi} = (\phi_{\text{muon}}, \phi_{\text{conv}}, \phi_{\text{prompt}}, \xi_E, \xi_A)$ assume their conditional best-fit values $\{\hat{\hat{\boldsymbol{\theta}}}, \hat{\hat{\boldsymbol{\xi}}}\}$, or their global best-fit values $\{\hat{f}_{\nu_e}, \hat{f}_{\nu_\mu}, \hat{\boldsymbol{\theta}}, \hat{\boldsymbol{\xi}}\}$ in the unconstrained fit.

As discussed in Section 2.3.3, the altered neutrino flavor composition expected at Earth due to neutrino oscillations is considered for three source scenarios:

Pion-production scenario:	$1:2:0$	$\rightarrow$	$0.31:0.35:0.34$
Muon-damped scenario:	$0:1:0$	$\rightarrow$	$0.19:0.43:0.38$
Neutron-beam scenario:	$1:0:0$	$\rightarrow$	$0.55:0.19:0.26$

The test statistic distributions for each of these scenarios (Figure C.2, right plot) is obtained by injecting the flavor fractions listed above into the Monte Carlo simulation. As described above, the conditional best-fit values of all remaining model parameters are injected at each point in the flavor composition phase space. It can be seen that the distributions do not deviate significantly from a χ^2-distribution with two degrees of freedom. Nevertheless, the p-values are obtained directly from the generated test statistic distributions. The observed test statistic values using the data sample of 49 events are $\lambda_{\text{obs}} \simeq 2.25$ for the pion-production scenario, $\lambda_{\text{obs}} \simeq 3.20$ for the muon-damped scenario, and $\lambda_{\text{obs}} \simeq 2.53$ for the neutron-beam scenario. The corresponding p-values α are derived from the cumulative test statistic distribution for which $\lambda > \lambda_{\text{obs}} = \alpha$. This yields $p = 37.5\%$ for the pion-production scenario, $p = 23.6\%$ for the muon-damped scenario, and $p = 26.1\%$ for the neutron-beam scenario. Hence, all tested source scenarios are in agreement with the measured flavor composition.

In addition to the source scenario tests, the validity of Wilks' theorem is assessed by comparing the coverage of the test statistic distribution from Monte Carlo pseudo experiments to the coverage of $\chi^2_{k=2}(\lambda)$. For each of the 68% and 95% confidence regions, five scan points are selected (see Figure C.3). The corresponding flavor fractions and observed test statistic value is listed in Table C.1. As described above, for each scan point 1 000 pseudo experiments are performed. The resulting test statistic distributions are depicted in Figure C.4. It can be seen that the distributions do not deviate significantly from a χ^2-distribution with two degrees of freedom. The coverage $1-\alpha$ for each scan point is calculated via the cumulative distribution for which $\lambda \leq \lambda_{\text{obs}} = 1-\alpha$. The results are depicted in Figure C.5. It can be seen that the coverage for a large fraction of scan points is well described by a χ^2-distribution. However, the central part of the 68% confidence region seems to suffer from under-coverage, albeit not significantly with respect to the target confidence level. In contrast, some of the scan points for the 95% confidence region slightly over-cover, i.e. Wilks' theorem yields a conservative confidence region. It can be concluded that the χ^2-approximation is sufficient for the presentation of the measurement result. The confidence regions depicted in Figure 7.6 can be approximated by using Wilks' theorem while the confidence levels of the source scenario tests (which happen to be in the phase space region where a slight under-coverage is expected) are derived by generating the exact test statistic distribution from Monte Carlo pseudo experiments.

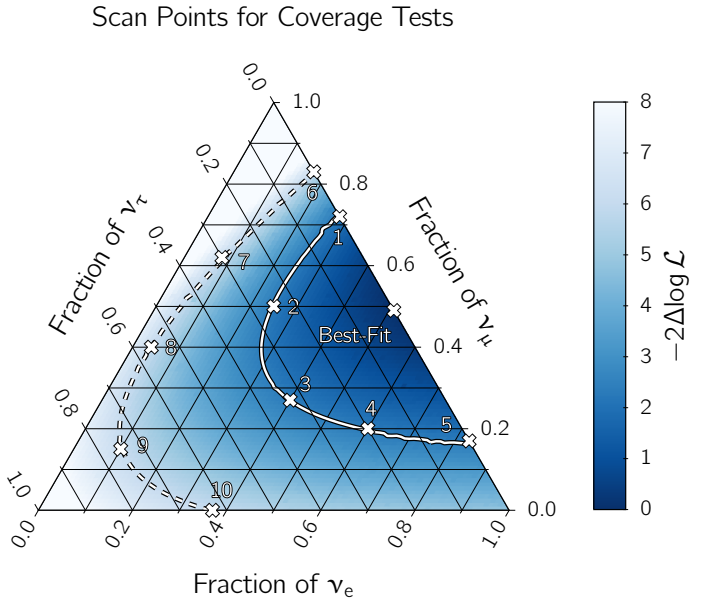

Figure C.3: Illustration of the selected scan points at 68% and 95% confidence level in the phase space of the astrophysical neutrino flavor composition. The profile likelihood scan for $\lambda = -2\Delta\log\mathcal{L}$ is the same as in Figure 7.6. The solid and dashed lines represent the 68% and 95% confidence regions, respectively, which are derived from $\chi^2_{k=2}(\lambda)$. Scan points $1-5$ are used to assess the 68% confidence level and scan points $6-10$ are used to assess the 95% confidence level.

68 % CL	**Flavor Composition**	λ_{obs}	**95 % CL**	**Flavor Composition**	λ_{obs}
Scan point 1	0.28 : 0.72 : 0.00	2.19	Scan point 6	0.17 : 0.83 : 0.00	6.11
Scan point 2	0.25 : 0.50 : 0.25	2.26	Scan point 7	0.08 : 0.62 : 0.30	6.20
Scan point 3	0.40 : 0.27 : 0.33	2.29	Scan point 8	0.04 : 0.40 : 0.56	5.99
Scan point 4	0.60 : 0.20 : 0.20	2.24	Scan point 9	0.10 : 0.15 : 0.75	6.04
Scan point 5	0.83 : 0.17 : 0.00	2.21	Scan point 10	0.37 : 0.00 : 0.63	5.97

Table C.1: Astrophysical neutrino flavor compositions $\nu_e : \nu_\mu : \nu_\tau$ and observed test statistic λ_{obs} for each scan point as depicted in Figure C.3. Note that these values are derived from Wilks' theorem with $\lambda_c \simeq 2.28$ for $\chi^2_{k=2}(\lambda \leq \lambda_c) = 0.68$ and $\lambda_c \simeq 5.99$ for $\chi^2_{k=2}(\lambda \leq \lambda_c) = 0.95$.

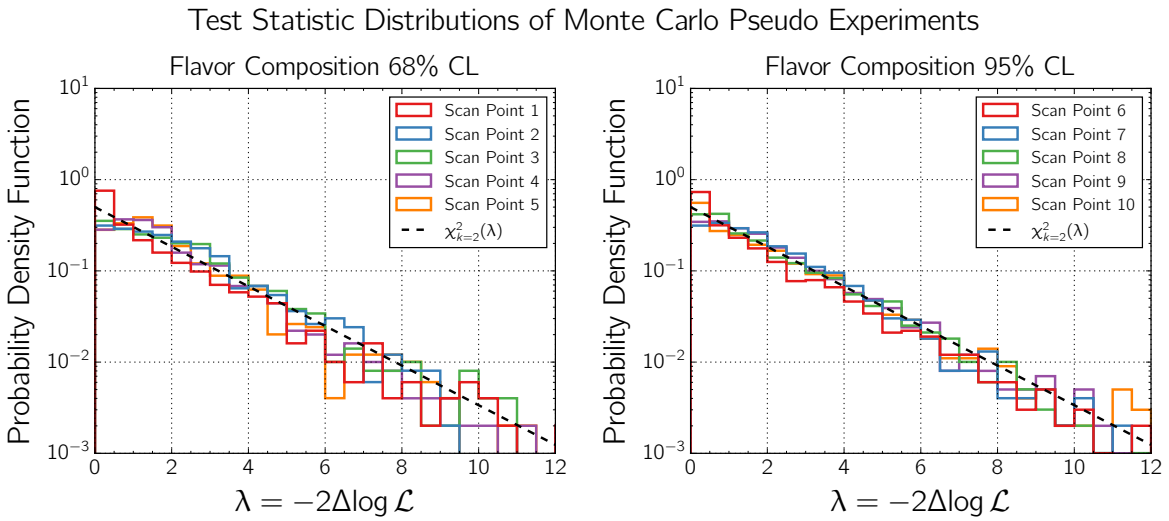

Figure C.4: Test statistic distributions for each scan point at 68% and 95% confidence level as illustrated in Figure C.3. The depicted likelihood ratio is defined in Equation C.3. Each distribution is generated by injecting the respective flavor composition into the Monte Carlo simulation, as listed in the text. The depiction of statistical uncertainties is omitted in order to enhance the visibility of each distribution. A χ^2-distribution with two degrees of freedom is shown in comparison for each plot.

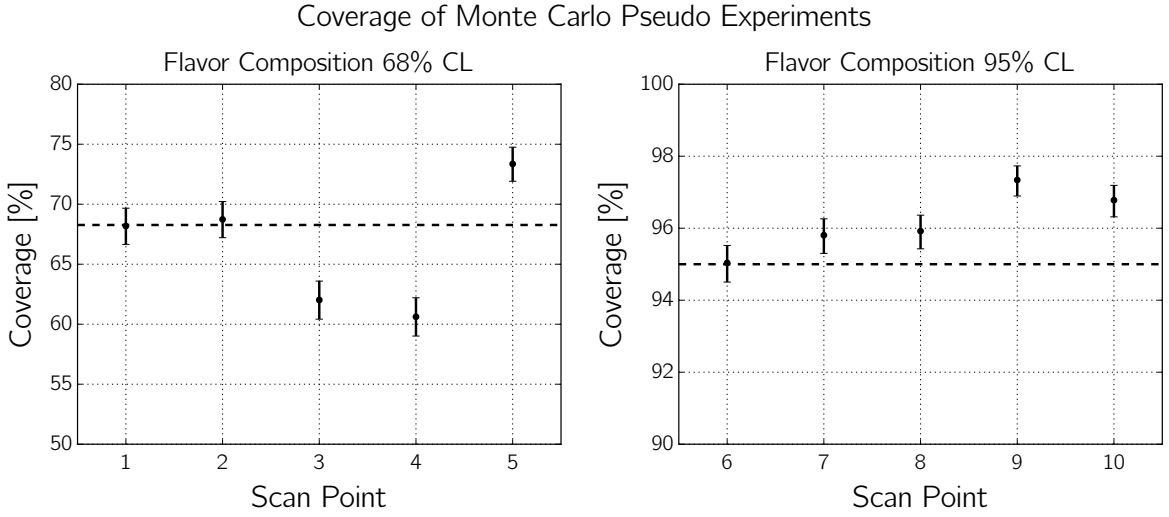

Figure C.5: Coverage of the generated test statistic distribution at each scan point for which $\lambda \leq \lambda_{\text{obs}}$ as listed in Table C.1. The horizontal dashed lines indicate the targeted 68% and 95% confidence levels. The depicted error bars reflect the statistical uncertainty of the coverage for 1 000 trials obtained from the 68% confidence intervals of a binomial distribution.

References

[1] M. Ackermann et al. The Spectrum of Isotropic Diffuse Gamma-Ray Emission between 100 MeV and 820 GeV. *The Astrophysical Journal*, 799(1):86, 2015. URL http://stacks.iop.org/0004-637X/799/i=1/a=86.

[2] Alexander Aab et al. The Pierre Auger Observatory: Contributions to the 33rd International Cosmic Ray Conference (ICRC 2013). In *Proceedings, 33rd International Cosmic Ray Conference (ICRC2013): Rio de Janeiro, Brazil, July 2-9, 2013*, 2013. URL http://lss.fnal.gov/archive/2013/conf/fermilab-conf-13-285-ad-ae-cd-td.pdf.

[3] T. Abu-Zayyad et al. The Cosmic-Ray Energy Spectrum Observed with the Surface Detector of the Telescope Array Experiment. *The Astrophysical Journal Letters*, 768(1): L1, 2013. URL http://stacks.iop.org/2041-8205/768/i=1/a=L1.

[4] M. G. Aartsen et al. Observation of Astrophysical Neutrinos in Six Years of IceCube Data. *Proceedings of Science (ICRC2017) 0981*, 2017. URL https://pos.sissa.it/cgi-bin/reader/contribution.cgi?id=PoS(ICRC2017)0981.

[5] Lars Mohrmann. *Characterizing Cosmic Neutrino Sources*. PhD thesis, Humboldt-Universität zu Berlin, Mathematisch-Naturwissenschaftliche Fakultät, 2015.

[6] Victor F. Hess. Über Beobachtungen der durchdringenden Strahlung bei sieben Freiballonfahrten. *Physikalische Zeitschrift*, 13:1084–1091, 1912.

[7] John H. Boyer, Bruce C. Knapp, Eric J. Mannel, and Michal Seman. FADC-based DAQ for HiRes Fly's Eye. *Nuclear Instruments and Methods in Physics Research A*, 482(1):457 – 474, 2002. ISSN 0168-9002. doi: https://doi.org/10.1016/S0168-9002(01)01517-0. URL http://www.sciencedirect.com/science/article/pii/S0168900201015170.

[8] A. Aab et al. The Pierre Auger Cosmic Ray Observatory. *Nuclear Instruments and Methods in Physics Research A*, 798:172 – 213, 2015. ISSN 0168-9002. doi: https://doi.org/10.1016/j.nima.2015.06.058. URL http://www.sciencedirect.com/science/article/pii/S0168900215008086.

[9] H. Tokuno et al. The Status of the Telescope Array experiment. *Journal of Physics: Conference Series*, 293(1):012035, 2011. URL http://stacks.iop.org/1742-6596/293/i=1/a=012035.

[10] P. Morrison. On Gamma-Ray Astronomy. *Il Nuovo Cimento (1955-1965)*, 7(6):858–865, Mar 1958. ISSN 1827-6121. doi: 10.1007/BF02745590. URL https://doi.org/10.1007/BF02745590.

[11] W. L. Kraushaar, G. W. Clark, G. P. Garmire, R. Borken, P. Higbie, V. Leong, and T. Thorsos. High-Energy Cosmic Gamma-Ray Observations from the OSO-3 Satellite. *Astrophysical Journal*, 177:341, November 1972. doi: 10.1086/151713.

[12] C. Winkler. INTEGRAL - Status of the Mission After 10 Years. In *Proceedings of "An INTEGRAL view of the high-energy sky (the first 10 years)" - 9th INTEGRAL Workshop and celebration of the 10th anniversary of the launch (INTEGRAL 2012). 15-19 October 2012. Bibliotheque Nationale de France, Paris, France*, page 1, 2012.

[13] N. Gehrels et al. The Swift Gamma-Ray Burst Mission. *The Astrophysical Journal*, 611:

1005–1020, 2004. doi: 10.1086/422091,10.1086/427409. [Erratum: The Astrophysical Journal 621,558(2005)].

[14] W. B. Atwood et al. The Large Area Telescope on the Fermi Gamma-Ray Space Telescope Mission. *The Astrophysical Journal*, 697:1071–1102, June 2009. doi: 10.1088/0004-637X/697/2/1071.

[15] W. Hofmann. Status of the High Energy Stereoscopic System (H.E.S.S.) Project. In *27th International Cosmic Ray Conference (ICRC 2001) Hamburg, Germany, August 7-15, 2001*, pages 2785–2788, 2001. URL https://www.mpi-hd.mpg.de/hfm/HESS/pages/publications/proceedings/icrc2001/ici6509_p.pdf.

[16] Enrique Fernandez. The MAGIC Gamma-Ray Telescope: Status and First Results. *Nuclear Physics B - Proceedings Supplements*, 151(1):381 – 392, 2006. ISSN 0920-5632. doi: https://doi.org/10.1016/j.nuclphysbps.2005.07.039. URL http://www.sciencedirect.com/science/article/pii/S0920563205009606.

[17] T. C. Weekes et al. VERITAS: The Very Energetic Radiation Imaging Telescope Array System. *Astroparticle Physics*, 17:221–243, 2002. doi: 10.1016/S0927-6505(01)00152-9.

[18] Wolfgang Pauli. Offener Brief, December 1930. URL http://microboone-docdb.fnal.gov/cgi-bin/RetrieveFile?docid=953;filename=pauli%20letter1930.pdf.

[19] F. Reines and C. L. Cowan. Detection of the Free Neutrino. *Physical Review*, 92:830–831, Nov 1953. doi: 10.1103/PhysRev.92.830. URL https://link.aps.org/doi/10.1103/PhysRev.92.830.

[20] G. Danby, J-M. Gaillard, K. Goulianos, L. M. Lederman, N. Mistry, M. Schwartz, and J. Steinberger. Observation of High-Energy Neutrino Reactions and the Existence of Two Kinds of Neutrinos. *Physical Review Letters*, 9:36–44, Jul 1962. doi: 10.1103/PhysRevLett.9.36. URL https://link.aps.org/doi/10.1103/PhysRevLett.9.36.

[21] K. Kodama et al. Observation of Tau Neutrino Interactions. *Physics Letters*, B504: 218–224, 2001. doi: 10.1016/S0370-2693(01)00307-0.

[22] N. Agafonova et al. Observation of a First ν_τ Candidate Event in the OPERA Experiment in the CNGS Beam. *Physics Letters B*, 691(3):138 – 145, 2010. ISSN 0370-2693. doi: https://doi.org/10.1016/j.physletb.2010.06.022. URL http://www.sciencedirect.com/science/article/pii/S0370269310007537.

[23] Raymond Davis, Don S. Harmer, and Kenneth C. Hoffman. Search for Neutrinos from the Sun. *Physical Review Letters*, 20:1205–1209, May 1968. doi: 10.1103/PhysRevLett.20.1205. URL https://link.aps.org/doi/10.1103/PhysRevLett.20.1205.

[24] John N. Bahcall, Neta A. Bahcall, and Giora Shaviv. Present Status of the Theoretical Predictions for the ^{37}Cl Solar-Neutrino Experiment. *Physical Review Letters*, 20:1209–1212, May 1968. doi: 10.1103/PhysRevLett.20.1209. URL https://link.aps.org/doi/10.1103/PhysRevLett.20.1209.

[25] Bruno Pontecorvo. Neutrino Experiments and the Problem of Conservation of Leptonic Charge. *Soviet Physics Journal of Experimental and Theoretical Physics*, 26:984, 1968.

[26] A. Bellerive, J. R. Klein, A. B. McDonald, A. J. Noble, and A. W. P. Poon. The Sudbury Neutrino Observatory. *Nuclear Physics*, B908:30–51, 2016. doi: 10.1016/j.nuclphysb.2016.04.035.

[27] Christopher W. Walter. The Super-Kamiokande Experiment. *arXiv:0802.1041 [hep-ex]*, 2008. doi: 10.1142/9789812771971_0002.

[28] I. Shelton, W. Kunkel, and B. Madore. 1987A; N Cen 1986 - Supernova 1987A in the

Large Magellanic Cloud. *International Astronomical Union Circular*, 4316, February 1987. URL http://www.cbat.eps.harvard.edu/iauc/04300/04316.html.

[29] Kazuto Hirata et al. Observation of a Neutrino Burst from the Supernova SN1987A. *Physical Review Letters*, 58:1490–1493, 1987.

[30] R. M. Bionta et al. Observation of a Neutrino Burst in Coincidence with Supernova 1987A in the Large Magellanic Cloud. *Physical Review Letters*, 58:1494–1496, Apr 1987. doi: 10.1103/PhysRevLett.58.1494. URL https://link.aps.org/doi/10.1103/PhysRevLett.58.1494.

[31] E. N. Alexeyev, L. N. Alexeyeva, I. V. Krivosheina, and V. I. Volchenko. Detection of the Neutrino Signal from SN 1987A in the LMC Using the INR Baksan Underground Scintillation Telescope. *Physics Letters B*, 205:209–214, April 1988. doi: 10.1016/0370-2693(88)91651-6.

[32] F. Reines, M. F. Crouch, T. L. Jenkins, W. R. Kropp, H. S. Gurr, G. R. Smith, J. P. F. Sellschop, and B. Meyer. Evidence for High-Energy Cosmic Ray Neutrino Interactions. *Physical Review Letters*, 15:429–433, 1965. doi: 10.1103/PhysRevLett.15.429.

[33] C. V. Achar et al. Detection of Muons Produced by Cosmic Ray Neutrinos Deep Underground. *Physics Letters*, 18:196–199, 1965. doi: 10.1016/0031-9163(65)90712-2.

[34] K. Greisen. Cosmic Ray Showers. *Annual Review of Nuclear Science*, 10(1):63–108, 1960. doi: 10.1146/annurev.ns.10.120160.000431. URL https://doi.org/10.1146/annurev.ns.10.120160.000431.

[35] F. Reines. Neutrino Interactions. *Annual Review of Nuclear Science*, 10(1):1–26, 1960. doi: 10.1146/annurev.ns.10.120160.000245. URL https://doi.org/10.1146/annurev.ns.10.120160.000245.

[36] M. A. Markov. On High Energy Neutrino Physics. In E. C. G. Sudarshan, J. H. Tinlot, and A. C. Melissinos, editors, *Proceedings of Annual International Conference on High Energy Physics at Rochester*, pages 578–581. University of Rochester, 1960.

[37] J. Babson et al. Cosmic-Ray Muons in the Deep Ocean. *Physical Review D*, 42:3613–3620, Dec 1990. doi: 10.1103/PhysRevD.42.3613. URL https://link.aps.org/doi/10.1103/PhysRevD.42.3613.

[38] V. Balkanov et al. The BAIKAL Neutrino Project: Status Report. *Nuclear Physics B - Proceedings Supplements*, 118:363 – 370, 2003. ISSN 0920-5632. doi: http://dx.doi.org/10.1016/S0920-5632(03)01334-3. URL http://www.sciencedirect.com/science/article/pii/S0920563203013343.

[39] J. A. Aguilar et al. First Results of the Instrumentation Line for the Deep-Sea ANTARES Neutrino Telescope. *Astroparticle Physics*, 26(4):314 – 324, 2006. ISSN 0927-6505. doi: http://dx.doi.org/10.1016/j.astropartphys.2006.07.004. URL http://www.sciencedirect.com/science/article/pii/S0927650506001071.

[40] Francis Halzen and John G. Learned. High-Energy Neutrino Detection in Deep Polar Ice. *MAD-PH-428 ; UH-511-659*, June 1988.

[41] E. Andres et al. The AMANDA Neutrino Telescope: Principle of Operation and First Results. *Astroparticle Physics*, 13:1–20, 2000. doi: 10.1016/S0927-6505(99)00092-4.

[42] M. G. Aartsen et al. The IceCube Neutrino Observatory: Instrumentation and Online Systems. *Journal of Instrumentation*, 12(03):P03012, 2017. doi: 10.1088/1748-0221/12/03/P03012.

[43] M. G. Aartsen et al. Evidence for High-Energy Extraterrestrial Neutrinos at the IceCube

Detector. *Science*, 342:1242856, 2013. doi: 10.1126/science.1242856.

[44] M. G. Aartsen et al. Observation of High-Energy Astrophysical Neutrinos in Three Years of IceCube Data. *Physical Review Letters*, 113:101101, 2014. doi: 10.1103/PhysRevLett.113.101101.

[45] M. G. Aartsen et al. Atmospheric and Astrophysical Neutrinos above 1 TeV Interacting in IceCube. *Physical Review D*, 91(2):022001, 2015. doi: 10.1103/PhysRevD.91.022001.

[46] M. G. Aartsen et al. A Combined Maximum-Likelihood Analysis of the High-Energy Astrophysical Neutrino Flux Measured with IceCube. *The Astrophysical Journal*, 809(1):98, 2015. doi: 10.1088/0004-637X/809/1/98.

[47] M. G. Aartsen et al. Evidence for Astrophysical Muon Neutrinos from the Northern Sky with IceCube. *Physical Review Letters*, 115(8):081102, 2015. doi: 10.1103/PhysRevLett.115.081102.

[48] M. G. Aartsen et al. Combined Analysis of the High-Energy Cosmic Neutrino Flux at the IceCube Detector. *Proceedings of Science (ICRC2015) 1066*, 2016. URL `https://pos.sissa.it/cgi-bin/reader/contribution.cgi?id=PoS(ICRC2015)1066`.

[49] M. G. Aartsen et al. Observation and Characterization of a Cosmic Muon Neutrino Flux from the Northern Hemisphere using six years of IceCube data. *The Astrophysical Journal*, 833(1):3, 2016. doi: 10.3847/0004-637X/833/1/3.

[50] M. G. Aartsen et al. Observation of Astrophysical Neutrinos in Four Years of IceCube Data. *Proceedings of Science (ICRC2015) 1081*, 2016. URL `https://pos.sissa.it/cgi-bin/reader/contribution.cgi?id=PoS(ICRC2015)1081`.

[51] M. G. Aartsen et al. A Measurement of the Diffuse Astrophysical Muon Neutrino Flux Using Eight Years of IceCube Data. *Proceedings of Science (ICRC2017) 1005*, 2017. URL `https://pos.sissa.it/cgi-bin/reader/contribution.cgi?id=PoS(ICRC2017)1005`.

[52] M. G. Aartsen et al. Searches for Extended and Point-Like Neutrino Sources with Four Years of IceCube Data. *The Astrophysical Journal*, 796(2):109, 2014. doi: 10.1088/0004-637X/796/2/109.

[53] M. G. Aartsen et al. Search for Prompt Neutrino Emission from Gamma-Ray Bursts with IceCube. *The Astrophysical Journal Letters*, 805(1):L5, 2015.

[54] M. G. Aartsen et al. Searches for Time Dependent Neutrino Sources with IceCube Data from 2008 to 2012. *The Astrophysical Journal*, 807(1):46, 2015. URL `http://stacks.iop.org/0004-637X/807/i=1/a=46`.

[55] Thorsten Glüsenkamp. Analysis of the Cumulative Neutrino Flux from Fermi-LAT Blazar Populations Using 3 Years of IceCube Data. *EPJ Web of Conferences*, 121:05006, 2016. doi: 10.1051/epjconf/201612105006.

[56] M. G. Aartsen et al. The IceCube Neutrino Observatory - Contributions to ICRC 2017 Part I: Searches for the Sources of Astrophysical Neutrinos. *Proceedings of Science, 35th International Cosmic Ray Conference (ICRC 2017)*, 2017.

[57] Alexander J. Stasik. *Search for High Energetic Neutrinos from Core Collapse Supernovae using the IceCube Neutrino Telescope*. PhD thesis, Humboldt-Universität zu Berlin, Mathematisch-Naturwissenschaftliche Fakultät, 2018.

[58] Paolo Lipari, Maurizio Lusignoli, and Davide Meloni. Flavor Composition and Energy Spectrum of Astrophysical Neutrinos. *Physical Review D*, 75:123005, Jun 2007. doi: 10.1103/PhysRevD.75.123005. URL `https://link.aps.org/doi/10.1103/PhysRevD.`

75.123005.

[59] Sandhya Choubey and Werner Rodejohann. Flavor Composition of Ultrahigh Energy Neutrinos at Source and at Neutrino Telescopes. *Physical Review D*, 80:113006, Dec 2009. doi: 10.1103/PhysRevD.80.113006. URL https://link.aps.org/doi/10.1103/PhysRevD.80.113006.

[60] M. G. Aartsen et al. Constraints on Galactic Neutrino Emission with Seven Years of IceCube Data. *The Astrophysical Journal*, 849(1):67, 2017. doi: 10.3847/1538-4357/aa8dfb.

[61] M. G. Aartsen et al. High Energy Astrophysical Neutrino Flux Measurement Using Neutrino-induced Cascades Observed in 4 Years of IceCube Data. *Proceedings of Science (ICRC2017) 0968*, 2017. URL https://pos.sissa.it/cgi-bin/reader/contribution.cgi?id=PoS(ICRC2017)0968.

[62] H. Athar, C. S. Kim, and J. Lee. Intrinsic and Oscillated Astrophysical Neutrino Flavor Ratios Revisited. *Modern Physics Letters A*, 21(13):1049–1065, 2006. doi: 10.1142/S021773230602038X.

[63] P. Lipari, M. Lusignoli, and D. Meloni. Flavor Composition and Energy Spectrum of Astrophysical Neutrinos. *Physical Review D*, 75:123005, Jun 2007. doi: 10.1103/PhysRevD.75.123005.

[64] Mauricio Bustamante, John F. Beacom, and Walter Winter. Theoretically Palatable Flavor Combinations of Astrophysical Neutrinos. *Physical Review Letters*, 115(16):161302, 2015. doi: 10.1103/PhysRevLett.115.161302.

[65] M. G. Aartsen et al. Flavor Ratio of Astrophysical Neutrinos above 35 TeV in IceCube. *Physical Review Letters*, 114(17):171102, 2015. doi: 10.1103/PhysRevLett.114.171102.

[66] S. Dusini et al. Observation of $\nu_\mu \to \nu_\tau$ Oscillations by the OPERA Experiment. *AIP Conference Proceedings*, 1666(1):110003, 2015. doi: 10.1063/1.4915575. URL http://aip.scitation.org/doi/abs/10.1063/1.4915575.

[67] K. Kodama et al. Final Tau-Neutrino Results from the DONuT Experiment. *Physical Review D*, 78:052002, Sep 2008. doi: 10.1103/PhysRevD.78.052002. URL https://link.aps.org/doi/10.1103/PhysRevD.78.052002.

[68] M. G. Aartsen et al. Search for Astrophysical Tau Neutrinos in Three Years of IceCube Data. *Physical Review D*, 93:022001, January 2016. doi: 10.1103/PhysRevD.93.022001. URL https://link.aps.org/doi/10.1103/PhysRevD.93.022001.

[69] John N. Bahcall and Roger K. Ulrich. Solar Models, Neutrino Experiments, and Helioseismology. *Reviews of Modern Physics*, 60:297–372, Apr 1988. doi: 10.1103/RevModPhys.60.297. URL https://link.aps.org/doi/10.1103/RevModPhys.60.297.

[70] Lawrence M. Krauss, Sheldon L. Glashow, and David N. Schramm. Antineutrino Astronomy and Geophysics. *Nature*, 310:191 EP –, 07 1984. URL http://dx.doi.org/10.1038/310191a0.

[71] F. Vissani and G. Pagliaroli. The Diffuse Supernova Neutrino Background: Expectations and Uncertainties Derived from SN1987A. *Astronomy and Astrophysics*, 528:L1, 2011. doi: 10.1051/0004-6361/201016109. URL https://doi.org/10.1051/0004-6361/201016109.

[72] T. K. Gaisser and M. Honda. Flux of Atmospheric Neutrinos. *Annual Review of Nuclear and Particle Science*, 52(1):153–199, 2002. doi: 10.1146/annurev.nucl.52.050102.090645. URL https://doi.org/10.1146/annurev.nucl.52.050102.090645.

[73] F. W. Stecker, C. Done, M. H. Salamon, and P. Sommers. High-Energy Neutrinos from Active Galactic Nuclei. *Physical Review Letters*, 66:2697–2700, May 1991. doi: 10.1103/PhysRevLett.66.2697. URL https://link.aps.org/doi/10.1103/PhysRevLett.66.2697.

[74] F. W. Stecker, C. Done, M. H. Salamon, and P. Sommers. Erratum: "High-Energy Neutrinos from Active Galactic Nuclei" [Physical Review Letters 66, 2697 (1991)]. *Physical Review Letters*, 69:2738–2738, Nov 1992. doi: 10.1103/PhysRevLett.69.2738. URL https://link.aps.org/doi/10.1103/PhysRevLett.69.2738.

[75] F. W. Stecker. Note on High-Energy Neutrinos from Active Galactic Nuclei Cores. *Physical Review D*, 72:107301, Nov 2005. doi: 10.1103/PhysRevD.72.107301. URL https://link.aps.org/doi/10.1103/PhysRevD.72.107301.

[76] John Bahcall and Eli Waxman. High Energy Astrophysical Neutrinos: The Upper Bound is Robust. *Physical Review D*, 64:023002, Jun 2001. doi: 10.1103/PhysRevD.64.023002. URL https://link.aps.org/doi/10.1103/PhysRevD.64.023002.

[77] M. Ahlers, L. A. Anchordoqui, M. C. Gonzalez-Garcia, F. Halzen, and S. Sarkar. GZK Neutrinos after the Fermi-LAT Diffuse Photon Flux Measurement. *Astroparticle Physics*, 34(2):106 – 115, 2010. ISSN 0927-6505. doi: https://doi.org/10.1016/j.astropartphys.2010.06.003. URL http://www.sciencedirect.com/science/article/pii/S0927650510001155.

[78] C. Patrignani et al. Review of Particle Physics. *Chinese Physics C*, C40(10):100001, 2016. doi: 10.1088/1674-1137/40/10/100001.

[79] Jörg R. Hörandel. Cosmic Rays from the Knee to the Second Knee: 10^4 to 10^{18} eV. *Modern Physics Letters A*, 22:1533–1552, 2007. doi: 10.1142/S0217732307024139.

[80] Kenneth Greisen. End to the Cosmic-Ray Spectrum? *Physical Review Letters*, 16:748–750, 1966.

[81] G. T. Zatsepin and V. A. Kuzmin. Upper Limit of the Spectrum of Cosmic Rays. *Journal of Experimental and Theoretical Physics Letters*, 4:78, 1966.

[82] E. S. Seo, J. F. Ormes, R. E. Streitmatter, S. J. Stochaj, W. V. Jones, S. A. Stephens, and T. Bowen. Measurement of Cosmic-Ray Proton and Helium Spectra During the 1987 Solar Minimum. *The Astrophysical Journal*, 378:763–772, September 1991. doi: 10.1086/170477.

[83] N. Grigorov et al. Energy Spectrum of Primary Cosmic Rays in the $10^{11} - 10^{15}$ eV According to the Data of Proton-4 Measurements. *Proceedings of the 12th International Conference on Cosmic Rays, Hobart, Australia, University of Tasmania Press*, 1971. URL http://adsabs.harvard.edu/abs/1971ICRC....1..170G.

[84] M. Nagano, M. Teshima, Y. Matsubara, H. Y. Dai, T. Hara, N. Hayashida, M. Honda, H. Ohoka, and S. Yoshida. Energy Spectrum of Primary Cosmic Rays above 10^{17} eV Determined from Extensive Air Shower Experiments at Akeno. *Journal of Physics G: Nuclear and Particle Physics*, 18(2):423, 1992. URL http://stacks.iop.org/0954-3899/18/i=2/a=022.

[85] T. Antoni et al. KASCADE Measurements of Energy Spectra for Elemental Groups of Cosmic Rays: Results and Open Problems. *Astroparticle Physics*, 24:1–25, 2005. doi: 10.1016/j.astropartphys.2005.04.001.

[86] J. Abraham et al. Observation of the Suppression of the Flux of Cosmic Rays above 4×10^{19} eV. *Physical Review Letters*, 101:061101, Aug 2008. doi: 10.1103/PhysRevLett.101.061101. URL https://link.aps.org/doi/10.1103/PhysRevLett.101.061101.

[87] Lorenzo Perrone. Measurement of the UHECR Energy Spectrum from Hybrid Data of the Pierre Auger Observatory. In *Proceedings of the 30th International Cosmic Ray Conference (ICRC 2007): Merida, Yucatan, Mexico, July 3-11, 2007*, volume 4, pages 331–334, 2007. URL http://lss.fnal.gov/cgi-bin/find_paper.pl?conf-07-087.

[88] M. Takeda et al. Energy Determination in the Akeno Giant Air Shower Array Experiment. *Astroparticle Physics*, 19(4):447 – 462, 2003. ISSN 0927-6505. doi: https://doi.org/10.1016/S0927-6505(02)00243-8. URL http://www.sciencedirect.com/science/article/pii/S0927650502002438.

[89] R. U. Abbasi et al. First Observation of the Greisen-Zatsepin-Kuzmin Suppression. *Physical Review Letters*, 100:101101, Mar 2008. doi: 10.1103/PhysRevLett.100.101101. URL https://link.aps.org/doi/10.1103/PhysRevLett.100.101101.

[90] James J. Beatty and Stefan Westerhoff. The Highest-Energy Cosmic Rays. *Annual Review of Nuclear and Particle Science*, 59(1):319–345, 2009. doi: 10.1146/annurev.nucl.58.110707.171154. URL https://doi.org/10.1146/annurev.nucl.58.110707.171154.

[91] M.-H. Y. Kim, J. W. Wilson, F. A. Cucinotta, L. C. Simonsen, W. Atwell, F. F. Badavi, and J. Miller. Contribution of High Charge and Energy (HZE) Ions During Solar-Particle Event of September 29, 1989. Technical report, NASA Johnson Space Center; Langley Research Center, 1999. URL http://hdl.handle.net/2060/19990051001.

[92] Enrico Fermi. On the Origin of the Cosmic Radiation. *Physical Review*, 75:1169–1174, 1949.

[93] Thomas K. Gaisser. *Cosmic Rays and Particle Physics*. Cambridge University Press, 1990.

[94] Donald Perkins. *Particle Astrophysics*. Oxford University Press, 2009.

[95] Rafael Alves Batista and Günter Sigl. Diffusion of Cosmic Rays at EeV Energies in Inhomogeneous Extragalactic Magnetic Fields. *Journal of Cosmology and Astroparticle Physics*, 1411(11):031, 2014. doi: 10.1088/1475-7516/2014/11/031.

[96] A. P. Snodin, A. Shukurov, G. R. Sarson, P. J. Bushby, and L. F. S. Rodrigues. Global Diffusion of Cosmic Rays in Random Magnetic Fields. *Monthly Notices of the Royal Astronomical Society*, 457(4):3975–3987, 2016. doi: 10.1093/mnras/stw217.

[97] J. G. Kirk and P. Schneider. On the Acceleration of Charged Particles at Relativistic Shock Fronts. *The Astrophysical Journal*, 315:425–433, April 1987. doi: 10.1086/165147.

[98] A. F. Heavens and L. O'C. Drury. Relativistic Shocks and Particle Acceleration. *Monthly Notices of the Royal Astronomical Society*, 235(3):997–1009, 1988. doi: 10.1093/mnras/235.3.997. URL +http://dx.doi.org/10.1093/mnras/235.3.997.

[99] Masaaki Yamada, Russell Kulsrud, and Hantao Ji. Magnetic Reconnection. *Reviews of Modern Physics*, 82:603–664, Mar 2010. doi: 10.1103/RevModPhys.82.603. URL https://link.aps.org/doi/10.1103/RevModPhys.82.603.

[100] Feng-Yin Chang, Pisin Chen, Guey-Lin Lin, Robert Noble, and Richard Sydora. Magnetowave Induced Plasma Wakefield Acceleration for Ultrahigh Energy Cosmic Rays. *Physical Review Letters*, 102:111101, Mar 2009. doi: 10.1103/PhysRevLett.102.111101. URL https://link.aps.org/doi/10.1103/PhysRevLett.102.111101.

[101] Anthony M. Hillas. The Origin of Ultra-High-Energy Cosmic Rays. *Annual Review of Astronomy and Astrophysics*, 22:425–444, 1984.

[102] Hans-Walter Rix and Jo Bovy. The Milky Way's Stellar Disk. *Astronomy and Astrophysics Review*, 21:61, 2013. doi: 10.1007/s00159-013-0061-8.

[103] M. Haverkorn. Magnetic Fields in the Milky Way. In A. Lazarian, E. M. de Gouveia Dal Pino, and C. Melioli, editors, *Magnetic Fields in Diffuse Media*, volume 407 of *Astrophysics and Space Science Library*, page 483, 2015. doi: 10.1007/978-3-662-44625-6_17.

[104] Francis Halzen and Spencer Klein. Invited Review Article: IceCube: An Instrument for Neutrino Astronomy. *Review of Scientific Instruments*, 81:081101, 2010.

[105] Raymond J. Protheroe and Anthony P. Szabo. High Energy Cosmic Rays from Active Galactic Nuclei. *Physical Review Letters*, 69:2885–2888, 1992.

[106] Xiang-Yu Wang, Soebur Razzaque, and Peter MÈsz·ros. On the Origin and Survival of Ultra-High-Energy Cosmic-Ray Nuclei in Gamma-Ray Bursts and Hypernovae. *The Astrophysical Journal*, 677:432–440, 2008.

[107] Bradley M. Peterson. *An Introduction to Active Galactic Nuclei*. Cambridge University Press, 1997.

[108] Kumiko Kotera and Angela V. Olinto. The Astrophysics of Ultrahigh-Energy Cosmic Rays. *Annual Review of Astronomy and Astrophysics*, 49(1):119–153, 2011. doi: 10.1146/annurev-astro-081710-102620. URL `https://doi.org/10.1146/annurev-astro-081710-102620`.

[109] P. Mészáros. Gamma-Ray Bursts. *Reports on Progress in Physics*, 69(8):2259, 2006. URL `http://stacks.iop.org/0034-4885/69/i=8/a=R01`.

[110] T. Piran. Gamma-Ray Bursts and the Fireball Model. *Physics Reports*, 314:575–667, 1999. doi: 10.1016/S0370-1573(98)00127-6.

[111] C. Kouveliotou, R. A. M. J. Wijers, and S. Woosley, editors. *The Gamma-Ray Burst - Supernova Connection*, pages 169–190. Cambridge University Press, November 2012.

[112] B. P. Abbott et al. Gravitational Waves and Gamma-rays from a Binary Neutron Star Merger: GW170817 and GRB 170817A. *The Astrophysical Journal*, 848(2):L13, 2017. doi: 10.3847/2041-8213/aa920c.

[113] H. Th. Janka, Th. Eberl, M. Ruffert, and C. L. Fryer. Black Hole: Neutron Star Mergers as Central Engines of Gamma-Ray Bursts. *The Astrophysical Journal*, 527:L39, 1999. doi: 10.1086/312397.

[114] Frank G. Schröder. Radio Detection of Cosmic-Ray Air Showers and High-Energy Neutrinos. *Progress in Particle and Nuclear Physics*, 93:1–68, 2017. doi: 10.1016/j.ppnp.2016.12.002.

[115] Jose I. Illana, Paolo Lipari, Manuel Masip, and Davide Meloni. Atmospheric Lepton Fluxes at Very High Energy. *Astroparticle Physics*, 34:663–673, 2011. doi: 10.1016/j.astropartphys.2011.01.001.

[116] E. V. Bugaev, A. Misaki, V. A. Naumov, T. S. Sinegovskaya, S. I. Sinegovsky, and N. Takahashi. Atmospheric Muon Flux at Sea Level, Underground, and Underwater. *Physical Review D*, 58:054001, Jul 1998. doi: 10.1103/PhysRevD.58.054001. URL `https://link.aps.org/doi/10.1103/PhysRevD.58.054001`.

[117] M. G. Aartsen et al. Characterization of the Atmospheric Muon Flux in IceCube. *Astroparticle Physics*, 78:1–27, 2016. doi: 10.1016/j.astropartphys.2016.01.006.

[118] Thomas K. Gaisser. Spectrum of Cosmic-Ray Nucleons, Kaon Production, and the Atmospheric Muon Charge Ratio. *Astroparticle Physics*, 35:801–806, 2012. doi: 10.1016/j.astropartphys.2012.02.010.

[119] Thomas K. Gaisser and Spencer R. Klein. A New Contribution to the Conventional Atmospheric Neutrino Flux. *Astroparticle Physics*, 64:13 – 17, 2015. ISSN 0927-

6505. doi: https://doi.org/10.1016/j.astropartphys.2014.10.006. URL http://www.sciencedirect.com/science/article/pii/S0927650514001613.

[120] Anatoli Fedynitch, Ralph Engel, Thomas K. Gaisser, Felix Riehn, and Todor Stanev. Calculation of Conventional and Prompt Lepton Fluxes at Very High Energy. *EPJ Web of Conferences*, 99:08001, 2015. doi: 10.1051/epjconf/20159908001.

[121] Rikard Enberg, Mary H. Reno, and Ina Sarcevic. Prompt Neutrino Fluxes from Atmospheric Charm. *Physical Review D*, 78:043005, 2008. doi: 10.1103/PhysRevD.78.043005.

[122] E. Richard et al. Measurements of the Atmospheric Neutrino Flux by Super-Kamiokande: Energy Spectra, Geomagnetic Effects, and Solar Modulation. *Physical Review D*, 94(5): 052001, 2016. doi: 10.1103/PhysRevD.94.052001.

[123] K. Daum et al. Determination of the Atmospheric Neutrino Spectra with the Fréjus Detector. *Zeitschrift für Physik C Particles and Fields*, 66(3):417–428, Sep 1995. ISSN 1431-5858. doi: 10.1007/BF01556368. URL https://doi.org/10.1007/BF01556368.

[124] M. G. Aartsen et al. Measurement of the Atmospheric ν_e Spectrum with IceCube. *Physical Review D*, 91:122004, 2015. doi: 10.1103/PhysRevD.91.122004.

[125] M. Honda, T. Kajita, K. Kasahara, S. Midorikawa, and T. Sanuki. Calculation of Atmospheric Neutrino Flux Using the Interaction Model Calibrated with Atmospheric Muon Data. *Physical Review D*, 75:043006, 2007. doi: 10.1103/PhysRevD.75.043006.

[126] M. G. Aartsen et al. Development of a General Analysis and Unfolding Scheme and its Application to Measure the Energy Spectrum of Atmospheric Neutrinos with IceCube. *European Physical Journal C*, 75(3):116, 2015. doi: 10.1140/epjc/s10052-015-3330-z.

[127] R. Abbasi et al. Search for a Diffuse Flux of Astrophysical Muon Neutrinos with the IceCube 40-String Detector. *Physical Review D*, 84:082001, Oct 2011. doi: 10.1103/PhysRevD.84.082001. URL https://link.aps.org/doi/10.1103/PhysRevD.84.082001.

[128] M. G. Aartsen et al. Measurement of the atmospheric ν_e flux in icecube. *Physical Review Letters*, 110:151105, Apr 2013. doi: 10.1103/PhysRevLett.110.151105. URL https://link.aps.org/doi/10.1103/PhysRevLett.110.151105.

[129] G. D. Barr, T. K. Gaisser, P. Lipari, S. Robbins, and T. Stanev. Three-Dimensional Calculation of Atmospheric Neutrinos. *Physical Review D*, 70:023006, Jul 2004. doi: 10.1103/PhysRevD.70.023006. URL https://link.aps.org/doi/10.1103/PhysRevD.70.023006.

[130] M. G. Aartsen et al. Search for a Diffuse Flux of Astrophysical Muon Neutrinos with the IceCube 59-String Configuration. *Physical Review D*, 89(6):062007, 2014. doi: 10.1103/PhysRevD.89.062007.

[131] Julia K. Becker. High-energy Neutrinos in the Context of Multimessenger Physics. *Physics Reports*, 458:173–246, 2008.

[132] Albrecht Karle Thomas Gaisser, editor. *Neutrino Astronomy – Current Status, Future Prospects*. World Scientific, 2017.

[133] Eli Waxman and John Bahcall. High Energy Neutrinos from Astrophysical Sources: An Upper Bound. *Physical Review D*, 59:023002, Dec 1998. doi: 10.1103/PhysRevD.59.023002. URL https://link.aps.org/doi/10.1103/PhysRevD.59.023002.

[134] Karl Mannheim, R. J. Protheroe, and Jörg P. Rachen. Cosmic Ray Bound for Models of Extragalactic Neutrino Production. *Physical Review D*, 63:023003, Dec

2000. doi: 10.1103/PhysRevD.63.023003. URL https://link.aps.org/doi/10.1103/PhysRevD.63.023003.

[135] Matthias Mandelartz and Julia Becker Tjus. Prediction of the Diffuse Neutrino Flux from Cosmic Ray Interactions near Supernova Remnants. *Astroparticle Physics*, 65:80 – 100, 2015. ISSN 0927-6505. doi: https://doi.org/10.1016/j.astropartphys.2014.12.002. URL http://www.sciencedirect.com/science/article/pii/S0927650514001881.

[136] Kohta Murase, Todd A. Thompson, Brian C. Lacki, and John F. Beacom. New Class of High-Energy Transients from Crashes of Supernova Ejecta with Massive Circumstellar Material Shells. *Physical Review D*, 84:043003, 2011. doi: 10.1103/PhysRevD.84.043003.

[137] A. Mücke, R.J. Protheroe, R. Engel, J.P. Rachen, and T. Stanev. BL Lac Objects in the Synchrotron Proton Blazar Model. *Astroparticle Physics*, 18(6):593 – 613, 2003. ISSN 0927-6505. doi: https://doi.org/10.1016/S0927-6505(02)00185-8. URL http://www.sciencedirect.com/science/article/pii/S0927650502001858.

[138] Soebur Razzaque, Peter Mészáros, and Eli Waxman. Neutrino Tomography of Gamma Ray Bursts and Massive Stellar Collapses. *Physical Review D*, 68:083001, Oct 2003. doi: 10.1103/PhysRevD.68.083001. URL https://link.aps.org/doi/10.1103/PhysRevD.68.083001.

[139] Eli Waxman and John N. Bahcall. Neutrino Afterglow from Gamma-Ray Bursts: 1018 eV. *The Astrophysical Journal*, 541(2):707, 2000. URL http://stacks.iop.org/0004-637X/541/i=2/a=707.

[140] R. Abbasi et al. An Absence of Neutrinos Associated with Cosmic-Ray Acceleration in γ-Ray Bursts. *Nature*, 484:351–354, April 2012. doi: 10.1038/nature11068.

[141] M. G. Aartsen et al. Extending the Search for Muon Neutrinos Coincident with Gamma-Ray Bursts in IceCube Data. *The Astrophysical Journal*, 843(2):112, 2017. doi: 10.3847/1538-4357/aa7569.

[142] V. S. Beresinsky and G. T. Zatsepin. Cosmic Rays at Ultra High Energies (Neutrino?). *Physics Letters B*, 28(6):423 – 424, 1969. ISSN 0370-2693. doi: https://doi.org/10.1016/0370-2693(69)90341-4. URL http://www.sciencedirect.com/science/article/pii/0370269369903414.

[143] M. G. Aartsen et al. Constraints on Ultrahigh-Energy Cosmic-Ray Sources from a Search for Neutrinos above 10 PeV with IceCube. *Physical Review Letters*, 117(24):241101, 2016. doi: 10.1103/PhysRevLett.117.241101,10.1103/PhysRevLett.119.259902. [Erratum: Physical Review Letters119,no.25,259902(2017)].

[144] Luis A. Anchordoqui, Dan Hooper, Subir Sarkar, and Andrew M. Taylor. High Energy Neutrinos from Astrophysical Accelerators of Cosmic Ray Nuclei. *Astroparticle Physics*, 29(1):1 – 13, 2008. ISSN 0927-6505. doi: https://doi.org/10.1016/j.astropartphys.2007.10.006. URL http://www.sciencedirect.com/science/article/pii/S0927650507001491.

[145] S. Richter and F. Spanier. AGN Neutrino Flux Estimates for a Realistic Hybrid Model. *Astroparticle Physics*, 100:61 – 68, 2018. ISSN 0927-6505. doi: https://doi.org/10.1016/j.astropartphys.2018.02.008. URL http://www.sciencedirect.com/science/article/pii/S0927650517302499.

[146] Luis A. Anchordoqui, Haim Goldberg, Francis Halzen, and Thomas J. Weiler. Neutrinos as a diagnostic of high energy astrophysical processes. *Physics Letters B*, 621(1):18 – 21, 2005. ISSN 0370-2693. doi: https://doi.org/10.1016/j.physletb.2005.06.056. URL http://www.sciencedirect.com/science/article/pii/S0370269305008658.

[147] Daniel Biehl, Anatoli Fedynitch, Andrea Palladino, Tom J. Weiler, and Walter Winter. Astrophysical Neutrino Production Diagnostics with the Glashow Resonance. *Journal of Cosmology and Astroparticle Physics*, 1701:033, 2017. doi: 10.1088/1475-7516/2017/01/033.

[148] Thomas K. Gaisser, Kyle Jero, Albrecht Karle, and Jakob van Santen. Generalized Self-Veto Probability for Atmospheric Neutrinos. *Physical Review D*, 90(2):023009, 2014. doi: 10.1103/PhysRevD.90.023009.

[149] Francis Halzen and Logan Wille. Charm Contribution to the Atmospheric Neutrino Flux. *Physical Review D*, 94:014014, Jul 2016. doi: 10.1103/PhysRevD.94.014014. URL https://link.aps.org/doi/10.1103/PhysRevD.94.014014.

[150] M. G. Aartsen et al. The IceCube Neutrino Observatory - Contributions to ICRC 2017 Part II: Properties of the Atmospheric and Astrophysical Neutrino Flux. *Proceedings of Science, 35th International Cosmic Ray Conference (ICRC 2017)*, 2017.

[151] M. C. Gonzalez-Garcia, Michele Maltoni, and Thomas Schwetz. Updated Fit to Three Neutrino Mixing: Status of Leptonic CP Violation. *Journal of High Energy Physics*, 2014 (11):52, Nov 2014. ISSN 1029-8479. doi: 10.1007/JHEP11(2014)052. URL https://doi.org/10.1007/JHEP11(2014)052.

[152] Christian Weinheimer and Kai Zuber. Neutrino Masses. *Annalen der Physik*, 525(8-9): 565–575, 2013. doi: 10.1002/andp.201300063.

[153] P. A. R. Ade et al. Planck 2015 Results. XIII. Cosmological Parameters. *Astronomy and Astrophysics*, 594:A13, 2016. doi: 10.1051/0004-6361/201525830.

[154] G. Bellini, L. Ludhova, G. Ranucci, and F. L. Villante. Neutrino Oscillations. *Advances in High Energy Physics*, 2014:191960, 2014. doi: 10.1155/2014/191960.

[155] S. Schael et al. Precision Electroweak Measurements on the *Z* Resonance. *Physics Reports*, 427:257–454, 2006. doi: 10.1016/j.physrep.2005.12.006.

[156] Ziro Maki, Masami Nakagawa, and Shoichi Sakata. Remarks on the Unified Model of Elementary Particles. *Progress of Theoretical Physics*, 28(5):870–880, 1962. doi: 10.1143/PTP.28.870. URL +http://dx.doi.org/10.1143/PTP.28.870.

[157] Y. Abe et al. Reactor Electron Antineutrino Disappearance in the Double Chooz Experiment. *Physical Review D*, 86:052008, 2012. doi: 10.1103/PhysRevD.86.052008.

[158] A. Gando et al. Constraints on θ_{13} from A Three-Flavor Oscillation Analysis of Reactor Antineutrinos at KamLAND. *Physical Review D*, 83:052002, 2011. doi: 10.1103/PhysRevD.83.052002.

[159] Feng Peng An et al. Measurement of Electron Antineutrino Oscillation Based on 1230 Days of Operation of the Daya Bay Experiment. *Physical Review D*, 95(7):072006, 2017. doi: 10.1103/PhysRevD.95.072006.

[160] P. Adamson et al. Measurement of Neutrino and Antineutrino Oscillations Using Beam and Atmospheric Data in MINOS. *Physical Review Letters*, 110(25):251801, 2013. doi: 10.1103/PhysRevLett.110.251801.

[161] K. Abe et al. Combined Analysis of Neutrino and Antineutrino Oscillations at T2K. *Physical Review Letters*, 118(15):151801, 2017. doi: 10.1103/PhysRevLett.118.151801.

[162] P. Adamson et al. Measurement of the Neutrino Mixing Angle θ_{23} in NOvA. *Physical Review Letters*, 118(15):151802, 2017. doi: 10.1103/PhysRevLett.118.151802.

[163] Roger Wendell. Atmospheric Results from Super-Kamiokande. *AIP Conference Proceedings*, 1666:100001, 2015. doi: 10.1063/1.4915569.

[164] M. G. Aartsen et al. Measurement of Atmospheric Neutrino Oscillations at 6–56 GeV with IceCube DeepCore. *Physical Review Letters*, 120(7):071801, 2018. doi: 10.1103/PhysRevLett.120.071801.

[165] Jörg P. Rachen and P. Mészáros. Photohadronic Neutrinos from Transients in Astrophysical Sources. *Physical Review D*, 58:123005, Nov 1998. doi: 10.1103/PhysRevD.58.123005. URL https://link.aps.org/doi/10.1103/PhysRevD.58.123005.

[166] Tamar Kashti and Eli Waxman. Astrophysical Neutrinos: Flavor Ratios Depend on Energy. *Physical Review Letters*, 95:181101, Oct 2005. doi: 10.1103/PhysRevLett.95.181101. URL https://link.aps.org/doi/10.1103/PhysRevLett.95.181101.

[167] Luis A. Anchordoqui, Haim Goldberg, Francis Halzen, and Thomas J. Weiler. Galactic Point Sources of TeV Antineutrinos. *Physics Letters B*, 593(1):42 – 47, 2004. ISSN 0370-2693. doi: https://doi.org/10.1016/j.physletb.2004.04.054. URL http://www.sciencedirect.com/science/article/pii/S0370269304006847.

[168] Walter Winter, Julia Becker Tjus, and Spencer R. Klein. Impact of Secondary Acceleration on the Neutrino Spectra in Gamma-Ray Bursts. *Astronomy and Astrophysics*, 569:A58, 2014. doi: 10.1051/0004-6361/201423745.

[169] Poonam Mehta and Walter Winter. Interplay of Energy Dependent Astrophysical Neutrino Flavor Ratios and New Physics Effects. *Journal of Cosmology and Astroparticle Physics*, 1103:041, 2011. doi: 10.1088/1475-7516/2011/03/041.

[170] S. Hummer, M. Maltoni, W. Winter, and C. Yaguna. Energy Dependent Neutrino Flavor Ratios from Cosmic Accelerators on the Hillas Plot. *Astroparticle Physics*, 34:205–224, 2010. doi: 10.1016/j.astropartphys.2010.07.003.

[171] A. Yu. Smirnov. The MSW Effect and Solar Neutrinos. In *Neutrino Telescopes. Proceedings, 10th International Workshop, Venice, Italy, March 11-14, 2003. Vol. 1+2*, pages 23–43, 2003.

[172] L. Wolfenstein. Neutrino Oscillations in Matter. *Physical Review D*, 17:2369–2374, May 1978. doi: 10.1103/PhysRevD.17.2369. URL https://link.aps.org/doi/10.1103/PhysRevD.17.2369.

[173] L. Wolfenstein. Neutrino Oscillations and Stellar Collapse. *Physical Review D*, 20:2634–2635, Nov 1979. doi: 10.1103/PhysRevD.20.2634. URL https://link.aps.org/doi/10.1103/PhysRevD.20.2634.

[174] S. P. Mikheyev and A. Y. Smirnov. Resonance Enhancement of Oscillations in Matter and Solar Neutrino Spectroscopy. *Yadernaya Fizika*, 42:1441–1448, 1985.

[175] Stephen Parke and Mark Ross-Lonergan. Unitarity and the Three Flavor Neutrino Mixing Matrix. *Physical Review D*, 93(11):113009, 2016. doi: 10.1103/PhysRevD.93.113009.

[176] Carlo Giunti and Marco Laveder. Statistical Significance of the Gallium Anomaly. *Physical Review C*, 83:065504, Jun 2011. doi: 10.1103/PhysRevC.83.065504. URL https://link.aps.org/doi/10.1103/PhysRevC.83.065504.

[177] J. N. Abdurashitov et al. Measurement of the Response of a Ga Solar Neutrino Experiment to Neutrinos from a ^{37}Ar Source. *Physical Review C*, 73:045805, Apr 2006. doi: 10.1103/PhysRevC.73.045805. URL https://link.aps.org/doi/10.1103/PhysRevC.73.045805.

[178] A. A. Aguilar-Arevalo et al. Evidence for Neutrino Oscillations from the Observation of Anti-Neutrino(electron) Appearance in a Anti-Neutrino(muon) Beam. *Physical Review D*, 64:112007, 2001. doi: 10.1103/PhysRevD.64.112007.

[179] A. A. Aguilar-Arevalo et al. Improved Search for $\bar{\nu}_\mu \to \bar{\nu}_e$ Oscillations in the MiniBooNE Experiment. *Physical Review Letters*, 110:161801, 2013. doi: 10.1103/PhysRevLett.110.161801.

[180] G. Mention, M. Fechner, Th. Lasserre, Th. A. Mueller, D. Lhuillier, M. Cribier, and A. Letourneau. The Reactor Antineutrino Anomaly. *Physical Review D*, 83:073006, 2011. doi: 10.1103/PhysRevD.83.073006.

[181] K. N. Abazajian et al. Light Sterile Neutrinos: A White Paper. *arXiv:1204.5379 [hep-ph]*, 2012.

[182] Francesco Capozzi, Carlo Giunti, Marco Laveder, and Antonio Palazzo. Joint Short- and Long-Baseline Constraints on Light Sterile Neutrinos. *Physical Review D*, 95(3):033006, 2017. doi: 10.1103/PhysRevD.95.033006.

[183] M. G. Aartsen et al. Search for Sterile Neutrino Mixing Using Three Years of IceCube DeepCore Data. *Physical Review D*, 95(11):112002, 2017. doi: 10.1103/PhysRevD.95.112002.

[184] John F. Beacom, Nicole F. Bell, Dan Hooper, Sandip Pakvasa, and Thomas J. Weiler. Decay of High-Energy Astrophysical Neutrinos. *Physical Review Letters*, 90:181301, May 2003. doi: 10.1103/PhysRevLett.90.181301. URL `https://link.aps.org/doi/10.1103/PhysRevLett.90.181301`.

[185] Philipp Baerwald, Mauricio Bustamante, and Walter Winter. Neutrino Decays over Cosmological Distances and the Implications for Neutrino Telescopes. *Journal of Cosmology and Astroparticle Physics*, 2012(10):020, 2012. URL `http://stacks.iop.org/1475-7516/2012/i=10/a=020`.

[186] Mauricio Bustamante, John F. Beacom, and Kohta Murase. Testing Decay of Astrophysical Neutrinos with Incomplete Information. *Physical Review D*, 95(6):063013, 2017. doi: 10.1103/PhysRevD.95.063013.

[187] P. F. de Salas, R. A. Lineros, and M. Tórtola. Neutrino Propagation in the Galactic Dark Matter Halo. *Physical Review D*, 94(12):123001, 2016. doi: 10.1103/PhysRevD.94.123001.

[188] Dan Hooper, Dean Morgan, and Elizabeth Winstanley. Lorentz and *CPT* Invariance Violation in High-Energy Neutrinos. *Physical Review D*, 72:065009, Sep 2005. doi: 10.1103/PhysRevD.72.065009. URL `https://link.aps.org/doi/10.1103/PhysRevD.72.065009`.

[189] Rasmus W. Rasmussen, Lukas Lechner, Markus Ackermann, Marek P. Kowalski, and Walter Winter. Astrophysical Neutrinos Flavored with Beyond the Standard Model Physics. *Physical Review D*, 96(8):083018, 2017. doi: 10.1103/PhysRevD.96.083018.

[190] Mary Hall Reno. Neutrino Cross Sections at HERA and Beyond. *Nuclear Physics Proceedings Supplements*, 151:255–259, 2006. doi: 10.1016/j.nuclphysbps.2005.07.063.

[191] C. Adloff et al. Measurement and QCD Analysis of Neutral and Charged Current Cross Sections at HERA. *The European Physical Journal C - Particles and Fields*, 30(1):1–32, Sep 2003. ISSN 1434-6052. doi: 10.1140/epjc/s2003-01257-6. URL `https://doi.org/10.1140/epjc/s2003-01257-6`.

[192] S. Chekanov et al. High Q^2 Neutral Current Cross-Sections in e+p Deep Inelastic Scattering at $\sqrt{s} = 318$ GeV. *Physical Review D*, 70:052001, 2004. doi: 10.1103/PhysRevD.70.052001.

[193] Raj Gandhi, Chris Quigg, Mary H. Reno, and Ina Sarcevic. Neutrino Interactions at Ultrahigh Energies. *Physical Review D*, 58:093009, 1998.

[194] Bernhard Voigt. *Sensitivity of the IceCube Detector for Ultra-High Energy Electron-Neutrino Events*. PhD thesis, Humboldt-Universität zu Berlin, Mathematisch-Naturwissenschaftliche Fakultät I, 2008.

[195] Dmitry Chirkin and Wolfgang Rhode. Propagating Leptons Through Matter with Muon Monte Carlo (MMC). *arXiv:hep-ph/0407075*, 2004.

[196] L. D. Landau and I. J. Pomeranchuk. The Limits of Applicability of the Theory of Bremsstrahlung by Electrons and of the Creation of Pairs at Large Energies. *Doklady Akademii Nauk SSSR*, 92(535), 1953.

[197] L. D. Landau and I. J. Pomeranchuk. Electron-Cascade Processes at Ultra-High Energies. *Doklady Akademii Nauk SSSR*, 92(735), 1953.

[198] A. B. Migdal. Bremsstrahlung and Pair Production in Condensed Media at High Energies. *Physical Review*, 103:1811–1820, Sep 1956. doi: 10.1103/PhysRev.103.1811. URL https://link.aps.org/doi/10.1103/PhysRev.103.1811.

[199] Lisa Gerhardt and Spencer R. Klein. Electron and Photon Interactions in the Regime of Strong Landau-Pomeranchuk-Migdal Suppression. *Physical Review D*, 82:074017, Oct 2010. doi: 10.1103/PhysRevD.82.074017. URL https://link.aps.org/doi/10.1103/PhysRevD.82.074017.

[200] W. Heitler. *Quantum Theory of Radiation*. Oxford University Press, London, 1954.

[201] C. Wiebusch. *The Detection of Faint Light in Deep Underwater Neutrino Telescopes*. PhD thesis, Rheinisch-Westfaelische Technische Hochschule Aachen, 1995.

[202] Leif Rädel. *Simulation Studies of the Cherenkov Light Yield from Relativistic Particles in High-Energy Neutrino Telescopes with Geant4*. Master's thesis, Rheinisch-Westfaelische Technische Hochschule Aachen, 2012.

[203] Marek P. Kowalski. *Search for Neutrino-Induced Cascades with the AMANDA-II Detector*. PhD thesis, Humboldt-Universität zu Berlin, Mathematisch-Naturwissenschaftliche Fakultät I, 2004.

[204] P. A. Cerenkov. Visible Radiation Produced by Electrons Moving in a Medium with Velocities Exceeding that of Light. *Physical Review*, 52:378–379, Aug 1937. doi: 10.1103/PhysRev.52.378. URL https://link.aps.org/doi/10.1103/PhysRev.52.378.

[205] Stephen G. Warren. Optical Constants of Ice from the Ultraviolet to the Microwave. *Applied Optics*, 23(8):1206–1225, Apr 1984. doi: 10.1364/AO.23.001206. URL http://ao.osa.org/abstract.cfm?URI=ao-23-8-1206.

[206] Leif Rädel and Christopher Wiebusch. Calculation of the Cherenkov Light Yield from Low Energetic Secondary Particles Accompanying High-Energy Muons in Ice and Water with Geant4 Simulations. *Astroparticle Physics*, 38:53 – 67, 2012. ISSN 0927-6505. doi: http://dx.doi.org/10.1016/j.astropartphys.2012.09.008. URL http://www.sciencedirect.com/science/article/pii/S0927650512001831.

[207] IceCube Collaboration. IceCube Gallery. http://icecube.wisc.edu/gallery/index, March 2018. URL http://icecube.wisc.edu/gallery/index.

[208] Ryan C. Bay et al. South Pole Paleowind from Automated Synthesis of Ice Code Records. *Journal of Geophysical Research (Atmospheres)*, 115:D14126, 2010.

[209] M. Ackermann et al. Optical Properties of Deep Glacial Ice at the South Pole. *Journal of Geophysical Research: Atmospheres (1984–2012)*, 111(D13), 7 2006. ISSN 2156-2202. doi: 10.1029/2005JD006687. URL http:https://doi.org/10.1029/2005JD006687.

[210] N. E. Bramall, R. C. Bay, K. Woschnagg, R. A. Rohde, and P. B. Price. A Deep

High-Resolution Optical Log of Dust, Ash, and Stratigraphy in South Pole Glacial Ice. *Geophysical Research Letters*, 32, 11 2005.

[211] M. G. Aartsen et al. Measurement of South Pole Ice Transparency with the IceCube LED Calibration System. *Nuclear Instruments and Methods in Physics Research A*, 711:73–89, 2013. doi: 10.1016/j.nima.2013.01.054.

[212] M. G. Aartsen et al. Evidence of Optical Anisotropy of the South Pole Ice. *Proceedings of ICRC2013 0580*, 2014. URL http://www.cbpf.br/%7Eicrc2013/papers/icrc2013-0580.pdf.

[213] P. B. Price, K. Woschnagg, and D. Chirkin. Age vs Depth of Glacial Ice at South Pole. *Geophysical Research Letters*, 27(14):2129–2132, 2000. ISSN 1944-8007. doi: 10.1029/2000GL011351. URL http://dx.doi.org/10.1029/2000GL011351.

[214] Craig F. Bohren and Donald R. Huffman. *Absorption and Scattering of Light by Small Particles*. Wiley-VCH Verlag GmbH, 2007. ISBN 9783527618156. doi: 10.1002/9783527618156. URL http://dx.doi.org/10.1002/9783527618156.

[215] D. Heck, G. Schatz, T. Thouw, J. Knapp, and J. N. Capdevielle. CORSIKA: A Monte Carlo Code to Simulate Extensive Air Showers. Technical report, Forschungszentrum Karlsruhe, 1998.

[216] Jakob van Santen. *Neutrino Interactions in IceCube above 1 TeV - Constraints on Atmospheric Charmed-Meson Production and Investigation of the Astrophysical Neutrino Flux with 2 Years of IceCube Data taken 2010–2012*. PhD thesis, University of Wisconsin-Madison, 2014.

[217] Askhat Gazizov and Marek P. Kowalski. ANIS: High Energy Neutrino Generator for Neutrino Telescopes. *Computer Physics Communications*, 172:203–213, 2005.

[218] J.-H. Koehne, K. Frantzen, M. Schmitz, T. Fuchs, W. Rhode, D. Chirkin, and J. Becker Tjus. PROPOSAL: A Tool for Propagation of Charged Leptons. *Computer Physics Communications*, 184(9):2070 – 2090, 2013. ISSN 0010-4655. doi: https://doi.org/10.1016/j.cpc.2013.04.001. URL http://www.sciencedirect.com/science/article/pii/S0010465513001355.

[219] S. Agostinelli et al. GEANT4: A Simulation Toolkit. *Nuclear Instruments and Methods in Physics Research A*, 506:250–303, 2003. doi: 10.1016/S0168-9002(03)01368-8.

[220] D. Chirkin et al. Photon Tracking with GPUs in IceCube. *Nuclear Instruments and Methods in Physics Research A*, 725(Supplement C):141 – 143, 2013. ISSN 0168-9002. doi: https://doi.org/10.1016/j.nima.2012.11.170. URL http://www.sciencedirect.com/science/article/pii/S0168900212015173.

[221] Johan Lundberg, Predrag Miocinovic, Kurt Woschnagg, et al. Light Tracking Through Ice and Water - Scattering and Absorption in Heterogeneous Media with PHOTONICS. *Nuclear Instruments and Methods in Physics Research A*, 581:619–631, 2007.

[222] Nathan Whitehorn, Jakob van Santen, and Sven Lafebre. Penalized Splines for Smooth Representation of High-Dimensional Monte Carlo Datasets. *Computer Physics Communications*, 184(9):2214 – 2220, 2013. ISSN 0010-4655. doi: http://dx.doi.org/10.1016/j.cpc.2013.04.008. URL http://www.sciencedirect.com/science/article/pii/S0010465513001434.

[223] R. Abbasi et al. Calibration and Characterization of the IceCube Photomultiplier Tube. *Nuclear Instruments and Methods in Physics Research A*, 618(1):139 – 152, 2010. ISSN 0168-9002. doi: https://doi.org/10.1016/j.nima.2010.03.102. URL http://www.sciencedirect.com/science/article/pii/S0168900210006662.

[224] Gerhard Bohm and Guenter Zech. *Introduction to Statistics and Data Analysis for Physicists*. Verlag Deutsches Elektronen-Synchrotron, 2010.

[225] Roger Barlow. *Statistics: A Guide to the Use Of Stastistical Methods in the Physical Sciences*. John Wiley & Sons, 2008.

[226] M. G. Aartsen et al. Energy Reconstruction Methods in the IceCube Neutrino Telescope. *Journal of Instrumentation*, 9(03):P03009, 2014. URL `http://stacks.iop.org/1748-0221/9/i=03/a=P03009`.

[227] C. L. Lawson and R. J. Hanson. *Solving Least Squares Problems*. Prentice-Hall, Englewood Cliffs, New Jersey, 1974. doi: 10.1137/1.9781611971217. URL `http://epubs.siam.org/doi/abs/10.1137/1.9781611971217`.

[228] John G. Learned and Sandip Pakvasa. Detecting Tau-Neutrino Oscillations at PeV Energies. *Astroparticle Physics*, 3:267–274, 1995. doi: 10.1016/0927-6505(94)00043-3.

[229] Patrick Hallen. *On the Measurement of High-Energy Tau Neutrinos with IceCube*. Master's thesis, Rheinisch-Westfaelische Technische Hochschule Aachen, 2013.

[230] D. Cowen et al. Tau Neutrinos in IceCube. *Journal of Physics: Conference Series*, 60(1): 227, 2007. URL `http://stacks.iop.org/1742-6596/60/i=1/a=048`.

[231] Marek P. Kowalski. On the Cherenkov Light Emission of Hadronic and Electro-Magnetic Cascades. AMANDA Internal Report 20020803, DESY Zeuthen, 2002.

[232] Paul Bourke. Distributing Points on a Sphere. `http://paulbourke.net/geometry/circlesphere/`, June 1996.

[233] Alan Stuart, Keith Ord, and Steven Arnold. *Kendall's Advanced Theory of Statistics, Classical Inference and the Linear Model (Volume 2A)*. Wiley, 2010.

[234] S. S. Wilks. The Large-Sample Distribution of the Likelihood Ratio for Testing Composite Hypotheses. *Annals of Mathematical Statistics*, 9(1):60–62, 1938. doi: 10.1214/aoms/1177732360.

[235] Gary J. Feldman and Robert D. Cousins. A Unified Approach to the Classical Statistical Analysis of Small Signals. *Physical Review D*, 57:3873–3889, 1998. doi: 10.1103/PhysRevD.57.3873.

[236] Sen Bodhisattva, Matthew Walker, and Michael Woodroofe. On the Unified Method with Nuisance Parameters. *Statistica Sinica*, 19:301–314, 2009.

[237] Glen Cowan, Kyle Cranmer, Eilam Gross, and Ofer Vitells. Asymptotic Formulae for Likelihood-Based Tests of New Physics. *European Physics Journal C*, 71:1554, 2011. doi: 10.1140/epjc/s10052-011-1554-0,10.1140/epjc/s10052-013-2501-z.

[238] Eun-Joo Ahn, Ralph Engel, Thomas K. Gaisser, Paolo Lipari, and Todor Stanev. Cosmic Ray Interaction Event Generator SIBYLL 2.1. *Physical Review D*, 80:094003, 2009. doi: 10.1103/PhysRevD.80.094003.

[239] Shirley Weishi Li, Mauricio Bustamante, and John F. Beacom. Echo Technique to Distinguish Flavors of Astrophysical Neutrinos. *arXiv:1606.06290 [astro-ph.HE]*, 2016.

[240] M. G. Aartsen et al. Measurement of Atmospheric Tau Neutrino Appearance with IceCube DeepCore. Paper in preparation.

[241] Hans P. Dembinski, Ralph Engel, Anatoli Fedynitch, Thomas Gaisser, Felix Riehn, and Todor Stanev. Data-Driven Model of the Cosmic-Ray Flux and Mass Composition from 10 GeV to 10^{11} GeV. *Proceedings of Science, 35th International Cosmic Ray Conference (ICRC 2017)*, page 533, 2017.

[242] Anatoli Fedynitch, Julia Becker Tjus, and Paolo Desiati. Influence of Hadronic Interaction Models and the Cosmic Ray Spectrum on the High Energy Atmospheric Muon and Neutrino Flux. *Physical Review D*, 86:114024, Dec 2012. doi: 10.1103/PhysRevD.86.114024. URL https://link.aps.org/doi/10.1103/PhysRevD.86.114024.

[243] Amanda Cooper-Sarkar, Philipp Mertsch, and Subir Sarkar. The High Energy Neutrino Cross-Section in the Standard Model and Its Uncertainty. *Journal of High Energy Physics*, 08:042, 2011. doi: 10.1007/JHEP08(2011)042.

[244] M. G. Aartsen et al. Measurement of the Multi-TeV Neutrino Cross Section with IceCube Using Earth Absorption. *Nature*, 2017. doi: 10.1038/nature24459.

[245] Thorsten Glüsenkamp. Probabilistic Treatment of the Uncertainty from the Finite Size of Weighted Monte Carlo Data. *arXiv:1712.01293 [physics.data-an]*, 2017.

[246] M. G. Aartsen et al. Multi-Flavour PeV Neutrino Search with IceCube. *Proceedings of Science (ICRC2017) 1002*, 2017. URL https://pos.sissa.it/cgi-bin/reader/contribution.cgi?id=PoS(ICRC2017)1002.

[247] M. G. Aartsen et al. All-flavor Multi-Channel Analysis of the Astrophysical Neutrino Spectrum with IceCube. *Proceedings of Science (ICRC2017) 0976*, 2017. URL https://pos.sissa.it/cgi-bin/reader/contribution.cgi?id=PoS(ICRC2017)0976.

[248] Marek P. Kowalski. Neutrino Astronomy with IceCube-Gen2. In *The Icecube Particle Astrophysics Symposium (IPA)*. University of Wisconsin-Madison, 2017.

[249] M. G. Aartsen et al. Improving the Search for High-Energy Tau Neutrino Interaction in IceCube. *Proceedings of Science (ICRC2017) 0973*, 2017. URL https://pos.sissa.it/cgi-bin/reader/contribution.cgi?id=PoS(ICRC2017)0973.

[250] M. G. Aartsen et al. Search for Astrophysical Tau Neutrinos with Improved Double Pulse Method. *Proceedings of Science (ICRC2017) 1009*, 2017. URL https://pos.sissa.it/cgi-bin/reader/contribution.cgi?id=PoS(ICRC2017)1009.

[251] M. G. Aartsen et al. IceCube-Gen2: A Vision for the Future of Neutrino Astronomy in Antarctica. *Proceedings of Science, Frontier Research in Astrophysics - II (FRAPWS 2016)*, page 004, 2017.

[252] P. Allison et al. Performance of Two Askaryan Radio Array Stations and First Results in the Search for Ultrahigh Energy Neutrinos. *Physical Review D*, 93(8):082003, 2016. doi: 10.1103/PhysRevD.93.082003.

[253] J. Nam and T. C. Liu. Feasibility of Antenna Array Experiment for Earth Skimming Tau-Neutrino Detection in Antarctica. *Proceedings of Science (ICRC2017) 0944*, 2017. URL https://pos.sissa.it/cgi-bin/reader/contribution.cgi?id=PoS(ICRC2017)0944.

[254] D. Gora et al. Sensitivity for Tau Neutrinos at PeV Energies and Beyond with the MAGIC Telescopes. *Proceedings of Science (ICRC2017) 0992*, 2017. URL https://pos.sissa.it/cgi-bin/reader/contribution.cgi?id=PoS(ICRC2017)0992.

[255] B.S. Acharya et al. Introducing the CTA Concept. *Astroparticle Physics*, 43:3 – 18, 2013. ISSN 0927-6505. doi: https://doi.org/10.1016/j.astropartphys.2013.01.007. URL http://www.sciencedirect.com/science/article/pii/S0927650513000169.

[256] R. Coniglione et al. The KM3NeT Neutrino Telescope. *Journal of Physics: Conference Series*, 632(1):012002, 2015. URL http://stacks.iop.org/1742-6596/632/i=1/a=012002.

[257] R. Bormuth. *Chasing Cosmic Tau Neutrinos in the Abyss*. PhD thesis, Leiden University,

2017.

[258] B. P. Abbott et al. Observation of Gravitational Waves from a Binary Black Hole Merger. *Physical Review Letters*, 116:061102, Feb 2016. doi: 10.1103/PhysRevLett.116.061102. URL https://link.aps.org/doi/10.1103/PhysRevLett.116.061102.

[259] S. Adrian-Martinez et al. High-Energy Neutrino Follow-Up Search of Gravitational Wave Event GW150914 with ANTARES and IceCube. *Physical Review D*, 93(12):122010, 2016. doi: 10.1103/PhysRevD.93.122010.

[260] Erik Blaufuss and Claudio Kopper. IceCube-170922A - IceCube Observation of a High-Energy Neutrino Candidate Event. *GCN Circular*, 21916, 2017. URL https://gcn.gsfc.nasa.gov/gcn3/21916.gcn3.

[261] Yasuyuki T. Tanaka, Sara Buson, and Daniel Kocevski. Fermi-LAT Detection of Increased Gamma-Ray Activity of TXS 0506+056, Located inside the IceCube-170922A Error Region. *The Astronomer's Telegram*, 10791, 2017. URL http://www.astronomerstelegram.org/?read=10791.

[262] Razmik Mirzoyan. First-Time Detection of VHE Gamma Rays by MAGIC from a Direction Consistent with the Recent EHE Neutrino Event IceCube-170922A. *The Astronomer's Telegram*, 10817, 2017. URL http://www.astronomerstelegram.org/?read=10817.

List of Figures

1.1 Comparison of the diffuse fluxes of cosmic rays, gamma rays, and neutrinos . . 1

2.1 Measured and predicted neutrino fluxes from natural sources 7
2.2 The all-particle cosmic-ray flux as a function of the energy per nucleus 9
2.3 Hillas diagram relating the magnetic field strength B and size R of a source . . 11
2.4 Sketch of an extensive air shower and suitable detection techniques 12
2.5 Measurement of the all-sky atmospheric muon spectrum above 10 TeV obtained from single muon events in the IceCube detector 13
2.6 Measurement of the conventional atmospheric neutrino flux with the IceCube detector 15
2.7 Dependence of the atmospheric and astrophysical neutrino fluxes on the energy and zenith angle 19
2.8 Theoretically possible astrophysical neutrino flavor compositions at Earth . . . 24
2.9 Astrophysical neutrino flavor compositions at Earth for select beyond-standard-model scenarios 25

3.1 Schematic view of the IceCube detector 27
3.2 Feynman graphs of deep-inelastic neutrino-nucleon scattering 28
3.3 Neutrino-nucleon cross sections as a function of the neutrino energy 29
3.4 Longitudinal shower profiles for visible energy losses of an electromagnetic cascade and a hadronic cascade 32
3.5 Sketch of the Cherenkov effect 33
3.6 Schematic view of the hexagonal IceCube detector layout 35
3.7 Schematic view and photo of the digital optical module 36
3.8 Scattering and absorption of light in South Pole ice 38
3.9 Event topologies in IceCube: single cascade, double cascade, and track 40
3.10 Sketch of the `millipede` unfolding 45

4.1 A simulated "double bang" event in the IceCube detector 47
4.2 Tau-neutrino topologies in IceCube 48
4.3 Sketch of the veto region and fiducial volume of the high-energy starting event selection 50
4.4 Neutrino effective areas for the high-energy starting event selection 51
4.5 Sketch of the topology estimators 55
4.6 Probability density distribution of the true energy asymmetry and true energy confinement 57
4.7 Probability density distribution of the true second cascade energy and the true tau decay length 59
4.8 Probability density distribution of the true total deposited energy as a function of the true tau decay length 59
4.9 Event classification scheme of the topology ID 61
4.10 Expected event rate distribution of the reconstructed energy asymmetry and reconstructed energy confinement 62
4.11 Expected event rate distribution of the reconstructed energy asymmetry and reconstructed energy confinement with respective selections 62

4.12 Expected event rate distribution of the reconstructed energy asymmetry and reconstructed energy confinement zoomed in with respective selections 63
4.13 Neutrino effective areas for the reconstructed event topology samples 65
4.14 Neutrino effective areas for the double cascade and double pulse samples . . . 67
4.15 Observable and resolution distributions of the total deposited energy and zenith angle for the total high-energy starting event sample 69
4.16 Observable and resolution distributions of the total deposited energy and length for the reconstructed double cascade sample 71
4.17 Median energy resolution and directional resolution as a function of the true tau decay length 72
4.18 Correlation of the total deposited energy and length 74
4.19 Tau-neutrino identification efficiency and purity as a function of the neutrino energy, the total deposited energy and the double cascade length 75
4.20 Signal probability density distribution for the reconstructed double cascade sample 77
4.21 Background probability density distribution for the reconstructed double cascade sample 77

5.1 Sketch of the ice anisotropy and tilt in the top view of the IceCube detector . 79
5.2 Sketch of the content of a cascade photo spline table 82
5.3 Sketch of an isotropic light source 84
5.4 Expected charge as a function of the azimuth angle for an isotropic source at $z = 0\,\mathrm{m}$ 85
5.5 Expected charge as a function of the azimuth angle for an isotropic source at $z = -400\,\mathrm{m}$ 85
5.6 Sketch of the effective distance 87
5.7 Effective distance parametrization for any cascade source at $z = -400\,\mathrm{m}$ and hypothetical DOMs at $\theta = 10°$ 88
5.8 Effective distance parametrization for any cascade source at $z = -400\,\mathrm{m}$ and hypothetical DOMs at $\theta = 90°$ 89
5.9 Sketch of how the effective distance parametrization is implemented 90
5.10 Example of the expected charge as a function of the azimuthal angle for a specific cascade source at a depth of $z = -400\,\mathrm{m}$ with an orientation of zenith $= 90°$ and azimuth $= 180°$ 92
5.11 Example of expected delay time distributions for the same cascade source as in Figure 5.10 93
5.12 Event view of a cascade in the artificial testing detector geometry and the standard IC86 geometry 94
5.13 Example of the expected charge as a function of the azimuthal angle for a source at $z = 0\,\mathrm{m}$ pointing along the x-axis of the detector and hypothetical DOMs at $\theta = 90°$ in comparison to direct simulation using the testing geometry 95
5.14 Example of the expected charge as a function of the azimuthal angle for a source at $z = 0\,\mathrm{m}$ pointing along the x-axis of the detector and hypothetical DOMs at $\theta = 10°$ in comparison to direct simulation using the testing geometry 95
5.15 Sketch of the relative orientation between cascade and DOMs for which detected waveforms are depicted 96
5.16 Waveforms of horizontally aligned DOMs around an exemplary source at $z = 0\,\mathrm{m}$ pointing along the x-axis of the detector in comparison to direct simulation using the standard IC86 geometry 97
5.17 Waveforms of vertically aligned DOMs around an exemplary source at $z = 0\,\mathrm{m}$ pointing along the x-axis of the detector in comparison to direct simulation using the standard IC86 geometry 97

5.18 Median length bias of reconstructed double cascade events depicted as a function of the zenith angle and the azimuth angle for different ice model combinations in simulation and reconstruction . . . 101
5.19 Misidentification fraction of reconstructed double cascade events as a function of the zenith angle and the azimuth angle for different ice model combinations in simulation and reconstruction . . . 101
5.20 Sketch of the different horizontal LEDs and flashing modes used for the anisotropy flasher data sample . . . 103
5.21 Location of selected flasher DOMs in the detector and sketch of the constructed double flasher event . . . 104
5.22 Sketch of two double flashers located on DeepCore and surrounded by IceCube strings . . . 105
5.23 Event view of an artificially constructed double flasher using experimental single flasher events . . . 106
5.24 Averaged waveforms of the double flasher event (A) at surrounding IceCube DOMs at the same depth as the flasher LEDs . . . 108
5.25 Averaged waveforms of the double flasher event (B) at surrounding IceCube DOMs at the same depth as the flasher LEDs . . . 108
5.26 Reconstructed length for double flasher event (A) and (B) using a short flasher duration of 10 ns and a long flasher duration of 70 ns . . . 112
5.27 Reconstructed length and reconstructed energy asymmetry of single and double flashers shown for simulation data and experimental data . . . 114

6.1 Astrophysical flavor composition at Earth measured by using multiple IceCube data samples in a global fit . . . 117
6.2 Observable distributions for the total high-energy starting event sample . . . 123
6.3 Observable distributions for the single cascade, double cascade, and track event samples . . . 124
6.4 Observable distributions including systematic error due to the uncertainty of the atmospheric muon flux . . . 128
6.5 Observable distributions including systematic error due to the uncertainty of the conventional atmospheric neutrino flux . . . 129
6.6 Observable distributions including systematic error due to the uncertainty of the prompt atmospheric neutrino flux . . . 130
6.7 Observable distributions including systematic error due to the uncertainty of the energy scale . . . 130
6.8 Observable distributions including systematic error due to the uncertainty of ice anisotropy scale . . . 131
6.9 Observable distributions for the single cascade, double cascade, and track event samples including systematic uncertainties . . . 135
6.10 Median astrophysical tau-neutrino flux detection sensitivity . . . 137
6.11 Median astrophysical tau-neutrino upper limit flux . . . 138
6.12 Comparison of the median profile likelihood scan of ϕ_{ν_τ} for fits using a binary or ternary topology ID and for different flux injections . . . 139
6.13 Median sensitivity to the astrophysical neutrino flavor composition using a binary and ternary topology ID . . . 141
6.14 Observable distributions of the double cascade sample for different spectral shapes of the astrophysical tau-neutrino flux . . . 144
6.15 Likelihood scan of the astrophysical tau-neutrino fraction and the spectral index 146
6.16 Likelihood scan of the astrophysical tau-neutrino fraction and the spectral cutoff energy . . . 147

6.17 Likelihood scan of the astrophysical tau-neutrino fraction and the spectral break energy . . . 147
6.18 Median detection sensitivity and expected number of signal and background events as a function of the spectral shape . . . 148

7.1 Event displays of all 49 high-energy starting events observed in six years with a deposited energy above 60 TeV . . . 151
7.2 Observable distributions of the total deposited energy and the zenith angle for experimental data and the sum of all Monte Carlo best-fit flux templates . . . 154
7.3 Observable distributions of the energy asymmetry and the energy confinement for experimental data and the sum of all Monte Carlo best-fit flux templates . 154
7.4 Observable distributions of the length separation and the topology ID for experimental data and the sum of all Monte Carlo best-fit flux templates . . . 154
7.5 Profile likelihood scan of the astrophysical tau-neutrino flux . . . 155
7.6 Profile likelihood scan of the astrophysical neutrino flavor composition at Earth 157
7.7 Deposited energy distributions expected for the benchmark $\sim E_\nu^{-2.3}$ and the observed $\sim E_\nu^{-2.9}$ energy spectra of the astrophysical neutrino flux . . . 159
7.8 Measured astrophysical neutrino spectrum for the differential unfolding and the single power-law model . . . 159
7.9 Comparison of the measured and theoretical astrophysical neutrino flavor compositions at Earth . . . 160

8.1 Projected sensitivity to the astrophysical neutrino flavor composition over 15 years of detector operation time . . . 163

A.1 Sketch of the starting point for the parametrization . . . 168
A.2 Length bias $L_{\text{reco}} - L_{\text{true}}$ . . . 169
A.3 Distribution and sinusoidal fit of the length bias as a function of the azimuth angle 170
A.4 Distribution and fit of the amplitude and offset as a function of the zenith angle 171
A.5 Distribution and linear fit of the length bias as a function of the magnitude of the ice anisotropy . . . 172
A.6 Sketch of the finish point for the parametrization . . . 174
A.7 Length bias as a function of the azimuth angle . . . 175
A.8 Reconstructed length of true single cascade events and true double cascade events as a function of the ice anisotropy realization . . . 176

C.1 Test statistic distribution for estimating the sensitivity to the astrophysical tau-neutrino flux . . . 180
C.2 Test statistic distributions for calculating the upper limit of the astrophysical tau-neutrino flux and the p-values of the astrophysical neutrino flavor composition for different source scenarios . . . 181
C.3 Illustration of the selected scan points at 68% and 95% confidence level in the phase space of the astrophysical neutrino flavor composition . . . 183
C.4 Test statistic distributions for each scan point at 68% and 95% confidence level as illustrated in Figure C.3 . . . 184
C.5 Coverage of the generated test statistic distribution at each scan point for which $\lambda \leq \lambda_{\text{obs}}$ as listed in Table C.1 . . . 184

List of Tables

2.1 Neutrino oscillation parameters from a three-flavor global fit 22

4.1 Fractions of true event topologies in each reconstructed event topology sample 66

5.1 Comparison of flasher and cascade light sources as building blocks of the double flasher and double cascade event topologies 107
5.2 Reconstructed length bias and resolution of experimental and simulated double flasher events 110
5.3 (Mis)identification fractions of experimental and simulated single flasher and double flasher events 115

6.1 Model parameters of the likelihood fit 121
6.2 Systematic uncertainties 126
6.3 Event expectations for the six-year high-energy starting event sample 134
6.4 Overview of different spectral fits of the diffuse astrophysical neutrino flux with the IceCube detector 142

7.1 Best-fit parameter values using the six-year high-energy starting event sample . 152

A.1 Deviation of the integrated signal and background event rates from the baseline case of the ice anisotropy 176

B.1 Selected DOMs of the single flasher LED anisotropy data sample collected in January, 2015 177

C.1 Astrophysical neutrino flavor compositions $\nu_e : \nu_\mu : \nu_\tau$ and observed test statistic λ_{obs} for each scan point as depicted in Figure C.3 183

List of Frequently Used Acronyms

AGN	active galactic nucleus
CC	charged current
CL	confidence level
CDF	cumulative distribution function
CMB	cosmic microwave background
CP(T)	charge conjugation, parity transformation, (time reversal)
CPU	central processing unit
dof	degrees of freedom
DOM	digital optical module
EAS	extensive air shower
FWHM	full width at half maximum
GPU	graphics processing unit
GRB	gamma-ray burst
GZK	K. Greisen, G. Zatsepin, V. Kuzmin; refers to a spectral cutoff of the cosmic ray flux
HESE	high-energy starting event
IACT	imaging atmospheric Cherenkov telescope
IC	IceCube
(P)ID	(particle) identifier
IH	inverted neutrino mass hierarchy
LED	light-emitting diode
LPM	L. Landau, I. Pomeranchuk, A. Migdal; refers to lepton propagation in matter
NC	neutral current
NH	normal neutrino mass hierarchy
PDF	probability density function, parton distribution function
pe	photoelectron
PMNS	B. Pontecorvo, Z. Maki, M. Nakagawa, S. Sakata; refers to neutrino mixing matrix
PMT	photomultiplier tube
RDE	relative DOM efficiency
SN(R)	supernova (remnant)
SPICE	South Pole ice
(UHE)CR	(ultra-high-energy) cosmic ray

Acknowledgements

This work was substantially supported by the Humboldt-Universität zu Berlin, the Deutsches Elektronen-Synchrotron Zeuthen, and the Konrad-Adenauer-Stiftung, as well as in parts by the Rheinische Friedrich-Wilhelms-Universität Bonn, the Deutscher Akademischer Austauschdienst, and the University of Wisconson-Madison. I would also like to thank the IceCube collaboration for sharing resources and knowledge and for many constructive meetings and discussions.

I would like to express my sincerest gratitude to my supervisors Marek Kowalski and Markus Ackermann for their continuous support and for enabling me to work on such an inspiring research topic. I would also like to thank my additional referees Sebastian Böser and Achim Stahl for having an interest in this dissertation and for offering their time to examine it.

In one way or another, this dissertation makes use of prior work achieved by several people who I would like to thank. Claudio Kopper and Nathan Whitehorn developed the high-energy starting event selection and have always been willing to answer any of my questions. Patrick Hallen developed the initial reconstruction algorithm for double cascade events. Nancy Wandowsky prepared a large amount of simulation data that she made selflessly available to others. Donglian Xu, Lutz Köpke, Christian Haack, and Albrecht Karle have contributed to the IceCube-internal review of my analysis. Lukas Lechner and Lars Mohrmann provided code snippets for reproducing some of their original figures. On countless occasions, Jakob van Santen, Hans Niederhausen, and Chris Weaver have helped me out with inspiring discussions and teaching moments. Alexander Stasik and Thomas Kintscher, among many others of the IceCube group at DESY, have always had an open ear for technical problems and have been supportive in solving them.

I am very grateful for having been at the South Pole in order to collect the single flasher LED anisotropy data sample used in this dissertation. I appreciate the support from Sebastian Böser, Marek Kowalski, and Dawn Williams in this endeavor. I would also like to thank my fellow IceCubers with whom I spent my time at the South Pole: Mike DuVernois, Stephan Richter, Erik Beiser, Elisa Pinat, Hans Niederhausen, Lionel Brayeur, Sam De Ridder, and James Casey.

I would like to thank Albrecht Karle and Francis Halzen for their invitation to spend the beginning of my time as a graduate student at the University of Wisconsin-Madion. I learned a lot during my stay, which was extremely useful for finishing this dissertation. I would also like to thank Kim Kreiger and Megan Madsen for their support in Madison, for marvelously organizing many collaboration meetings, and for keeping me entertained during the time between meetings.

I would like to thank numerous people for proof-reading parts of my thesis: Juliana Stachurska, Summer Blot, Federica Bradascio, Jakob van Santen, Thomas Kintscher, Robert Stein, Ludwig Rauch, Samridha Kunwar, Richard Hanson, Lukas Schulte, Stefan Bittihn, Sina Lenski, Lea Wrobel, and Carolin Kubaczka. I am especially grateful to Markus Ackermann, who almost read the entire thesis and provided valuable feedback, and to James Doing, who did read the entire thesis and also taught me about punctuation in the process.

Ich möchte mich bei Gernot Uhl bedanken, der mir als Referent in der Konrad-Adenauer-Stiftung stets mit Rat zur Seite stand. Ich bin meinen Eltern Meggy und Harald sowie meinem Bruder Dominique für ihre langjährige Unterstützung dankbar. Zu guter Letzt danke ich meiner Freundin Lena von ganzem Herzen für ihren niemals nachlassenden Rückhalt: Du hast mich auch in den langen und schwierigen Zeiten stets bekräftigt und unterstützt.

Selbstständigkeitserklärung

Ich erkläre, dass ich die vorliegende Dissertation selbständig und nur unter Verwendung der von mir gemäß § 7 Abs. 3 der Promotionsordnung der Mathematisch-Naturwissenschaftlichen Fakultät, veröffentlicht im Amtlichen Mitteilungsblatt der Humboldt-Universität zu Berlin Nr. 126/2014 am 18.11.2014, angegebenen Hilfsmittel angefertigt habe.

Berlin, den 11. April 2018 Marcel Usner